



HAL
open science

Generic approach of refrigerant HFC-134a emission modes from mobile air conditioning (MAC) systems

Yingzhong Yu

► **To cite this version:**

Yingzhong Yu. Generic approach of refrigerant HFC-134a emission modes from mobile air conditioning (MAC) systems. Engineering Sciences [physics]. École Nationale Supérieure des Mines de Paris, 2008. English. NNT : 2008ENMP1555 . pastel-00004889

HAL Id: pastel-00004889

<https://pastel.hal.science/pastel-00004889>

Submitted on 12 Mar 2009

HAL is a multi-disciplinary open access archive for the deposit and dissemination of scientific research documents, whether they are published or not. The documents may come from teaching and research institutions in France or abroad, or from public or private research centers.

L'archive ouverte pluridisciplinaire **HAL**, est destinée au dépôt et à la diffusion de documents scientifiques de niveau recherche, publiés ou non, émanant des établissements d'enseignement et de recherche français ou étrangers, des laboratoires publics ou privés.



ED n° 432 : « Sciences des Métiers de l'Ingénieur »

N° attribué par la bibliothèque

_____|_____|_____|_____|_____|_____|_____|_____|_____|_____|

T H E S E

pour obtenir le grade de
Docteur de l'Ecole Nationale Supérieure des Mines de Paris
Spécialité "Energétique"

présentée et soutenue publiquement par
Yingzhong YU
le 23 octobre 2008

**GENERIC APPROACH OF REFRIGERANT HFC-134a EMISSION
MODES FROM MOBILE AIR CONDITIONING (MAC) SYSTEMS
APPROCHE GENERIQUE DES MODES D'EMISSIONS DE HFC-134a
DES SYSTEMES DE CLIMATISATION AUTOMOBILE**

Directeur de thèse : Denis CLODIC

Jury :

M. D. MARCHIO – Mines ParisTech.....Président
M. S. MARAIS – URF Sciences et Université de RouenRapporteur
M. F. MEUNIER – CNAM.....Rapporteur
M. L. GAGNEPAIN – ADEME..... Examineur
M. D. CLODIC – Mines ParisTech..... Examineur

Acknowledgments

In thesis acknowledgements I would like to thank all those persons who have made my work in the CEP so fruitful.

First of all, I would like to thank my thesis director, Mr. Denis Clodic. He exemplifies the high quality scholarship to which I aspired. He guided me, gave me instructive comments and evaluation through every stage of the thesis.

I also express my deepest gratitude to Mrs. Anne-Marie Pougin for showering me with care and concerns. Her support is gratefully acknowledged.

This thesis has been supported by HUTCHINSON. My special thanks to Mr. Jean-Philippe Lemoine and Mr. Thierry Travers for their cooperation that provided me with solid support for obtaining experimental results to my work.

I wish to express my appreciation to David Sousa for his availability when I needed a helping hand and for his nice suggestions during the preparation of the thesis.

My very special thanks go to Franck Fayolle for his constant, friendly support, and help for the development and realization of test benches that are the basis of my research.

Sincere thanks are due to Lionel Palandre who leaded me to discover the interest of the research work, gave me important advice and encouragement.

I thank Assaad Zoughaib for his useful suggestions, which indeed helped improve this thesis.

My keen appreciation goes to Arnaud Tremoulet for his valuable assistance in the field. Without his help, the field work would not have been perfectly accomplished on time.

I would like to acknowledge Isabelle Morgado for her comments on uncertainty calculations and for her friendship.

Special thanks to Aline Garnier and Philippe Calvet who take care of administrative and computer matters, and so have greatly facilitated this research work.

I would also like to acknowledge all my colleagues in the CEP for their support and their friendship. I enjoyed the atmosphere.

Finally, I am thankful that my parents offered me the opportunity to come and study in France. I would like to express special thanks to my husband Li CHEN who always stays on my side and encourage me. I would like to thank my son Wanli for his love, which gives me courage and power. Without the support of family, I would never have succeeded.

Table of contents

Acknowledgments	1
Nomenclature	i
General introduction	1
CHAPTER 1 Context	3
1.1 Description of Mobile Air Conditioning System	5
1.2 Current Refrigerant HFC-134a Emissions	6
1.3 Classification of MAC Refrigerant Loss And Leakage Source.....	7
1.4 References.....	14
CHAPTER 2 Leak flow rate method	15
2.1 Leak flow rate measurements.....	19
2.1.1 Test method based on measurement of concentration in an accumulation volume	19
2.1.2 Test benches for systems and components.....	35
2.1.3 Leak flow rate measurements of MAC system and components in standstill mode	38
2.2 Correlation factor based on leakage behavior	45
2.2.1 Standstill mode tests considering the climate conditions	45
2.2.2 Analysis of running mode leakage.....	46
2.2.3 Standstill and running mode contribution	48
2.2.4 Fleet test – annual leakage of MAC system on vehicles by recovery operation	48
2.2.5 Establishing the correlation factor.....	51
2.3 References.....	53
CHAPTER 3 Emission predictions of hoses used in MAC systems	55
3.1 Introduction of polymer materials.....	59
3.1.1 The classification of polymers.....	60
3.1.2 Crystallization, melting, and glass transition phenomena	61
3.1.3 Polymers commonly used in MAC components.....	63
3.2 Gas permeation theory through polymers.....	64
3.2.1 Fundamentals of transport phenomena.....	64
3.2.2 Diffusion	64
3.2.3 Sorption.....	65
3.2.4 Permeability	67
3.3 Permeation tests through membrane samples	67
3.3.1 Test method for transport coefficients determination based on leak flow rate tests	67
3.3.2 Description and qualification of permeation test bench.....	68
3.3.3 Identification of transports coefficients	70
3.3.4 Permeation tests on membrane samples	71
3.3.5 Factors influencing transport coefficients	73
3.3.6 Basic hypothesis coming from membrane measurements.....	80
3.4 First approach to establish leakage behavior of MAC hoses.....	83
3.4.1 Conversion from membrane to tube form.....	83
3.4.2 Permeation tests of MAC hoses	84
3.4.3 Prediction model of MAC hoses	86
3.5 References.....	89
CHAPTER 4 Leakage behavior of fittings used in MAC systems	91
4.1 Introduction of seals commonly used in MAC systems	95
4.1.1 Basic O-ring description.....	95
4.2 Leakage sources from O-ring fittings	97
4.2.1 Permeation in polymers - Leakage by permeation through seal material	97
4.2.2 Gas transport in micro channels.....	100
4.3 Analysis of a radial O-ring sealing performance using the Finite Element Method (FEM)	106
4.3.1 Hypothesis for O-ring material.....	106
4.3.2 O-ring simulation model.....	108
4.3.3 Results and discussions	109

4.4	Establishment of Leak flow rate laws	117
4.4.1	Leakage behavior of an O-ring fitting	117
4.4.2	Leak flow rates of two separate modes	117
4.4.3	Analysis of leak flow rate contributions as a function of permeability.....	121
4.5	Complementary Analyses	122
4.5.1	Effect of torque on an axial-radial O-ring.....	122
4.5.2	Analysis of multiple O-rings	122
4.6	References.....	126
General Conclusions		128
APPENDIX - LEAK FLOW RATE OF MAC SYSTEMS AND COMPONENTS		133

Nomenclature

A	area	m^2
a	distance	m
b	distance	m
C	concentration	molm^{-3}
C	concentration of HFC-134a	ppm
c	compression set	%
c_1	pre-exponential factor for permeability coefficient of a given hose	
c_2	pressure influence factor for permeability coefficient of a given hose	
c_3	temperature influence factor for permeability coefficient of a given hose	
C_p	heat capacity at constant pressure	$\text{kJkg}^{-1}\text{K}^{-1}$
C_v	heat capacity at constant volume	$\text{kJkg}^{-1}\text{K}^{-1}$
D	diffusion coefficient	m^2s^{-1}
D_0	pre-exponential factor of diffusion	m^2s^{-1}
D	diameter	m
d	diameter	m
E	activation energy	kJmol^{-1}
e	thickness	m
f_c	modulation frequency	Hz
G	depth	m
H	height	m
ΔH	partial molar enthalpy of sorption	kJmol^{-1}
h	height	m
I_o	incident light	
J	molar flux	$\text{mols}^{-1}\text{m}^{-2}$
K	cell and gas dependent constant	
k	parameter for linear regression	
k_D	solubility coefficient	$\text{mol m}^{-3} \text{MPa}^{-1}$
L	length	m
l	length	m
M	molar mass	gmol^{-1}
\dot{m}	mass flow rate	Kgs^{-1}
n	number of moles	mol
n	sample number	
P	pressure	Pa

\bar{P}	average pressure	Pa
Pe	permeability coefficient	mol mm ⁻² s ⁻¹ MPa ⁻¹
Pe ₀	pre-exponential factor of permeation	mol mm ⁻² s ⁻¹ MPa ⁻¹
P ₀	vapor pressure at the temperature	Pa
Q	gas amount	mol
Q _v	volume flow rate	m ³ s ⁻¹
R _L	Resistance related to contact width	m ⁻¹
R _a	roughness average	m
R _q	root mean square roughness	m
r	radius	m
S	solubility coefficient	mol m ⁻³ MPa ⁻¹
S ₀	pre-exponential factor of sorption	mol m ⁻³ MPa ⁻¹
s	standard deviation	
T	temperature	K
t	time	s
u	uncertainty	
V	volume	m ³
v	velocity	ms ⁻¹
w	resolution	m
x	distance	m

Greek letters

κ	Constant of regression	
κ ₁	pre-exponential factor for permeability coefficient of a given material	
κ ₂	pressure influence factor for permeability coefficient of a given material	
κ ₃	temperature influence factor for permeability coefficient of a given material	
θ	time lag	s
β	slip factor	
δ	clearance	m
λ	length	m
μ	gas dynamic viscosity	μPa s
ξ	magnification	
ρ	density	kgm ⁻³
σ	stress	Pa
ε	shore A hardness	
υ	volume fraction of the dissolved gas	

χ	Flory-Huggins parameter
γ	parameter defining the inverse ratio between successive wavelengths in Weierstrass profile

Non dimensional numbers

Kn	Knudsen number
Re	Reynolds number

Constants

k_B	Boltzmann's constant(= 1.38×10^{-23})	kJK^{-1}
$M_{\text{HFC-134a}}$	molar mass of HFC-134a(=102.03)	gmol^{-1}
R	universal gas constant (= 8.314×10^3)	$\text{kJ kmol}^{-1} \text{K}^{-1}$
γ	gas constant of HFC-134a(=0.0815)	$\text{kJg}^{-1} \text{K}^{-1}$

Subscripts

accum	accumulation volume
amb	ambient
atm	atmospheric
ch	channel
c	critical
component	component
FreeVolume	free volume
upstream	upstream
downstream	downstream
D	diffusion
D	normal sorption mode
H	sorption into the excess free volume
inner	inner
m	mean free path
max	maximum
mol	molar
outer	outer
overall	overall
P	pressure
p	representative physical length scale
Pe	permeation
regression	regression

S	solubility
sound	sound

Superscripts

lateral	lateral
bottom	bottom
top	top

Abbreviations

ACEA	European Automobile Manufacturers' Association
ADEME	Environment and Energy Management Agency
CEP	Center for Energy and Processes
CFC-12	dichlorodifluoromethane
CIIR	Chloro Isobutene Isoprene Rubber
CR	Chloroprene Rubber
DN	Nominal Diameter
EPDM	Ethylene Propylene Diene Monomer
HFC-134a	1,1,1,2-tetrafluoroethane
HNBR	Hydrogenated Nitrile Butadiene Rubber
HP	High Pressure
IIR	Isobutene Isoprene Rubber
IR	Infrared
LFR	Leak flow rate
LP	Low Pressure
PA	Polyamide
PAG	Poly-alkyl-glycol
PAS	Photo-Acoustic Spectroscopy
PES	Polyethersulfone
PET	Polyethylene terephthalate
ppb	Parts per billion volume/volume equivalent to mol/mol
ppm	Parts per million volume/volume equivalent to mol/mol
PTFE	Polytetrafluoroethylene
TXV	Thermal Expansion Valve

General introduction

CFC-12 used in mobile air conditioning (MAC) system has been replaced by HFC-134a as of 1991 and by 1994 almost all new vehicles sold in developed countries used HFC-134a. The leakage behavior of MAC systems is still not fully understood. The aim of this research work is to establish a test method of leak flow rate measurement for MAC systems and components, and furthermore to give a generic approach of refrigerant emissions in MAC systems.

Background

A large number of MAC systems and components were required for this research work. In the context of ACEA/ARMINES research project for establishing the EU regulation 706/2007, leak flow rate measurements have been carried out and supply solid experimental data for this thesis. Research projects with ADEME have given complementary support for the analysis of emissions of MAC systems in running mode. Concerning the characterization of polymers for hoses and O-ring seals used in MAC system, it has been done with the cooperation of HUTCHINSON. Due to confidential issues, some results of this research are not disclosed in this thesis. Nevertheless, predictions of MAC system emissions are achievable based on tests and simulations performed in this work.

Outline of the thesis

Chapter 1 gives the context of MAC system emissions. Main types of emissions from the MAC system during the life cycle of the vehicle are classified. Regular leakages due to different MAC components are evaluated by explaining their design and sealing principles.

In Chapter 2, a laboratory test method, based on measurement of concentration in an accumulation volume, is introduced for determining the leak flow rate of MAC systems and components. Measurement accuracy is justified. Measurements in standstill mode and at several controlled temperatures are performed to compare the overall system leak flow rate and the sum of leak flow rates of all components. Simulation of temperature variation allows predicting the annual climate condition impacts for any climates. Running mode tests are also discussed to study the contribution of the running time of the system to the annual MAC system emissions. In order to verify the laboratory test method, recovery operations are performed on vehicles with an accuracy of ± 0.1 g. Based on results of laboratory tests and fleet tests, a correlation factor is established for MAC systems between real life emissions and laboratory tests.

Chapter 3 focuses on the emission provisions of hoses used in MAC systems. Permeation process of refrigerant through polymers is studied. Six polymers are characterized by determining their transport coefficients, especially the coefficients of permeability. Both temperature and pressure influences on permeability are analyzed based on experimental data in order to establish the relationship between permeability, temperature, and pressure. Prediction models have been developed to estimate the leak flow rate of hoses taking into consideration the T-P double effects.

Chapter 4 deals with the leakage behavior of fittings used in MAC systems. Typical O-ring seals are discussed and two leakage modes: permeation through sealing materials and gas flow through micro channels are distinguished. Sealing performance of a radial O-ring is studied in detail. With the help of Finite Elements Method, non-linear stress-strain behavior of polymers is taken into account. Main factors such as stress, maximum contact pressure, and contact width are analyzed based on numerical simulation results. Establishing the leakage behavior combining two leakage modes: permeation and leak through micro channels allows understanding the key points of emission dependence and improving the sealing performances.

CHAPTER 1

Context

List of Figures

Figure 1.1 Basic components of a MAC system and circuit of the refrigerant flow.....	5
Figure 1.2 Mobile air conditioning fleet evolution from 1990 to 2015 in the BAU scenario [IPC05].....	6
Figure 1.3 MAC refrigerant emissions from 1990 to 2015. [IPC05].	6
Figure 1.4 MAC refrigerant emissions from 1990 to 2015 in CO ₂ -eq. [IPC05].....	6
Figure 1.5 Cross section of a compressor.....	8
Figure 1.6 Details of a compressor shaft lip seal [SOU007].	8
Figure 1.7 Three different types of MAC (by courtesy of MAFLOW).	9
Figure 1.8 Cross section of crimps.....	9
Figure 1.9 Different types of crimps (by courtesy of MAFLOW).....	10
Figure 1.10 Typical connectors.	10
Figure 1.11 Condenser and the micro-channel structure.....	11
Figure 1.12 Evaporator and the micro-channel structure.....	11
Figure 1.13 Photo of “H block” type TXV.....	12
Figure 1.14 TXV structure.	12
Figure 1.15 Sealing technology of service valve (by courtesy of VENTREX).....	12

List of Tables

Table 1.1 Evolution of the CFC-12 and HFC-134a fleet [CLOD4].	6
Table 1.2 MAC refrigerants emissions [IPC05].	6
Table 1.3 MAC refrigerants emissions in CO ₂ _eq [IPC05].....	6

1.1 Description of Mobile Air Conditioning System

Mobile Air Conditioning system is an integrated system of components that provides cooling to vehicles. Any MAC system uses four basic parts as shown in Figure 1.1 :

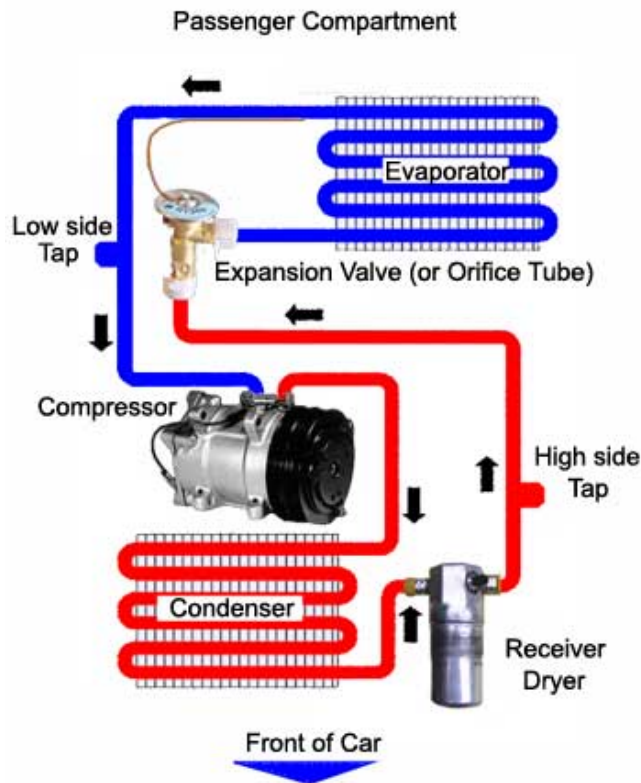


Figure 1.1 Basic components of a MAC system and circuit of the refrigerant flow.

- A belt-driven mechanical compressor, driven by the vehicle engine
- A thermal expansion valve (TXV) for the expansion of refrigerant from the high-pressure side to the low-pressure side; when the MAC system is stopped the TXV is open
- Two heat exchangers: condenser and evaporator;
- Suction line, discharge line, and liquid line that connect each component to the other making a single circuit.

The belt-driven compressor uses engine power to compress and circulate the refrigerant gas throughout the system. The refrigerant passes through the condenser on its way from the compressor outlet to the TXV. The condenser is located outside the passenger compartment, in front of the vehicle radiator.

The refrigerant passes from the TXV to the evaporator, and after passing through the evaporator circuit, it is returned to the compressor inlet. The evaporator is located inside the vehicle passenger compartment.

When the compressor starts running, it pulls refrigerant from the evaporator and forces it into the condenser, thus lowering the evaporator pressure and increasing the condenser pressure. When proper operating pressures have been established, the TXV expands the refrigerant to return to the evaporator, the refrigerant mass flow rate leaving the TXV equals the refrigerant mass flow rate entering the compressor in steady state regime. Under these conditions, the pressure at each point in the system will reach a constant level; the condenser pressure will be in the range of 1.3 to 2.7 MPa depending on the outdoor temperature and the refrigerant mass flow rate; the evaporator pressure is controlled by the TXV in the range of 0.3 to 0.4 MPa. Those values of pressures are related to HFC-134a refrigerant.

The pressure in the evaporator is controlled in order to be in any case just above the water frosting temperature (0°C). In summary the evaporation of refrigerant at low temperature removes heat from the vehicle cabin and heat is transferred through the compression at a temperature higher than the ambient air in front of the car under hood.

1.2 Current Refrigerant HFC-134a Emissions

As of 1991, CFC-12 used in MAC systems has been replaced by HFC-134a, which is non-ozone-depleting refrigerant, and by 1994 almost all new vehicles sold in developed countries used this refrigerant thanks to the enforcement of the Montreal Protocol.

Table 1.1 Evolution of the CFC-12 and HFC-134a fleet [IPC05].

Year	AC vehicle fleet (million)	
	CFC-12	HFC-134a
1990	212	-
1991	220	-
1992	229	0.7
1993	229	10
1994	222	27
1995	215	49
1996	206	74
1997	197	100
1998	186	128
1999	175	161
2000	163	198
2001	149	238
2002	134	285
2003	119	338

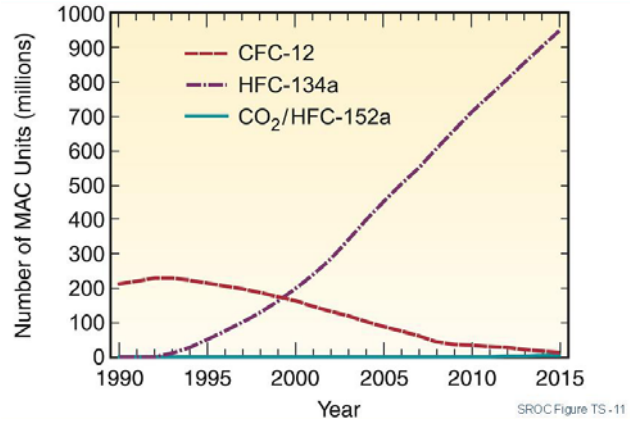


Figure 1.2 Mobile air conditioning fleet evolution from 1990 to 2015 in the BAU scenario [IPC05].

According to Table 1.1, the global CFC-12 fleet has decreased from about 212 million vehicles in 1990 to 119 million vehicles in 2003, while the HFC-134a fleet has increased from 1 million in 1992 up to 338 million in 2003. According to a business as usual (BAU) scenario, this value will reach 965 million by 2015 [IPC05]. Table 1.2 and Figure 1.3 present emission contributions for each refrigerant. Figure 1.3 and Figure 1.4 translate the emissions into equivalent CO₂ emissions based on refrigerant GWP. Due to the huge difference of their GWPs, Figure 1.4 shows the significant decrease of refrigerants emissions from 848 Mt CO₂-eq in 1990 to 610 Mt CO₂-eq in 2003. Hence, it is clear that the conversion from CFC-12 to HFC-134a has a positive effect for limiting global warming.

Table 1.2 MAC refrigerants emissions [IPC05].

Year	CFC-12 (tonne)	HFC-134a (tonne)	CO ₂ / HFC-152a (tonne)
1990	104,707	-	-
2003	63,431	73,956	-
2015	5192	175,174	934

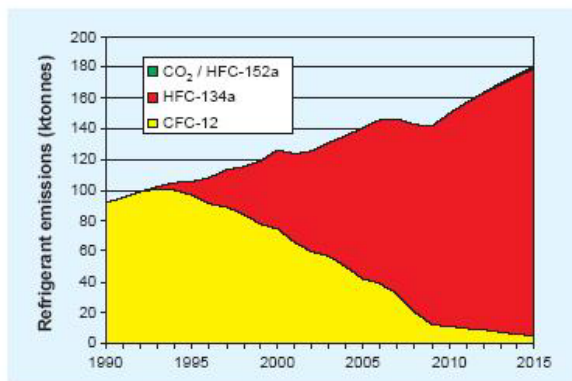


Figure 1.3 MAC refrigerant emissions from 1990 to 2015. [IPC05].

Table 1.3 MAC refrigerants emissions in CO₂-eq [IPC05].

Year	CFC-12 (MtCO ₂ -eq)	HFC-134a (MtCO ₂ -eq)	CO ₂ / HFC-152a (MtCO ₂ -eq)
1990	848	-	-
2003	514	96	-
2015	42	228	0.11

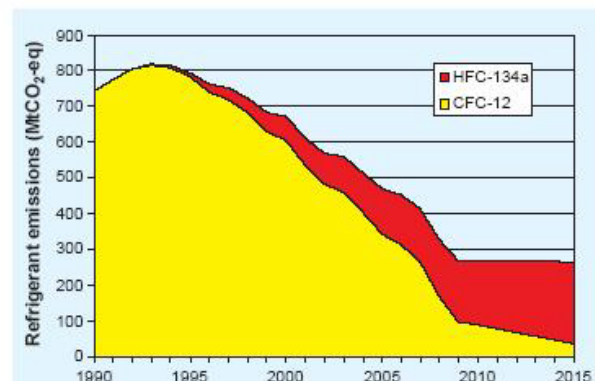


Figure 1.4 MAC refrigerant emissions from 1990 to 2015 in CO₂-eq. [IPC05].

1.3 Classification of MAC Refrigerant Loss And Leakage Source

According to test data, 50% to 60% of identified leaks are due to the compressor, hoses or crimps. Other leak sources are the expansion valve (TXV, or orifice tube), the receiver, the control switch, the service valve, etc. It could be said that almost all the MAC components leak.

There are six main types of leaks or emissions during the life cycle of the vehicle. Emissions have to be distinguished from leaks in this section. Leaks are coming from the clearance of mechanical part and from diffusion through elastomer materials. Emissions are linked to any operation on the MAC system where refrigerant is handled.

1. Emissions at initial charge of the MAC system

They are usually low due to the use of proper evacuation and refrigerant charging equipment. Nevertheless, the cylinder management leads to emissions varying from 1 to 10% depending on the recovery of the remaining refrigerant in the cylinder refrigerant heels.

2. Regular leak for new system

Hoses, O-rings, and the rotary shaft seal of the compressor are weak points in the sealing system constituting the essential points of regular refrigerant leakage from MAC systems. Leakage sources coming from this part will be discussed in detail.

3. Leaks due to leak tightness degradation

The aging process for leak tightness is difficult to simulate, even if some compressors tests show that the degradation seems low providing correct lubrication. Moreover, studies of vehicles older than 8 years are difficult to perform, and until now few specific data are available. Except that the refrigerant market for servicing indicates that leak degradation is the sole explanation for the use of those refrigerant quantities.

4. Irregular leakage caused by accident and component failures

Accidents are the main factors of the irregular leakage of MAC systems, such as the puncture of the condenser, exposition of hoses, damages of crimps, and road accidents.

5. Emissions during servicing

During the system servicing, leakages could occur due to the low skill, inadequate knowledge of operators, and improper use of refrigerant connecting lines from the refrigerant recovery & recharge equipment. Moreover, in some countries the use of small cans lead to significant emissions for servicing.

6. Emissions at end of life (EOL) of the system

The lack of recovery or the poor recovery efficiency of the refrigerant, when the system is disassembled at the end of lifetime, has to be taken into account.

Different leakage sources are discussed as follows.

- **Compressor**

The MAC compressor is belt-driven and with open shaft compressor. The shaft is linked to the engine by a pulley/belt system. The leak tightness is ensured by the rotary shaft seal, which plays an important role to guarantee the leak tightness of refrigerant gas both in running and standstill modes. Moreover, the coupling and the drive-belt pulley are two significant causes of the refrigerant leakage. In running mode, the belt presents the risk of pulling the shaft away from its centerline, which will decrease the tightness of the seal. The leak tightness depends also on appropriate lubrication of the seal.

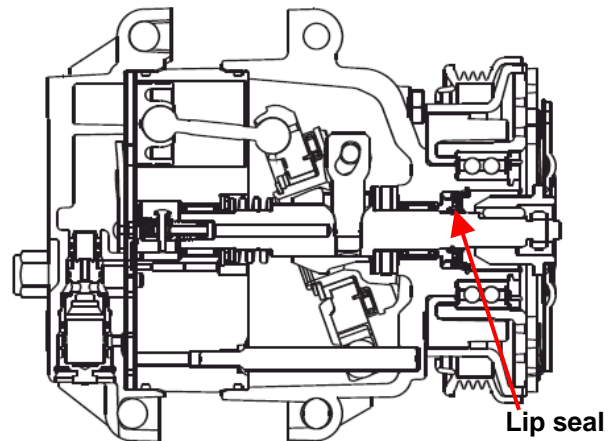


Figure 1.5 Cross section of a compressor.

The most common compressor shaft seals are of the lip seal type. The lip seal is typically made of highly saturated rubber encased in steel. One typical lip seal used in MAC compressors is illustrated in Figure 1.6. The first lip is placed at the high-pressure side and is responsible for sealing fluid in standstill mode. The second lip, normally made of PTFE, is placed at the low-pressure side (atmospheric pressure) and is responsible for sealing fluid in running mode. Shaft compressor is then inserted in the seal and, as a result, the two lips contact the shaft surface. Experimental results show a contribution of 50% of shaft seal to total leak flow rate of a compressor [SOU08].

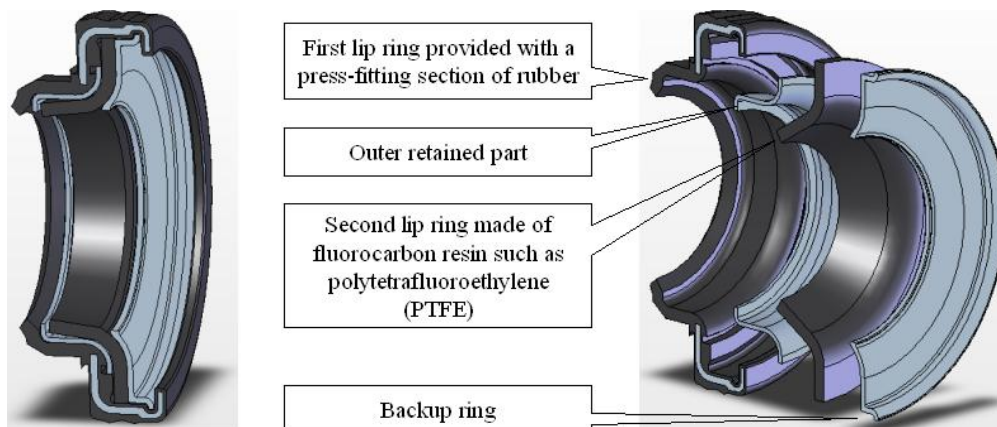


Figure 1.6 Details of a compressor shaft lip seal [SOU007].

Results on 24 new compressors at 40°C in standstill mode show that the leak flow rates vary from 5 to 22 g/yr leading to an average value of 14 g/yr. The shaft seal is not recovering its original leak tightness by aging and the leak flow rate of a compressor from an end of life vehicle may rise up to 180 g/yr. In running mode, leak flow rate strongly depends on the velocity of compressor and on the viscosity of lubrication oil [SOU07].

- **Hoses**

Flexible material hoses are used in MAC systems to connect different parts of the system because they absorb vibrations and accommodate movement of the engine. They are also a

source of significant refrigerant leak. Therefore it is important to choose low permeation hoses, which appear suitable for MAC systems.

The hose permeation is the most important parameter to determine the leakage of this component. Permeations of hoses are quite different depending on their material compositions and diameters. According to the results of several tests carried out during this research work (see Chapter 3), the presence of refrigerant oil has only a modest effect on permeation. That means that the leak flow rate of a hose with the charge of HFC-134a and oil is lower than the LFR of the same hose charged only of HFC-134a.

Different types of hose technologies are currently used in MAC systems.

All rubber, nylon composite (so called veneer) and nylon barrier hoses are currently used for MAC HFC-134a systems. Veneer hoses typically have a thin nylon inner liner that acts as permeation barrier. Nylon barrier hoses also use a thin nylon layer to prevent refrigerant permeation. However, they also contain a nitril or chloroprene (also known as neoprene) liner inside the nylon, which presents an excellent sealing against the coupling surface.

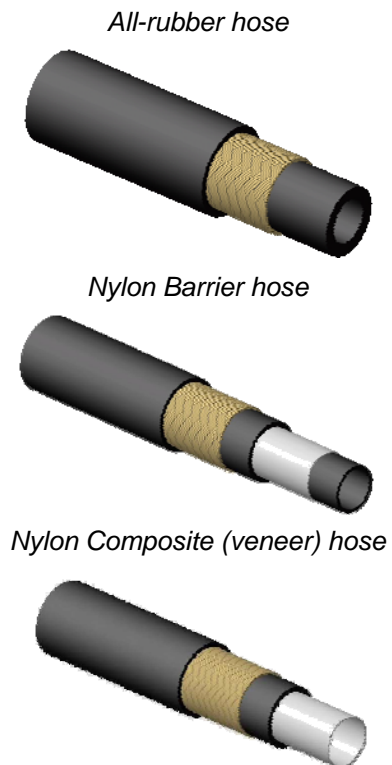


Figure 1.7 Three different types of MAC (by courtesy of MAFLOW).

All of liquid line, discharge line, and suction line have always elastomer sections as well as metallic ones. Commonly used internal diameters are 8, 10, 13, and 16 mm. All rubber hoses are often chosen for suction line due to their high performance in absorbing the compressor vibrations and noises.

- **Crimps**

Hose crimps are used to connect the flexible hose and the aluminum tube. The aluminum is exclusively chosen for its easiness of shaping and cost. An example of barrier hose is given in Figure 1.8 with the construction from inner to outer: a CR (Chloroprene Rubber) inner tube, a PA (polyamide) barrier, a layer of braid reinforcement, and an EPDM (Ethylene Propylene Diene Monomer) cover.

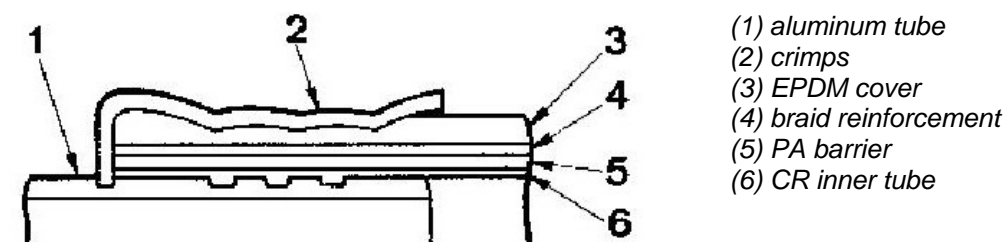


Figure 1.8 Cross section of crimps.

Figure 1.9 shows the 3D drawing and photo of different crimps. The designs vary according to materials used for the hose inner layer. In the case of veneer hose, the inner layer is rigid thermoplastic polymer (polyamide), seals (Figure 1.9(a) and (b)) are necessary to prevent

leakage. If the inner layers are soft elastomer as shown in Figure 1.9(c), glue or nothing is used instead of seals because of the good deformation of soft polymers.

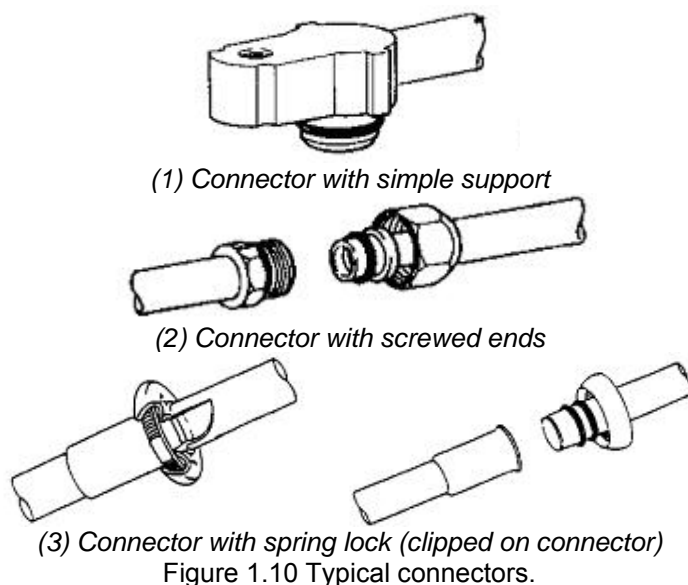


Figure 1.9 Different types of crimps (by courtesy of MAFLOW).

Possible leakage due to the crimps includes the damage of the crimps by accident, and progressive performance loss of the sealing technology. However, the leak flow rates of crimps are low (< 0.1 g/yr) compared to other MAC components.

- **Fittings/Connectors**

Connectors connect different parts of MAC systems. Assembly of connectors on the pipes or with the principal components has to guarantee a rigorous tightness to contain the pressures of the system in both standstill and running modes.



In general, connectors used for MAC systems consist of connectors with simple support, connectors with screwed ends, and connectors with spring lock (3) (see Figure 1.10).

Connectors with support (1) are the most commonly used on MAC systems. Advantages of those connectors are: easy assembly of the MAC components and simplification of the angular orientation of the pipes.

For connectors with screwed ends (2), torques applied to connectors seem to be more important to determine the emission level.

The spring lock connector (3) is the most practical for assembly but may be the most emissive due to the free rotation along the axis.

- **Evaporator and Condenser**

Since the mid '90s, condensers are made of louvered fins micro-channel tubes connected in parallel and in series. Some of them have integrated high-pressure receiver. Condensers are mounted in front of the radiator to take advantage of the forced air provided by the fan and the motion of the car. Figure 1.11 shows the principle of a multi-flow condenser and the micro-channel structure. Evaporator could be of plate-and-fin technology or, recently, of the same louvered-micro-channel technology as the condenser, but with a specific arrangement for refrigerant distribution. Figure 1.12 shows a multi-tank evaporator and the micro-channel structure. Both of them are fully brazed and leak tight, and the emission level is assumed lower than 0.1 g/yr.

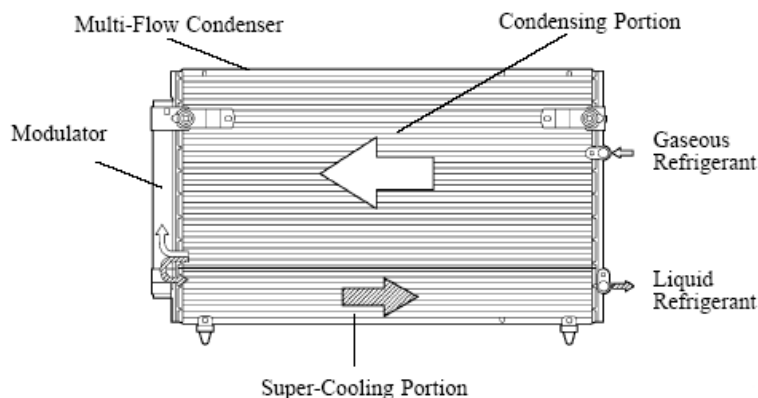


Figure 1.11 Condenser and the micro-channel structure



Figure 1.12 Evaporator and the micro-channel structure

The condenser is the highest risk component in case of crashes or stone hits because it is placed in the vehicle front end. A thrown stone can destroy the surface of one of the flat tubes that will then corrode at the point of impact. At the end of a period of time, leakage will take place. When the condenser is damaged, 100% of the refrigerant is lost. According to Valéo Clim Service nearly 7000 condensers have been replaced in 2002.

- **Thermal Expansion Valve (TXV)**

The function of a TXV is to expand the refrigerant from the condensation pressure to the evaporation pressure to control the refrigerant flow depending on the cooling needs. "H block" type TXV (Figure 1.13) is commonly used in MAC systems. It is located between evaporator inlet and outlet tubes, the liquid line, the compressor, and sealed by O-rings at each tube. Figure 1.14 shows the structure of a TXV. The valve diaphragm senses the

temperature and controls the refrigerant flow rate to the evaporator. When the operating pin pushes the ball away, the connection between the inlet side of the liquid line and the outlet side to the evaporator is connected so that gas can pass through. The valve spring is used to put the ball to the initial position when the connection is closed. As shown in Figures 1.13 and 1.14, not only leakage emissions are due to four O-ring seals but also to the top-side sensing parts which are also assembled by seals.



Figure 1.13 Photo of "H block" type TXV.

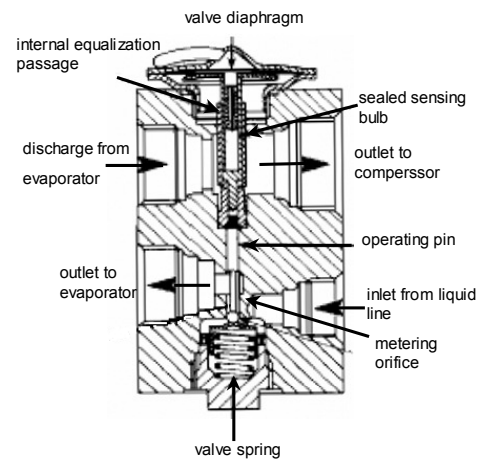


Figure 1.14 TXV structure.

- **Service valve**

Figures 1.15 illustrates the cross section of the service valve with its usual location on suction line for low pressure and liquid line for high pressure in order to charge the refrigerant to the MAC system or to recover it. Generally two seals are mounted with the purpose of improving the valve leak tightness. They are respectively:

- a micro lip seal inside the valve core, which protects the refrigerant from leaking by the force of the spring,
- a barrel seal, which is deformed by the valve housing when fixing the valve core inside the valve body,
- additionally, the cap is also a complementary prevention to the refrigerant leakage.

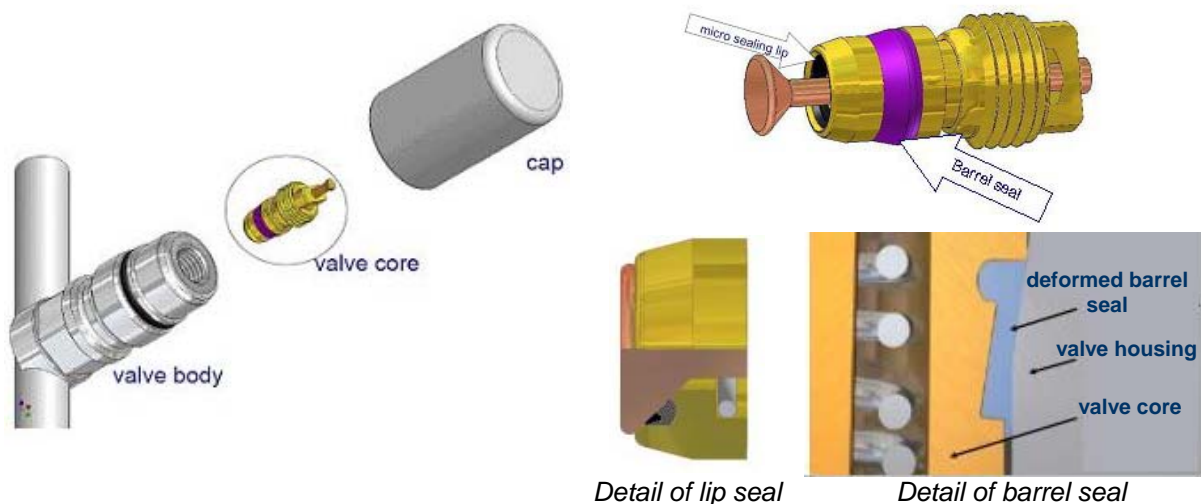


Figure 1.15 Sealing technology of service valve (by courtesy of VENTREX).

- **High pressure sensor**

A MAC system is equipped with a high-pressure sensor, which senses the pressure of the refrigerant discharged from the compressor and controls the fan coupled to condenser. As shown in Figure 1.16, an O-ring seal is used to seal the part by screwing the pressure sensor on the tube.



Figure 1.16 High-pressure sensor.

- **Other factors**

Compressors require a lubricant to protect its internal moving parts and ensure its operation. Lubrication oil (PAG Poly-alkyl-glycol) presents a better suitability with HFC-134a. Additionally, lubrication oil has a positive effect on leak flow rates of the MAC system since the fluid viscosity of lubrication oil is quite higher than that of refrigerant gas.

To conclude, the leakage phenomena are quite complex and depend on many factors: the refrigerant temperature and pressure; environment factors such as vibrations; the geometry and material of each component of the MAC system; torques applied to fittings, assembly process of the system, etc. This thesis focuses on the research of regular leak from new MAC systems and investigates emission predictions from those systems.

1.4 References

- [IPC05] IPCC Special report. 2005. Safeguarding the ozone layer and the global climate system. Issues related to hydrofluorocarbons and perfluorocarbons. Cambridge University Press. ISBN 13 978-0-521-68206-0.
- [SOU07] Sousa, D., Denis, C., 2007. Measurement of mobile AC compressor fugitive emissions in running mode. 6th EDF/LMS workshop: Role and effect of contact surfaces in dynamic sealing. Poitiers, France, 2007.
- [SOU08] Sousa, D., Denis, C., 2007. Sealing performance of a Mobile AC compressor shaft seal. 2008 International compressor engineering and refrigeration and air conditioning conferences. Purdue, USA, July 14-17, 2008

CHAPTER 2

Leak flow rate method

List of Figures

Figure 2.1 Scheme of the measurement system.....	19
Figure 2.2 IR spectrophotometry Uras-14 measurement principle (by courtesy of ABB).....	21
Figure 2.3 Simplified layout of the IR photo-acoustic (PAS).....	22
Figure 2.4 PAS Innova-1314 Measurement principle (by courtesy of Innova).....	22
Figure 2.5 Flowchart of test protocol.....	25
Figure 2.6 Standardized gas of HFC-134a/N ₂	25
Figure 2.7 HFC-134a calibrated leak.....	25
Figure 2.8 Volume calibration data.....	26
Figure 2.9 Temperature and pressure variation vs. time.....	28
Figure 2.10 Tolerance band as a function of temperature.....	29
Figure 2.11 Concentration measurement and LFR.....	31
Figure 2.12 Uncertainty contributions on leak flow rate measurement.....	32
Figure 2.13 Measurement uncertainties as a function of the sample size.....	33
Figure 2.14 Relative uncertainty of LFR vs. test duration (system test bench).....	34
Figure 2.15 Relative uncertainty of LFR vs. test duration (component test bench).....	34
Figure 2.16 Test bench for system measurements.....	35
Figure 2.17 System test mini-shed for running mode tests.....	36
Figure 2.18 Layout of the component measurement test bench.....	37
Figure 2.19 Layout of component measurement test bench.....	37
Figure 2.20 Test bench for component leakage measurement.....	38
Figure 2.21 MAC system installed on a duckboard for LFR test.....	39
Figure 2.22 Concentration measurements during preconditioning.....	39
Figure 2.23 LFRs of 10 MAC systems vs. pressure.....	39
Figure 2.24 MAC system cut into parts making macro-components.....	40
Figure 2.25 Welded end and connecting tube going through the wall of the cell.....	40
Figure 2.26 Wrapped welding.....	40
Figure 2.27 Leak detector.....	40
Figure 2.28 LFR contribution of components for system b.....	41
Figure 2.29 LFRs of crimps.....	42
Figure 2.30 LFRs of TXV.....	42
Figure 2.31 LFRs of compressor.....	43
Figure 2.32 Regression curves for systems and sum of macro-components.....	44
Figure 2.33 Daily average temperature of Seville.....	45
Figure 2.34 Test by simulating real climatic conditions.....	45
Figure 2.35 LFR of MAC system and regression curve.....	46
Figure 2.36 Test results in running mode for system V1 and system V2.....	47
Figure 2.37 Refrigerant Recovery equipment.....	49
Figure 2.38 Refrigerant loss during 9 months.....	50
Figure 2.39 Results of fleet tests.....	51
Figure 2.40 Establishing the correlation factor.....	52

List of Tables

Table 2.1 Accuracies of different apparatuses.....	20
Table 2.2 Comparison between IR spectrophotometer and IR PAS.....	23
Table 2.3 Statistical analysis of the slope.....	31
Table 2.4 Uncertainty budget for a given example.....	32
Table 2.5 Required sample size and measurement duration for 1 g/yr.....	33
Table 2.6 LFRs of 10 MAC systems.....	39
Table 2.7 LFRs of components of MAC system b.....	41
Table 2.8 LFRs of 6 crimps.....	42
Table 2.9 LFRs of 10 TXV.....	42
Table 2.10 LFRs of 10 compressors.....	43
Table 2.11 LFRs and linear regression.....	43
Table 2.12 LFRs of MAC system X at 3 different temperatures.....	46
Table 2.13 Annual LFR for systems V1, V2, and V3.....	47
Table 2.14 LFRs contribution in standstill and in running mode.....	48
Table 2.15 Results of charge and recovery operation.....	50
Table 2.16 Annual loss of Refrigerant – Vehicles A.....	50
Table 2.17 Average annual losses for 10 types of vehicles.....	51
Table 2.18 Arithmetical average LFRs of system A-J.....	51
Table 2.19 Annual LFR predictions of 3 MAC systems based on the method of correlation factor.....	52

2.1 Leak flow rate measurements

2.1.1 Test method based on measurement of concentration in an accumulation volume

The method used to determine the leak flow rate (LFR) [CLO04b],[CLO96] is based on Equation (2.1).

$$\dot{m}_{HFC-134a} = M_{HFC-134a} \cdot \frac{\partial n_{HFC-134a}}{\partial t} \quad (2.1)$$

Where,

$$n_{HFC-134a} = n_{total} \cdot C = \frac{P_{amb} \cdot V_{accum}}{R \cdot T_{amb}} \cdot C \quad (2.2)$$

The mass flow rate is the product of molar mass and the derivative of the number of moles of HFC-134a along the time in a tight volume, the test chamber. The perfect gas law is used to take into account the small variations of pressure and temperature inside the test chamber. According to Equation (2.2), the following parameters need to be determined for leak flow rate calculation: the accumulation volume of the test chamber, the temperature and the pressure inside the test chamber, and the evolution of concentration along the time.

As shown in Figure 2.1, the test bench is composed of an accumulation volume at atmospheric pressure (Figure 2.1) where the component to be analyzed is installed and connected to a HFC-134a boiler generating a given level of pressure inside the component. For system measurement, the operation becomes simpler because the refrigerant is directly charged in the MAC system. The temperature of the component is controlled by heat resistance and fans, in order to be maintained always above the saturated temperature of HFC-134a at the test pressure.

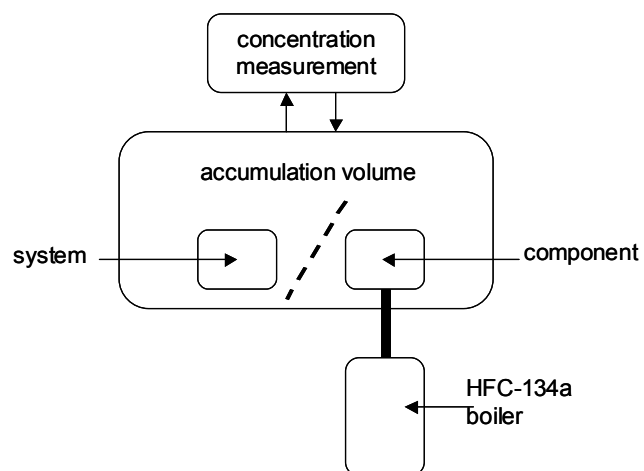


Figure 2.1 Scheme of the measurement system.

The concentration analyzer is connected to the accumulation volume by a closed circuit and measures continuously the accumulated concentration of HFC-134a inside the volume.

Knowing:

- the volume of the accumulation volume,
- the time,
- the concentration at each time step, and
- using Equations (2.1) and (2.2), the leak flow rate of can be calculated.

2.1.1.1 Concentration measurement methods

In order to measure leak flow rates in the range of 10^{-8} to 10^{-4} mole/s, four different types of apparatuses can be possibly used to measure the refrigerant concentration inside control volumes. Those apparatuses are based on different physical principles:

- mass spectrometry,
- gas chromatography,
- infrared spectrophotometer,
- Infrared photo-acoustic spectroscopy.

Accuracies of the different techniques are indicated in Table 1.1.

Table 2.1 Accuracies of different apparatuses.

Apparatuses	Mass spectrometer	Gas chromatography	Infrared photo-acoustic spectroscopy	Infrared spectrophotometry
Accuracy	± 1 ppb	± 1 ppb	± 0.01 ppm	± 0.5 ppm

Mass spectrometry

Mass spectrometry allows the mass measurement of molecules. The five basic parts of any mass spectrometer are:

- a vacuum system,
- a sample introduction device,
- an ionization source,
- a mass analyzer, and
- an ion detector.

A mass spectrometer determines the molecular weight of chemical compounds by ionizing, separating, and measuring molecular ions according to their mass-to-charge ratio (m/z). The ions are generated in the ionization source by inducing either the loss or the gain of a charge (e.g. electron ejection, protonation, or deprotonation). Once the ions are formed in the gas phase they can be electrostatically directed into a mass analyzer, separated according to mass, and finally detected. The result of ionization, ion separation, and detection is a mass spectrum that provides molecular weight or even structural information.

Gas chromatography

Gas chromatography is widely used in all chemical and processes laboratories. It is a reference method used to measure atmospheric concentration of a tracer gas. The accuracy is one of the best of all the methods (± 1 ppb).

The only difficulty associated to gas chromatography is related to the sampling method, which implies uncertainties on the concentration of the sample compared to the concentration in the control volume. Also a significant delay could occur between the sampling and the analysis depending on the design of the measurement system. However, this method can be used for MAC systems.

Infrared spectrophotometer

The principle of the non-dispersive infrared spectrophotometry method uses characteristics of individual gases when absorbing specific infrared wavelength when infrared light is radiated to the sample gas. The monitor measures the composition and concentration by

analysis of the absorbed wavelengths. The method that uses the infrared rays of all wavelengths radiated from the light source is referred to as "non-dispersive."

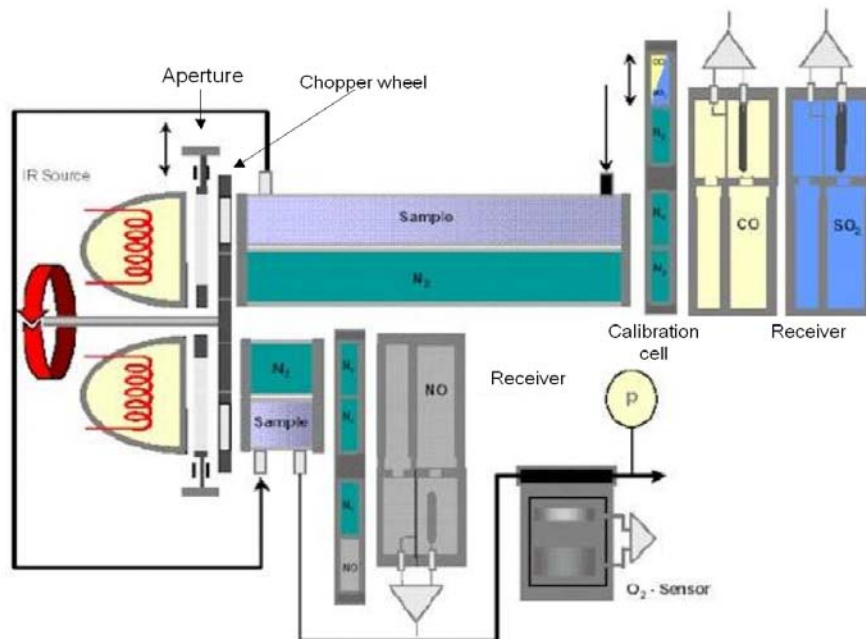


Figure 2.2 IR spectrophotometry Uras-14 measurement principle (by courtesy of ABB).

Figure 2.2 presents the measurement principle of IR spectrophotometry Uras-14. The photometer consists of an infrared source, the emissions of which reach a sample cell via a chopper wheel. The sample cell is in the shape of a tube divided by a wall into sample and reference sides. Two equal-energy infrared beams are directed through these two sides. The measurement effect produced in the receiver is a pressure effect resulting from the chopper frequency, received by a diaphragm capacitor and converted into an electrical signal by a pre-amplifier. The quantity of absorbed infrared radiation is proportional to the absorbing gas concentration. The receiver is a two-layer device. The back of the receiver has an optically transparent window so that any residual radiation can reach a second receiver that is sensitive to a second sample component. By adding a second beam path with an emitter, sample cell, and receivers, the photometer can measure 1 to 4 sample components at the same time.

Concerning the calibration, zero point calibration can be carried out with inert gas (N_2). The end point calibration necessitates gas-filled calibration cells or test gas mixture.

Infrared photo-acoustic spectroscopy (IR PAS)

The photo-acoustic effect is based on the conversion of light energy into sound energy, and a sound-measuring device detects the signal.

The gas to be measured is irradiated by modulated light of a pre-selected wavelength. Radiation absorbed by the molecule from a modulated infrared light beam is efficiently converted into heat energy of the gas molecules, and therefore a temperature and pressure increase in the gas. The pressure will result in an acoustic wave, which can be detected by a sound-measuring device, such as a microphone. The sound pressure, P_{sound} , can be calculated using the Equation 2.3.

$$P_{sound} = \frac{K \left(\frac{C_p}{C_v} - 1 \right) \cdot C \cdot I_o}{f_c} \quad (2.3)$$

where, K is a cell and gas dependent constant

C_p and C_v are heat capacities at constant pressure and volume

C is the gas concentration

f_c is the modulation frequency

I_o is incident light

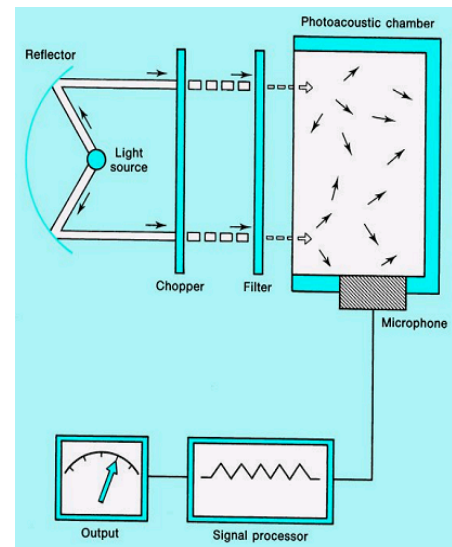


Figure 2.3 Simplified layout of the IR photo-acoustic (PAS).

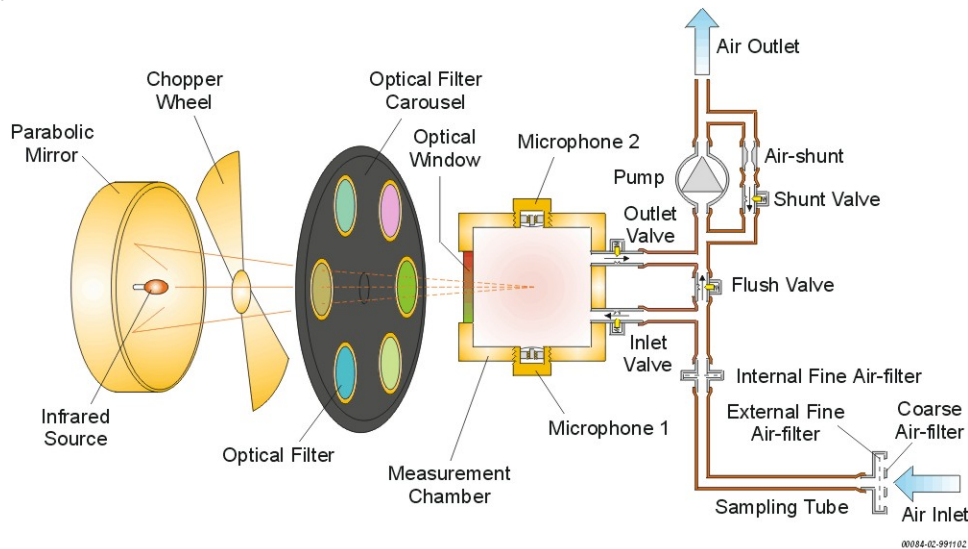


Figure 2.4 PAS Innova-1314 Measurement principle (by courtesy of Innova).

The IR PAS system presented here, named Innova-1314, is optimized for the quantitative detection of the gas concentration. As illustrated in Figure 2.4, the instrument uses a heated nickel-chrome wire as its infrared radiation source. The light from the source is focused by an ellipsoidal mirror, modulated with a mechanical chopper, which pulsates it, and passes through one of the optical filters in the wheel before entering the photo-acoustic gas cell. The filter allows irradiating the specific gas with the exact wavelength it absorbs best.

The pump draws a sample from the sampling point through the air-filter to flush out the “old” sample in the measurement system and replace it with a new sample. The “new” sample is hermetically sealed in the analysis cell by closing the inlet and outlet valves. The IR radiation is absorbed by the gas and generates heat and pressure variations in the closed cell. A pair of microphones mounted in the cell walls measures this acoustic signal. By selecting an appropriate resonant mode of opposite phase, the difference signal of the two microphones results in a doubling of the signal amplitude and noise reduction. The electrical signals from the microphones are amplified and added together before being sent to an analogue-to-digital converter. The digital signal is then converted to the concentration of the monitored gas sample present in the cell. The filter wheel turns so that light is transmitted through the next optical filter, and the new signal is measured.

The first calibration of the monitor is done just after the installation of the optical filters. Recalibration is accomplished by introducing the standardized concentration.

Comparison between the IR spectrophotometer (Uras-14) and PAS (Innova-1314)

Gas chromatography, IR spectrophotometer, and IR PAS are the three methods that could possibly be used at atmospheric pressure. Moreover, IR spectrophotometer and IR PAS are two powerful techniques commonly used to measure small absorptions and can be applied to detect trace gases in ambient air at atmospheric pressure. Both gas monitoring systems are available at the Center for Energy and Processes of Ecole des Mines in Paris and present a high accuracy, reliability, and stability. Table 2.2 makes some comparisons of IR spectrophotometer (Uras-14) and IR PAS (Innova –1314) specifications.

Table 2.2 Comparison between and IR spectrophotometer and IR PAS.

Specification	Concentration measurement	
	IR spectrophotometer (Uras-14)	IR PAS (Innova –1314)
Gas sample	Gas sample at atmospheric pressure	
Calibration	Zero and end point calibration with gas mixture & automatic calibration by means of internal calibration cell	Zero and end point calibration with gas mixture
Cross-compensation	Capable	
Measurement cell volume	Around 40 cm ³	3 cm ³
Measurement cell status	Open	Closed
Operation mode	Continuous scan	Step scan and nearly continuous scan
Stability	≤ 1% of measured value per week	Change in sensitivity at 25°C: <10%/600 yrs
Detection limit	0.5 ppm	10 ppb
Measuring range	Two ranges: 0-50 ppm, 0-500 ppm	100 000 times of detection limit
Response-time	1~2 min.	5-20 sec for one gas

According to the measurement principle of monitors, both are suitable for concentration measurement of gas in ambient air at atmospheric pressure and can measure as many samples as necessary.

Calibration can be done at least at zero and end point. Additionally, Uras-14 is equipped with an internal calibration cell for automatic calibration. As many gases absorb well in the IR area, it is often necessary to compensate for interfering components. For instance, CO₂ and H₂O often initiates cross sensitivity in the infrared spectrum. Uras-14 and Innova-1314 take this interference problem into consideration. All the cross-compensation factors are calibrated and stored in the monitor during the calibration.

Uras-14 is especially suitable for the continuous-scan mode. Innova-1314 is capable of operating in both step scan and nearly continuous modes, which means that each step of scan is performed one after the other. When measuring several samples of components simultaneously, Innova-1314 can be easily used to measure the concentration alternatively. Due to the high power pump of Uras-14, measurement is not limited by the distance between the accumulation volume and the analyzer, which is not the case for Innova-1314.

Concerning the stability, instruments based on PAS are quite stable because of the use of one of the most stable transducers: microphones. The two microphones enable to minimize interference from vibration.

The volume of the measurement cell Innova-1314 (3 cm³) is smaller than that of the Uras-14 (40 cm³). Because of its volume, the Innova cell can be emptied quickly; the samples of gases are small and so the response time is short.

Concerning HFC-134a measurements, the detection limit is 0.5 ppm for Uras-14 and 10 ppb for PAS Innova-1314, so that PAS Innova-1314 offers a higher sensitivity for concentration detection. However, because of the limit of resolution (1%) of PAS Innova-1314, it is better to perform low concentration measurement with Innova-1314. For long test period with rapid increase of concentration, Uras-14 is more convenient.

More extended comparison has been made [MOR07] not only theoretically but also experimentally by I. Morgado for the development of leak standard [MOR08]. Based on the operating principle, the photo-acoustic detection is more direct than the spectrophotometer. Microphones used in the PAS to detect the acoustic pressure generated by gas are extremely linear in a wide range of sound pressure. Their detection limits are defined as twice the detection limit of the pressure sensor, which is about the μPa . For HFC-134a, a sound pressure around the μPa corresponds to a concentration detection limit around 15 nmol.mol⁻¹. However, for the spectrophotometer, the pressure sensor is not linear. The signal is converted numerically and linearized. In terms of measuring environment, thus, the spectrophotometer seems to be more efficient to attenuate the noise signal. A series of experimental data show that the repeatability and linearity are about 10 times better than that of the spectrophotometer, at low concentrations.

2.1.1.2 Testing protocol

The test protocol for leak flow rate measurements is described step by step in Figure 2.5.

Step 1: Standardization of the concentration measurement apparatus

The first step is to verify the concentration measurement apparatus. As shown in Figure 2.5, a standardized concentration of HFC-134a in nitrogen (delivered by accredited companies) is connected to the measurement apparatus, and the measured value is compared to the standardized concentration. This verification is repeated with a second higher concentration. These two measurements verify both the offset and the linearity of the measurements of concentration by the apparatus.

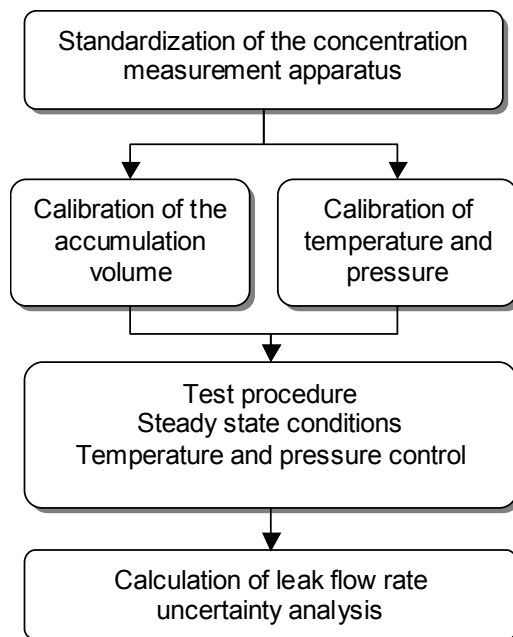


Figure 2.5 Flowchart of test protocol.

Step 2-1: Calibration of the test chamber

The uncertainty of the LFR is directly related to the uncertainties on the free volume of the test chamber. First the volume is calculated based on the geometric descriptions. Then a standard calibrated leak (see Figure 2.7), which has been calibrated on a specific test chamber, is installed inside the test chamber to be calibrated.

Figure 2.8 gives an example of calibration of the accumulation volume. The calibrated leak is measured at constant temperature of 26°C. As indicated in the figure, all parameters such as temperature, pressure, and concentration inside the test chamber are recorded at each time step. The leak flow rate of calibrated leak at 26°C is known as 51.1 g/yr. The accumulation volume can be obtained by reverse calculation of the mass flow rate, which is expressed by Equation (2.4) and consequently its uncertainty is established, which will be discussed in the following section.



Figure 2.6 Standardized gas of HFC-134a/N₂.



Figure 2.7 HFC-134a calibrated leak.

$$V_{accum} = \frac{\dot{m}_{HFC-134a}}{\frac{M_{HFC-134a} P_{amb}}{RT_{amb}} \frac{\partial C}{\partial t}} \quad (2.4)$$

Step 2-2: Calibration of temperature and pressure sensors

As shown in Equation (2.2), both temperature and pressure values inside the test chamber contribute to the LFR value. Before installation in the test bench, temperature and pressure sensors are carefully calibrated. The accuracy of both sensors is established through their calibration, which will be discussed later.

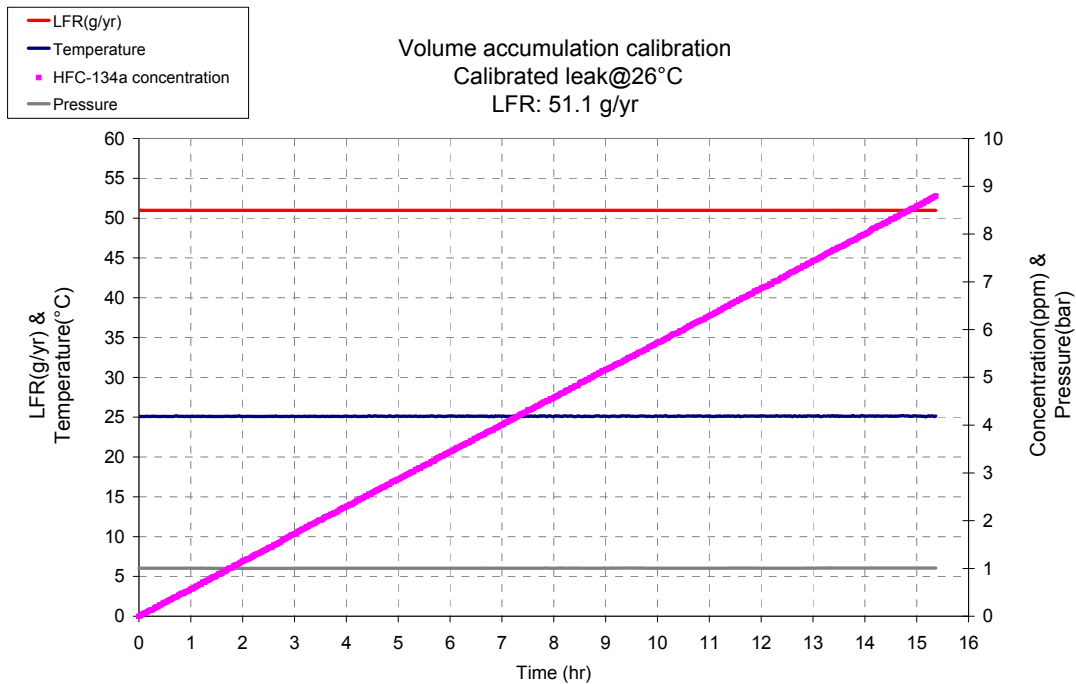


Figure 2.8 Volume calibration data.

Step 3: Testing procedure

After installation of the test sample, the test chamber is closed and then rinsed by a reference gas (reconstructed air: 80% N₂ + 20% O₂) in order to exclude all possible suspicious particles and guarantee the accuracy of measurement. The pressure is kept at atmospheric pressure. The temperature is maintained constant as well as during the test period. At each time interval, concentration, temperature, and pressure are recorded by the data acquisition system.

Tests can be performed either at a single temperature and pressure or at several temperatures and pressures. It is better to use at least three measurement points in order to verify the LFR variations according to saturating pressures.

Step 4: Calculation of leak flow rate

Based on Equations (2.1) and (2.2), the leak flow rate is calculated and the measurement uncertainty is established. Estimation on the uncertainty of leak flow rate test plays an important role, which indicates the reliability of a measurement, so that we will focus on the uncertainty analysis.

Other considerations

Repeatability

Repeatability is the property verified by using exactly identical procedures, identical testing systems, identical operators, and identical measurement apparatuses for identical components and to verify that identical results are obtained.

Reproducibility

Reproducibility is the property that verifies different variations either in the measurement operation or in the components to be tested. Reproducibility conditions mean independent test results are obtained with the same method on identical test items in different laboratories by different operators using different equipment.

Sample size

Accuracy of measurement has to be seen in the light of statistic measurements and not based on a too limited number of samples. When measuring the concentration in a control volume, when the raise of concentration is constant, the LFR is in steady state. Three to four points are the minimum sampling numbers. Some apparatuses can make hundreds of samplings within a measurement period from 10 to 12 hours, and so the statistical accuracy is significantly improved (see § 2.1.1.3).

2.1.1.3 Uncertainty analysis of LFR measurement

Based on the principle of indirect measurements from the propagation of distributions, the uncertainty of leak flow rate is achievable [GUI93]. Since the temperature and pressure are maintained constant during the test, the leak flow rate of the component under test can be calculated according to Equations (2.1) and (2.2). All these uncertainty sources and their influences will be analyzed based on the experimental data (presented in Figure 2.10 and Figure 2.11).

Identification of each uncertainty source

Two contributors to measurement uncertainties are distinguished here.

- **Type A:** this type of uncertainty can be determined statistically by measuring the dispersion of values obtained from well-chosen standard deviation of samples. In other words, the uncertainty of type A is quantified by calculating the standard deviation from repeated measurements.
- **Type B:** this type of uncertainty must be determined by non-statistical methods. Type B contributor will be the uncertainty of the reference standards and reference materials, which can never be picked up statistically.

The functional relationship between the leak flow rate (\dot{m}) and the input quantities

($T_{amb}, P_{amb}, V_{accum}, \frac{\partial C}{\partial t}$) is given by Equation (2.5).

$$\dot{m} = f(x_i) = f(T_{amb}, P_{amb}, V_{accum}, \frac{\partial C}{\partial t}) \quad (2.5)$$

The total uncertainty of the leak flow rate is a combination of 4 uncertainty components. By applying the law of propagation, the combined standard uncertainty of the mass flow is written in Equation (2.6):

$$u(m) = \sqrt{\left(\frac{\partial \dot{m}}{\partial V_{accum}}\right)^2 u^2(V_{accum}) + \left(\frac{\partial \dot{m}}{\partial T_{amb}}\right)^2 u^2(T_{amb}) + \left(\frac{\partial \dot{m}}{\partial P_{amb}}\right)^2 u^2(P_{amb}) + \left(\frac{\partial \dot{m}}{\partial C/\partial t}\right)^2 u^2(\partial C/\partial t)} \quad (2.6)$$

Therefore, the standard relative uncertainty is calculated according to Equation (2.7).

$$\frac{u_{\dot{m}}}{\dot{m}_{HFC-134a}} = \sqrt{\left(\frac{u_{V_{accum}}}{V_{accum}}\right)^2 + \left(\frac{u_{T_{amb}}}{T_{amb}}\right)^2 + \left(\frac{u_{P_{amb}}}{P_{amb}}\right)^2 + \left(\frac{u_{\partial C/\partial t}}{\partial C/\partial t}\right)^2} \quad (2.7)$$

Each uncertainty source is analyzed in detail as follows.

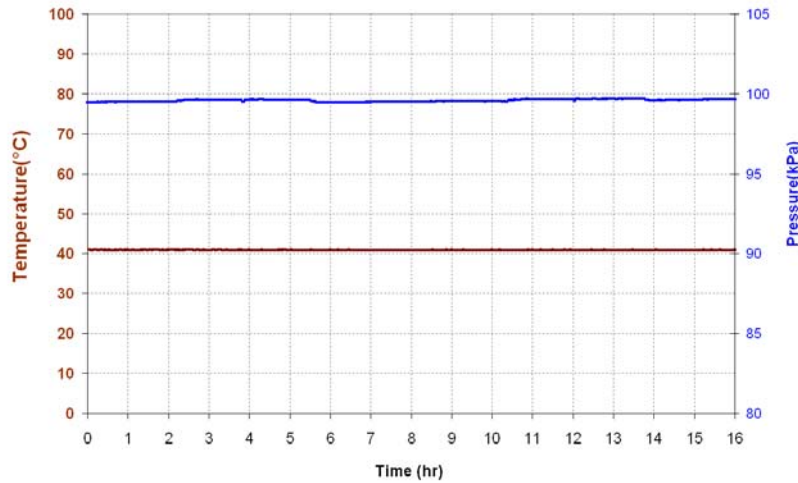


Figure 2.9 Temperature and pressure variation vs. time.

(1) Temperature inside the test chamber

According to manufacturer's specifications, the tolerance for a temperature sensor Pt100 of class A is written as: $\Delta T = 0.15 + 0.002 \times |T|$, where T is the measured temperature in °C. Figure 2.10 shows the tolerance with regards of measured temperature. The uniform distribution is applied to obtain Type B uncertainty estimate. Knowing the limits of temperature values, the uncertainty is estimated by Equation (2.8) using the assumption of a rectangular distribution for the temperature variation.

$$u_{T(\text{typeB})} = \frac{\Delta T}{\sqrt{3}} \quad (2.8)$$

The standard uncertainty of Ttype A means the repeatability standard deviation s_T , which can be obtained by statistic analysis of n observations of temperature. As shown in Figure 2.9, a series of temperature values are recorded during the test.

$$u_{T(\text{typeA})} = s_T = \sqrt{\frac{\sum_{i=1}^n (T_i - \bar{T})^2}{n-1}} \quad (2.9)$$

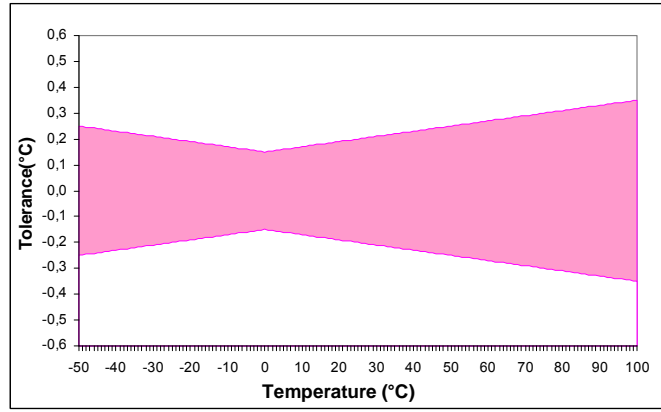


Figure 2.10 Tolerance band as a function of temperature.

Therefore, the uncertainty of the temperature u_T can be determined by combining the uncertainties of Type A and Type B using the technique of root mean square sum:

$$u_T = \sqrt{u_{T(\text{typeA})}^2 + u_{T(\text{typeB})}^2} = \sqrt{\frac{\sum_{i=1}^n (T_i - \bar{T})^2}{n-1} + \left(\frac{\Delta T}{\sqrt{3}}\right)^2} \quad (2.10)$$

Based on the temperature data shown in Figure 2.9, a mean value of 40.64°C and a standard deviation of 0.035°C are obtained.

$$u_T = \sqrt{u_{T(\text{typeA})}^2 + u_{T(\text{typeB})}^2} = \sqrt{s_T^2 + \left(\frac{\Delta T}{\sqrt{3}}\right)^2} = \sqrt{0.035^2 + \left(\frac{0.15 + 0.002 * 40.64}{\sqrt{3}}\right)^2} = 0.14^\circ\text{C} \quad (2.11)$$

Relative standard uncertainty is obtained by dividing the uncertainty by the mean temperature value:

$$\frac{u_T}{T} = \frac{0.14}{273.15 + 40.64} = 4.5 \times 10^{-4} \quad (2.12)$$

(2) Pressure inside the test chamber

Depending on the same principle, the uncertainty of the ambient pressure value is measured by using a pressure sensor of 0-200 kPa abs, which has an accuracy of 0.2% of full scale. The estimated uncertainty of type B can be calculated:

$$u_{P(\text{typeB})} = \frac{0.2\% \times 2 \cdot 10^5 \text{ Pa}}{\sqrt{3}} = \frac{400 \text{ Pa}}{\sqrt{3}} \quad (2.13)$$

The Type A uncertainty is obtained based on the data given by Figure 2.10. The uncertainty coming from the pressure is expressed by Equation (2.14).

$$u_P = \sqrt{u_{P(\text{typeA})}^2 + u_{P(\text{typeB})}^2} = \sqrt{\frac{\sum_{i=1}^n (P_i - \bar{P})^2}{n-1} + \left(\frac{400}{\sqrt{3}}\right)^2} \quad (2.14)$$

From the pressure data shown in Figure 2.9, a mean value of 99731 Pa and a standard deviation of 368 Pa are obtained.

$$u_P = \sqrt{u_{P(\text{typeA})}^2 + u_{P(\text{typeB})}^2} = \sqrt{s_P^2 + \left(\frac{400}{\sqrt{3}}\right)^2} = \sqrt{287^2 + \left(\frac{400}{\sqrt{3}}\right)^2} = 368 \text{ Pa} \quad (2.15)$$

The relative pressure uncertainty is:

$$\frac{u_P}{P} = \frac{368}{99731} = 3.7 \times 10^{-3} \quad (2.16)$$

(3) The accumulation volume

The accumulation volume consists of two parts: the free volume of the test chamber before installation of a MAC system or a component and the volume of the system/component, calculated by Equation (2.17).

$$V_{\text{accum}} = V_{\text{FreeVolume}} - V_{\text{component}} \quad (2.17)$$

The free volume of the test chamber is determined using a calibrated leak (Figure 2.7). The calibrated leak has been installed inside the test chamber and measured at constant temperature of 26°C, at which temperature the leak flow rate is already known (51.1 g/yr). The obtained leak flow rate value helps to calculate the free volume. This calibration step leads to an uncertainty of about 6%. Moreover, the volume of the system/component can only be obtained by geometrical measurement of all components, some of which include many complex parts. As a result, its uncertainty rises up to 20%. Nevertheless, the uncertainty of this part is negligible compared to the huge free volume inside the test chamber. As demonstrated in Equation (2.18), the relative combined standard uncertainty of the accumulation volume is 6%.

$$\frac{u_{V_{\text{accum}}}}{V_{\text{accum}}} = \frac{\sqrt{u_{V_{\text{FreeVolume}}}^2 + u_{V_{\text{component}}}^2}}{V_{\text{accum}}} = 0.06 \quad (2.18)$$

(4) Concentration vs. time $\frac{\partial C}{\partial t}$

As illustrated in Figure 2.11, the concentration evolution according to time is recorded at each time interval. By definition, C_i is a linear function of t_i : $\hat{C}_i = \hat{a} + \hat{b}t_i$, where $b = \frac{\partial C}{\partial t}$ is the slope of the line. As shown in Figure 2.11, a set of data values (t_i, C_i) is observed by continuous measurement. The basic technique for determining the term $\frac{\partial C}{\partial t}$ is the method of least squares, which ensures that the value fits the sample data best, in the sense of minimizing the sum of squared residuals.

The standard error of the regression is written as:

$$s_{\text{regression}} = \sqrt{\frac{\sum (C_i - \hat{C}_i)^2}{n - 2}} \quad (2.19)$$

where,

n is the number of samples

$\sum (C_i - \hat{C}_i)^2$ is the sum of squared residuals.

Without taking into account errors in t , the standard error of the slope ($\frac{\partial C}{\partial t}$), which should not to be confused with the standard error of the regression ($s_{regression}$), is calculated as follows:

$$s_{DC} = \sqrt{\frac{s_{regression}^2}{\sum (t_i - \bar{t})^2}} \quad (2.20)$$

where,

t_i is the time of the measurement

\bar{t} is the mean of all t_i

Equation (2.20) shows that a high degree of variation of t_i makes for a small standard deviation $s_{\partial C / \partial t}$. The results of linear regression analysis are indicated in Table 2.3.

Table 2.3 Statistical analysis of the slope.

Variable	Value(ppms ⁻¹)	Standard deviation(ppms ⁻¹)
$\frac{\partial C}{\partial t}$	1.3×10^{-4}	2.3×10^{-8}

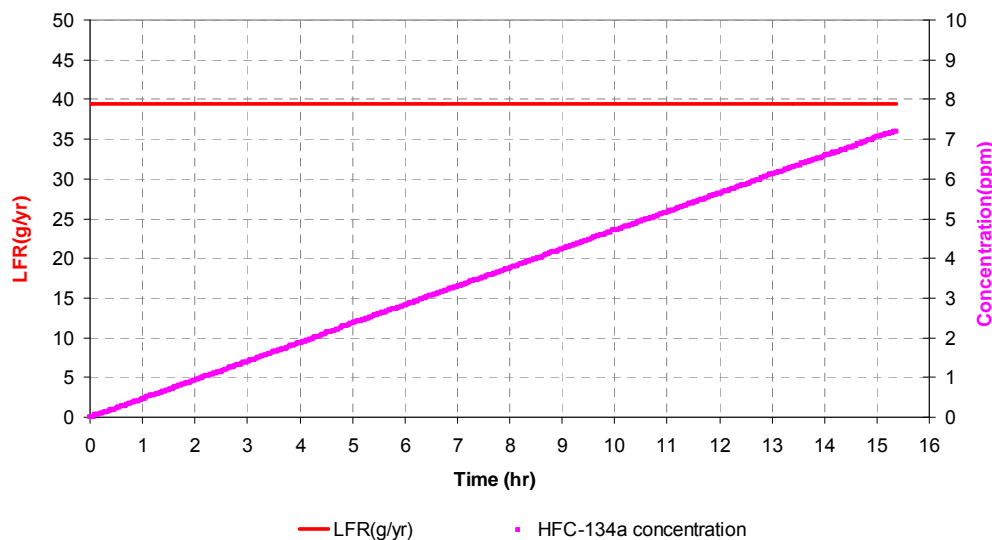


Figure 2.11 Concentration measurement and LFR.

Calculation of the combined standard uncertainty

Table 2.4 summarizes the mean and relative standard uncertainties of all input values that lead to a leak flow rate of 39.5 g/yr with a relative uncertainty of 6%.

Table 2.4 Uncertainty budget for a given example.

Parameter	Mean Value x_i	Standard uncertainty u_{x_i}	Relative standard uncertainty u_{x_i} / x_i
V_{accum} (m ³)	2.443	0.147	0.06
T_{amb} (K)	313.79	0.14	0.00045
P_{amb} (Pa)	99731	368	0.0037
$\frac{\partial C}{\partial t}$ (ppm)	1.3×10^{-4}	2.3×10^{-8}	0.00018

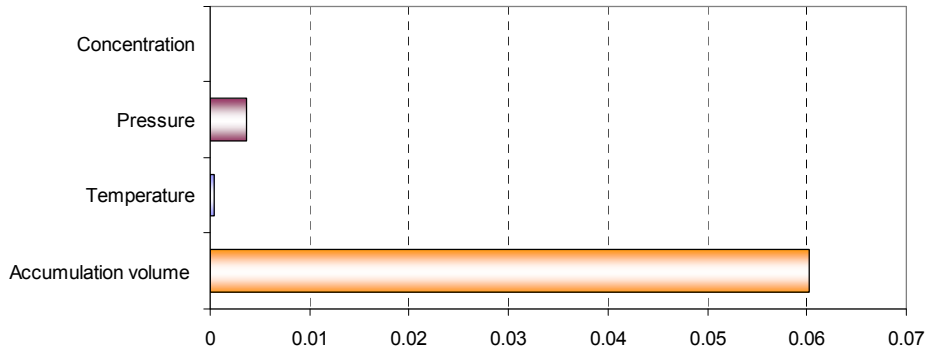


Figure 2.12 Uncertainty contributions on leak flow rate measurement.

As shown in Figure 2.12, the contribution of the accumulation volume in the test chamber to the overall uncertainty is by far the largest, which is followed by the pressure in the cell.

Moreover, with large sample sizes the contribution of $\frac{\partial C}{\partial t}$ is relatively small. Hence, the uncertainty associated to concentration evolution depends on the sample size on standard uncertainty of the flow rate. Longer test duration leads to more concentration samples, which reduces the standard uncertainty. A more detailed study should be done to analyze the effect of sample size on uncertainty.

Observation on required sample size

Test duration is related to the sensitivity of the measurement apparatus and to the size of the control volume. The larger the volume, the longer the raise in concentration. Depending on the measurement apparatus accuracy, a minimum concentration difference is needed in order to lower the measurement uncertainty. However, the measurement apparatus has to be sufficiently accurate to allow the measurement duration not to impact the LFR value.

As indicated in Figure 2.12, the dominant contributor is the accumulation volume. Thus the study focuses on the required sample number of concentration measurements, which means the standard of $\frac{\partial C}{\partial t}$. A general simplified formula for the approximation of the required sample size for detection of difference Δ with regard to the slope deviation is described by Equation (2.20). Both $\sum(t_i - \bar{t})^2$ and $s_{regression}^2$ are themselves functions of n . According to experience, the value of $s_{regression}$ varies from 0.01 to 0.10 (ppm.) for 200 measurements. Hence this term can be considered as n independent. Several $s_{regression}$ values will be chosen and analyzed in the next part.

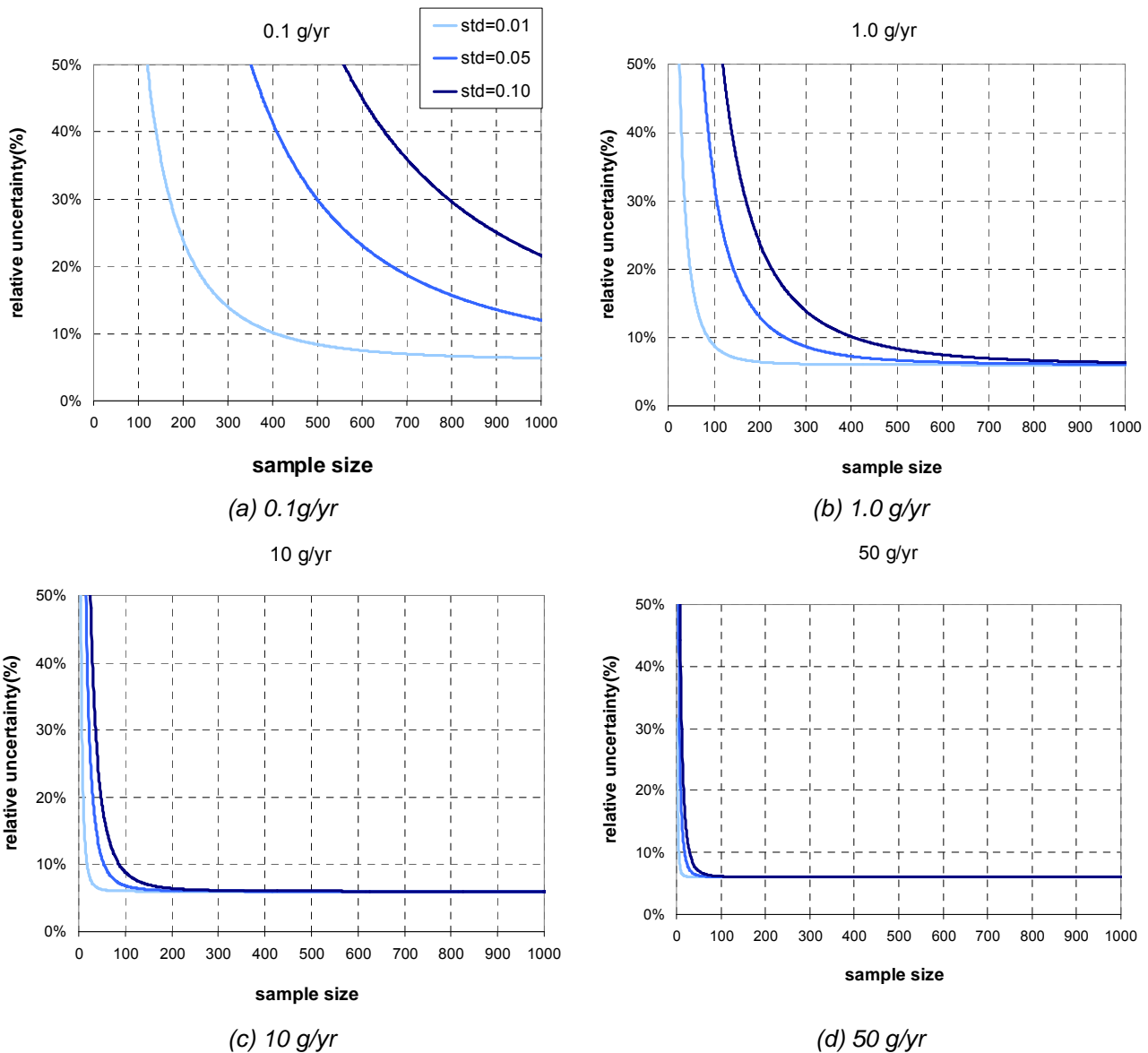


Figure 2.13 Measurement uncertainties as a function of the sample size.

Figure 2.13 shows the relative uncertainty of leak flow rate as a function of sample sizes under the standard deviation of regression of 0.01, 0.05, and 0.10 ppm/s. Taking an example from Figure 2.13 (b), for measuring a leak flow rate value of 1 g/yr with the standard deviation of 0.01 ppm/s, 80 samples are required to obtain a relative uncertainty of 10%, which is equal to about 0.1 g/yr as absolute uncertainty when the interval is set as 120 seconds. Consequently, the necessary measurement time is $120 \times 80 / 3600 = 2.7$ hours. Otherwise, the lower the standard deviation of regression, the lower the required sample size. As shown in Table 2.5, for the sample leak flow rate (1 g/yr), the estimated sample size decreases 5 times with the decrease of the standard deviation.

Table 2.5 Required sample size and measurement duration for 1 g/yr.

Standard deviation of regression	Relative uncertainty	Required sample size	Measurement duration min (interval: 120s)
0.10	10%	400	13.3 hours
0.05		250	8.3 hours
0.01		80	2.7 hours

Figure 2.14 shows the relative uncertainty of leak flow rate as a function of test duration (120 s for each interval step) with the highest standard deviation of 0.10. When the leak level ranges from 5 to 50 g/yr for MAC system tests, in spite of the standard deviation of the regression, it is useless to perform more than 24-hour tests because the relative uncertainty becomes negligible as compared to the contribution of the volume uncertainty.

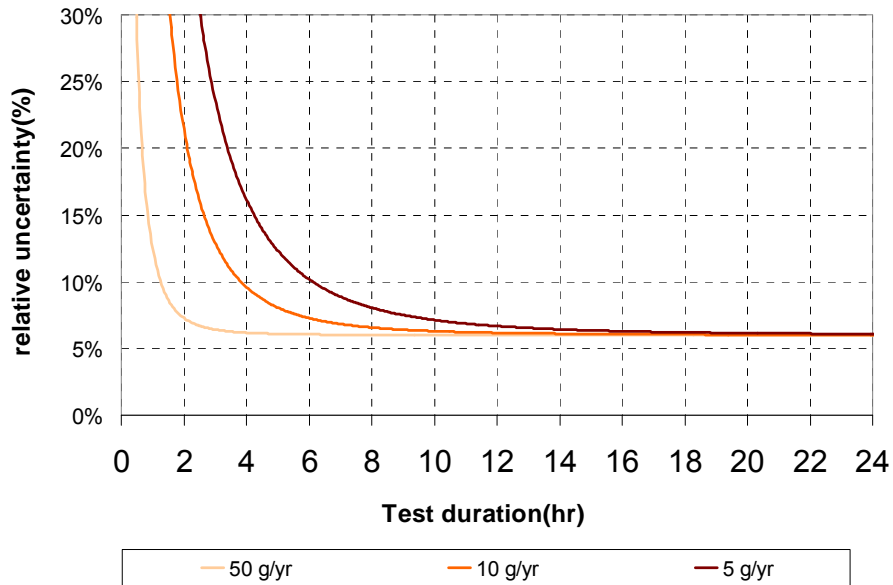


Figure 2.14 Relative uncertainty of LFR vs. test duration (system test bench).

For the component test bench, the test chambers are smaller than that of the system, so the relative uncertainty is smaller than that of system tests and can be managed in the range of 5%. Figure 2.15 illustrates the evolution of the relative uncertainty of leak flow rate according to test duration. Both Figures 2.14 and 2.15 can be used to give some ideas to determine the test duration based on required uncertainty value.

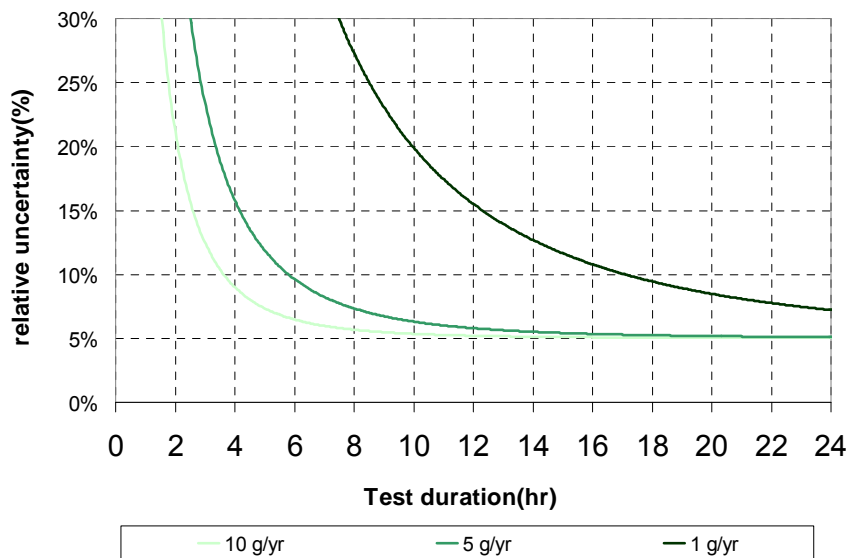


Figure 2.15 Relative uncertainty of LFR vs. test duration (component test bench).

2.1.2 Test benches for systems and components

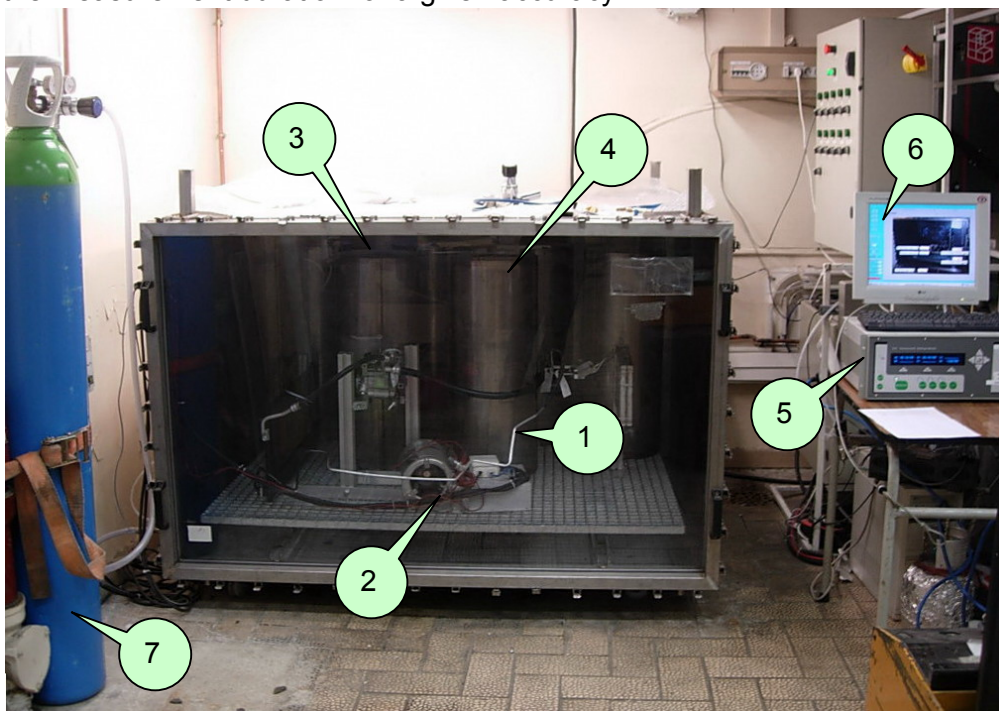
The development of a test bench for components started in 1995 at the CEP-Paris. A second generation test bench has been realized in 1998 by using an infrared spectrophotometer. The third generation test bench also available at the CEP-Paris consists of a system level test bench and component test benches with IR spectrophotometer and PAS, and developed during this research work.

These test benches include three main components:

- **The system/component to be tested**
- **The accumulation volume**, where the concentration of refrigerant is accumulated and measured
- **The analyzer**, used to measure the refrigerant concentration in the accumulation volume. Two types of analyzers are available at the laboratory: one is an IR spectrophotometer (Uras-14) and the other is an IR photo-acoustic spectroscopy (Innova-1314).

2.1.2.1 Description of the system test bench

Two types of mini-sheds have been built. The first one is dedicated to the measurement of LFRs in standstill mode only. Figure 2.16 presents the test bench for leak flow rate tests of MAC systems. Once installed inside the test chamber, the MAC system is heated and maintained at the required temperature by an electric heat resistance associated a powerful fan (1500 m³/hr) to reach homogenous temperature as well as homogenous concentration inside the test chamber. The constant temperature inside the accumulation volume allows controlling the corresponding saturation pressure. In order to reduce the control volume, leak tight cylinders are installed inside allowing accelerating the raise of concentration and so limiting the measurement duration for a given accuracy.



(1) MAC system to be tested; (2) electric heat resistance associated a powerful fan; (3) test chamber; (4) leak tight cylinder; (5) analyzer; (6) acquisition system; (7) reconstructed air bottle.

Figure 2.16 Test bench for system measurements.

The MAC system is charged with its original HFC-134a charge. The temperature inside the control volume allows controlling the saturating pressure in standstill mode. For refrigerant handling, the testing operation is simpler at the system level than at the component level, because the refrigerant charge is inside the MAC system, whereas a boiler outside of the control volume is necessary to set the component under pressure. The only circuits installed for the test of the system are: a reconstituted air (80% N₂, 20% O₂) circuit for rinsing the test chamber, and the measurement circuit between the concentration analyzer and the control volume.

A specific test bench has been built to measure the leak flow rate both in standstill mode and in running mode of MAC systems [CLO04a]. The test bench is more sophisticated as well as the installation of the MAC system to be tested. The main elements of the testing system for measurements in running mode are (see Figure 2.17):

- (a) a variable speed fan with a hopper are installed in front of the evaporator allowing to control the air flow rate circulating on the evaporator;
- (b) two fans, also with variable speed, blowing on a water heat exchanger and the condenser of the MAC system;
- (c) the water heat exchanger extracts heat by a water-cooling circuit and so maintains the temperature inside the test chamber at the set value;
- (d) an additional heating and ventilation system is used for tests in standstill mode and also for a fine tuning of the average temperature inside the test chamber;
- (e) the compressor is installed on a specific support and connected to an electrical motor via the classical belt-pulley system;
- (f) a variable speed electrical motor of 10-kW input power is used in order to simulate either driving profiles or steady state running speeds.

Additionally, temperatures are measured at the inlet and the outlet of the condenser, the expansion valve, the evaporator, and the compressor. Air temperatures are also measured at the inlets and the outlets of the evaporator and the condenser. This design enables to perform measurements of LFRs with different temperatures and different running speeds of the compressor.

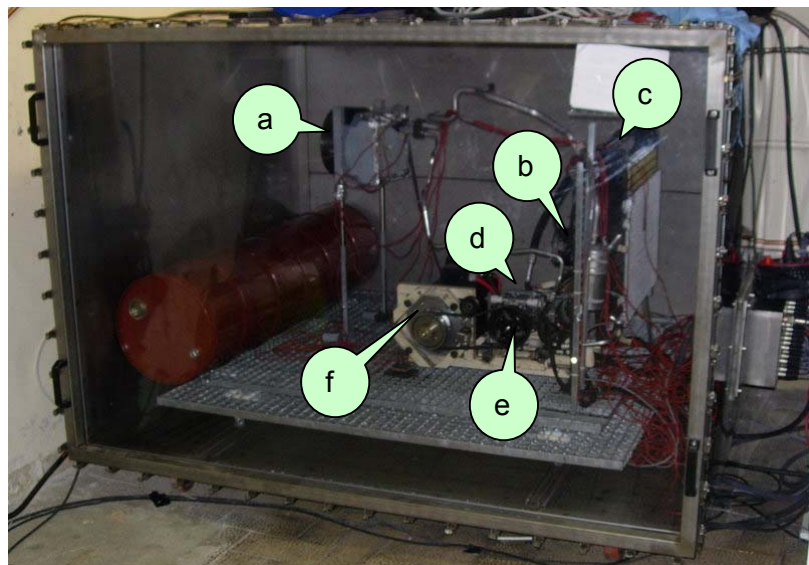


Figure 2.17 System test mini-shed for running mode tests.

2.1.2.2 Description of the component test bench

Figure 2.18 presents the layout of the test bench for leak flow rate measurements of components and its circuits.

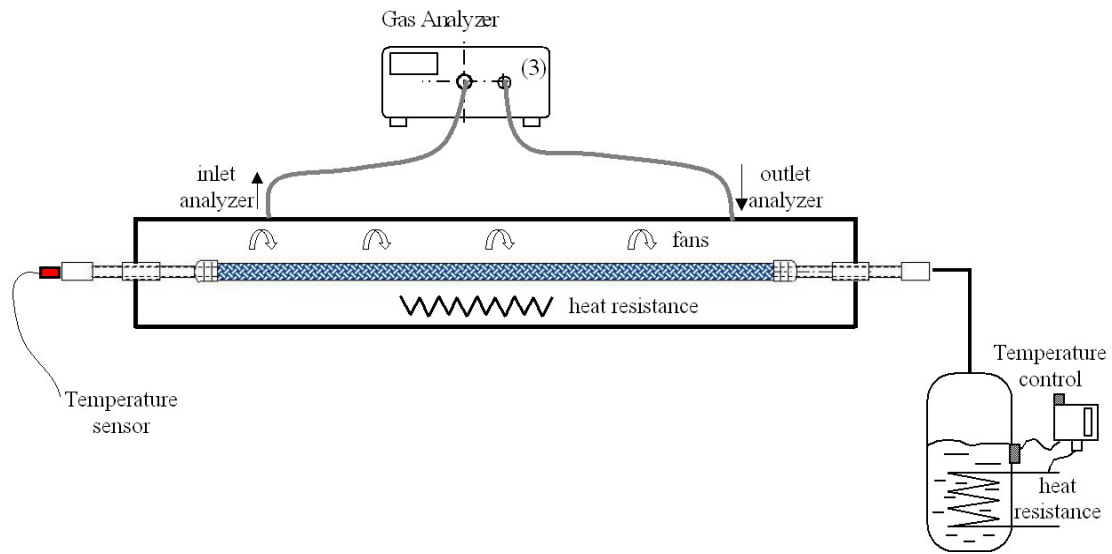


Figure 2.18 Layout of the component measurement test bench.

The test method for components is identical to the method of test for systems installed in test chamber, except that for the system tests the refrigerant charge is inside the MAC system, and for component tests, a refrigerant boiler is mounted outside the accumulation cell. This pressurization circuit is installed outside the accumulation volume and is separately controlled by a heat resistance to define the required pressure. Each cell can be evacuated by the vacuum pump. After evacuation, the volume is filled up with reconstituted air. Heat resistance and fans are installed inside the measurement cell to set the component under the required temperature condition. The component can be heated up in order that the temperature of the component is strictly higher than the saturating temperature so as to avoid any condensation. Once the steady state is reached, measurement using the gas analyzer is performed continuously in order to verify that a steady state LFR is reached. The measurement duration depends on the leak tightness of the component.

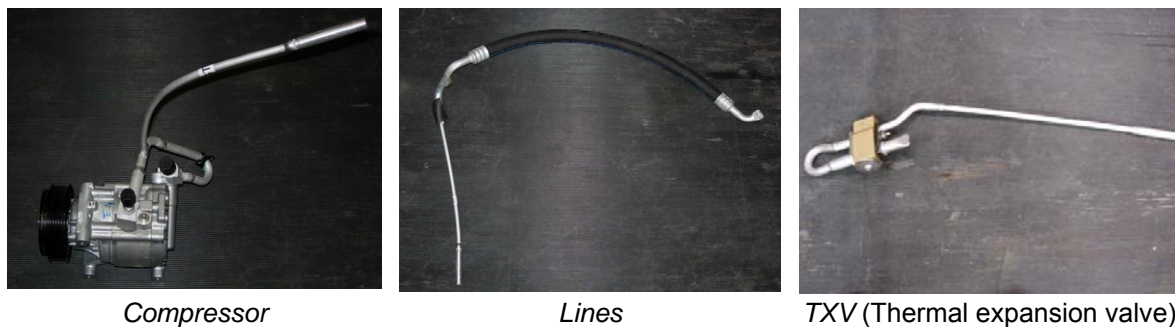


Figure 2.19 Layout of component measurement test bench.

Specific preparation is necessary for component before test. One end of the component is closed by welding and the other end is equipped with an ad hoc tube for going through the wall of the accumulation cell. Figure 2.19, gives some examples of prepared components

such as compressor, hoses with crimps, and TXV. The leakage level of these components will be measured and discussed in § 2.1.3.3.

Figure 2.20 presents different measurement cells designed for different types of components, such as fittings, hoses, and macro-components like condenser, evaporator, compressor etc.



Cell for fittings



Cell for macro-components



Cell for hoses

Figure 2.20 Test bench for component leakage measurement.

2.1.3 Leak flow rate measurements of MAC system and components in standstill mode

2.1.3.1 Preconditioning before measurements

The preconditioning step is necessary for all MAC components having polymer materials in order to reach a steady state permeation rate through these polymer materials. As presented in Figure 2.21, a MAC system is mounted on supports and then fixed on a duckboard. After applying the tightening torques to all fittings, the MAC system is evacuated and then charged with its nominal HFC-134a charge. Preconditioning can now be started.

Figure 2.22 gives an example of concentration measurements during the preconditioning phase of a MAC system at 50°C. The concentration evolution is recorded from the beginning. It can be seen that the curve becomes straight after 6-day measurements. That

means this system needs to be preconditioned during at least 6 days at 50°C before reaching a steady state leak flow rate. The emission behavior during the transient phase is very similar to the permeation curve of polymer materials that can be found in published data [CRA75], [FLA01]. Based on experimental data, 50°C during 10 days is an appropriate and sufficient condition for a MAC system reaching the steady state emission rate.



Figure 2.21 MAC system installed on a duckboard for LFR test.

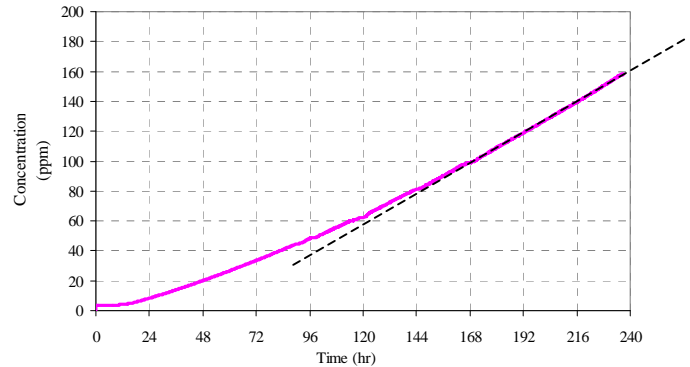


Figure 2.22 Concentration measurements during preconditioning.

2.1.3.2 Leak flow rates of MAC systems

Measurements of 10 types of MAC systems have been accomplished after preconditioning period at three different temperatures: 30, 40, and 50°C, which correspond to saturation pressure of 770, 1017, and 1318 kPa. Results are summarized in Table 2.6.

Table 2.6 LFRs of 10 MAC systems.

LFRs of system a to j (g/yr)				
MAC system	Temperature(°C)	30°C	40°C	50°C
	Saturation Pressure(kPa)	770	1017	1318
a		11	29	41
b		17	35	57
c		14	27	43
d		20	36	54
e		21	35	58
f		15	27	39
g		8	15	28
h		20	34	50
i		10	20	31
j		12	25	45
Average LFR(g/yr)		15	28	45

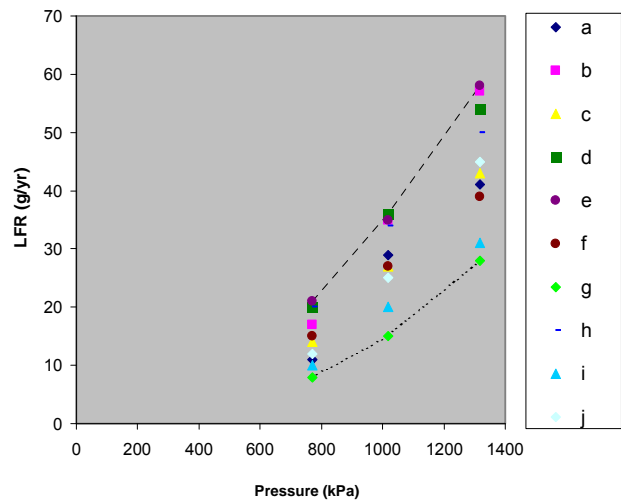


Figure 2.23 LFRs of 10 MAC systems vs. pressure.

Tests of MAC systems inside the test chamber allow measuring accurately the leak flow rate for different pressures. As shown in Figure 2.23, leak flow rates have been plotted as a function of the saturation pressure. It has been seen that the leak flow rate depends on the pressure. Those tests of MAC systems allow elaborating an emission law as a function of saturation pressure.

2.1.3.3 Leak flow rates of MAC components

One way to test components is strictly speaking to cut them from the system as built. Doing so, except the measurement accuracy issue, the sum of the leak flow rates of the components should be equal to the LFR of the system for a given saturating pressure. Another possible interpretation of component tests is not to measure the components cut into pieces from the system, but to measure the components as manufactured and before assembly.

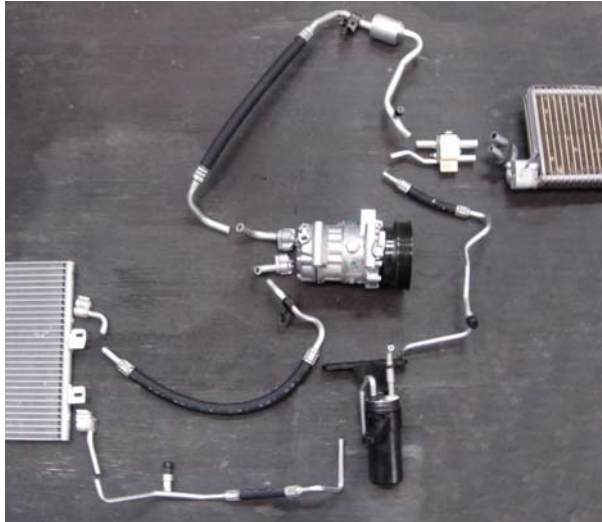


Figure 2.24 MAC system cut into parts making macro-components.



Figure 2.25 Welded end and connecting tube going through the wall of the cell.

Component results mentioned here are based on the 10 MAC systems that have already been tested and cut into parts to make macro-components. Depending on the complexity of the system, the number of components may vary from 6 to 20. As shown in Figure 2.24, the system has been decomposed into: compressor, condenser, evaporator, Thermo expansion valve (TXV), liquid lines 1 and 2, suction line, discharge line, liquid receiver, inlet and outlet compressor fittings, and inlet and outlet condenser fittings, making 13 components.

Once one component has been cut, a complementary preparation is necessary. As illustrated in Figure 2.25, one end of the component is closed by welding and the other end is equipped with a special tube for going through the wall of the accumulation cell. Depending on the component type, different preparatory actions have to be made:

- for fittings, the tightening torque needs to be known and applied,
- for compressor, test can be carried out with lubrication oil, etc.



Figure 2.26 Wrapped welding.



Figure 2.27 Leak detector.

Before tests, each component is put under a pressure of 1500 kPa of a HFC-134a / nitrogen blend and each welding is wrapped in a vinyl sheet in order to create an accumulation volume for verification of leak tightness by a sensitive leak detector (see Figure 2.27). The possible raise of concentration in the wrapping is verified after a period of time varying between 20 minutes and 1 hour. If the test is good (no leak), the component is installed in the accumulation volume. If not, the welding is done again and the leak tightness is verified one more time.

Table 2.7 LFRs of components of MAC system b.

Reference	Component list	LFR(g/yr)		
		50°C	40°C	30°C
		1318 kPa	1017 kPa	770 kPa
1	compressor without fittings	19.5	16.0	8.0
2	discharge line	13.4	7.5	4.63
3	condenser	1.3	0.7	0.3
4	liquid branch 1	2.5	2.0	1.0
5	liquid receiver + fittings	1.55	0.62	0.28
6	liquid line 2	1.5	0.6	0.3
7	TXV	4.52	2.52	1.5
8	evaporator	3.9	3.3	2.6
9	suction line	7.2	2.9	1.8
10	BP compressor fitting	0.3	0.15	0.08
11	HP compressor fitting	0.3	0.14	0.1
12	inlet condenser fitting	0.25	0.15	0.1
13	outlet condenser fitting	0.24	0.12	0.05
Component tests	Sum of LFRs	56.46	36.7	20.74
System tests results		57	35	17

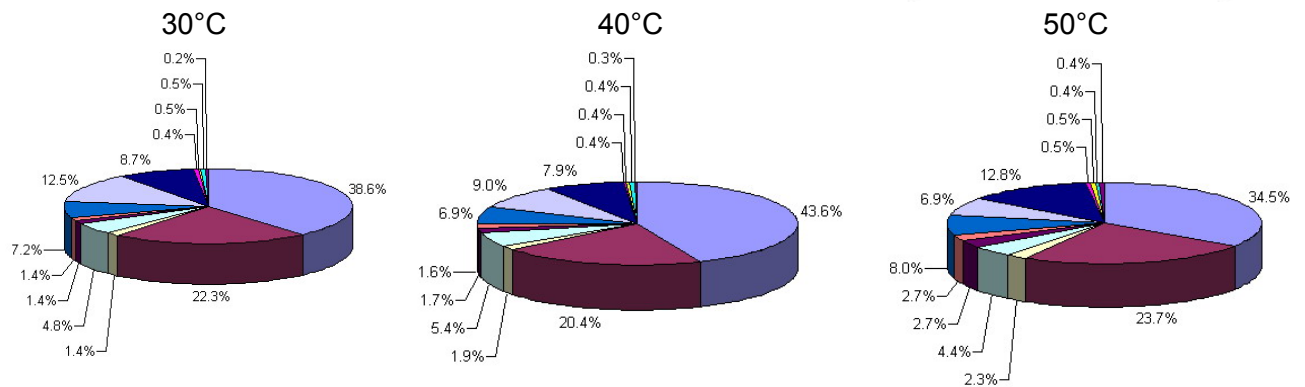
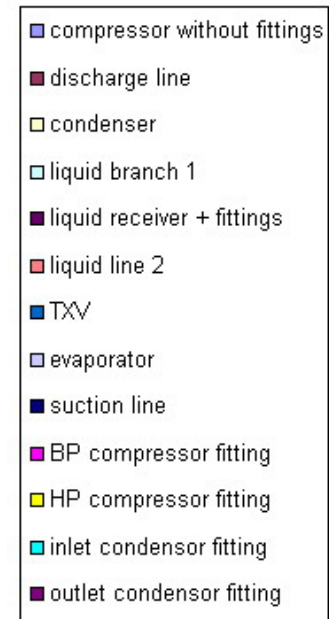


Figure 2.28 LFR contribution of components for system b.

Once the leak tightness of the welding is verified, each component has been tested at 3 different temperatures: 30, 40, and 50°C. Leak flow rates of all macro-components have been summed with the purpose of being compared to the leak flow rate of the system. Results are presented in Table 2.7. The sum of all parts leads to 20.7 g/yr at 30°C, 36.7 g/yr at 40°C, and 56.5 g/yr at 50°C, which are very close to the leakage values of system level: 17, 35, and 57g/yr.

Figure 2.28 shows the contribution of components. It can be seen that the main contributors are the compressor, followed by the suction line. These two components account for about 60% of total leak flow rates.

Test results at the component level have been classified to draw some conclusions in terms of leakage value of different components.

Table 2.8 LFRs of 9 hoses.

system	DN [mm]	TECHNOLOGY	LFR(g/yr)		
			50°C	40°C	30°C
Temperature(°C)			50°C	40°C	30°C
Saturation Pressure(kPa)			1318	1017	770
A	16	IIR-EPDM	15.6	9.7	7.4
B	16	IIR-EPDM	15.6	9.7	7.4
C	16	CIIR-PET-CR	8.4	2.9	1.5
D	16	PA-IIR-PET-EPDM	8.8	3.9	1.4
E	16	EPDM-SF-CIIR	26.5	13.9	8.7
F	16	CIIR-PVA-PA-CR	7.8	1.7	0.5
I	16	PA-IIR-PET-EPDM	1.34	0.51	0.21
I'	16	PA-IIR-PES-EPDM	4.79	1.03	0.56
J	16	CIIR-PET-CR	8.4	2.9	1.5

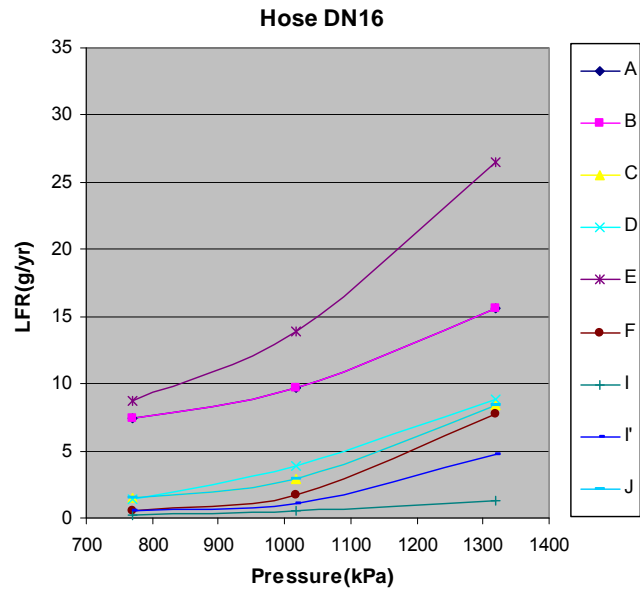


Figure 2.29 LFRs of hoses.

As indicated in Table 2.8 and Figure 2.29, leak flow rates of nine new hoses vary in the range of 0.2 to 8.7 g/yr at 30°C which directly depend on the technology.

Table 2.9 LFRs of 10 TXV

TXV	LFR(g/yr)		
	50°C	40°C	30°C
Temperature(°C)			
Saturation Pressure(kPa)			
	1318 kPa	1017 kPa	770 kPa
A	1.95	0.95	0.5
B	4.52	2.52	1.5
C n°1	4.1	2.3	1
C n°2	4.9	2.9	1.6
D	3.5	1.7	1.2
E	19.7	9.3	4.8
F	11.7	6.8	4
H n°1	2.6	1.6	1
H n°2	3.6	2.4	1.5
I	7	4	2

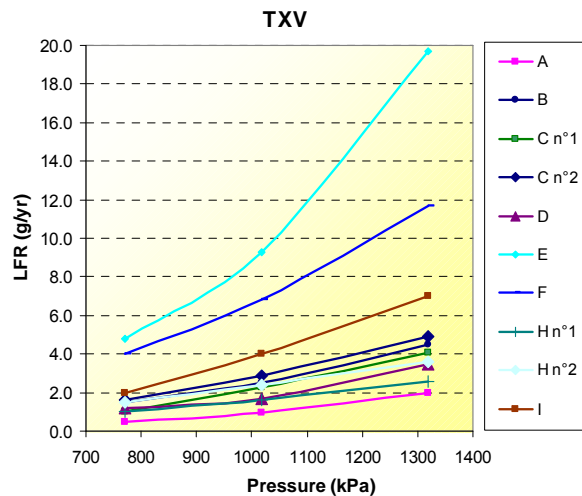


Figure 2.30 LFRs of TXV.

Table 2.9 and Figure 2.30 show the leak flow rates of 10 TXV. At 30°C, the leak flow rates vary from 0.5 for A to 4.8 g/yr for E. At 40°C, the lowest leakage is 0.95 g/yr and the highest value is 9.3 g/yr. At 50°C, the leak flow rates vary from 1.95 g/yr to 19.7 g/yr. It can be seen that, depending on the technology and design, emissions coming from TXV are quite different. One can be 10 times higher than another. Improvement of the technology can significantly lower the LFRs of TXVs.

As summarized in Table 2.10 and Figure 2.31, leak flow rates of compressor are the highest of all components. It contributes to about 40-60% of the total leak flow rate of a MAC system. The LFRs are technology dependent leading to a leakage difference of 17 g/yr between the compressor of system G (10.1 g/yr) and that of system E (27.4 g/yr).

Table 2.10 LFRs of 10 compressors

COMPRESSOR	LFR(g/yr)		
	50°C	40°C	30°C
Temperature(°C)	50°C	40°C	30°C
Saturation Pressure(kPa)	1318 kPa	1017 kPa	770 kPa
A	18.2	16.5	8
B	20.1	16.3	8.2
C	21	14.2	8
D	19	13	9.5
E	27.4	17.9	9
F	15	10.6	7.7
G	10.1	6.2	3.2
H	20.1	14.15	10.3
I	17.7	12.4	7.4
J	19	13.6	8

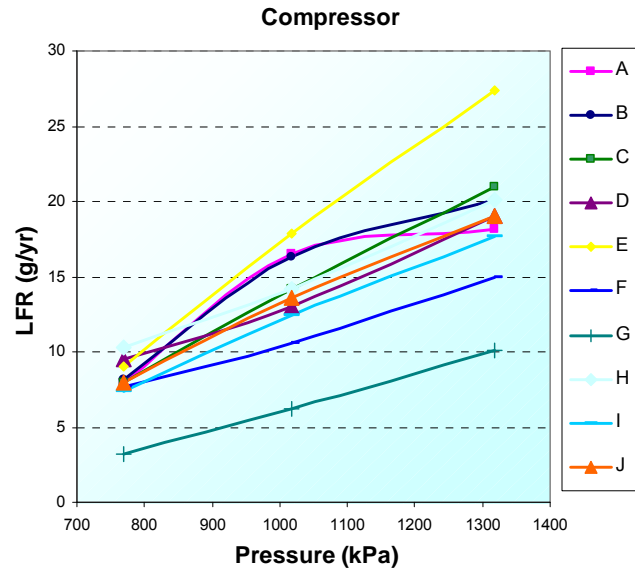


Figure 2.31 LFRs of compressor.

2.1.3.4 Leak flow rates of MAC systems vs. components

Table 2.11 summarizes the mean leak flow rates of 10 systems, both in terms of system and macro-components level. Comparing 15.6 to 15 g/yr at 30°C, 27.4 to 28 g/yr at 40°C, and 44.5 to 45 g/yr at 50°C, the sum of the emissions of components equals the emission of these systems within the uncertainty level. By consequence, the tests can be carried out either at the system level or at the component level. In fact both are necessary. Tests at the system level verify an overall leak tightness performance. Tests at the component level indicate what are the most leak prone components and so define the necessary changes in designs, clearances or materials.

Table 2.11 LFRs and linear regression.

Temperature (°C)	Mean LFRs of 10 MAC systems			Linear Regression	
	30°C	40°C	50°C	k	R^2
Sum of macro-components	15.6	27.4	44.5	2.61E-11	0.998
System level	15	28	45	2.63E-11	0.997

2.1.3.5 Leakage behavior based on regression curve

Seals made of polymer materials are used in the MAC system to connect different elements and prevent the refrigerant loss from inside the MAC system. Hoses are commonly used to prevent the propagation of vibrations. Therefore two types of leakage sources are distinguished here [MUL98].

a) Leakage due to the escape of refrigerant between sealing parts. The contact area between the seal and the rigid parts of fittings is never perfect. It always exist micro-passages for gas to pass through [MUL98]. According to the Poiseuille's law, the mass flow rate due to the viscous flow between sealing parts is approximately proportional to the differences of the squares of the upstream and downstream pressures.

b) Leakage due to gas permeation through polymer materials is the other contributor of leak flow rate. The phenomenon of gas diffusion through polymer is also related to the pressure [KIM92], [MAG90], [MOO04].

Figure 2.32 illustrates the evolution of leak flow rate as a function of pressure. Using the method of least squares, a good agreement between the measured values and the regression curve of binomial expression has been verified and is expressed by Equation (2.21).

$$LFR = k(P_{upstream}^2 - P_{downstream}^2) \quad (2.21)$$

The objective of this approximation is to find a general approach for MAC system leakage behavior as a function of pressure, which will be useful in the following section for establishing the correlation factor.

Based on data presented in Table 2.11, regression models have been made for systems and components. Related parameters have been calculated and summarized in Table 2.11. Constants k are respectively 2.63×10^{-11} and 2.61×10^{-11} . The parameter R^2 , the coefficient of determination, gives a statistical measure of how well the regression line approximates the real data points. As shown in Table 2.11, R^2 in both cases being very close to 1 (0.998 and 0.997) indicates that the regression model fits correctly the data.

Figure 2.32 shows regression curves at system levels and sum of system components. It is obvious that both curves are very close to each other. In a word, the tests carried out at the system level or the component level lead to the same leak flow rate. Both can be used to determine the leakage value of a given MAC system.

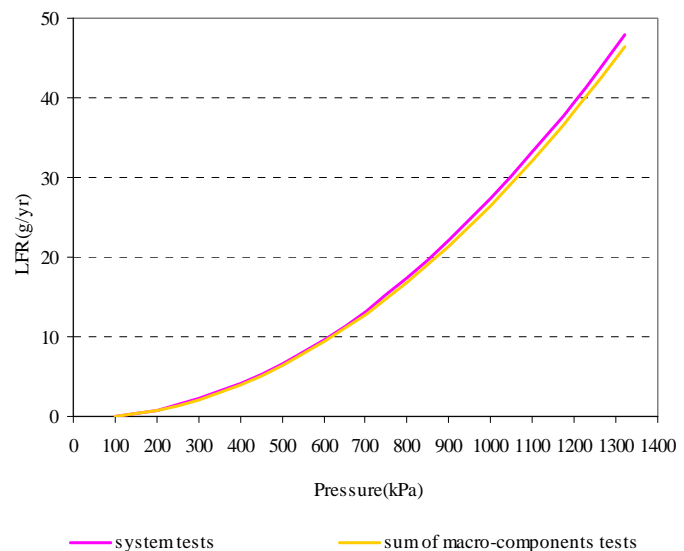


Figure 2.32 Regression curves for systems and sum of macro-components.

2.2 Correlation factor based on leakage behavior

2.2.1 Standstill mode tests considering the climate conditions

In real life conditions, the temperature is never constant and varies along the time. In order to compare the test methods performed in the laboratory to the real life of MAC systems, further tests are required to simulate the climatic conditions. Figure 2.33 gives an example of the daily temperature variation in Seville along the time. Tests have been accomplished to analyze the effect of temperature variation.

A test on a MAC system in standstill mode has been performed by simulating the real daily climatic conditions with the purpose of comparing the result to that of average constant temperature tests. Simulation has been carried out on MAC system X according to the temperature variation of Seville city meaning the temperature inside the test chamber has been controlled to reproduce the temperature variation of Seville along the time.

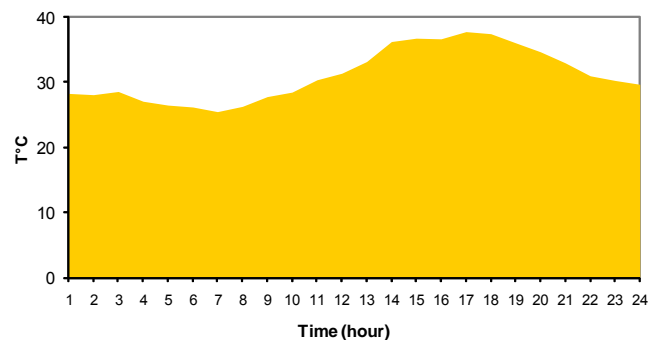


Figure 2.33 Daily average temperature of Seville.

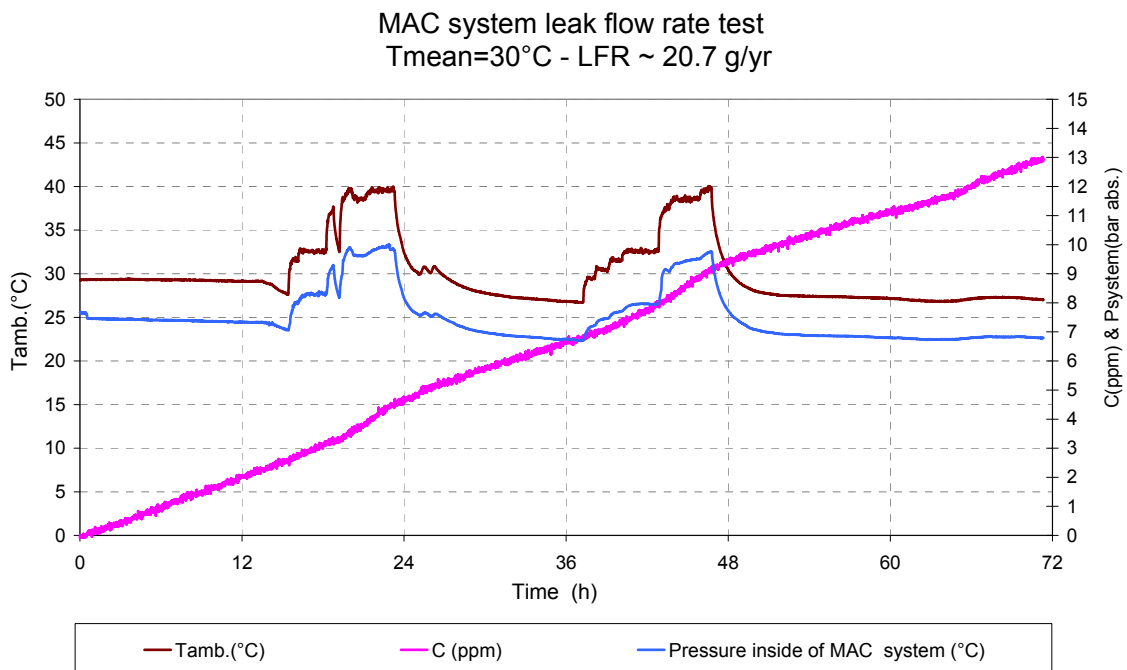


Figure 2.34 Test by simulating real climatic conditions.

As illustrated in Figure 2.34, test being performed for 72 hours leads to an average temperature of 30°C. The brown curve represents the temperature variation inside the test chamber and the blue one shows that of the pressure inside the MAC system, which changes immediately with temperature. The pink curve presents the accumulated HFC-134a

concentration inside the test chamber along the time. The total quantity of HFC-134a (0.17 gram) permits evaluating the annual HFC-134a emission: 20.7 g/yr. The same system has also been tested at constant temperatures of 30, 40, and 50°C and results are summarized in Table 2.12. An important result has been found: the annual LFR of the system (20.7 g/yr) is very close to the calculation obtained by LFR obtained at constant temperature of 30°C (20.7 g/yr) where the temperature value is the yearly average temperature.

Table 2.12 LFRs of MAC system X at 3 different temperatures.

Temperature (°C)	Saturation pressure (kPa)	Leak flow rate (g/yr)
30	770	21
40	1017	36
50	1318	58

To conclude, in spite of the temperature variation, the leak flow rate corresponding to the annual average temperature can be used to predict the real life annual emissions of the MAC system.

Based on the assumption made in § 2.1.3.5, the leakage behavior of a MAC system can be described by Equation (2.21). Figure 2.35 presents the regression curve of leak flow rate of a system X as a function of the pressure. The constant $k = 3.42 \cdot 10^{-11}$, allows finding out the leak flow rate at any temperature. For example, annual temperature in Paris is 11°C corresponding to saturation pressure of 429 kPa. Using the constant k , the leak flow rate corresponding to this pressure is 5.9 g/yr. In Rome, where the yearly average temperature is 15.4°C, a leak flow rate value of 8.0 g/yr is found at saturation pressure of 495 kPa.

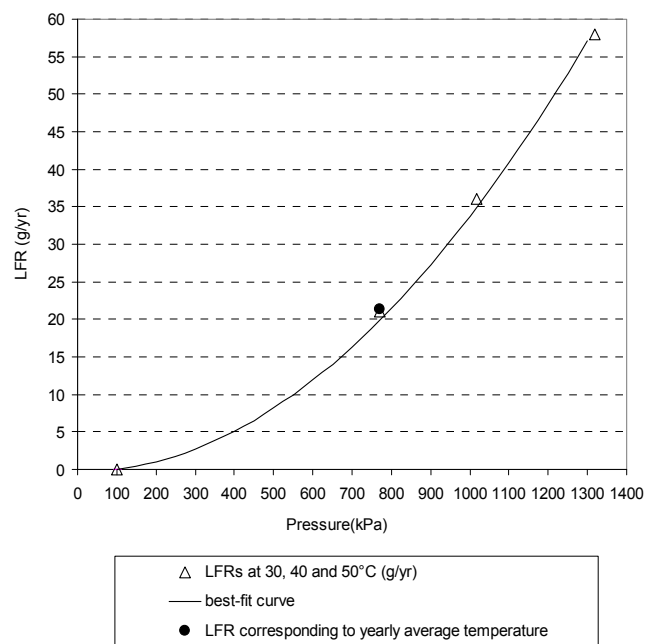


Figure 2.35 LFR of MAC system and regression curve

To conclude, knowing the mean annual temperature of a city, one can predict the leak flow rate in standstill mode by testing the MAC system at constant temperature.

2.2.2 Analysis of running mode leakage

In order to measure the contribution of the running mode emissions, several analyses have been performed. Taking into account the current average mileage of vehicles in the European Union, the running time of the vehicle is comprised between 250 and 450 hours per year, representing 3 to 5% of the annual time. Moreover, the MAC system operates only

a limited part of this running time, so the annual use of MAC systems ranges typically from 80 to 250 hours.

The test bench introduced in § 2.1.2.1 is used to perform the running mode tests. The NEDC (New European Driving Cycle) is supposed to represent the typical usage of a car in Europe, and is commonly used to assess the emission levels of car engines. For this reason, the NEDC has been produced for running mode tests.

When one MAC system is in running mode, the conditions of different MAC systems become complex. Therefore, several tests have been carried out in order to analyze the dynamic effects on leak flow rate of the system.

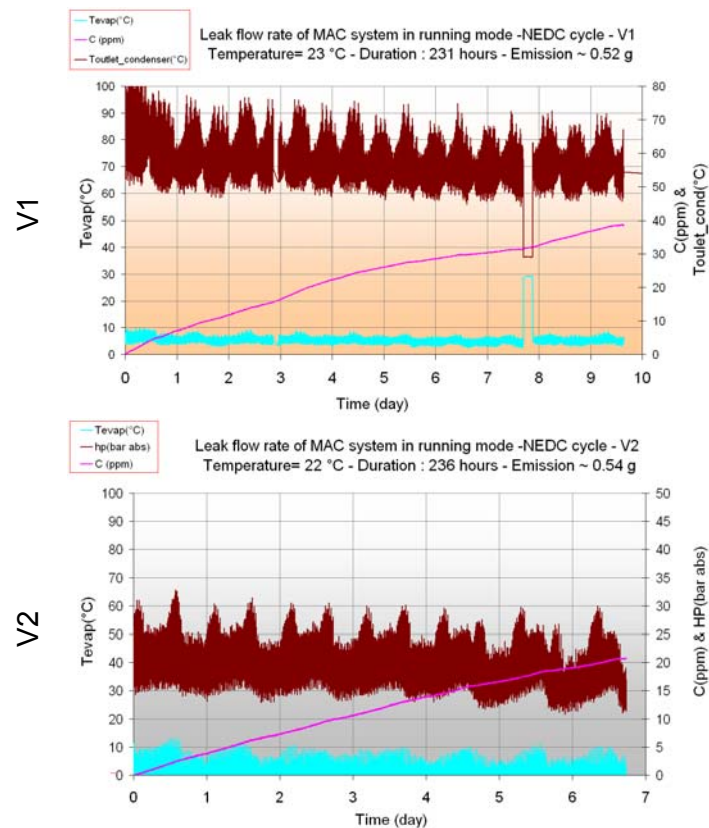


Figure 2.36 Test results in running mode for system V1 and system V2.

The evolution of accumulated concentration inside the test chamber, high pressure inside the system, and evaporation temperature are recorded and presented in Figures 2.36. It can be observed in the figures that the increases of concentration are not constant which seems reasonable due to the complex pressure and temperature conditions inside the MAC system. In the first case, at the end of 231-hour test, the mass of HFC-134a accumulated in the mini-shed is 0.52 gram. That means 0.52 gram has been emitted after the 231-hour running period. Therefore, it can be concluded that in the case of MAC system V1, the annual leakage in running mode is 0.52 g. Following the same test procedure, the MAC system V2 emits 0.54 gram after 236-hour running period.

Converting the emissions in running mode into annual leak flow rate, one obtains respectively 19.7, 20.0, and 10.1 g/yr (see Table 2.13).

Table 2.13 Annual LFR for systems V1, V2, and V3.

MAC system	Running mode		
	Duration(h)	Emission(g)	Annual LFR(g/yr)
V1	231	0.52	19.7
V2	236	0.54	20.0
V3	217	0.25	10.1

2.2.3 Standstill and running mode contribution

System tests in standstill mode have been performed at three different pressures, 770, 1017, and 1318 kPa. Test results are shown in Figure 6.1.

As shown in Table 2.14, three MAC systems have been tested both in standstill and in running modes. The MAC system V1 kept running during 231 hours, the mass of HFC-134a accumulated in the test chamber is 0.52 gram. Test in standstill mode of this system gives 8.8 g/yr. By assuming that the rest of the year the MAC system is not running, this period in standstill mode is then translated into $365 * 24 - 231 = 8529$ hours. Therefore the leakage due to the standstill mode is 8.57 g/yr. The total leak flow rate rises up to $8.57 + 0.52 = 9.1$ g/yr.

Table 2.14 LFRs contribution in standstill and in running mode.

MAC system	Standstill mode			Running mode		LFR (g/yr)	Contribution of running mode	<u>Standstill mode</u> Total LFR
	LFR (g/yr)	Duration (h)	Emission (g)	Duration (h)	Emission (g)			
V1	8.8	8529	8.57	231	0.52	9.1	5.7%	8.8/9.1= 0.97
V2	7.7	8524	7.49	236	0.54	8.0	6.7%	7.7/8.0= 0.96
V3	5.2	8543	5.07	217	0.25	5.3	4.7%	5.2/5.3= 0.98

To conclude, although running mode shows a leakage value twice higher than that of standstill mode, its contribution remains low (about 5-6%) due to the short operation period referred to the year. When predicting the total leak flow rate of a MAC system, taking into consideration the running mode, one can use the convention ratio between standstill mode and total leak flow rate. As detailed in Table 2.14, the factor varies from 0.96 to 0.98. Considering the worse case, 0.96 can be used to calculate the running part contribution.

2.2.4 Fleet test – annual leakage of MAC system on vehicles by recovery operation

Recovery operation of vehicles allows verifying the LFRs during “real life”. Tests of 40 vehicles have been carried out for the comparison between the emissions of the complete MAC system as measured in the mini shed and the real life test, during the nine-month test period. The 40 vehicles were of ten different types with four samples of each type in order to cover the different MAC system technologies, the different vehicle manufacturers as well as the types of vehicles (small, medium, and luxury as well as SUVs, and convertibles). The choice has been made by the European Association of Car Manufacturers (ACEA).

The major test procedures are:

Initial charge: four vehicles have been carefully charged in December 2004 or January 2005. The accuracy of the recovery method has been demonstrated. That means the recovered refrigerant has been equal to the charged refrigerant within 1g.

Final recovery: after 9 months, the refrigerant recovery procedures for these four vehicles have been performed in August 2005 or September 2005.

As shown in Figure 2.37, the recovery equipment consists of the following parts:

- an oil less compressor
- a recovery cylinder of 5-liter volume;
- a balance of precision in the scale of ± 0.1 gram;
- a pair of suction and discharge hoses equipped with ball valves at their ends.

Recovery thermal conditions

In order to avoid variation of the thermal conditions, vehicle to be tested is installed in a location where the room temperature is controlled at $20 \pm 1^\circ\text{C}$. The engine is run at least 20 minutes in order to heat the entire engine compartment to above 50°C . A heating system with fans is installed in front of the vehicle front end in order to warm the condenser to above 50°C .



Figure 2.37 Refrigerant Recovery equipment.

The recovery procedure

The recovery cylinder is evacuated firstly and weighed alone. The recovery equipment is connected to the low pressure valve of the MAC system by the suction line and to the recovery cylinder by the discharge line, the system is evacuated down to 20 Pa abs. The first recovery is then carried out with a low mass flow rate (10g/mn). This flow can be controlled by a throttling valve in order to avoid any recovery of liquid where oil can be easily dissolved. A temperature sensor indicates the possible flow of liquid by observing the wall temperature drop. This first recovery step is performed until reaching to final pressure of 20 kPa abs. Then the recovery system with all connections is weighed and the engine compartment is heated up during 30 minutes so as to facilitate the evaporation of liquid refrigerant trapped inside the circuit. Usually the pressure can rise up to 70 kPa. Thereafter, a second recovery is performed down to 15 to 17 Pa abs.

Demonstration

For each of the 10 different systems, the MAC system is charge precisely (± 0.5 g) and the recovery procedure is done right after. Comparing the recovered mass and the initial charge, the uncertainty should be less than 1 g. This demonstration proves the accuracy and rationality of the recovery procedure. Once the demonstration is made, the four vehicles of the same type are charged carefully with the nominal charges, both high and low pressure service valves are wrapped with a plastic cover in order to prevent any opening during the testing period.

Recovery after nine months

Once charged, the fleet of the 40 vehicles has run in different European regions. Nine months later the recovery process has been carried out in the same locations under the same thermal conditions. Apart from two vehicles which have been sold and one procedure

failed for wrong reporting, 37 of 40 vehicles have undergone the complete process. Results of the charge and recovery operation are indicated in Table 2.15.

Table 2.15 Results of charge and recovery operation.

Vehicle	Charge Operation		Recovery Operation		Duration (days)	Refrigerant Loss(g)
	Date of charge(g)	Initial charge(g)	Date of charge(g)	Recovery mass(g)		
VA1	Dec. 10 04	594,5	Aug. 30 05	589,0	264	5,5
VA2	Dec. 13 04	595,4	Aug. 30 05	591,5	261	3,9
VA3	Dec. 14 04	597,7	Aug. 29 05	592,4	260	5,3
VA4	Dec. 14 04	606,3	Aug. 30 05	598,0	260	8,3

Figure 2.38 illustrates the refrigerant loss of 4 vehicles VA, used in Paris during 9 months, with the accuracy of ± 0.5 g. From the date of initial charge in December 2004 to the date of recovery in August 2005, the vehicles go through between 260 and 264 days representing 72% of the whole year. Therefore the annual loss of these vehicles can be calculated by dividing the LFR by the number of operation days (for example 264 for VA1), then multiplied by 365 days (see Table 2.15).

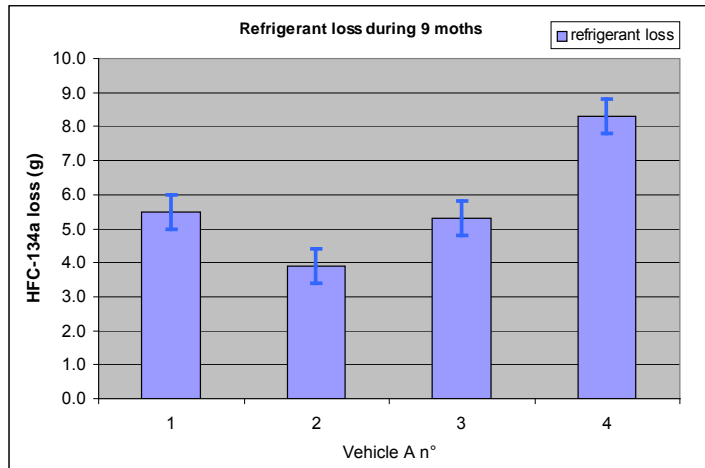


Figure 2.38 Refrigerant loss during 9 months.

In order to compare the results between systems tests and recovery operation, it is useful to introduce the climatic data in Paris during these 9 months. Accordingly the relationship between refrigerant loss and the temperature can be established. The daily temperature in Paris from December 2004 to the end of August 2005 is assumed to be equal to the typical daily temperatures as edited by Meteonorm¹. The average temperature during this period of time is 11.5°C, which corresponds to saturation pressure of 436 kPa.

Table 2.16. Annual loss of Refrigerant – Vehicles A.

Vehicle	Duration	loss (g/ 9 months)	annual loss (g/yr)
VA1	264	5.5	7.6
VA2	261	3.9	5.4
VA3	260	5.3	7.4
VA4	260	8.3	11.7
Average mass(g)			8.0

The recovery operation has been carried out with a precise procedure with a high recovery accuracy, which means an uncertainty of ± 0.1 g on initial refrigeration charge and on refrigerant recovery made nine months later, with less than 1g not recovered [CLO07].

Same recovery operations have been accomplished. As presented in Table 2.17 and Figure 2.39, the annual leak flow rates vary from 7.2 to 21.6 g/yr. It is necessary to point out that

¹ Meteonorm data are daily temperatures averaged for each day on a 10-yr period.

vehicles C and H are double-evaporator systems. The mean leak flow rate of all 37 vehicles makes 10.0 g/yr.

Table 2.17 Average annual losses for 10 types of vehicles.

Vehicle	Annual loss (g/yr)
J	7.2
B	7.6
G	7.6
I	7.8
A	8.1
F	9.4
D	12.1
E	14.8
C	15.0
H	21.6
Average value	10.0

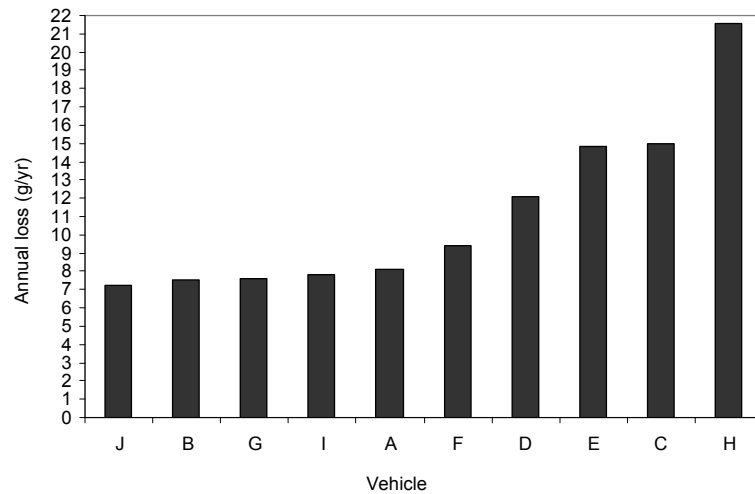


Figure 2.39 Results of fleet tests.

2.2.5 Establishing the correlation factor

These 10 types of MAC systems have also been tested in laboratory (4 samples for each type) at three different temperatures. Results are summarized in Table 2.18.

Table 2.18 Arithmetical average LFRs of system A-J.

System	Leak flow rates (g/yr)		
	30°C	40°C	50°C
A	15.8 ^{+5.2} _{-3.8}	34.7 ^{+4.3} _{-3.7}	67 ^{+9.0} _{-10.0}
B	18.2 ^{+1.8} _{-2.2}	45 ^{+2.0} _{-2.0}	82.5 ^{+3.5} _{-4.5}
C	17.2 ^{+4.8} _{-5.5}	33 ^{+2.0} _{-3.0}	60.6 ^{+6.4} _{-7.6}
D	26.5 ^{+17.5} _{-9.5}	47.5 ^{+15.5} _{-13.5}	87.2 ^{+53.8} _{-33.2}
E	33.5 ^{+2.5} _{-2.5}	58.5 ^{+3.5} _{-1.5}	118.2 ^{+6.8} _{-5.2}
F	22.7 ^{+1.3} _{-2.7}	33.5 ^{+5.5} _{-6.5}	52.7 ^{+6.3} _{-4.7}
G	11.7 ^{+3.3} _{-3.7}	26.2 ^{+5.8} _{-5.2}	49.7 ^{+21.3} _{-15.7}
H	21.0 ^{+3.0} _{-3.0}	45.0 ^{+12.0} _{-8.0}	80.2 ^{+14.8} _{-10.2}
I	12.1 ^{+1.9} _{-1.1}	24.7 ^{+3.3} _{-2.7}	41.5 ^{+5.5} _{-3.5}
J	12.5 ^{+2.5} _{-1.5}	26.2 ^{+0.8} _{-1.2}	46.2 ^{+7.7} _{-7.2}
Average value	19.2^{+24.8}_{-11.2}	37.6^{+25.4}_{-16.6}	68.8^{+72.2}_{-34.8}

A correlation factor can be established between the results of laboratory tests and fleet tests. The mean leak flow rates of these 10 types of MAC systems at 3 temperatures are respectively 19.2, 37.6, and 68.8 g/yr. The regression curve (see Figure 2.40) is then established according to these points with $k = 3.856 \times 10^{-11}$. Taking into account the hour-by-hour temperature in different European climatic zones where the 40 vehicles have run, the annual average temperature is 15.5°C. Finding out the point, which corresponds to this

temperature: 9.1 g/yr at 496 kPa. Supposing there is additionally 5-6% coming from running mode of MAC system, the total leak flow rate makes $9.1/0.96 = 9.5$ g/yr. This acceptable difference between laboratory tests and fleet tests (10.0 g/yr) proves the possibility to predict the leak flow rate of a MAC system only by laboratory tests at constant temperatures.

In brief, the procedure for leak flow rate prediction of a given MAC system consists of three steps:

- (1) Tests at 3 different temperatures to establish the leakage behavior of a given MAC system;
- (2) Finding out the leak flow rate value on the regression curve, corresponding to the average annual temperature of a city;
- (3) Real life leak flow rate calculation taking into account the running mode.

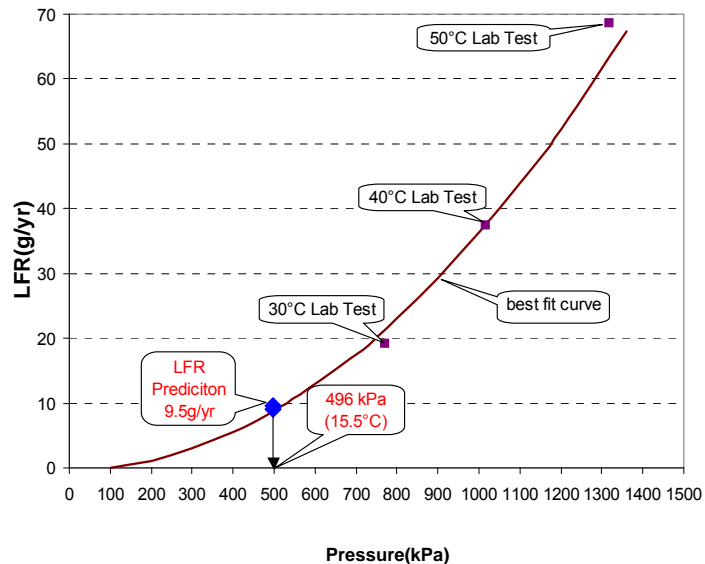


Figure 2.40 Establishing the correlation factor.

Table 2.19 gives some examples for annual leak flow rate predictions. Firstly, tests at 3 temperatures allow calculating the regression curve using the least square method. For system n°1, the parameter k is 3.79×10^{-11} . Using Equation (2.21), the leak flow rate at constant temperature of 15.5°C is 9.0 g/yr. As a result, the predictive annual leak flow rate of system n°1 is 9.4 g/yr. Annual leak flow rates for two other systems are obtained likewise, which lead to 7.7 and 15.5 g/yr.

Table 2.19 Annual LFR predictions of 3 MAC systems based on the method of correlation factor.

T(°C)	P(kPa)	Leak flow rate (g/yr)		
		System n°1	System n°2	System n°3
30	770	21.1	19.9	36.4
40	1017	40.0	33.3	64.2
50	1318	65.3	52.8	109.4
(1) parameter k		3.80×10^{-11}	3.13×10^{-11}	6.31×10^{-11}
(2) LFR @ 15.5°C		9.0	7.4	14.9
(3) Annual LFR prediction (g/yr)		9.4	7.7	15.5

To conclude, this chapter introduces a laboratory test method to determine the leak flow rate of MAC systems ensuring good measurement accuracy. The qualified test method has been a basis for establishing the EU regulation 706/2007. Results on either an overall system or the sum of all system components are equal under the uncertainty level, so that both methods are proved suitable for determining the leak flow rate of a MAC system. Knowing the running mode contribution, which is about 5-6% of total emissions, the major part of the refrigerant is emitted during the period where the vehicle is standstill, so that the leak flow rate of the MAC system can be determined without performing running mode tests. Once the leakage behavior of a MAC system is determined, the mean annual temperature of a city is sufficient for leakage prediction based on the proposed correlation factor method.

2.3 References

- [CLO04a] Clodic, D., Palandre, L., 2004. Measurement of leak flow rates of mobile air-conditioning systems. Proceedings of the 15th annual earth technologies forum and mobile air conditioning summit", Washington, D.C., April 13-15.
- [CLO04b] Clodic, D., Zoughaib, A., 2004. Measurement of leak flow rates of MAC components by infrared spectrophotometry, and calculations of annual leak flow rates. VDA Alternate Refrigerant Wintermeeting, Saalfelden, Austria, 18 - 19 February.
- [CLO96] Clodic, D., 1996. Zero leaks - Limiting emissions of Refrigerants. Ashrae. 189 p.
- [CLO07] Clodic, D., Yu, Y., 2007. Elaboration of a correlation factor based on fleet tests and Mobile Air Conditioning(MAC) system laboratory tests. SAE technical paper 2007-01-1187.
- [CRA75] Crank, J., 1975. The mathematics of diffusion. Clarendon Press, Oxford, 432 p.
- [FLA01] Flaconnèche, B., Martin, J., Kolpffer, MH., 2001. Transport properties of gases in polymers: experimental methods. Oil and Gas Science and Technology, Vol. 56, pp. 245-259.
- [GUI93] Guide to the Expression of Uncertainty in Measurement. ISO, Geneva, Switzerland, 1993.
- [KIM92] Kimura, S., Hirose, T., 1992. Polymers for Gas Separation. Wiley, 245 p.
- [MAG90] Magg, H.,1990. Elastomers for automotive air-conditioning hoses. SAE technical paper 900575.
- [MOO04] Moore, T.T., Damle, S., Willams, P.J., Koros, W.J., 2004. Characterization of low permeability gas separation membranes and barrier materials; design and operation considerations. Journal of Membrane Science, Vol. 245, pp. 227-231.
- [MOR07] Morgado, I., Legras, J-C., Clodic, D., 2007. Primary standard for measuring refrigerant leak flow rate. Congrès de métrologie. Lille, France, 18-21 juin.
- [MUL98] Müller, H.K., and Nau, B.S., 1998. Fluid sealing technology. Hardcover. pp.2-16.

CHAPTER 3

Emission predictions of hoses used in MAC systems

List of Figures

Figure 3.1 Structure of ethane and polyethylene.	59
Figure 3.2 3D models of ethane and polyethylene.....	59
Figure 3.3 Schematic representations of 3 types of polymers	60
Figure 3.4 Amorphous and crystalline state of polymers.	61
Figure 3.5 Specific volume-temperature curve.	62
Figure 3.6 hoses types used in MAC system.....	63
Figure 3.7 Schematic of permeation process.....	64
Figure 3.8 Typical sorption isotherms vs. vapor pressure.....	65
Figure 3.9 Membrane permeation measurement apparatus.....	68
Figure 3.10 Temperature distribution of test bench.	69
Figure 3.11 temperature distribution of membrane sample	69
Figure 3.12 A typical time lag for HFC-134a gas permeation in polymer A (thickness 1.7 mm).	70
Figure 3.13 leak flow rate measurement for membrane A at 3 temperatures.....	72
Figure 3.14 Evolution of leak flow rates as a function of temperature.	73
Figure 3.15 Evolution of leak flow rates as a function of pressure.....	73
Figure 3.16 Evolution of gas amount as a function of time for membranes A.	73
Figure 3.17 Evolution of gas amount as a function of time for membranes type G.	74
Figure 3.18 Evolution of gas mole number vs. time at three different temperatures (membrane A). ...	76
Figure 3.19 Evolution of gas mole number vs. time at three different temperatures (membrane E). ...	76
Figure 3.20 Arrhenius plot for membrane samples A, E and F.....	78
Figure 3.21 Evolution of permeability coefficient as a function of pressure.....	79
Figure 3.22 Relative error due to regression.....	81
Figure 3.23 Pe vs. saturation pressure for 6 membranes.....	81
Figure 3.24 Permeation prediction model for membrane A to F.	82
Figure 3.25 LFR of membrane D=30mm and e=1mm for membranes A to F.	82
Figure 3.26 Suciton profil of a hose.....	83
Figure 3.27 Cylindrical shell.	83
Figure 3.28 Hose sample n°1 for permeation test.....	85
Figure 3.29 Emission prediction model for hose sample n°2.....	87
Figure 3.30 Emission prediction model for hose sample n°3.....	87
Figure 3.31 Veneer hose sample.	87

List of Tables

Table 3.1 List of MAC hoses.	63
Table 3.2 Materials list.....	63
Table 3.3 List of membrane samples.	71
Table 3.4 LFRs of membrane B and calculated coefficients of permeability.	72
Table 3.5 Permeability, diffusion, and solubility coefficients of membrane samples A.	74
Table 3.6 Permeability, diffusion, and solubility coefficients of membrane samples G.	74
Table 3.7 LFRs and Pe of membrane A of different thicknesses.....	75
Table 3.8 Test conditions for membranes A, E, and F.....	76
Table 3.9 Permeability coefficients of HFC-134a in membrane samples A, E, and F.	77
Table 3.10 Pe_0 and E_{pe} of three membrane samples.	77
Table 3.11 LFR and Pe for membrane A, B, and F for pressure effect study.....	78
Table 3.12 Coefficients of permeability of 6 membrane samples.	80
Table 3.13 Parameters κ_1 , κ_2 and κ_3 for membranes A to F.	81
Table 3.14 Pe and LFR calculated for each membrane.....	82
Table 3.15 Calculated and measured leak flow rate of the hose sample n°1.....	85
Table 3.16 Hose sample n°2 - LFR and permeation parameters.	87
Table 3.17 Hose sample n°3 - LFR and permeation parameters.	87
Table 3.18 Hose technology analysis.....	88

Introduction

As described in Chapter 1, flexible material hoses made of polymers are commonly used in MAC systems to connect different components of the system because they absorb vibrations and accommodate engine movements. Permeation through these polymers is an important issue in the leakage prediction of MAC system. Permeation of refrigerants through MAC hoses had been analyzed early in 1971[GOL71] in order to find a hose material suitable for the possible use of CFC-22, R-500, or R-502. Magg [MAG90] studied then elastomers used for CFC-22 and HFC-134a, and has done some comparisons of the permeation constants of materials based on different elastomers. This chapter focuses on the determination of permeability of different polymer materials and hoses, and their temperature and pressure dependence.

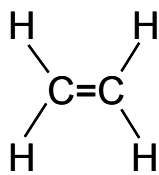
3.1 Introduction of polymer materials

The word “polymer” is coined from two Greek words: “poly” means many and “mer” means unit. Polymer means a particular class of macromolecules consisting of a set of regularly repeated chemical units of the same type, or possibly of very limited number of different types (usually two), joined end to end, or sometimes in more complicated ways, to form a chain of molecules [BOW02, JEN72].

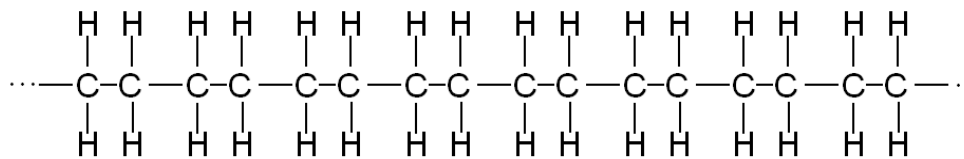
The simplest polymers are chain-like molecules of the type:

-A-A-A-A-A-A-A-A-A-A-...

where A is small group of covalently bounded atoms and the groups are covalently linked. Taking polyethylene as an example: the ethene molecule C_2H_4 is $CH_2=CH_2$, Two CH_2 groups connected by a double bond, as shown in Figure 3.1(a). Polyethylene is obtained by polymerization of ethene (see Figure 3.1(b)), by repeating about 20,000 times the elementary unit. Figures 3.2(a) and (b) illustrate the space filling model of ethene molecule and a polyethylene chain. The typical length of the chain is about $3 \mu m$ and the diameter of the polyethylene chain is about 1 nm, which lead to a ratio of 3000. Properties of polymers are determined by their molecular structure such as molecular weight, length, backbone structure, etc.



(a) Ethene molecule

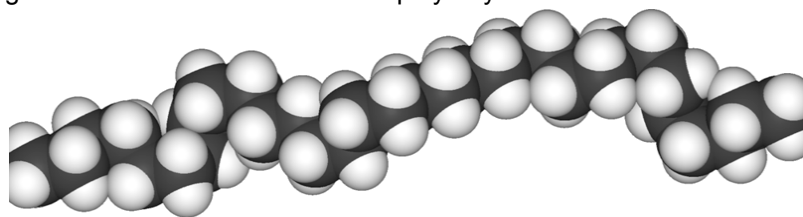


(b) Polyethylene molecule structure

Figure 3.1 Structure of ethane and polyethylene.



(a) Ethene model



(b) Space-filling model of a polyethylene chain

Figure 3.2 3D models of ethane and polyethylene.

Polymer like polyethylene is called homo-polymer in which all structural units are identical. If there are two or more chemically different types of structural unit in the chain, they termed copolymers. When copolymers contain two types of structural unit, they are called binary copolymers. Three typical binary polymers should be envisaged:

- *Random copolymers* in which the two units A and B are arranged in random sequence along the chain:
..... **ABAABBAABABAABB**.....
- *Block copolymers* in which the chain consists of large groups of identical units
..... **AAAABBBBAAAABBBB**.....
- *Alternating copolymers* in which the units alternate along the chain:
..... **ABABABABABABABAB**.....

3.1.1 The classification of polymers

There are many possible ways of classifications of polymers according to their structures, the general types of polymerization processes used to produce them, their physical properties, or their technological uses. Two common classifications are introduced based on structure or on properties.

3.1.1.1 Classifications based on structure

Figure 3.3 shows these types of polymer schematically. It should be noted that the real structures are three-dimensional, which is particularly important for networks.

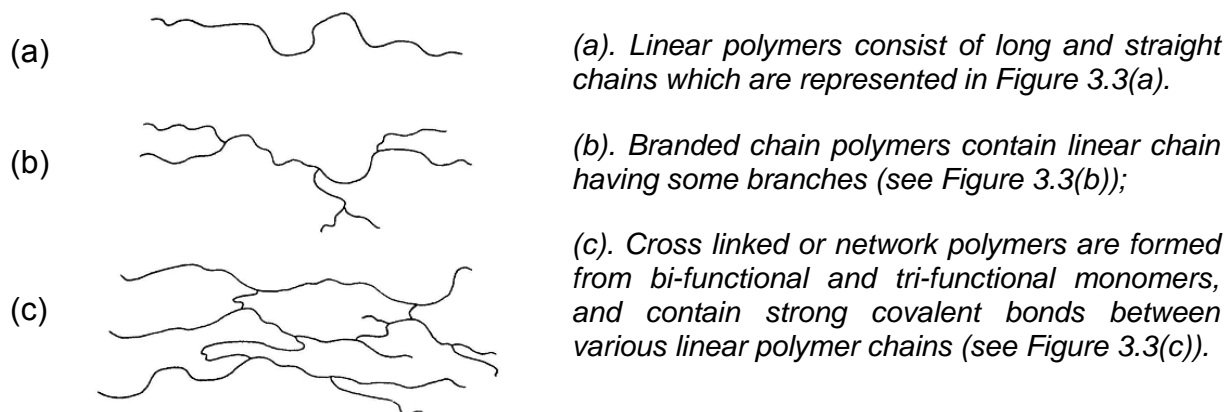


Figure 3.3 Schematic representations of 3 types of polymers

3.1.1.2 Classifications based on properties

The most important structural characteristics allowing determining the properties of polymers are:

- (1) the degree of rigidity of the polymer molecules,
- (2) the electrostatic and attractive forces between the chains,
- (3) the degree to which the chains tend to form crystalline domains,
- (4) the degree of cross-linking between chains.

From these standpoints of general physical properties, we recognize three types of polymers: elastomers, thermoplastic polymers, and thermosetting polymers.

Elastomers

Elastomers, which consist of long cross-linked molecules, are rubbers or rubber like elastic materials with elastic properties. Elastomers have a low cross-link density. The polymer chains are held together by the weakest intermolecular forces so that the polymer chains still have some freedom to move, but are prevented from permanently moving relative to each other by the cross-links. Elastomers are rubbery polymers that can be stretched easily to several times their unstretched length and which rapidly return to their original dimensions when the applied stress is released.

Elastomers may be strengthened by vulcanization process (heat treatment in presence of chemical agents). Vulcanization results in increasing the cross-linking of the molecules. Vulcanized elastomers are elastic for small deformations.

Thermoplastics

Molecules in thermoplastic are held together by relatively weak intermolecular forces so that the material softens when exposed to heat and then returns to its original condition when cooled. Most linear and slightly branched polymers are thermoplastic. Thermoplastic polymers are hard at room temperature, but when heated become soft and more or less fluid and can be molded. In melted conditions, thermoplastics may be formed by various methods (injection molding, extrusion, thermoforming).

Thermosets

Thermosets usually are three-dimensional networked polymers in which there is a high degree of cross-linking between polymer chains. The cross-linking restricts the motion of the chains and leads to a rigid material. Thermosets are stronger and stiffer than thermoplastics.

3.1.2 Crystallization, melting, and glass transition phenomena

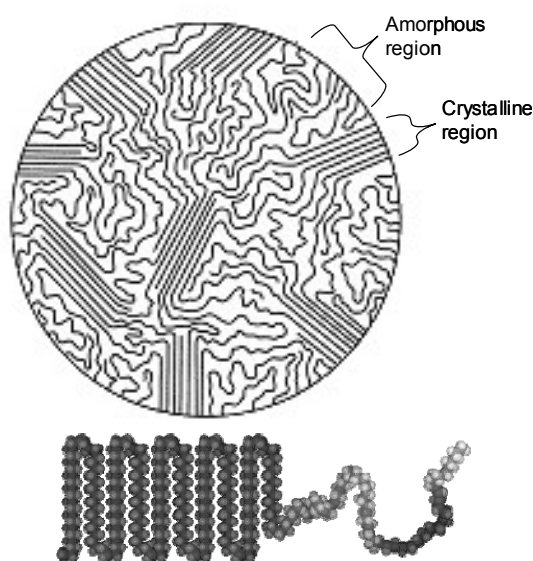


Figure 3.4 Amorphous and crystalline state of polymers.

- (a) The arrangement of polymer chain forming crystalline and amorphous regions is shown in Figure 3.4(a). Polymers may crystallize by aggregation of the chains to form highly ordered crystalline regions. The polymer crystal is made up from one-dimensional chain-folded sequences, shown in Figure 3.4(b). It can be seen that part of molecules are arranged in regular order; these regions are called crystalline regions. In between these ordered regions, molecules are arranged in random disorganized state, called amorphous regions.
- (b)

The difference between amorphous and crystalline polymers is reflected in important differences in their physical properties. Generally, highly crystalline polymers have a higher density than the corresponding amorphous ones, and they exhibit brittle fracture on deformation. Amorphous polymers are softer, have lower melting points, and are more penetrated by solvents than are their crystalline counterparts.

Both the amorphous and crystalline regions undergo a thermodynamic transition at a particular temperature. The amorphous regions undergo what is called the glass transition. Below the glass transition temperature, T_g , the polymer chains do not have the thermal energy to move and slide against each other. Molecular motion slows down, and the polymer resin becomes brittle and glassy. Above T_g , the polymer chains are mobile and the polymer is ductile, soft, and plastic. At T_g a dramatic change occurs in the local movement of polymer chains, which leads to great changes in their physical properties such as: density, heat capacity, mechanical modulus, and rate of gas or liquid diffusion through polymers.

As shown in Figure 3.5, the specific volume changes with temperature ABCD. The change along BC, seen at the melting point, T_m , with its associated change in properties, is termed a first order transition. In Figure 3.5, from DCEF the discontinuity occurring at point E, which is associated with the loss of rotational freedom on solidification, is termed a second order transition. Above this glass transition temperature, T_g , polymers become flexible and rubbery, and become rigid in the region EF. In brief, T_g represents the boundary between the rubbery and glassy states.

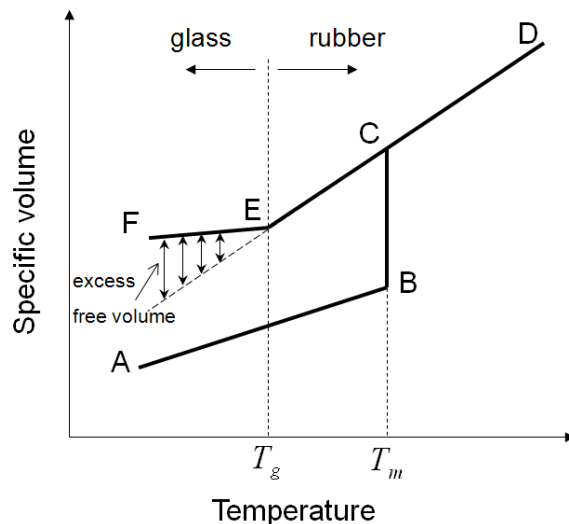


Figure 3.5 Specific volume-temperature curve.

Polymers can be divided into rubbery and glassy categories. In a rubbery polymer, segments of the polymer backbone can rotate freely around their axis; this makes the polymer soft and elastic. In a glassy polymer, steric hindrance along the polymer backbone prohibits rotation of polymer segments; the result is a rigid, tough polymer. When a glassy polymer is heated and reaches T_g , the thermal energy is sufficient to overcome the hindrance restricting rotation of polymer backbone segments. In general, values of T_g well below room temperature define the domain of elastomers, whereas values above room temperature define rigid, structural polymers.

A good example of the importance of these two temperatures is polyethylene, in which T_g is -80°C and T_m is 110°C . Below the glass transition temperature, polyethylene is glassy and brittle, which is not suitable for commercial use. Above the melting point, the polymer is fluid, and can be processed by injection molding, extrusion, etc.. The intermediate temperatures (between -80° and 110°C) are the region where polyethylene is tough and plastic, yet strong and rigid.

A small amount of unfilled volume is associated with the end of a polymer chain. This volume is called the *free volume*. The concept of polymer free volume is illustrated in Figure 3.4. At high temperature, polymers are in rubbery state; free volume is due to the amorphous structure. As the temperature decreases, the free volume also decreases until the glass transition temperature, where the free volume is reduced to a point at which the polymer chains can no longer rotate. The excess free volume between the polymer chains is frozen in to the polymer matrix.

3.1.3 Polymers commonly used in MAC components

Ten different technologies of hoses with different diameters have been identified in ten different types of MAC systems (Table 3.1).

Table 3.1 List of MAC hoses.

Hose Type	Technology	DN
All Rubber	IIR-EPDM	8,10,16
	CIIR-PET-CR	16
	EPDM-SF-CIIR	8,10,16
Barrier	CIIR-PVA-PA-CR	8,10,16
Veneer	PA-EPDM	8,10,5
	PA-IIR-PET-EPDM	8,10,16
	PA-IIR-PES-EPDM	8,13
	PA-IIR-PET-CIIR	8
	PA6-HNBR-AR-HNBR	13
	PA6-EPDM-PVAL-AEM	13

Table 3.2 Materials list.

Material	Abbreviations	Classification
PA	Polyamide	Thermoplastic
EPDM	Ethylene Propylene Diene Monomer	Thermoplastic
HNBR	Hydrogenated Nitril Butadiene Rubber	Elastomer
CR	Chloroprene Rubber	Elastomer
IIR	Isobutene Isoprene Rubber	Elastomer
CIIR	Chloro Isobutene Isoprene Rubber	Elastomer

According to the technology of these hoses summarized in Table 3.1, six materials commonly used in MAC hoses have been classified and shown in Table 3.2. Except PA (polyamide) and EPM, which are thermoplastic polymers, others commonly used materials are all elastomers. Due to the high leakage resistance of PA to refrigerant, the hoses are classified into three types (see Figure 3.6) : all rubber, barrier, and veneer. As discussed previously in § 1.3, all rubber hoses consist of only elastomers. Barrier and veneer hoses use a thin polyamide (PA) layer to prevent refrigerant permeation.

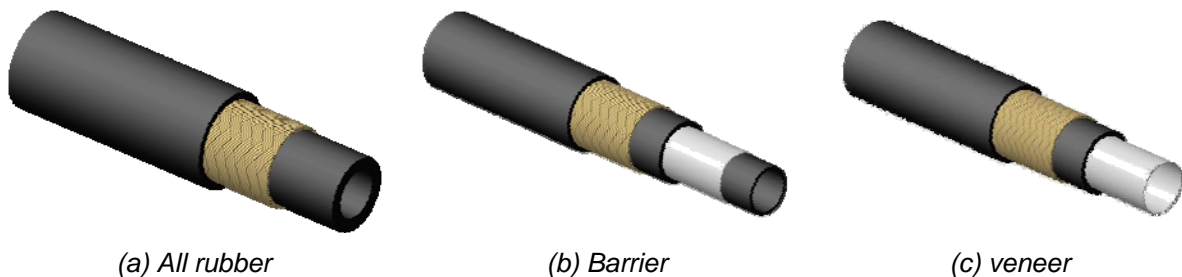


Figure 3.6 hoses types used in MAC system.

Due to the multiple-layer structures, gas transport through hoses appears quite complex to characterize and to analyze. For example, permeations are fairly different depending on their material compositions and diameters. This chapter focuses on refrigerant permeation through polymers, in order to understand transport phenomena through the different materials and try to establish a prediction model to forecast leak flow rate of MAC hoses.

3.2 Gas permeation theory through polymers

3.2.1 Fundamentals of transport phenomena

The refrigerant charge in a MAC system depends on the internal volume of the system. Taking a simple evaporator of MAC system for an example, 600 grams is charged in the volume of 5 dm³; the refrigerant is in two-phase equilibrium. At 20°C, the volume of the liquid is 0.385 dm³, which only occupies 8% of total internal volume of the MAC system in contrast to 92% of gas volume. Moreover, liquid is stocked in the coldest location of the system, due to the “heat pipe effect”.

Note: Heat pipe effect: when a MAC system is stopped for a long time, the TXV or the orifice tubes (which are the 2 possible expansion devices) are open so there is a single pressure in all the system. This pressure is defined at the liquid / vapor interface and the liquid “migrates” at the coldest location because condensation occurs there. In winter, liquid will be typically stored in the condenser when the vehicle is running because it is the coldest point. In summer, when the MAC system has run and the vehicle is parked under the sun, the coldest point is the evaporator. The Mac system behaves partially as a heat pipe, condensation occurring at the lowest temperature location.

Therefore, all the circuit (except where the liquid is stored) is under the saturated pressure and in gas phase. The leakage through hoses is related to gas permeation through polymers, excepted for their fittings that will be studied in Chapter 4.

The gas transport through dense polymers is usually described by a solution-diffusion model. As shown in Figure 3.7, application of gas pressure on upstream of a membrane leads to the following steps:

- Dissolution of molecules in the polymer following **adsorption** at the surface;
- Random movement of the dissolved gas in and through the polymer: a **diffusion** process driven by concentration gradients;
- Release of the gas at the opposite interface, **desorption** from the surface of the polymer.

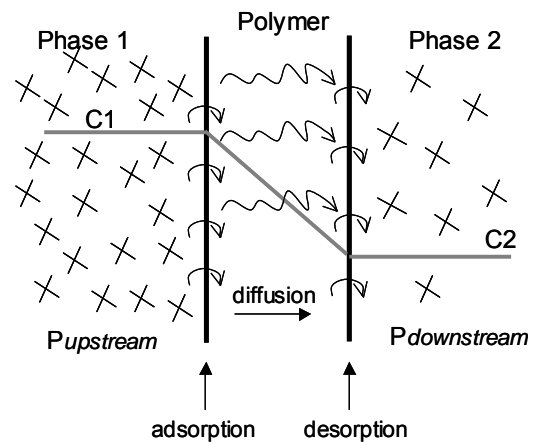


Figure 3.7 Schematic of permeation process.

Each step depends on the characteristics of the polymer and the molecules. It should be pointed out that permeation describes the overall mass transport phenomena, whereas the term diffusion refers only to the movement of the gas molecules inside the polymer.

3.2.2 Diffusion

The diffusion of a gas in a polymer occurs as a result of random motions of individual molecules of the gas and the cooperative motion of polymer chain segments surrounding these molecules. Gas transport through polymers is generally described by Fick's first law of

diffusion [FIC85, CRA68], which describes a linear relationship between the molar flux of substance diffusing through a membrane and the concentration gradient:

$$J = -D\nabla C \quad (3-1)$$

Where,

J is molar flux of substance ($\text{mol s}^{-1} \text{m}^{-2}$)

D is known as the diffusion coefficient (m^2s^{-1}).

C is molar concentration (mol m^{-3})

For membrane sample, when the thickness is much smaller than the diameter, one considers that the diffusion occurs only in one direction x (see Equation 3-2).

$$J = -D \frac{\partial C}{\partial x} \quad (3-2)$$

In transient state, the mass transfer by diffusion is different from zero and the concentration is a function of position and time. This transient state is described by Fick's second law expressed by Equation (3-3).

$$\frac{\partial C}{\partial t} = D \frac{d^2 C}{dx^2} \quad (3-3)$$

The diffusion coefficient depends on the nature of the polymer, the temperature, and generally the concentration and it can be determined from permeability measurements.

3.2.3 Sorption

At a given temperature, the concentration C of gas dissolved in a polymer is determined by the solubility of the penetrant in the polymer and the penetrant pressure P:

$$C = S(C)P \quad (3-4)$$

Where S is the solubility coefficient expressed in $\text{mol m}^{-3} \text{Pa}^{-1}$. Generally, S is a function of the temperature, the pressure, and the concentration.

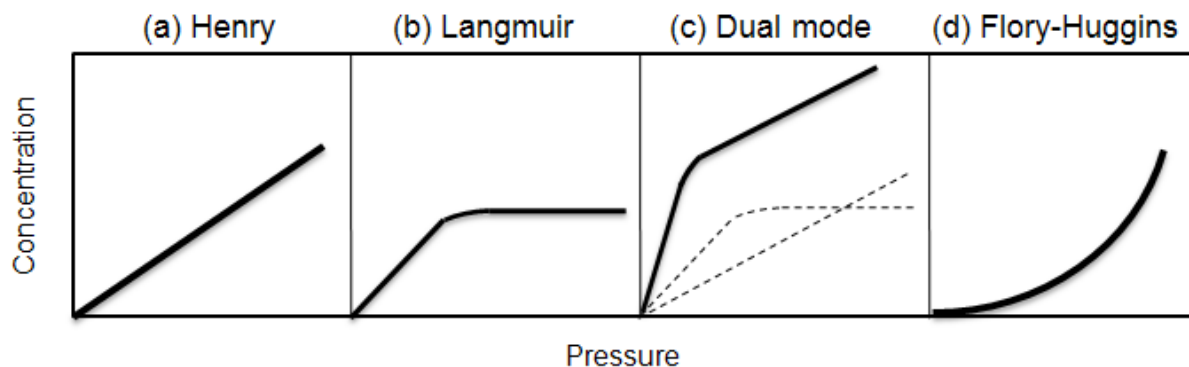


Figure 3.8 Typical sorption isotherms vs. vapor pressure.

The mechanism of diffusion is quite different in rubbery and glassy polymers. This is mainly due to the fact that glassy polymers are not in a true state of equilibrium.

Sorption of rubbery polymers

Gas solubility in rubbery polymers is either linear or convex to the pressure as shown in Figure 3.8(a) and 3.8(d). In the low pressure and ideal gas cases, Henry's law (Figure 3.8(a)) is obtained:

$$C = SP \quad (3-5)$$

In some other case, the sorption isotherm is described by the Flory-Huggins sorption mode (Figure 3.8(d)) expressed by Equation (3-5):

$$\ln(P/P_0) = \ln(v) + \ln(1-v) + \chi(1-v)^2 \quad (3-5)$$

Where P is the pressure of the gas, P_0 is its vapor pressure at the temperature, v is the volume fraction of the dissolved gas, and χ is the Flory-Huggins parameter.

Sorption of glassy polymers

The sorption isotherm for glassy polymers is commonly observed to be dual mode (Figure 3.8(c)). Concentration is the sum of the concentrations of two thermodynamically distinct phenomena: molecules dissolved in the matrix and molecules dissolved in the excess free volume.

$$C = C_D + C_H = k_D P + C_H \quad (3-6)$$

Where C_D , which is dissolved in the equilibrium free volume, behaves as in normal sorption mode by a linear expression as in the rubbery case. C_H depends on Langmuir saturation constant, C'_H , holes affinity constant, b , and pressure, P . C_H is assumed to be adsorbed into the excess free volume and the sorption will cease when all the sites are filled (expressed by Equation(3-7)).

$$C_H = \frac{C'_H b P}{1 + b P} \quad (3-7)$$

So the total concentration is obtained by combining Equations (3-6) and (3-7). This dual sorption is well illustrated in Figure 3.8(c).

$$C = C_D + C_H = k_D P + \frac{C'_H b P}{1 + b P} \quad (3-8)$$

From Equation (3-8), the solubility coefficient for this sorption mode can be written as:

$$S = \frac{C}{P} = k_D + \frac{C'_H b}{1 + b P} \quad (3-9)$$

It can be seen that the solubility decreases with the increase of pressure.

3.2.4 Permeability

The steady state flux can be related to pressure units, when Henry's law is obeyed. The concentration of the gas dissolved in elastomer is determined by the solubility and the partial pressure P , $Pe = DS$. Then, the coefficient of permeability is introduced to determine the gas flux.

$$J = -DS \frac{\partial P}{\partial x} = -Pe \frac{\partial P}{\partial x} \quad (3-10)$$

Stern and Frisch [STE81] pointed out that for small molecules in rubbery polymers, the phenomena are rather simple and the diffusion is Fickian. For more condensable gases or vapors, the transport mechanism becomes more complicated, and transport coefficients are functions of concentration, temperature and pressure.

3.3 Permeation tests through membrane samples

In standstill mode of a MAC system, the temperature varies with the ambient temperature, which means lower than 40°C. Therefore, the test condition is defined to vary from 30°C to 50°C. Under these moderate temperature and pressure conditions, the mass transport is supposed to be basic diffusion phenomena.

3.3.1 Test method for transport coefficients determination based on leak flow rate tests

By introducing the definition of the permeation coefficient, Pe , the leak flow rate of a planar membrane of thickness, e (in the case where the diameter of the membrane is much larger than the thickness), can be obtained by Equation (3-11).

$$J = \frac{dn}{dt} \frac{1}{A} = Pe \frac{\Delta P}{e} \quad (3-11)$$

Therefore, the leak flow rate of HFC-134a can be calculated by Equation (3-12).

$$\dot{m} = \frac{dm}{dt} = M_{\text{HFC-134a}} \cdot \frac{dn}{dt} = M_{\text{HFC-134a}} \cdot J \cdot A = M_{\text{HFC-134a}} Pe A \frac{\Delta P}{e} \quad (3-12)$$

Equation (3-12) can also be written as Equation (3-13), where r is the radius of the section where the pressure is applied to:

$$\dot{m} = M_{\text{HFC-134a}} \cdot Pe \cdot \pi r^2 \frac{(P_{\text{upstream}} - P_{\text{downstream}})}{e} \quad (3-13)$$

Knowing the mass flow rate of a membrane with a given thickness e and radius r , the coefficient of permeability of this material can be calculated from Equation (3-14).

$$Pe = \frac{\dot{m}}{M_{\text{HFC-134a}}} \cdot \frac{e}{\pi r^2 (P_{\text{upstream}} - P_{\text{downstream}})} \quad (3-14)$$

3.3.2 Description and qualification of permeation test bench

Several measuring technologies have been developed for permeation tests [KAN04, MOO04, TOS92, TRE06]. [ISO06] describes also two procedures for measuring the permeability of gases through rubber under steady-state conditions.

As illustrated in Figure 3.9, an apparatus has been developed to perform permeation tests of HFC-134a through membrane samples (Figure 3.9). As shown in Figure 3.9(a), the membrane sample (Figure 3.9(c)) is fixed by two stainless steel parts (Figure 3.9(b)). Pressure is applied on one side of the membrane and measured by a pressure gauge. Measurement of permeation is performed by allowing the gas penetrant to permeate through a polymer membrane and accumulated in an accumulation volume. The rise of concentration at constant volume is monitored along the time. The temperature of the membrane sample is controlled using two heating resistances controlled by a thermocouple via a regulation system JUMO with a accuracy of $\pm 1^\circ\text{C}$ (see Figure 3.9(d)).

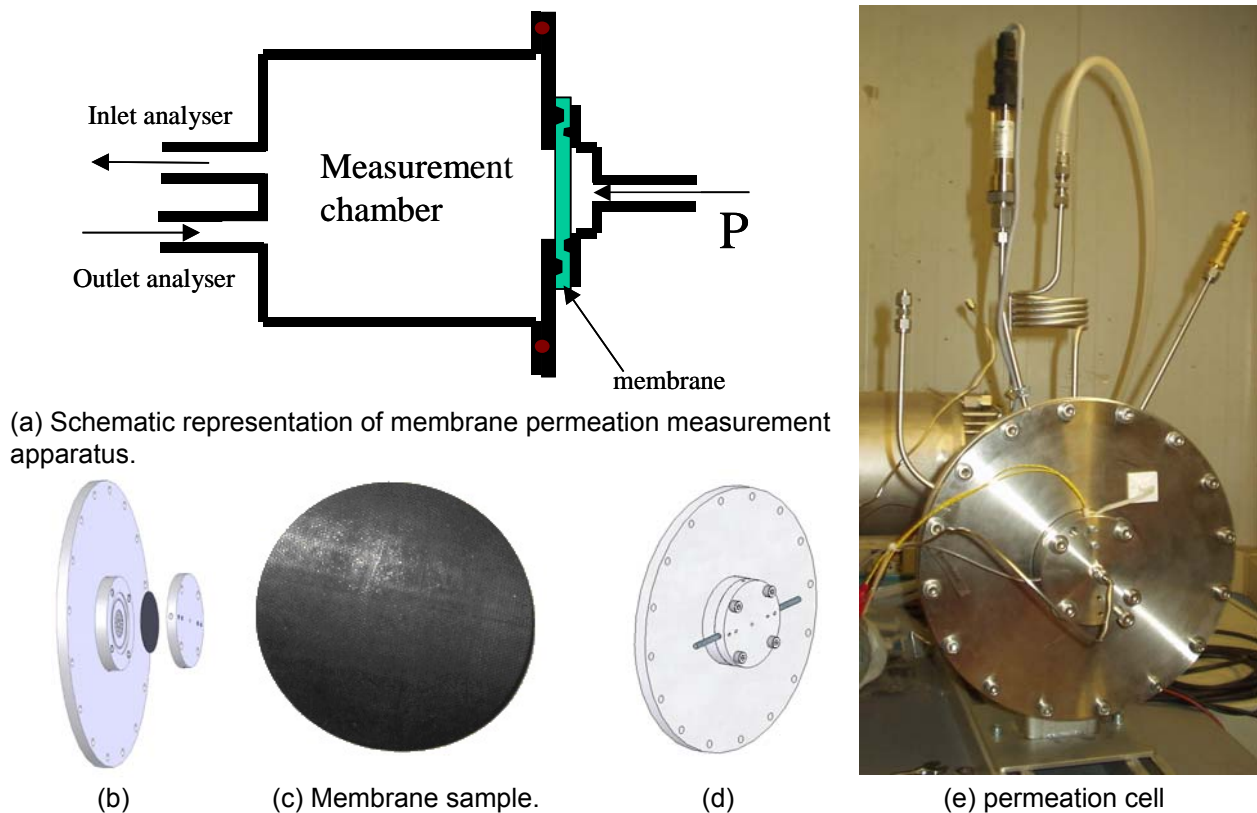


Figure 3.9 Membrane permeation measurement apparatus.

Pressure of the fluid HFC-134a is initially applied to one side of the membrane; on the other side the pressure is maintained at atmospheric pressure. Evolutions of concentration, pressure and temperature inside the accumulation volume as a function of time are measured and saved continuously by an acquisition system. According to the leak flow rate measurement method described in Chapter 2, the leak flow rate of the membrane can be determined and its transport coefficients can be identified as well. The actual test cell is shown in Figure 3.9(d).

Temperature homogenous verification

As shown in Figure 3.9(d), two heating resistances are introduced into the holes in the flange to control the temperature of the membrane sample. As it is impossible to directly measure the temperature of the membrane, simulations have been made to analyze the temperature distribution in the membrane and results are shown in Figure 3.10.

Front side refers to the surface where the upstream pressure is applied to the membrane and the back side faces to the atmospheric pressure. The diameter of the membrane sample is 65 mm, however the available diffusion area is the surface bounded by the chamfer. As illustrated in Figure 3.10(b), the real area being in contact with the upstream pressure is a circle of diameter 30 mm.

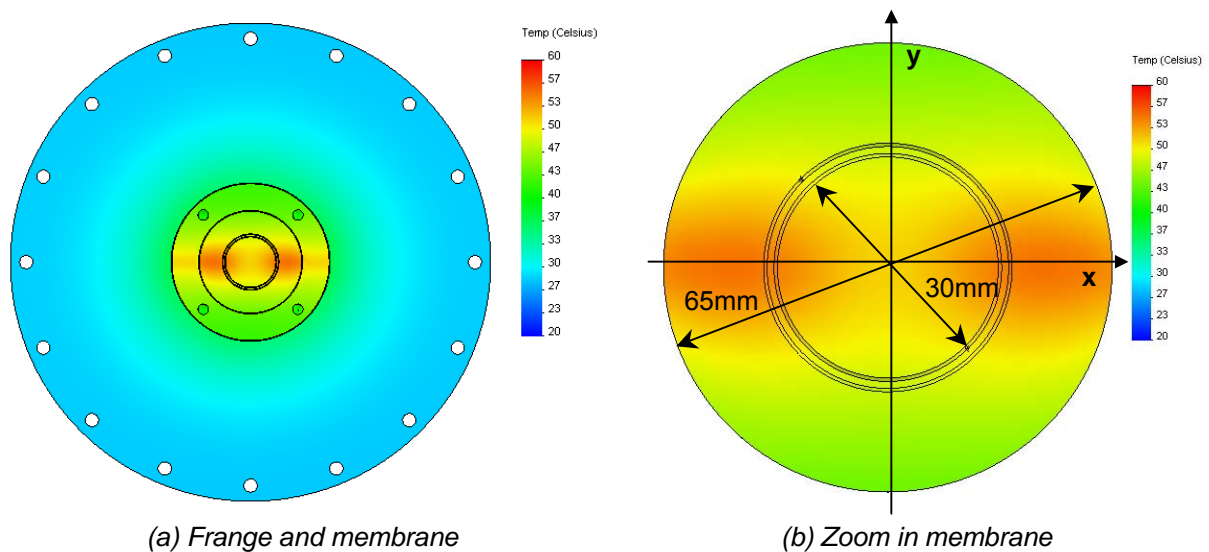


Figure 3.10 Temperature distribution of test bench.

As shown in Figure 3.11, except the edge, the temperature contribution on the front side is very homogeneous in the membrane area. On the back side, even better homogeneity of the temperature of the membrane has been observed, on x-axis, the temperature is $50.5\text{ }^{\circ}\text{C} \pm 0.7\text{ K}$ and on y-axis the temperature is $50.1\text{ }^{\circ}\text{C} \pm 0.1\text{ K}$. The diffusion area (30 mm) is at constant temperature and will be the reference surface for all membrane permeation tests.

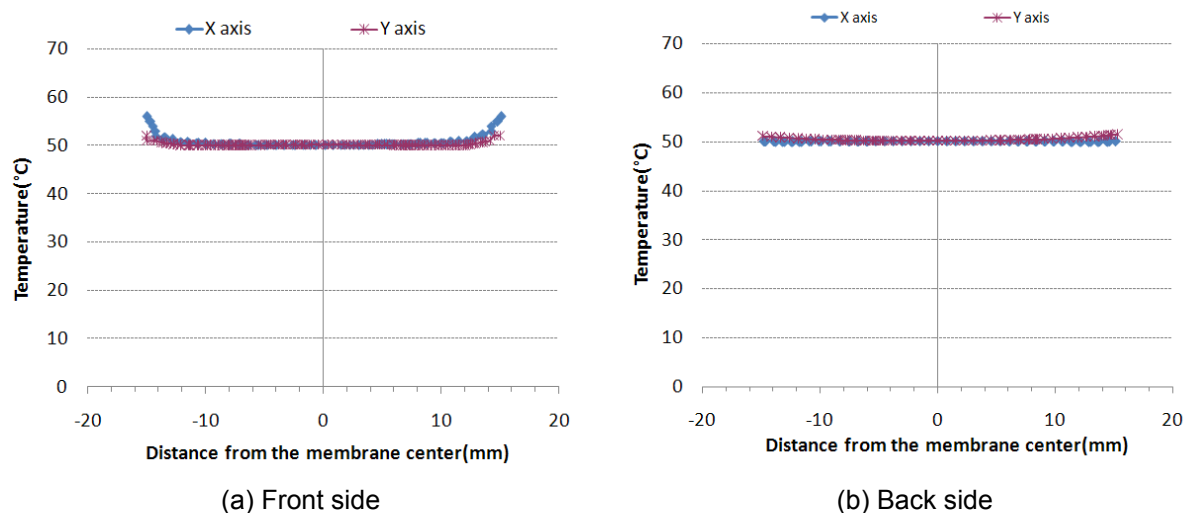


Figure 3.11 temperature distribution of membrane sample

3.3.3 Identification of transports coefficients

Permeability, diffusion, and solubility coefficients are determined based on the experimental curves using the “time lag” method [CRA68, CRA75, FLA01b, TRE06]. At the initial time, the pressure is applied on one side of the membrane and the concentration on the other side of the membrane is zero. The flux and the gas concentration in every point of the membrane vary along the time until the steady state diffusion regime through the membrane is achieved. The gas amount Q , which crosses the membrane, is given by the limited series development approaching the integration of Fick’s second law [NEO96, STA71].

$$\frac{Q}{eC} = \frac{Dt}{e^2} - \frac{1}{6} - \frac{2}{\pi^2} \sum_1^{\infty} \frac{(-1)^n}{n^2} \exp\left(\frac{-Dn^2\pi^2t}{e^2}\right) \quad (3-15)$$

When t tends towards long times, the exponential term can be neglected and the straight line is expressed as:

$$Q = \frac{DC_0}{e} \left(\theta - \frac{e^2}{6D} \right) \Rightarrow \theta = \frac{e^2}{6D}, \text{ thus } D = \frac{e^2}{6\theta} \quad (3-16)$$

Therefore, the diffusion coefficient can be obtained by finding the intercept, θ , commonly called “lag time”, on t-axis due to Equation (3-16). Knowing the upstream and downstream pressures, the permeability coefficient, Pe , is directly proportional to the slope of the straight line respecting the gas flow versus the applied pressure, as written in Equation (3-14), and the solubility coefficient, S , is calculated as the ratio of Pe/D .

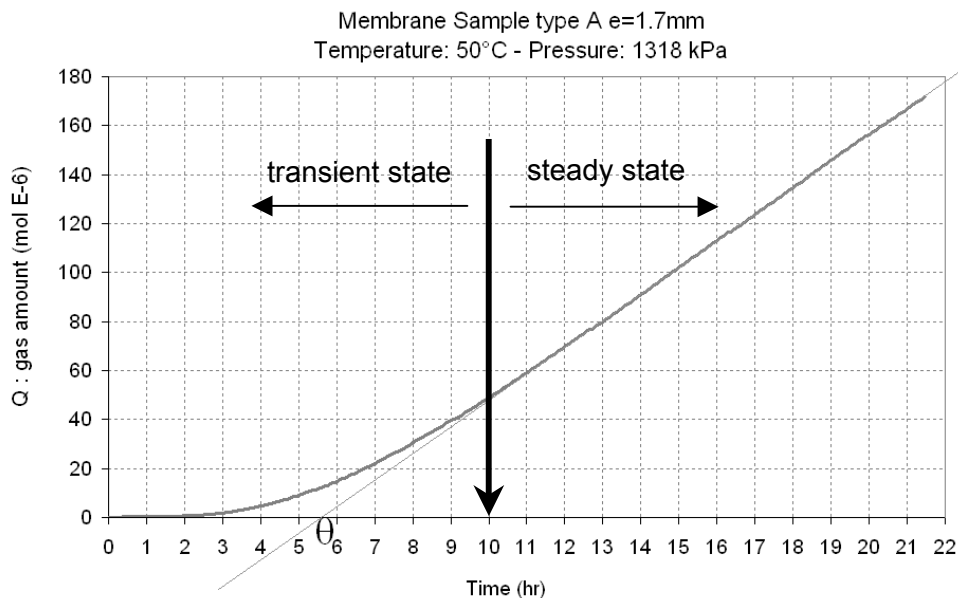


Figure 3.12 A typical time lag for HFC-134a gas permeation in polymer A (thickness 1.7 mm).

As illustrated in Figure 3.12, the gas amount of HFC-134a accumulated inside the accumulation volume is plotted along the time. The straight line is achieved after 10 hours. The time lag is obtained by finding the intercept of the straight line on time axis. 5.6 hours is found, which permits to calculate the coefficient of diffusion. The slope of the line gives the coefficient of permeability.

3.3.4 Permeation tests on membrane samples

Six commonly used polymers called A to G are chosen. Each type of membrane has been tested with given thickness and descriptions of each membrane are summarized in Table 3.3.

Table 3.3 List of membrane samples.

Membrane type	Thickness(mm)	Diameter(mm)
A	1.7, 2.5, 3.8	30
B	2.5	30
C	3.8	30
D	1.7	30
E	2.4	30
F	2.7	30
G	2.3, 3.1	30

The test procedures are as follows:

- Before the permeation tests, membrane samples are kept at ambient temperature ;
- Once mounted on the test bench, each membrane sample is heated to 50°C and concentration increase inside the accumulation volume is recorded until the steady state regime is achieved, which means the curve becomes a straight line as shown in Figure 3.12 ;
- Thereafter, tests have been carried out at 30, 40, and 50°C corresponding to saturation pressure of 770, 1017, and 1318 kPa. Results for each sample are given below.

Tests results for membrane A to F at temperatures of 30, 40 and 50°C

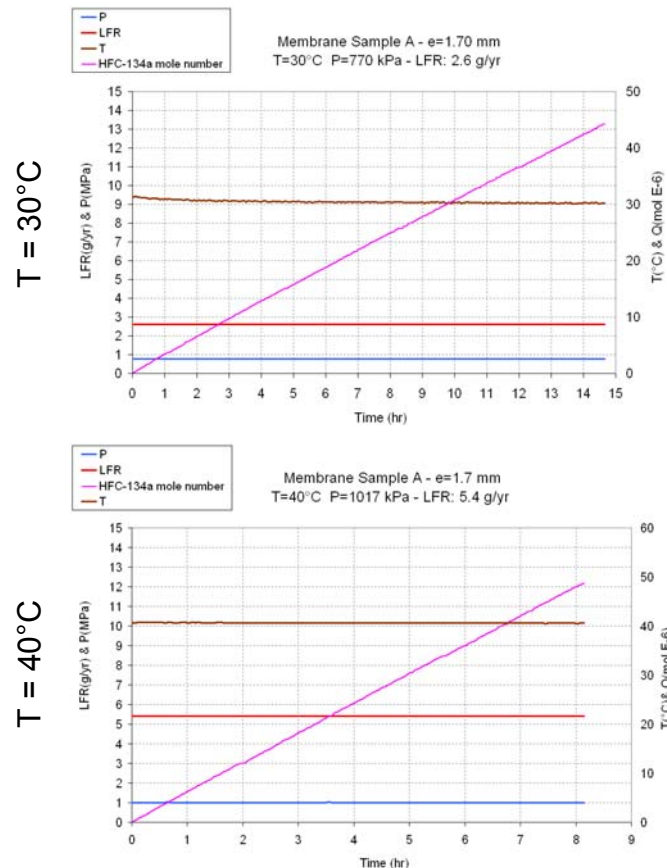


Figure 3.13 gives an example of leak flow rate measurement for membrane A; the temperature of the membrane, the pressure, and HFC-134a mole number are plotted along the time and the leak flow rate is calculated for each temperature and pressure condition.

Table 3.4 summarizes the leak flow rates and coefficient of permeability calculated for each case. For membrane A of 1.7 mm, leak flow rates vary from 2.6 g/yr at 30°C to 10.7 g/yr at 50°C. Corresponding coefficients of permeability are respectively 29.1, 44.1 and $65.7 \times 10^{-10} \text{ mol mm}^{-2} \text{ s}^{-1} \text{ MPa}^{-1}$.

By definition of the permeability, for a given membrane sample with constant r and e , the mass flow rate is

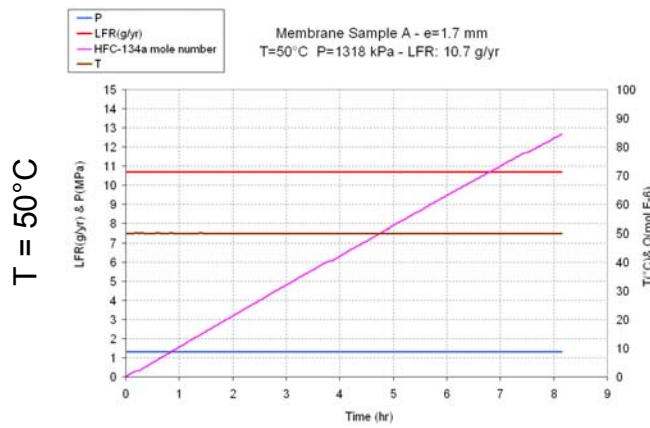


Figure 3.13 leak flow rate measurement for membrane A at 3 temperatures.

proportional to the pressure difference and the permeability. From these data, it is obvious that the coefficient of permeability for each membrane is not constant and depends on pressure and temperature conditions.

From Table 3.4, it can be seen that the highest coefficients of permeability occur for membrane B which rise up to 145.1 at 50°C. The lowest among these 6 membrane materials happens to membrane F for 0.54 at 50°C. There is a factor of 272 at 50°C and a factor of 195 at 30°C. Huge differences have been observed among these six membranes samples.

Table 3.4 LFRs of 6 membranes and calculated coefficients of permeability.

Membrane Type	Thickness e(mm)	T(°C)	Saturation Pressure (kPa)	LFR (g/yr)	$Pe \left[\frac{10^{-10} \text{ mol} \cdot \text{m}}{\text{m}^2 \cdot \text{s} \cdot \text{MPa}} \right]$
A	1.7mm	T=30°C	770	2.6	29.1
		T=40°C	1017	5.4	44.1
		T=50°C	1318	10.7	65.7
B	2.5 mm	T=30°C	770	5.6	58.9
		T=40°C	1017	12.8	98.3
		T=50°C	1318	25.1	145.1
C	3.8 mm	T=30°C	770	1.4	12.9
		T=40°C	1017	2.7	18.2
		T=50°C	1318	5.5	27.8
D	1.7 mm	T=30°C	770	0.22	2.46
		T=40°C	1017	0.43	3.51
		T=50°C	1318	0.80	4.91
E	2.4 mm	T=30°C	770	0.10	1.58
		T=40°C	1017	0.17	1.96
		T=50°C	1318	0.29	2.52
F	2.7 mm	T=30°C	770	0.017	0.30
		T=40°C	1017	0.030	0.39
		T=50°C	1318	0.055	0.54

Figure 3.14 and 3.15 illustrate evolutions of Pe with respect to the temperature and the saturation pressure. It is obvious that Pe increases as a function of temperature. This temperature and pressure dependence is not simply linear and will be discussed in detail in the following section.

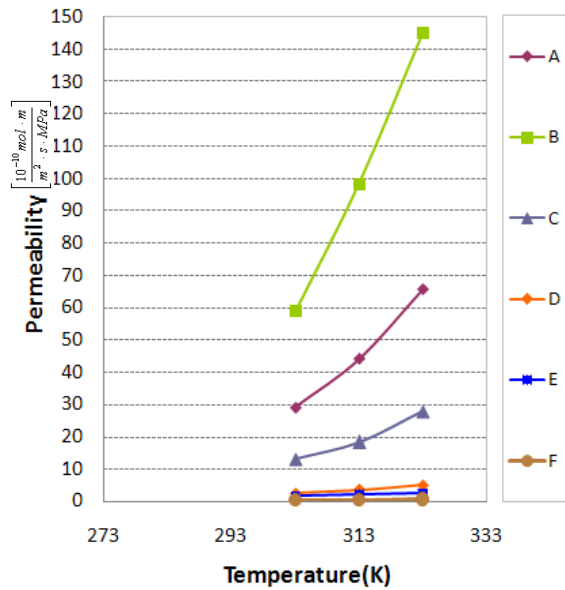


Figure 3.14 Evolution of leak flow rates as a function of temperature.

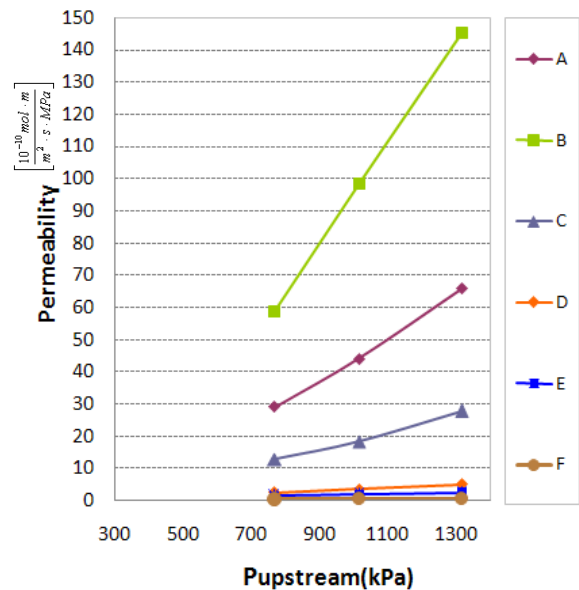


Figure 3.15 Evolution of leak flow rates as a function of pressure.

3.3.5 Factors influencing transport coefficients

It can be seen that the coefficients of permeability are not constant and depend on several conditions under which the measurements have been carried out. The effects of various parameters such as the thickness of membrane, the temperature and the pressure are studied in this section.

3.3.5.1 Effect of thickness

Study has been focused on identification of transport coefficients of HFC-134a in membrane samples. For each type of material A and G, membrane samples of two different thicknesses have been measured in order to verify the influence of membrane thickness.

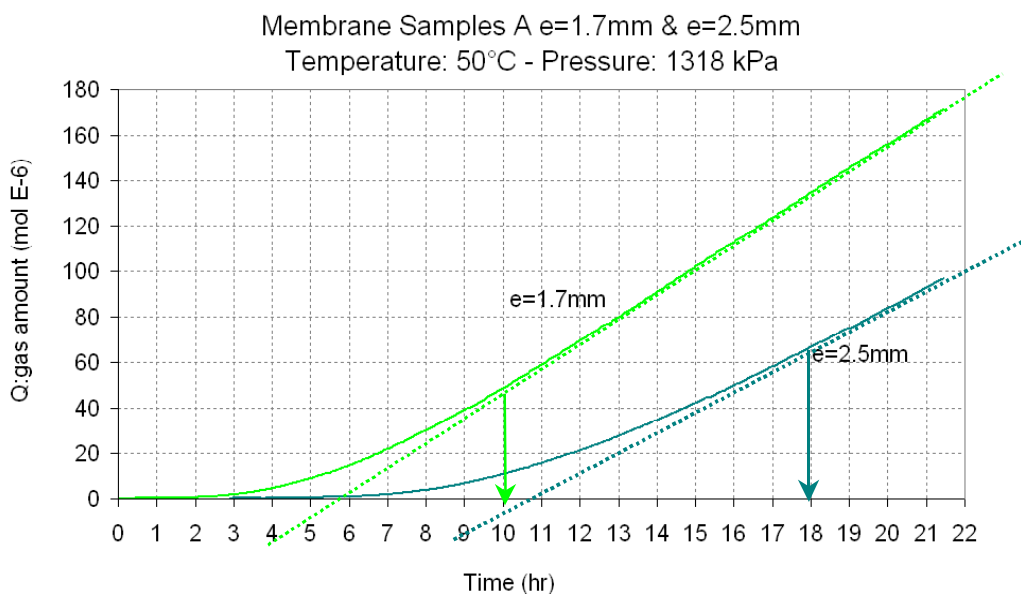


Figure 3.16 Evolution of gas amount as a function of time for membranes A.

Figure 3.16 presents the evolution of gas throughput through membrane samples of material A as a function of time. For material A, the time lags vary from 5.6 hours for the sample of 1.7 mm to 10.9 hours for the sample of 2.5 mm, which shows that the transient state depends strongly on the membrane thickness. The thicker the membrane, the longer the time to obtain the standstill permeation rate. The time lag is equal to the time necessary for diffusion front to cross the membrane and is proportional to the thickness of the membrane. For material G, membranes have been tested with 2.2 and 3.1 mm thicknesses. As illustrated in Figure 3.17, the time lag varies from 11 hours for the sample of 2.2 mm to that of 3.1mm. Membrane of 2.2 mm requires about 21 hours to achieving the steady state regime. For the 3.1mm membrane, the transient state lasted 39 hours.

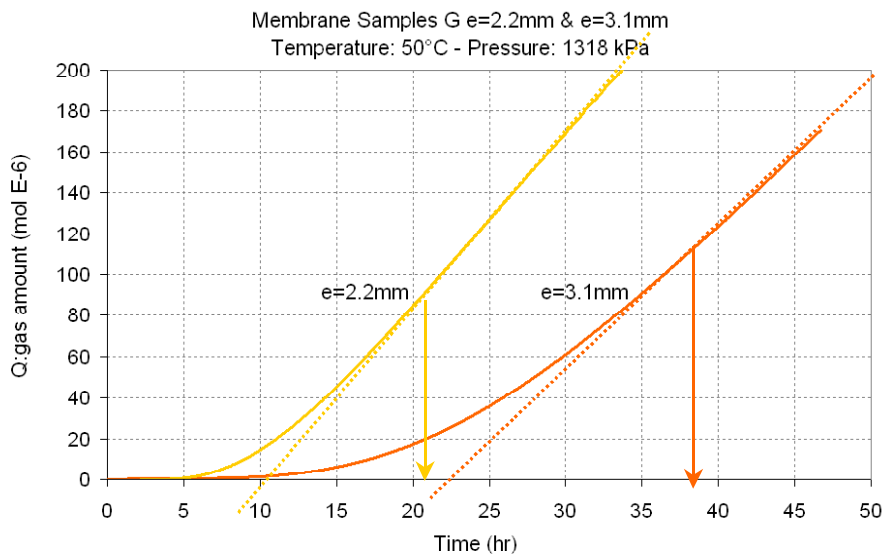


Figure 3.17 Evolution of gas amount as a function of time for membranes type G.

Tables 3.5 and 3.6 summarize the transport coefficients of two polymers. For membrane A, leak flow rate for 1.7mm thick is 10.7 g/yr and 7.3 g/yr for 2.5mm thick. 7.4 and 5.3 g/yr have been measured for membrane G.

Table 3.5 Permeability, diffusion, and solubility coefficients of membrane samples A.

	T=50°C P=1318kPa	LFR (g/yr)	$Pe \left[\frac{10^{-10} \text{ mol} \cdot \text{m}}{\text{m}^2 \cdot \text{s} \cdot \text{MPa}} \right]$	$D \left[\frac{\text{m}^2}{\text{s}} \right]$	$S \left[\frac{\text{m}^3}{\text{m}^3 \cdot \text{MPa}} \right]$
Membrane A	e=1.7mm	10.7	65.7	2.39E-11	275
	e=2.5mm	7.3	66.0	2.65E-11	249

Table 3.6 Permeability, diffusion, and solubility coefficients of membrane samples G.

	T=50°C P=1318kPa	LFR (g/yr)	$Pe \left[\frac{10^{-10} \text{ mol} \cdot \text{m}}{\text{m}^2 \cdot \text{s} \cdot \text{MPa}} \right]$	$D \left[\frac{\text{m}^2}{\text{s}} \right]$	$S \left[\frac{\text{m}^3}{\text{m}^3 \cdot \text{MPa}} \right]$
Membrane G	e=2.2mm	7.4	58.8	2.04E-11	288
	e=3.1mm	5.3	59.4	1.98E-11	300

Pe values are calculated by Equation (3-16) and the respective values are 65.7×10^{-10} and 66.0×10^{-10} g/yr. For membrane G, Pe varies from 65.7×10^{-10} to 66.0×10^{-10} . Taking into consideration the measurement uncertainties, both permeability coefficients for each material are very close to each other. Two diffusion coefficients are slightly different, which seems reasonable because of the determination method itself. More measurements have been performed for membrane A with a third thickness (3.8 mm) and all three membranes have been measured at temperatures of 30, 40, and 50°C. Table 3.7 gives the leak flow rates and the corresponding coefficients of permeability. Results show that regardless of temperature the Pe values are very close whatever is the thickness in the studied interval. In brief, the thickness of the polymer membranes does not influence the transport coefficients in a significant way.

Table 3.7 LFRs and Pe of membrane A of different thicknesses.

Thickness e(mm)	T(°C)	Saturation Pressure (kPa)	LFR (g/yr)	$Pe \left[\frac{10^{-10} \text{ mol} \cdot \text{m}}{\text{m}^2 \cdot \text{s} \cdot \text{MPa}} \right]$
1.7mm	T=30°C	770	2.6	29.1
	T=40°C	1017	5.4	44.1
	T=50°C	1318	10.7	65.7
2.5mm	T=30°C	770	1.8	29.6
	T=40°C	1017	3.6	43.2
	T=50°C	1318	7.5	67.8
3.8mm	T=30°C	770	1.2	30.0
	T=40°C	1017	2.4	43.8
	T=50°C	1318	4.9	67.3

3.3.5.2 Effect of temperature

Data available in the following papers [FLA01a, FLA01b, KLO01, KLU05] show that the transport coefficients (Pe, D and S) depend on temperature at a given pressure. The temperature dependence is commonly expressed in term of Arrhenius' law, which allows observing the relationship between diffusivity, solubility, permeability and temperature:

$$D(T) = D_0 \exp\left(-\frac{E_D}{RT}\right) \quad (3-17)$$

$$S(T) = S_0 \exp\left(-\frac{\Delta H_s}{RT}\right) \quad (3-18)$$

$$Pe(T) = Pe_0 \exp\left(-\frac{E_{Pe}}{RT}\right) \quad (3-19)$$

Thus, a linear relation exists between logarithmic plot of permeability and T^{-1} . Experimental measurements have been performed to verify this temperature-dependent behavior of permeability. Three membrane samples A, E, and F have been tested at constant pressure of 770 kPa and temperatures varying from 30 to 50°C (see Table 3.8).

Table 3.8 Test conditions for membranes A, E, and F.

Sample	Membrane A	Membrane E	Membrane F
Thickness	1.7 mm	2.4mm	2.7 mm
Pressure	770 kPa	770 kPa	770 kPa
Temperature	30, 40, and 50°C	30, 40, and 50°C	30, 40, and 50°C

Corresponding parameters are shown in Figure 3.18. It can be observed from the figure that the pressure (bleu curve) is kept constant. The pink curve represents the number of moles of HFC-134a passing through the membrane along the time. One can see that the slope changes rapidly with the change of temperature (green curve). Leak flow rates are calculated and summarized in Table 3.9.

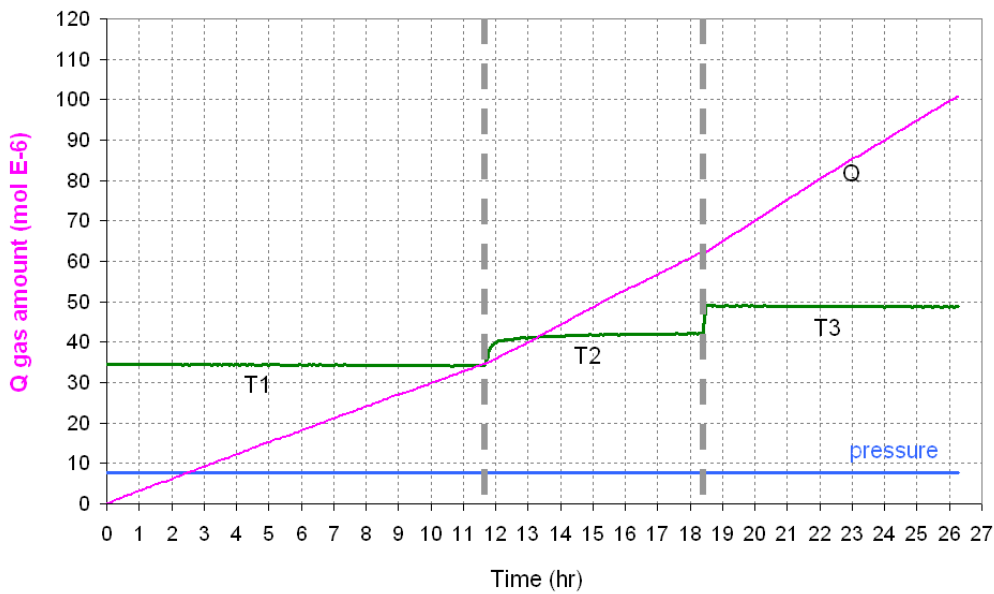


Figure 3.18 Evolution of gas mole number vs. time at three different temperatures (membrane A).

Figure 3.19 shows similar results to those of membrane A, confirming that the temperature effect on permeation is rapid and significant. A similar phenomenon can also be observed for membrane F. Leak flow rates and coefficients of permeability are summarized in Table 3.9.

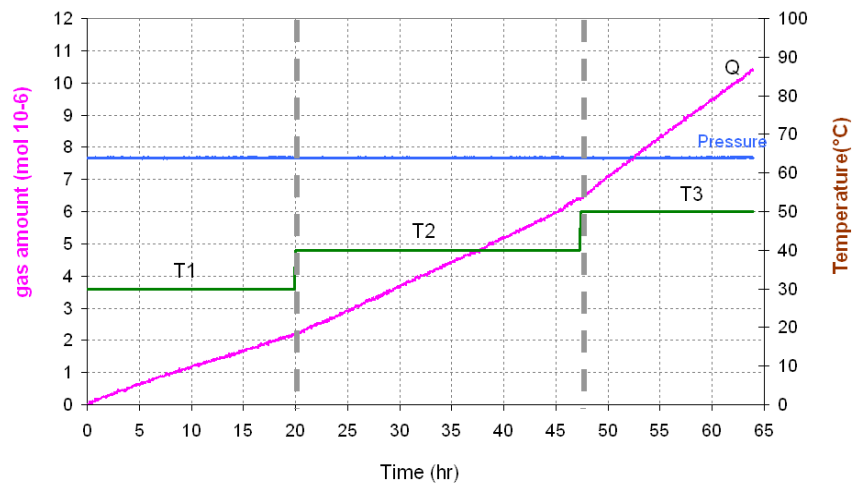


Figure 3.19 Evolution of gas mole number vs. time at three different temperatures (membrane E).

Equation (3-20) is used to determinate coefficients Pe_0 and E_{Pe} according to Equation (3-19).

$$\ln(Pe) = \ln(Pe_0) + \left(-\frac{E_{Pe}}{R}\right)T^{-1} \quad (3-20)$$

Table 3.9 Permeability coefficients of HFC-134a in membrane samples A, E, and F.

Pressure (kPa)	T(°C)	Membrane A		Membrane E		Membrane F	
		LFR (g/yr)	$Pe \left[\frac{10^{-10} \text{ mol} \cdot \text{m}}{\text{m}^2 \cdot \text{s} \cdot \text{MPa}} \right]$	LFR (g/yr)	$Pe \left[\frac{10^{-10} \text{ mol} \cdot \text{m}}{\text{m}^2 \cdot \text{s} \cdot \text{MPa}} \right]$	LFR (g/yr)	$Pe \left[\frac{10^{-10} \text{ mol} \cdot \text{m}}{\text{m}^2 \cdot \text{s} \cdot \text{MPa}} \right]$
770	T1 = 30	2.6	29.1	0.10	1.58	0.017	0.30
	T2 = 40	3.7	41.4	0.15	2.37	0.022	0.39
	T3 = 50	5.1	57.0	0.22	3.47	0.034	0.60

The slope and the intercept are obtained by using the method of least squares and results are summarized in Table 3.10. A good linear relationship between $\ln(Pe)$ and $1/T$ is found in Figure 3.20. The determination coefficient, R^2 , for membranes A and E is equal to 1 and for membrane F, R^2 is very close to 1, which shows a good agreement between experimental data and the regression values.

Table 3.10 summarizes the activation energy and the Pe_0 for three membrane samples. The activation energy of permeation of membrane E is 32.1 kJ/mol, which is higher than those of membrane A and F. That means the temperature effect on membrane E is more significant than on membrane A and F.

Table 3.10 Pe_0 and E_{Pe} of three membrane samples.

Samples	$E_{Pe} \left[\frac{\text{J}}{\text{mol}} \right]$	$Pe_0 \left[\frac{10^{-10} \text{ mol} \cdot \text{m}}{\text{m}^2 \cdot \text{s} \cdot \text{MPa}} \right]$
Membrane A	27441	1.56×10^6
Membrane E	32107	5.38×10^5
Membrane F	28140	2.06×10^4

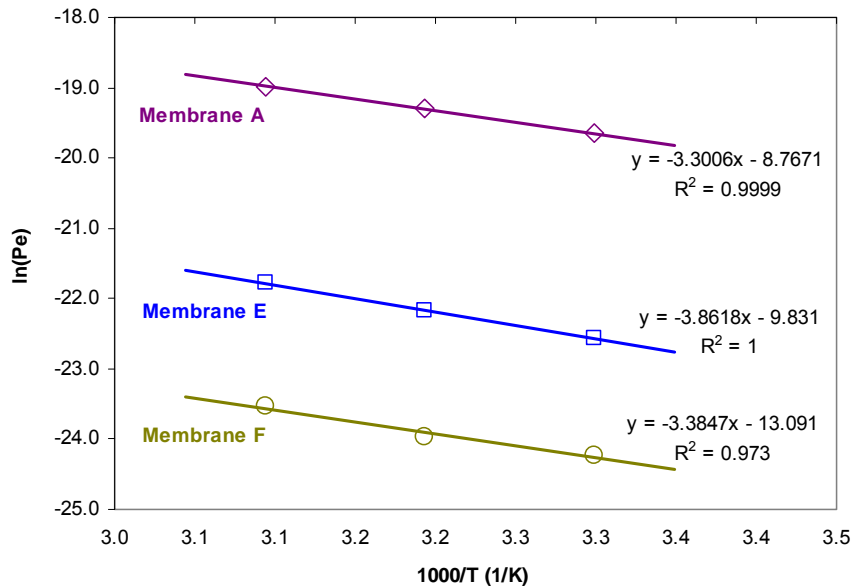


Figure 3.20 Arrhenius plot for membrane samples A, E and F.

3.3.5.3 Effect of pressure

As noted in several papers [KLO01, KIM92, WAN02], it is difficult to give a reliable conclusion for the pressure effect on the transport coefficients. In order to study the pressure effect on permeability coefficient, membranes A, B, and E have been measured at constant temperature of 50°C and the pressure changes for 3 or 4 times.

Table 3.11 LFR and Pe for membrane A, B, and F for pressure effect study.

T°(C)	Type	Thickness (mm)	Saturation Pressure (kPa)	LFR (g/yr)	Pe $\left[\frac{10^{-10} \text{ mol} \cdot \text{m}}{\text{m}^2 \cdot \text{s} \cdot \text{MPa}} \right]$
50°C	A	e=1.7mm	770	5.2	58.1
			1017	7.2	58.8
			1318	10.7	65.7
	B	e=1.6mm	660	6.8	85.6
			770	9.1	95.7
			1017	13.9	106.0
	E	e=2.4mm	1318	25.1	145.1
			770	0.22	3.47
			1017	0.25	2.88
			1318	0.29	2.52

Tables 3.11 shows the results of leak flow rates and permeability coefficients for membranes A, B, and E. As illustrated in Figure 3.21, for membrane A, there is a slight influence of pressure on permeability coefficient. When pressure varies from 770 to 1318 kPa, permeation increases from 58.1 to 65.7. This is not the case of membrane B, which reacts more significantly with the increase of pressure. On the contrary, for membrane E, the permeability decreases with pressure.

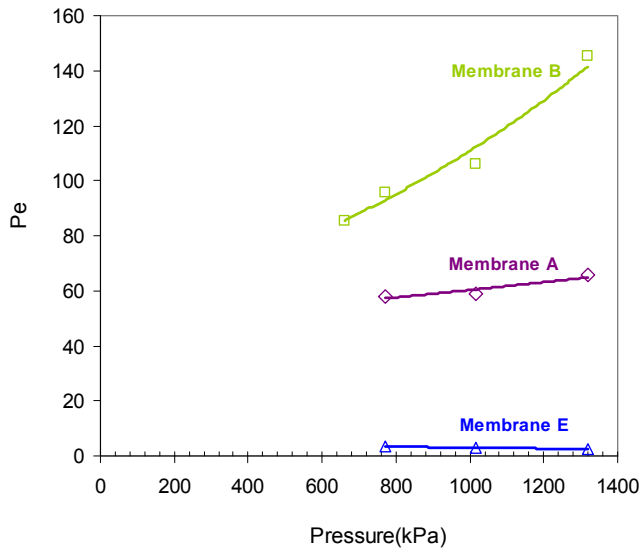


Figure 3.21 Evolution of permeability coefficient as a function of pressure.

In order to correlate the pressure effect with the permeability coefficients, an exponential relationship is initially proposed and the regression curve for each membrane is plotted in Figure 3.21 (line). Good agreement allows making an exponential hypothesis.

$$Pe_{T=const} \propto e^{k\Delta P} \quad (3-21)$$

$k > 0$ signifies a positive effect of pressure on permeation. If $k < 0$, permeation decreases with pressure.

3.3.6 Basic hypothesis coming from membrane measurements

Previous tests made on membrane samples show that Pe is not constant and depends strongly on temperature and on pressure. Taking into consideration this double effect, coefficient of permeability is initially proposed to behave like Equation (3-22):

$$Pe = \kappa_1 e^{\left(\kappa_2(\Delta P) - \frac{\kappa_3}{RT}\right)} \quad (3-22)$$

The leak flow rate is consequently expressed by Equation (3-23).

$$\dot{m} = M_{HFC-134a} \cdot \frac{\pi r^2}{e} \cdot \kappa_1 e^{\left(\kappa_2(\Delta P) - \frac{\kappa_3}{RT}\right)} \cdot \Delta P \quad (3-23)$$

Table 3.12 summarizes the coefficients of permeability for membranes A, B, C, D, E, and F at temperatures of 30, 40, and 50°C corresponding to saturation pressures of 770, 1017, and 1318 kPa. Based on the prediction model expressed by Equation (2-24), parameters of κ_1 , κ_2 and κ_3 calculated for each membrane type using the method of the least squares for solving and analyzing the optimization models. Results are detailed in Table 3.13. Relative errors have been calculated between experimental data and the regression values. As shown in Figure 3.22, the relative errors are relative low which vary in the limit of $\pm 5\%$.

Table 3.12 Coefficients of permeability of 6 membrane samples.

Temperature (°C)	Saturation Pressure (kPa)	$Pe \left[\frac{10^{-10} \text{ mol} \cdot \text{m}}{\text{m}^2 \cdot \text{s} \cdot \text{MPa}} \right]$					
		type A	type B	type C	type D	type E	type F
T1 = 30	770	29.1	58.9	12.9	2.46	1.58	0.30
T2 = 40	1017	44.1	98.3	18.2	3.51	1.96	0.39
T3 = 50	1318	65.7	145.1	27.8	4.91	2.52	0.54

The value of κ_1 vary strongly according to the type of membranes. In the case of κ_2 , it changes in the limit of 0.0001. It should be pointed out that $\kappa_2 > 0$ signifies a positive effect of pressure on permeability and vice versa. Taking E for an example, the value of κ_2 is -0.000609, which means that permeability decreases with the increase of the feed pressure. Dispersion is observed for κ_3 that varies from 19950 to 33293. Comparing to the results of membranes A, E, and F on temperature effect (Table 3.10), same values have been observed for membranes A and F that are 27441 and 28140, and the value for membrane E: 32107 is also very close to 33293.

Table 3.13 Parameters κ_1 , κ_2 and κ_3 for membranes A to F.

Membrane	Parameters κ_1 , κ_2 and κ_3		
	κ_1	κ_2	κ_3
A	1503897	0.000133	27441
B	101060	0.000675	19771
C	24880	0.000542	20043
D	5340	0.000358	19950
E	1260431	-0.000609	33293
F	23157	-0.000170	28140

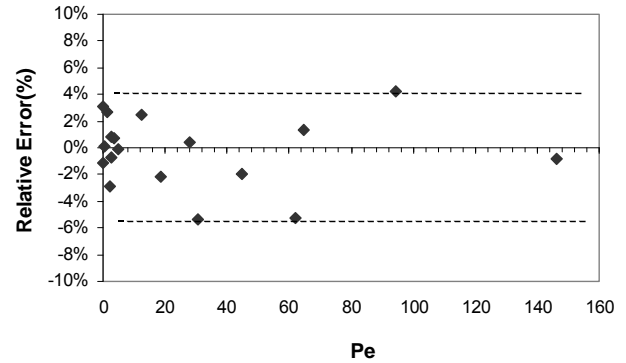
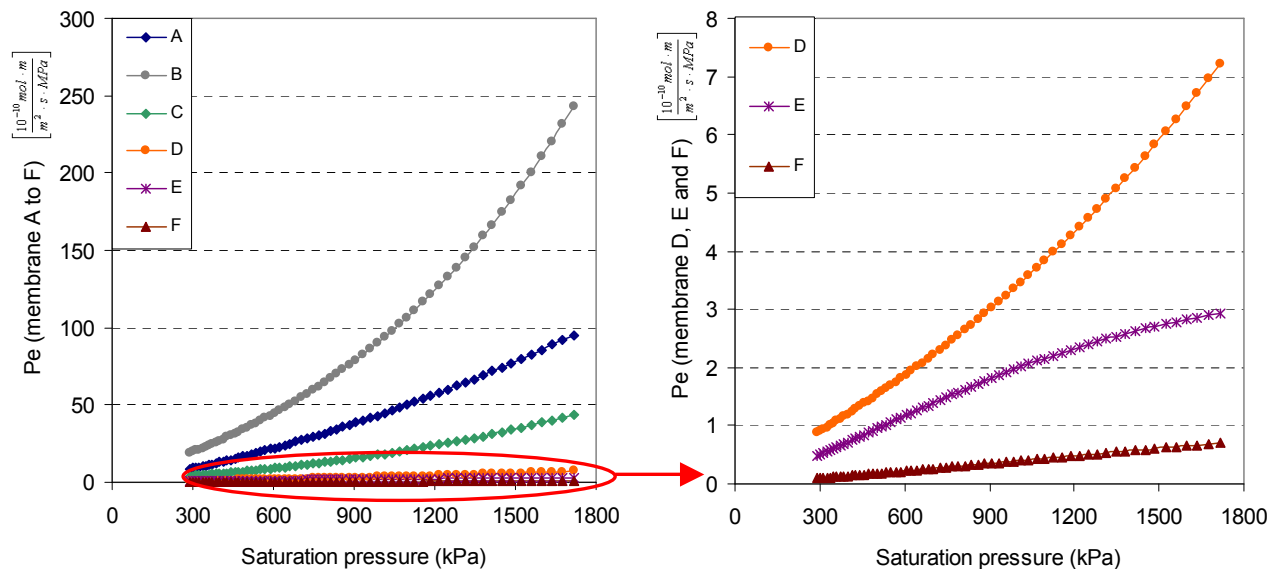


Figure 3.22 Relative error due to regression.

For a given upstream pressure, Equation (3-23) can be simplified as:

$$\dot{m} \propto Pe_{(P,T)} \cdot (P_{upstream} - P_{downstream}) \quad (3-24)$$

Based on the prediction model of membranes A to F, their leakage behaviors as a function of pressure have been plotted and presented in Figure 3.23(a). It can be observed that the evolution of Pe of membrane B is the most significant among these 6 membranes. Zooming (Figure 3.23(b)) D, E, and F, the lowest permeability happens to membrane F. It is interesting to see that the PE evolution is different from one membrane to another. The derivative of the permeability Pe of membrane E decreases with the pressure. In contrast, permeability of membrane D increases more rapidly with pressure.



(a) Pe for membrane A to F (b) Zoom of membrane D, E and F
Figure 3.23 Pe vs. saturation pressure for 6 membranes.

Knowing the coefficients of permeability, the leak flow rates can be calculated by Equation (3-23). Table 3.14 gives the estimated leak flow rates based on the prediction models for membranes A to F with a thickness of 1mm and a diameter of 30mm.

$$\dot{m} = 102 \cdot Pe \cdot \pi \cdot 0.015^2 \frac{(537000 - 101325)}{0.001} \quad (3.25)$$

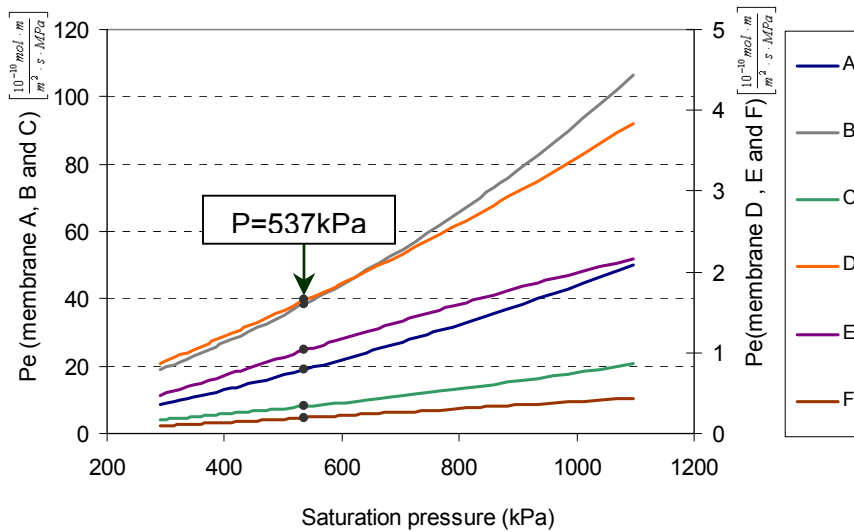


Figure 3.24 Permeation prediction model for membrane A to F.

Based on three constants for each type of membrane, the coefficient of permeability can be predicted at any temperature of the studied interval as shown in Figure 3.24. The prediction model allows forecasting the coefficient of permeability for each type of membrane. Taking an example at 18°C, which corresponds to the saturation pressure of 537 kPa, the point is plotted on the curve and the Pe is found on y-axis. The corresponding coefficients of permeability are calculated and summarized in Table 3.14.

Table 3.14 Pe and LFR calculated for each membrane.

	A	B	C	D	E	F
Pe@18°C						
$\left[\frac{10^{-10} \text{ mol} \cdot \text{m}}{\text{m}^2 \cdot \text{s} \cdot \text{MPa}} \right]$	18.9	38.3	7.96	1.64	1.02	0.19
LFR(g/yr)						
@18°C						
e=1mm	1.87	3.78	0.788	0.162	0.101	0.019
D=30mm						

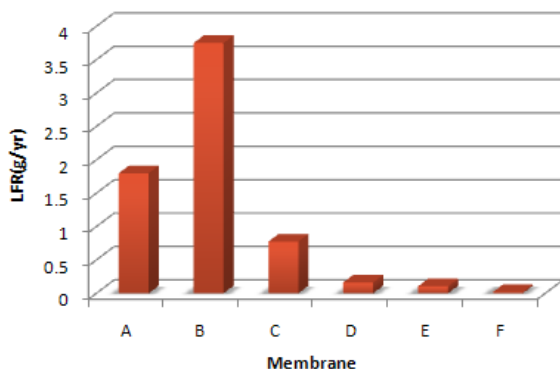


Figure 3.25 LFR of membrane D=30mm and e=1mm for membranes A to F.

As shown in Figure 3.25, membrane A, B and C have high leak flow rate than membrane D, E and F. The highest leak flow rate is found for membrane B: 3.78 g/yr following by membrane A (1.87 g/yr). The lowest leak flow rate of 0.019 for membrane F shows a good performance to prevent the refrigerant from going through the membrane.

To conclude, once the membrane has been characterized by establishing the three parameters κ_1 , κ_2 and κ_3 , the coefficient of permeability can be calculated at any temperature and pressure of the studied interval.

3.4 First approach to establish leakage behavior of MAC hoses

Permeation tests of MAC hose tube-shaped material will now be discussed. It is well known that membrane is generally formed by molding; however each layer of hoses is made by extrusion. Assuming that manufacturing process may change the microstructure of material, it is useful to carry out permeation tests for tubes made of polymers (i.e. hoses).

Based on overall permeation tests for MAC hoses, transport coefficients of typical hose material can be determined in the form of planar membrane as well as cylindrical hose. Once each layer is characterized, tests are carried out on multiple-layer hoses.

Figure 3.26 gives an example of MAC hose composed of two layers of polymers (1 and 3) and one reinforcement layer in order to maintain the high feed pressure. Therefore, refrigerant leakage through polymers used in MAC system can be well explained and understood. Accordingly, the contribution of each layer to the entire hose can be analyzed as well.

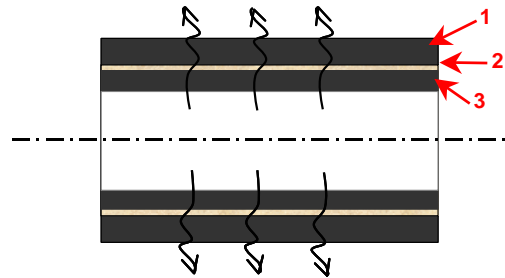


Figure 3.26 Suction profile of a hose.

3.4.1 Conversion from membrane to tube form

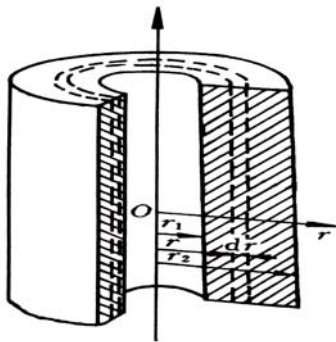


Figure 3.27 Cylindrical shell.

Once the coefficient of permeability of an elastomer material is determined by tests using plane membrane, the prediction model for hoses can be developed. To study the tube shape of MAC hoses, the coefficient of permeability of each layer is supposed to be the same as the one identified for the membrane. The coordinate system is shown in Figure 3.27, the tube length, L , is specified to very large with respect to the radius.

Based on Fick's first law, the molar flow through a single-layer cylinder is written as Equation (3-26).

$$J = -D \frac{dC}{dr} = -Pe \frac{dP}{dr} \quad (3-26)$$

The flow is the product of the cross-section area $2\pi r$. Equation (3-27) comes to:

$$\frac{\dot{n}}{2\pi L r} = -Pe \frac{dP}{dr} \quad (3-27)$$

where, r_1 and r_2 are respectively the inner and the outer radius of the cylinder. The flux is then obtained by integrating the pressure over the radius of the tube. Equation (3-27) may therefore be rearranged to:

$$\dot{n} \int_{r_1}^{r_2} \frac{dr}{r} = -2\pi L P e \int_{P_{upstream}}^{P_{downstream}} dP \quad (3-28)$$

Equation (3-28) results in:

$$\dot{n} \ln\left(\frac{r_2}{r_1}\right) = 2\pi L P e (P_{upstream} - P_{downstream}) \quad (3-29)$$

Therefore, the molar flow can be calculated according to Equation (3-30).

$$\dot{n} = 2\pi L P e \frac{(P_{upstream} - P_{downstream})}{\ln\left(\frac{r_2}{r_1}\right)} \quad (3-30)$$

The mass flow rate, which is the product of molar flow and molar mass, is then given by Equation (3-31).

$$\dot{m} = M_{HFC-134a} \dot{n} = M_{HFC-134a} 2\pi L \frac{(P_{upstream} - P_{downstream})}{\frac{1}{Pe} \ln\left(\frac{r_2}{r_1}\right)} \quad (3-31)$$

3.4.2 Permeation tests of MAC hoses

According to Equation (3-31), leak flow rate of a n-layer hose can be calculated by Equation (3-32).

$$\dot{m} = M_{HFC-134a} \cdot \frac{2\pi L}{\sum_{i=1}^n \frac{1}{Pe_i} \cdot \ln\left(\frac{r_{i+1}}{r_i}\right)} (P_{upstream} - P_{downstream}) \quad (3-32)$$

Equation (3-32) shows that, knowing the coefficient of permeability of each layer and the corresponding radius, the leak flow rate of a MAC hose with a given length can be determined. This hypothesis is true under some conditions:

- The coefficient of permeability is the same for membranes or for hoses;
- The layer of reinforcement is considered to be negligible referred to the permeation effect.

Measurements have been performed on a real MAC hose to verify the prediction model. Taking a simple technology as an example, an all-rubber hose is composed of an inner layer of polymers F and an outer layer of polymers A. Therefore, the leak flow rate of this hose can be obtained from Equation (3-33).

$$\dot{m} = M_{HFC-134a} \cdot \frac{2\pi L}{\frac{1}{Pe_A} \cdot \ln\left(\frac{r_3}{r_2}\right) + \frac{1}{Pe_F} \cdot \ln\left(\frac{r_2}{r_1}\right)} (P_{upstream} - P_{downstream}) \quad (3-33)$$

Table 3.15 Calculated and measured leak flow rate of the hose sample n°1.

Temperature (°C)	Saturation Pressure (kPa)	A		F		Calculated LFR (g/yr)	Hose LFR (g/yr)		
		Pe	Diameter (mm)		Pe			Diameter (mm)	
			d_2	d_3				d_1	d_2
T1 = 30	770	29.1			0.30	2.5	2.9		
T2 = 40	1017	44.1	19.6	24.8	0.39	4.5	5.3		
T3 = 50	1318	65.7			0.54	8.3	10.1		

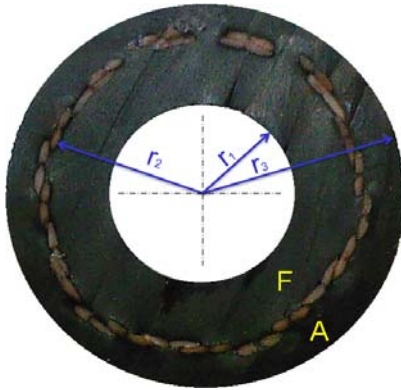


Figure 3.28 Hose sample n°1 for permeation test.

Figure 3.28 shows the hose sample composed of inner layer polymer F and outer layer polymer A. The inner, middle, and outer diameters are respectively 16.2, 19.6, and 24.8 mm. Hose itself has been measured at three temperatures, which lead to 2.9, 5.3, and 10.1 g/yr for a length of 1.17m. Using the coefficient of permeability for polymers A and F, prediction can be made by Equation (3-35) for the same length and results are given in Table 3.15. 2.5, 4.5, and 8.3 g/yr have been obtained by prediction model.

The difference between the prediction value and the real hose leakage can be explained by several reasons:

- Effect of manufacturing process for membrane are different to that of hoses;
- Diameters of each layer are not perfect and uncertainties on thicknesses are not known.

Nevertheless, the prediction model is acceptable to forecast hose leakage within a tolerable uncertainty.

It is helpful to see the contribution of each layer. According to the results shown in Table 3.12, $Pe_A \gg Pe_F$, there is a factor of about 200 between them. Therefore the term $Pe_F \ln(r_3/r_2)$ from Equation (3-34) is negligible and the coefficient of permeability of the hose is simplified to $Pe_F / \ln(r_2/r_1)$. That means the permeability of hose is determined by the layer having the lower permeability, and only the thickness of this layer (r_2 and r_1) is essential.

$$\dot{m} = M_{HFC-134a} \cdot 2\pi L \cdot \frac{Pe_A Pe_F}{Pe_F \ln\left(\frac{r_3}{r_2}\right) + Pe_A \ln\left(\frac{r_2}{r_1}\right)} (P_{upstream} - P_{downstream}) \quad (3-34)$$

If both layers have similar permeation values, the permeability coefficient becomes $Pe / \ln(r_3/r_1)$. This means that both layers contribute to the global permeation of the hoses, and that the inner and outer diameters of the hose are necessary for permeation calculation.

3.4.3 Prediction model of MAC hoses

From a practical point of view, it is of interest for hose suppliers to define an overall coefficient of permeability of hoses, based on a few number of measurements of permeability, so the same methodology can be applied even if the results are less generic and related to a specific hose process manufacturing.

Based on permeation prediction model of MAC hoses, an overall permeability coefficient is introduced:

$$\frac{1}{Pe_{overall}} \ln\left(\frac{r_{outer}}{r_{inner}}\right) = \sum_{i=1}^n \frac{1}{Pe_i} \cdot \ln\left(\frac{r_{i+1}}{r_i}\right) \quad (3-35)$$

As the permeability of each layer is an exponential function of temperature and pressure, the overall permeability coefficient is approximately an exponential function of temperature and pressure (Equation (3-38)).

$$Pe_{overall} = \frac{\ln(r_{outer} / r_{inner})}{\frac{\ln(r_2 / r_1)}{Pe_1} + \frac{\ln(r_3 / r_2)}{Pe_2} + \dots + \frac{\ln(r_{n+1} / r_n)}{Pe_n}} \quad (3-36)$$

Equation (3-37) proposes the pressure and temperature dependence of the overall coefficient of permeability of a MAC hose.

$$Pe_{overall} = c_1 e^{\left(c_2(\Delta P) - \frac{c_3}{RT}\right)} \quad (3-37)$$

Thus, the mass flow rate of a given hose is expressed as:

$$\begin{aligned} \dot{m} &= M_{HFC-134a} \cdot \frac{2\pi L}{\ln\left(\frac{r_{outer}}{r_{inner}}\right)} \cdot Pe_{overall} \cdot \Delta P \\ &= M_{HFC-134a} \cdot \frac{2\pi L}{\ln\left(\frac{r_{outer}}{r_{inner}}\right)} \cdot c_1 e^{\left(c_2(\Delta P) - \frac{c_3}{RT}\right)} \cdot (P_{upstream} - P_{downstream}) \end{aligned} \quad (3-38)$$

Based on Equation (3-38), MAC hoses can be characterized according to leak flow rate measurement at different temperatures. Table 3.16 shows an example of calculation. The hose sample is composed of an inner layer of EPDM and an outer layer of IIR. The corresponding diameters are respectively 10.3, 17.6, and 22.2 mm. Leak flow rates at 30, 40, and 50°C are 1.9, 4.7, and 10.2 g/yr per meter length. Based on Equation (3-38), corresponding permeation parameters are calculated by non-linear regression and values c_1 , c_2 , and c_3 are given in Table 3.16. Figure 3.29 presents the prediction model of refrigerant emission as a function of saturation pressure. Good agreement has been observed between the experimental data and the prediction model. Using this model, the leak flow rate of this

hose can be calculated at any wanted temperature of the studied interval and for other diameters.

Table 3.16 Hose sample n°2 - LFR and permeation parameters.

TECHNOLOGY	DN [mm]	LFR(g/yr) per meter length		
		30°C	40°C	50°C
Temperature(°C)		30°C	40°C	50°C
Saturation Pressure(kPa)		770	1017	1318
IIR-EPDM	10DN	10.2	4.7	1.9
Diameter(mm)	d_1	d_2	d_3	
		10.3	17.6	22.2
Permeation parameters	c_1	c_2	c_3	
		6216	0.000643	22495

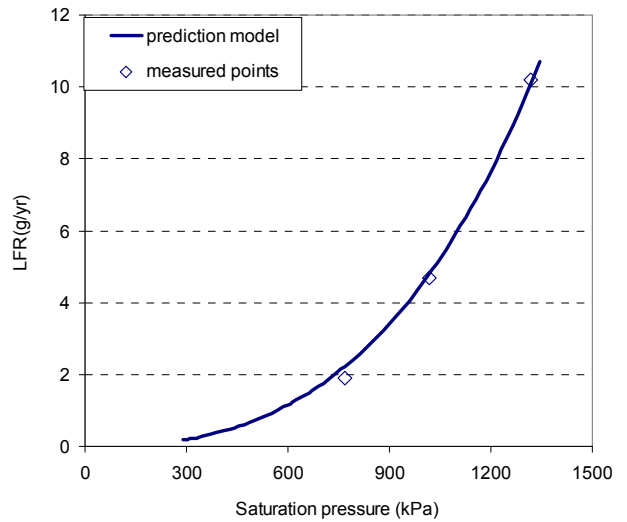


Figure 3.29 Emission prediction model for hose sample n°2.

Table 3.17 Hose sample n°3 - LFR and permeation parameters.

TECHNOLOGY	DN [mm]	LFR(g/yr) per meter length			
		30°C	40°C	50°C	
Temperature(°C)		30°C	40°C	50°C	
Saturation Pressure(kPa)		770	1017	1318	
PA-IIR-PES-EPDM	8DN	0.23	0.70	2.45	
Diameter(mm)	d_1	d_2	d_3	d_4	
		8.1	8.5	10.4	14.0
Permeation parameters	c_1	c_2	c_3		
		41	0.0024	19498	

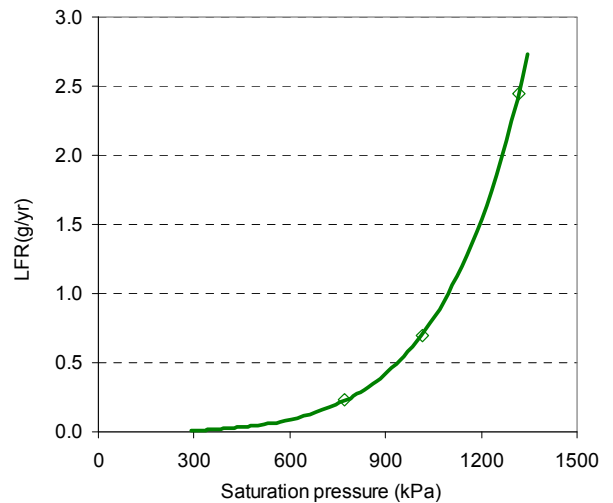


Figure 3.30 Emission prediction model for hose sample n°3.

Table 3.17 gives another hose sample. This hose sample n°3 belongs to a veneer type hoses that means the inner layer of the hose is a thermoplastic polymer: polyamide (PA) as shown in Figure 3.31. A good agreement has been found as illustrated in Figure 3.30.



Figure 3.31 Veneer hose sample.

PA layer is widely used for MAC hoses due to its low permeation for HFC-134a. Generally, a thin PA layer constitutes an efficient barrier against refrigerant leakage. However, the PA layer should be very thin in order not to make the hose rigid, so that it is often in the range of 0.15-0.20mm. From Equation (3-36), the lower the ratio between the outer and inner diameters of PA, the lower the permeation. Therefore, PA being positioned in the inner layer of a MAC hose is better than in the middle.

Leakage behaviors of hoses with the same technology but from different suppliers have been studied as well. Table 3.18 lists three hoses (DN16) consisting of: PA, IIR, and EPDM. Only the reinforcement layer for the third hose (PES) is different from the other two (PET).

Table 3.18 Hose technology analysis.

TECHNOLOGY	DN [mm]	LFR(g/yr) per meter length			
		Temperature(°C)	30°C	40°C	50°C
		Saturation Pressure(kPa)	770	1017	1318
PA-IIR-PET-EPDM	16		1.3	0.5	0.2
PA-IIR-PET-EPDM	16		8.8	3.9	1.4
PA-IIR-PES-EPDM	16		4.8	1.0	0.6

As shown in Table 3.18, the leak flow rates for these three hoses are quite different. A factor of 7 is noticed between the lowest and highest one. Those differences show that emissions from MAC hoses do not only depend on the material but also depend on hose suppliers who can have different recipes. This issue has to be verified on several suppliers claiming using the same basic materials.

Conclusions

Based on the results obtained in this chapter, some conclusions can be drawn:

- HFC-134a leakage through MAC hoses can be simplified to gas transport through polymer material;
- Coefficients of permeability for six membrane samples have been determined;
- A prediction model has been developed not only for membranes but also for hoses;
- An overall permeability coefficient has been introduced and good agreements have been observed between the prediction values and experimental data;
- Hoses with the same technology lead to different leakage values that depend on suppliers;
- An in-depth study on temperature and pressure relationship of refrigerant HFC-134a allows correlating the leakage behavior of hoses and the system leakage behavior.

3.5 References

- [BOW02] Bower, D.I., 2002. An Introduction to Polymer Physics. Cambridge University Press.444p.
- [CRA68] Crank, J., and Park, G.S., 1968. Diffusion in polymers. Academic Press. 452 p.
- [CRA75] Crank, J., 1975.The Mathematics of Diffusion. Oxford University Press, Oxford, 432 p.
- [FLA01a] Flaconnèche, B., Martin, J., Kolpffer, MH., 2001. Transport properties of gases in polymers: experimental methods. Oil and Gas Science and Technology, Vol. 56: 245-259.
- [FLA01b] Flaconnèche, B., Martin, J., Kolpffer, MH., 2001. Permeability, Diffusion and Solubility of gases in Polyethylene, Polyamide 11 and Poly(vinylidene fluoride). Oil and Gas Science and Technology, Vol. 56, No.3: 261-278.
- [GOL71] Goldman, R.F., and Rudy, D.D., 1971. Permeation of refrigerants through Elastomeric and Plastic hoses. SAE technical paper 710039.
- [ISO06] ISO 2782:2006, Rubber, vulcanized or thermoplastic - Determination of permeability to gases.
- [JEN72] JENKINS,A.D.,1972. Polymer science – A materials science handbook. Volume 1, 932p.
- [KAN04] Kanagae, H., Ogata, C., and Suetsugu, N., 2004. Developing a method for evaluation of high pressure gas permeability leakage. SAE technical paper 2004-01-1034
- [KIL01] Kim, JH., Ha, SY., Lee, YM., 2001. Gas permeation of Poly(amide-6-b-ethylene oxide) copolymer. Journal of Membrane Science, Vol. 190, Issue 2: 179-193.
- [KIM92] Kimura, S., Hirose, T., 1992. Polymers for Gas Separation. Wiley, 245 p.
- [KLU05] Klushrestha, V., Awasthi, K., Acharya, NK., Singh, M., and Vijay, YK., 2005. Effect of temperature and α -irradiation on gas permeability for polymeric membrane. Indian Academy of Science, Vol. 28, no. 7: 643-646.
- [MAG90] Magg, H., 1990. Elastomers for Automotive Air conditioning Hoses. SAE technical paper 900575.

- [MOO04] Moore, T.M., Damle, S., Williams, P.J., Koros, W.J. 2004. Characterization of low permeability gas separation membranes and barrier materials; design and operation considerations. *Journal of Membrane Science* 245(2004) 227-231p.
- [NEO96] Neogi,P., 1996. *Diffusion in Polymers*. Marcel Dekker INC., New York, 173-209
- [STA71] Stancel, A.F.,1971. *Diffusion through Polymers*. *Polymers science and materials*. Wiley Interscience 247p.
- [STE81] Stern, S.A., Frisch, H.L., 1981. The selective permeation of gases through polymers. *Annual Review of Materials Science*. 11:523-550p.
- [TOS92] Toshima, N., 1992. *Polymers for Gas Separation*. VCH, Weinheim. 245p pp.15-28
- [TRE06] Tremblay, P., Savard, M.M., Vermette, J., Paquin, R., 2006. Gas permeability, diffusivity and solubility of nitrogen, helium, methane, carbon dioxide and formaldehyde in dense polymeric membranes using a new on-line permeation apparatus. *Journal of membrane science* 282 (2006) 245-256p.
- [WAN02] Wang, R., Chan, S.S., Liu, Y., Chung, T.S., 2002. Gas transport properties of poly (1,5-naphthalene-2,2'-bis(3,4-phthalic) hexafluoropropane) diimide (6FDA-1,5-NDA) dens membranes. *Journal of membrane science* 199(2002) 191-202p.

CHAPTER 4

Leakage behavior of fittings used in MAC systems

List of Figures

Figure 4.1 Fittings used in MAC system.....	95
Figure 4.2 Seals used in MAC systems.	95
Figure 4.3 Top view and cross section of an O-ring.....	95
Figure 4.4 O-ring designs.	96
Figure 4.5 Compression set definition.....	96
Figure 4.6 Leakage sources from an O-ring seal.....	97
Figure 4.7 Relative errors due to regression.....	99
Figure 4.8 Permeation prediction model for membranes 1 to 6.....	99
Figure 4.9 Percolation theory of contact area.	100
Figure 4.10 Surface roughness definition.....	101
Figure 4.11 Gas flow through micro channel.....	102
Figure 4.12 Rarefaction effect analysis.....	105
Figure 4.13 Typical stress-strain relation of an elastomer.	106
Figure 4.14 Relationship between Young's modulus and shore-A hardness.	107
Figure 4.15 Photo of O-ring sample.	108
Figure 4.16 Axis-symmetric finite element model of a radial O-ring.	108
Figure 4.17 Axis-symmetric finite element model of a radial O-ring.	108
Figure 4.18 O-ring design parameters.	109
Figure 4.19 Distribution of the von Mises stress of O-ring before and after pressure load.....	109
Figure 4.20 Distribution of the normal stress in the area of O-ring before and after pressure load....	110
Figure 4.21 Contact stress in contact with the lateral wall of the groove.....	110
Figure 4.22 Max contact stress as a function of pressure load.....	111
Figure 4.23 Contact width as a function of pressure load.....	111
Figure 4.24 Transparent fitting specimen.....	112
Figure 4.25 Two ways to observe the con tact width.....	112
Figure 4.26 Test apparatus for contact width measurement.....	112
Figure 4.27 Test apparatus for contact width measurement.....	113
Figure 4.28 Contact width visualization of top and bottom wall.....	113
Figure 4.29 Measured contact width vs. simulation results.....	113
Figure 4.30 Squeeze impact on maxi contact stress.....	114
Figure 4.31 Distribution of the von Mises' stress of O-ring.....	115
Figure 4.32 Defective O-ring by extrusion.....	115
Figure 4.33 Variations of elastomer hardness vs. temperature.....	115
Figure 4.34 Contact stress in contact with the lateral wall of the groove considering hardness effect	116
Figure 4.35 Maximum contact stress and contact width as a function of pressure load.....	116
Figure 4.36 Control volume for mass flow calculation.....	117
Figure 4.37 Permeations prediction of 6 polymers.....	120
Figure 4.38 Leakage distribution assumptions.....	121
Figure 4.39 LFRs of 10 fitting samples.....	121
Figure 4.40 Fitting specimen.....	122
Figure 4.41 Fitting specimen with double O-rings.....	123
Figure 4.42 Test apparatus for a double O-ring fitting.....	123
Figure 4.43 Fitting sample.....	124
Figure 4.44 Test position for leakage tests.....	124

List of Tables

Table 4.1 List of membrane samples.	97
Table 4.2 LFRs of membranes 1 to 6 and calculated coefficients of permeability.	98
Table 4.3 Parameters κ_1 , κ_2 and κ_3 for membranes 1 to 6.	99
Table 4.4 Knudsen number and the corresponding flow regimes.	103
Table 4.5 Mooney-Rivlin constants.	108
Table 4.6 Max contact stress under different load pressures.	111
Table 4.7 Contact widths under different load pressures.	111
Table 4.8 Maxi contact stress vs. squeeze.	114
Table 4.9 Maximum contact stress under different load pressures.	116
Table 4.10 Micro-channel calculation based on measured LFRs.	119
Table 4.11 Predictions of LFRs of membranes 1 to 6.	120
Table 4.12 LFRs of fitting with axial-radial O-ring.	122
Table 4.13 Leak flow rate calculations for a double O-ring fitting.	123
Table 4.14 LFRs of triple O-ring fitting with 1, 2, and 3 O-rings at different positions.	124

4.1 Introduction of seals commonly used in MAC systems

As shown in Figure 4.1, different parts of MAC systems are connected by fittings using polymer seals. Fittings used to connect metallic pipes with other pipes or with the principal components such as the compressor, the TXV, and the condenser have to guarantee a tightness to contain the pressures of the MAC system. Generally there is no relative movement between the rigid parts, so that sealing performance analysis will focus on the static application.

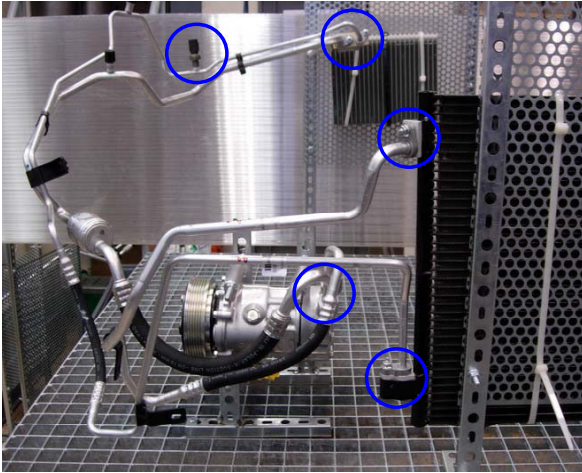


Figure 4.1 Fittings used in MAC system.



Figure 4.2 Seals used in MAC systems.

Figure 4.2 gives some examples of seals used for MAC systems. It can be seen that O-rings are widely used because they are inexpensive, reliable, easy to produce, and have simple mounting requirements. Therefore, the leakage behavior of O-ring seals will be studied in detail in this chapter.

4.1.1 Basic O-ring description

An o-ring is a torus of elastomer with an o-shaped cross-section. O-rings are vulcanized in moulds. They are characterized by their inside diameter d_1 and the cross section diameter d_2 as shown in Figure 4.3.

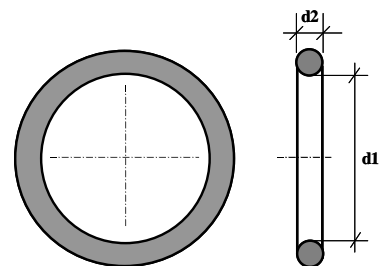


Figure 4.3 Top view and cross section of an O-ring.

Sealing mechanism of O-ring seals

O-Rings are used to seal fittings to prevent the refrigerant leak from inside the MAC system to the ambience. In order to seal and withstand the pressure of fluid, an O-ring must be compressed when inserted into glands. O-Rings perform their sealing action by deformation to take the shape of the cavity they are inserted in, they are slightly oversized to guarantee a predetermined interference fit.

Figure 4.4 shows two typical sealing designs: axial and radial:

- (a) Axial (face); O-ring seals are deformed by a force applied to the top and the bottom surfaces of the O-ring;
- (b) Radial O-ring seals are deformed by a force applied to the inside diameter and the outside diameter of the O-ring.

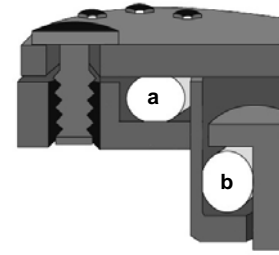


Figure 4.4 O-ring designs.

The sealing mechanism of O-ring seals is due to the elasticity and incompressibility of the polymers materials used for seals. O-ring is compressed by the metallic part of fittings during assembly. The maximum contact pressure between seal and the rigid walls should be higher than the fluid pressure in order to prevent leakage. Depending on the designs of O-ring seals, the axial O-ring is well influenced by torques, which increases the squeeze by increasing the torques. By contrast, only the geometry of the cavity determines its performance. A radial O-ring seal has been chosen to avoid supplementary external influence.

Hardness

O-ring hardness, typically defined by the Shore-A hardness, is one of the most important properties of seals. The softer the material, the better the seal material fits the rigid walls. However, the softer the material, the higher the risk of extrusion into the clearance gap between the mating seal surfaces due to pressure load. § 4.3.3.5 analyzes the effect of O-ring hardness and the temperature dependence on sealing performances.

Compression set and squeeze

The compression set of an O-ring is an important parameter for assessing the sealing behavior, which represents the deflection percentage that the polymers cannot recover after a fixed period of time under specific squeeze and temperature [PAR07].

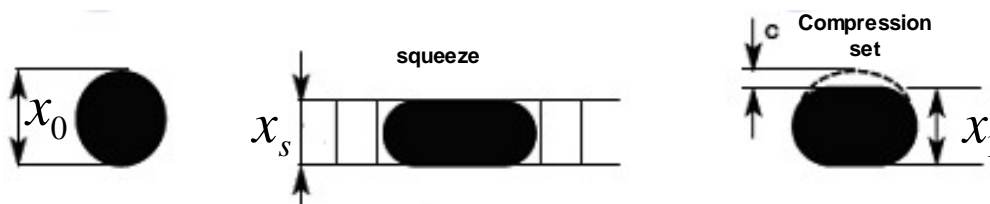


Figure 4.5 Compression set definition.

As shown in Figure 4.5, the compression set is calculated by Equation (4-1):

$$c = \frac{x_0 - x_1}{x_0 - x_s} \times 100\% \quad (4-1)$$

The compression set increases with temperature and time. Low compression set presents a good remaining sealing capacity of the polymer.

4.2 Leakage sources from O-ring fittings

Sealing performance of O-rings has been studied early in 1979 by Daniel [DAN79]. Seals are inserted in fittings to prevent the refrigerant leaks from inside the MAC system to the outside. Zero leak is impossible. O-rings intend to limit the leak at an “acceptable level”, typically in the range 0.1 to 0.5 g/yr for a typical pressure (P) of 1MPa of HFC-134a.

Two types of leakage sources should be distinguished (see Figure 4.6).

a - Leakage due to the escape of refrigerant between sealing parts: The contact area between the seal and the rigid parts of the connection is never perfect. Micro channels always exist for gas to pass through.

b - Leakage by permeation through the seal material: gas can pass through polymer materials;

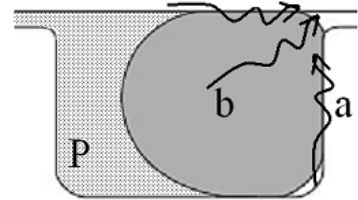


Figure 4.6 Leakage sources from an O-ring seal.

Both leakage sources and their relative importance are studied in this chapter.

4.2.1 Permeation in polymers - Leakage by permeation through seal material

Polymers used for O-ring seals should not have high coefficients of permeability so as to prevent the refrigerant from passing through the seal material by permeation. Six polymers proposed for MAC fittings, named 1 to 6, are chosen for permeation tests. Descriptions of each membrane are summarized in Table 4.1.

Permeation of six polymer samples at temperatures of 30, 40, and 50°C

Table 4.1 List of membrane samples.

Membrane type	Thickness (mm)	Diameter (mm)
1	1.0	30
2	1.0	30
3	1.0	30
4	1.0	30
5	2.2	30
6	1.0	30

The test procedure is the same as the one is described in Chapter 3. That means leak flow rate measurements have been performed at 30, 40, and 50°C corresponding to saturation pressure of 770, 1017, and 1318 kPa. Table 4.2 summarizes the leak flow rates and coefficients of permeability calculated for each case.

For membrane n°1, leak flow rates vary from 14.6 g/yr at 30°C to 53.8 g/yr at 50°C. Corresponding coefficients of permeability are respectively 92×10^{-10} , 145×10^{-10} and $187 \times 10^{-10} \text{ mol mm}^{-2} \text{ s}^{-1} \text{ MPa}^{-1}$, which is the highest of all six membranes. The lowest coefficients of permeability are found for membrane 6. Their values are respectively 1.1×10^{-10} , 1.5×10^{-10} , and $1.8 \times 10^{-10} \text{ mol mm}^{-2} \text{ s}^{-1} \text{ MPa}^{-1}$. There is a factor of 66 at 30°C and a factor of 104 at 50°C between membranes 1 and 6.

Table 4.2 LFRs of membranes 1 to 6 and calculated coefficients of permeability.

Membrane Type	Thickness e (mm)	T (°C)	Saturation Pressure (kPa)	LFR (g/yr)	$Pe \left[\frac{10^{-10} \text{ mol} \cdot \text{m}}{\text{m}^2 \cdot \text{s} \cdot \text{MPa}} \right]$
1	1.0 mm	T=30°C	770	14.6	92
		T=40°C	1017	31.4	145
		T=50°C	1318	53.8	187
2	1.0 mm	T=30°C	770	13.9	91
		T=40°C	1017	24.4	117
		T=50°C	1318	41.2	149
3	1.0 mm	T=30°C	770	5	33
		T=40°C	1017	11.3	54
		T=50°C	1318	19.2	69
4	1.0 mm	T=30°C	770	0.23	1.5
		T=40°C	1017	0.4	1.9
		T=50°C	1318	0.77	2.8
5	2.2 mm	T=30°C	770	0.65	9.4
		T=40°C	1017	1.22	12.9
		T=50°C	1318	1.73	13.8
6	1.0 mm	T=30°C	770	0.16	1.1
		T=40°C	1017	0.31	1.5
		T=50°C	1318	0.5	1.8

Taking into consideration the double effect of temperature and pressure, coefficient of permeability is proposed to behave like Equation (4-2):

$$Pe = \kappa_1 e^{\left(\kappa_2 (\Delta P) - \frac{\kappa_3}{RT} \right)} \quad (4-2)$$

The leak flow rate is consequently expressed by Equation (4-3).

$$\dot{m} = M_{134a} \cdot \frac{\pi r^2}{e} \cdot \kappa_1 e^{\left(\kappa_2 (\Delta P) - \frac{\kappa_3}{RT} \right)} \cdot \Delta P \quad (4-3)$$

Based on the prediction model expressed by Equation (4-3), parameters of κ_1 , κ_2 , and κ_3 are calculated for each membrane type using the method of the least squares for solving and analyzing the optimization models. Results are detailed in Table 4.3. Relative errors have been calculated from experimental data to regression values. As shown in Figure 4.7 the relative errors are relatively low and vary in the limit of $\pm 7\%$.

Results presented in Table 4.3 show that the value of κ_1 varies strongly according to membranes. High value of κ_1 generally indicates a high coefficient of permeability. For κ_2 , the changes are limited to 0.0001. It should be pointed out that $\kappa_2 < 0$ for all six membranes signifies a negative effect of pressure on permeability. The value of κ_3 varies from 23248 to 30072.

Table 4.3 Parameters κ_1 , κ_2 and κ_3 for membranes 1 to 6.

Membrane	Parameters κ_1 , κ_2 and κ_3		
	κ_1	κ_2	κ_3
1	16281486	-0.000141	30072
2	16282234	-0.000431	29772
3	16278922	-0.000204	32514
4	102443	-0.000076	28031
5	132438	-0.000408	23248
6	12944	-0.000114	23447

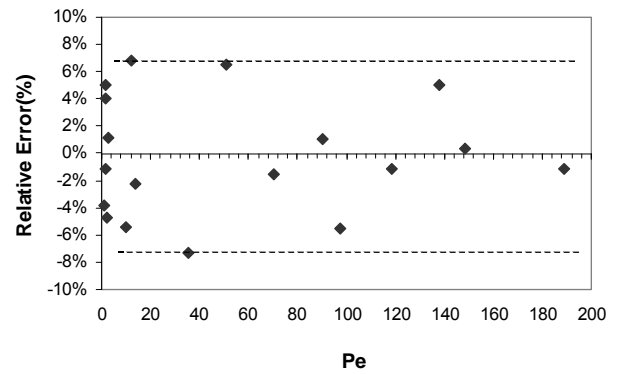


Figure 4.7 Relative errors due to regression.

Based on the prediction model of membranes 1 to 6, their leakage behaviors as a function of pressure have been plotted and are presented in Figure 4.8. It can be observed that the permeation evolution of membrane 1 is the most significant among these 6 membranes. It is interesting to see that the evolution does not behave always similarly from one membrane to another due to the double T-P effect. Evolution curves of membranes 2 and 5 shows that the increase rate decreases with the pressure, which is contradictory to the behavior of other membranes.

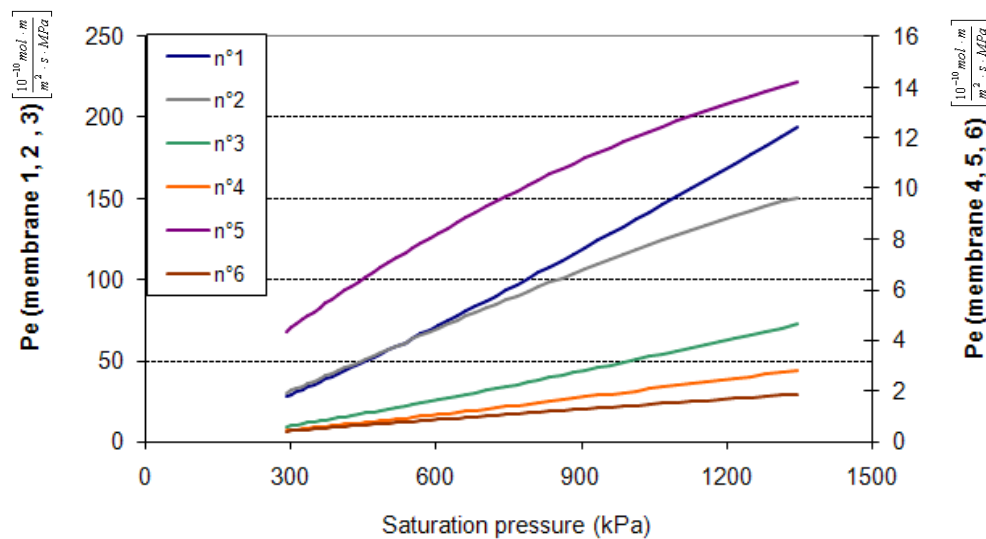


Figure 4.8 Permeation prediction model for membranes 1 to 6.

Establishing the prediction model for each membrane sample allows estimating leak flow rates of a given thickness for any other temperatures, as shown in Figure 4.8. The contribution of membrane permeation to the total leakage of an O-ring seal can be evaluated per se and, by difference, allow identifying the leak flow rate due to gas transport through micro channels.

4.2.2 Gas transport in micro channels

Leakage due to the escape of refrigerant between sealing parts is considered as gas flow in micro channels due to the non-perfect contact between seals and metallic parts.

4.2.2.1 Contact mechanics between seal and metallic parts

The contact mechanics is analyzed according to the percolation theory that has been widely studied [BOT07, PER04, PER06, PER08, OKA08]. Several papers studied the surface roughness of metallic parts. Okamura et al. [OKA02] analyzed experimentally the correlation between the micro surface roughness and the seal ability of O-rings. Bottiglione et al. [BOT07] have presented a method for fluid leakage computation in ball valves by considering a two-dimensional multi-scale theory of rough contact. Persson et al. [PER08] presented a theory of the leak rate of seals based on the percolation theory and has developed a contact mechanics theory.

The contact area between the O-ring seal and the metallic parts (bore and groove parts) is in the shape of a cylinder (see Figure 4.9(a)). Because the surface roughness of two contact bodies is not perfectly smooth, the real contact area is smaller than the nominal contact area (see Figure 4.9). By increasing the magnification of the contact area, the more non-contact regions are observed.

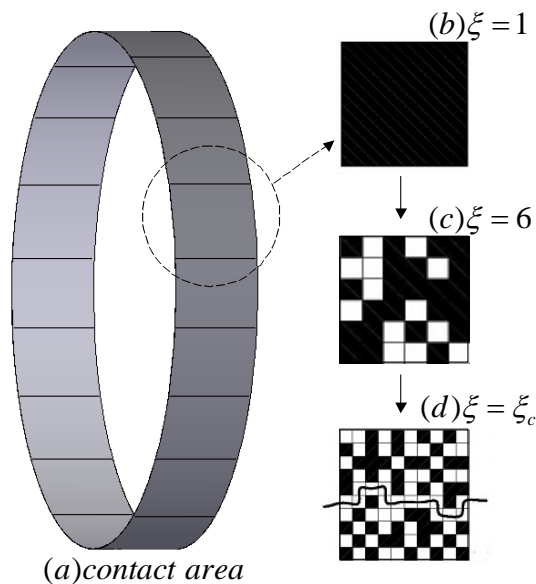


Figure 4.9 Percolation theory of contact area.

Taking one square for the contact area with a length and a width of L , and at the lowest magnification $\xi = 1$ (Figure 4.9 (b)), the entire square is black, which means the contact is perfect. With the increase of the magnification, the resolution increases, so that some non-contact regions are observed as shown in Figure 4.9(c). ξ is defined as magnification and is expressed as:

$$\xi = \frac{L}{w} \quad (4-4)$$

Where w is defined as the resolution.

Figure 4.9(d) gives an example of $\xi = 6$. That means the square in Figure 4.9 (b) is divided into 6×6 squares and the resolution is $w = L/6$. When the magnification is high enough, a path of non-contact regions appears. At this critical magnification ξ_c , fluid passes through this leakage path to another side of the contact area (Figure 4.9 (d)). More percolation channels can be found when the magnification is increased further, but these new channels are narrower than that of the critical magnification. Therefore, the leakage is supposed to be dominated by the path observed at critical magnification. This passage is considered as a rectangular bore of height, H , width w_c , and length L . Figure 4.10 gives an example of the leakage path observed at magnification ξ_c . Therefore, mass flow rate of the gas flow

channel is determined by several factors such as: the surface roughness, the contact pressure, the width of the channel w_c , and the contact width L .

4.2.2.2 Surface roughness considerations

The parameter H , which presents the height of the channel, is directly influenced by the surface roughness of the metallic parts. Figure 4.10 shows two commonly used surface roughness definitions to describe rough surface: R_a (roughness average) and R_q (root mean square roughness).

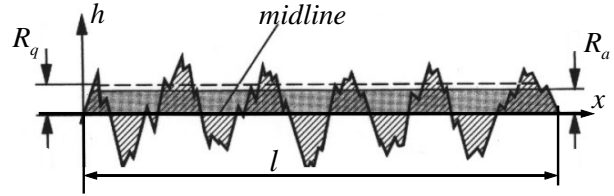


Figure 4.10 Surface roughness definition.

The Roughness Average, R_a , is defined as the arithmetical mean roughness of a surface that can be expressed by Equation (4-5).

$$R_a = \frac{1}{l} \int_0^l |h(x)| dx \quad (4-5)$$

The root mean square roughness, R_q , is defined as:

$$R_q = \sqrt{\frac{1}{l} \int_0^l h^2(x) dx} \quad (4-6)$$

Where h is the height of the profile with respect to its midline (see Figure 4.10).

In order to correlate the surface roughness with the channel height, the roughness of the contact surface is assumed to be in only one dimension. That is why the Weierstrass profile is chosen in this study to explain the roughness surface of rigid metallic parts of the fittings. The rough surface is assumed to contain a series of superposed sinusoids, which is written as:

$$h(x) = h_0 \sum_{n=0}^{\infty} \gamma^{(D-2)n} \cos\left(\frac{2\pi\gamma^n x}{\lambda_0}\right) \quad (4-7)$$

where h_0 and λ_0 are respectively the semi-amplitude and the wavelength of the first sinusoid; D is the fractal dimension, and γ is a parameter defining the inverse ratio between successive wavelengths in the profile. The amplitude and wavelength of the n th scale are given by:

$$h_n = h_0 \gamma^{(D-2)n} \quad (4-8)$$

$$\lambda_n = \lambda_0 \gamma^{-n} \quad (4-9)$$

Literature [CIA00, GAO06] suggests that $\gamma = 1.5$ and $D = 1.4$, which provides a good qualitative description of many real surface profiles. With these constant values, Ciavarella et al. [CIA04] proposed half the maximum possible peak to valley roughness of the Weierstrass profile.

$$\sum_{n=0}^{\infty} h_n = h_0 \sum_{n=0}^{\infty} \gamma^{(D-2)n} = \frac{h_0}{1 - \gamma^{D-2}} \quad (4-10)$$

This maximum distance between peak and valley of the surface profile can be approximated at half the channel height $H/2$.

$$H \approx \frac{2h_0}{1 - \gamma^{D-2}} \quad (4-11)$$

In brief, the surface roughness is directly related to the micro-channel height that plays an important role in mass flow rate calculation.

4.2.2.3 Mass flow rate calculation

The gas flow of compressible fluids is different from that of incompressible liquids, mainly because gases are much less viscous and increase the volume when pressure decreases. Leakage calculation has been analysed [MAN00, POL98, DAL00]. We assume that the gas leakage takes place through the percolation channel. The gas channel is considered as a rectangular bore of height H , width w_c , and length L . x and y are respectively the horizontal and vertical coordinates (see Figure 4.11).

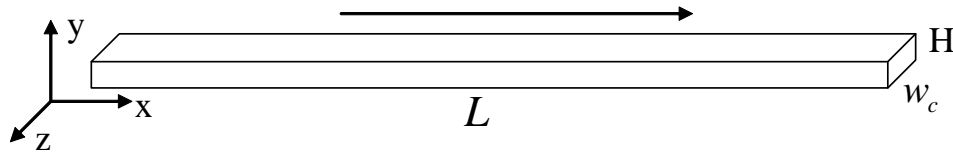


Figure 4.11 Gas flow through micro channel.

The flow regime is determined by the Knudsen number. By Definition, the **Knudsen number** (Kn) is the ratio of the molecular mean free path length to a representative physical length scale.

$$Kn = \frac{\lambda_m}{l_p} \quad (4-12)$$

Where

λ_m is the mean free path (m), and

l_p is the representative physical length scale (m).

For an ideal gas, the mean free path may be readily calculated according to Equation (4-12)

$$\lambda_m = \frac{k_B T}{\sqrt{2} \pi d^2 P} \quad (4-13)$$

Where

k_B is Boltzmann's constant ($1.38 \times 10^{-23} \text{ JK}^{-1}$)

d is the molecular diameter of HFC-134a (m)

T is the temperature (K)

D is the molecular diameter (m)

P is the pressure (Pa)

For HFC-134a, the saturation pressure at 20°C is 571 kPa. The molecular diameter of HFC-134a is about 0.42×10^{-10} m. The mean free path can be calculated from Equation (4-13) that leads to 0.903×10^{-8} m. For a representative physical length scale l_p of $0.1 \mu\text{m}$, Kn is obtained by the definition $Kn = \lambda_m / l_p = 0.903 \times 10^{-8} / 0.1 \times 10^{-6} = 0.09$. If l_p is in the order of $1 \mu\text{m}$, the Kn is 0.009. Therefore, the contact mechanics between seal and metallic parts play important roles for determining the flow regime of gas flow in the micro channel.

Table 4.4 Knudsen number and the corresponding flow regimes.

Kn	Flow regime
0~0.01	Continuum
0.01~0.1	Slip
0.1~10	Transition
10~	Free molecular

As shown in Table 4.4, according to the value of Kn the flow is divided into four regimes, which are respectively: continuum, slip, transition, and free molecular flows.

When Kn is between 0 and 0.01, the flow can be treated by continuum theories using the Navier-Stokes equations. When Kn is larger than 0.1, the continuum hypothesis breaks down.

The mass flow is assumed to be unidirectional laminar flow and the velocity simplified only in x direction is written in Equation (4-14).

$$v = \frac{1}{2\mu} \left(-\frac{\partial P}{\partial x} \right) (Hy - y^2) \quad (4-14)$$

Where μ is the dynamic viscosity of the sealed fluid HFC-134a. The volume flow rate can be calculated by Equation (4-15).

$$Q_v = w_c \int_0^H \frac{1}{2\mu} \left(-\frac{\partial P}{\partial x} \right) (Hy - y^2) dy \quad (4-15)$$

Then,

$$Q_v = w_c \frac{1}{2\mu} \left(-\frac{\partial P}{\partial x} \right) \left(H \frac{y^2}{2} - \frac{y^3}{3} \right) \Big|_0^H = \frac{w_c H^3}{12\mu} \left(-\frac{\partial P}{\partial x} \right) \quad (4-16)$$

Therefore, the mass flow rate can be obtained by introducing the density $\rho = \frac{P}{rT}$ from the assumption of ideal gas behaviour. T is temperature in K and r is the gas constant for HFC-134a.

$$\dot{m}_{ch} = Q_v \rho = \frac{w_c H^3}{12\mu r T} \left(-P \frac{\partial P}{\partial x} \right) \quad (4-17)$$

The mass flow rate per channel can be obtained by integrating Equation (4-17) from 0 to L, expressed by Equation (4-18)

$$\dot{m}_{ch} = Q_V \rho = \frac{w_c H^3}{24\mu r T} \frac{(P_{upstream}^2 - P_{downstream}^2)}{L} \quad (4-18)$$

The total mass flow rate through the entire cylindrical contact area is the mass flow rate per micro channel multiplied by the total number of channels (see Figure 4.9). It is equal to the circumference divided by contact width.

$$\dot{m} = n_{ch} \dot{m}_{ch} = \frac{\pi D}{L} \frac{w_c H^3}{24\mu r T} \frac{(P_{upstream}^2 - P_{downstream}^2)}{L} \quad (4-19)$$

Equation (4-19) is the basis of numerical model to calculate the mass flow rate of O-ring seals.

Slip flow taking into account the rarefaction effect

When the Knudsen number is between 0.01 and 0.1, the rarefactions effects should be taken into account for slip flow rate calculation. As reported by [MAN00, POL98, POL00], first order slip boundary conditions are applied to correct the velocity, which becomes:

$$v = \frac{1}{2\mu} \left(-\frac{\partial P}{\partial x} \right) (Hy - y^2 + \lambda_{m(P)} H) \quad (4-20)$$

Where $\lambda_{m(P)}$ is the mean free path of the fluid at pressure P. The volume flow rate can be written as Equation (4-21):

$$Q_V = \frac{w_c H^3}{12\mu} \left(-\frac{\partial P}{\partial x} \right) \left(1 + \frac{6\lambda_{m(P)}}{H} \right) \quad (4-21)$$

According to the basic kinetic theory,

$$\lambda_{m(atm)} P_{atm} = \lambda_{m(P)} P \quad (4-22)$$

$$\dot{m}_{ch} = Q_V \rho = -\frac{w_c H^3}{12\mu r T} \left(P \frac{\partial P}{\partial x} + \frac{6\lambda_{m(atm)} P_{atm}}{H} \frac{\partial P}{\partial x} \right) \quad (4-23)$$

Integration of x from 0 to L leads to:

$$\dot{m}_{ch} = \frac{w_c H^3}{12\mu r T L} \left(\frac{P_{upstream}^2 - P_{downstream}^2}{2} + \frac{6\lambda_{m(atm)} P_{atm}}{H} \cdot (P_{upstream} - P_{downstream}) \right) \quad (4-24)$$

In order to compare to Equation (4-19), Equation (4-24) is rearranged as:

$$\dot{m}_{ch} = \frac{w_c H^3}{24\mu r TL} (P_{upstream}^2 - P_{downstream}^2) \left(1 + \frac{6\lambda_{m(atm)}}{H} \frac{P_{atm}}{P_{upstream} + P_{downstream}} \right) \quad (4-25)$$

Since the downstream pressure is rightly the ambient pressure, Equation (4-25) can be finally expressed as:

$$\dot{m}_{ch} = \frac{w_c H^3}{24\mu r TL} (P_{upstream}^2 - P_{downstream}^2) \left(1 + \frac{6\lambda_{m(atm)}}{H} \frac{1}{1 + \frac{P_{upstream}}{P_{downstream}}} \right) \quad (4-26)$$

Here a slip factor is introduced which is written as:

$$\beta = \frac{6\lambda_{m(atm)}}{H} \frac{1}{1 + \frac{P_{upstream}}{P_{downstream}}} \quad (4-26)$$

Leak flow rate measurements of fittings (§ 4.4) allow evaluating the influence of rarefaction effect by analyzing the slip factor β .

Defining the temperature range of 10 ~ 50°C, the corresponding saturation pressure varies from 400 to 1400 kPa. The surface roughness of the rigid metallic parts of fittings is generally less than 1 μm . Knowing the $\lambda_{m(atm)} = 0.903 \times 10^{-8} m$ and varying H from $0.1 \times 10^{-6} m$ to $1 \times 10^{-6} m$, the relationship between the pressure ratio and rarefaction effect has been calculated.

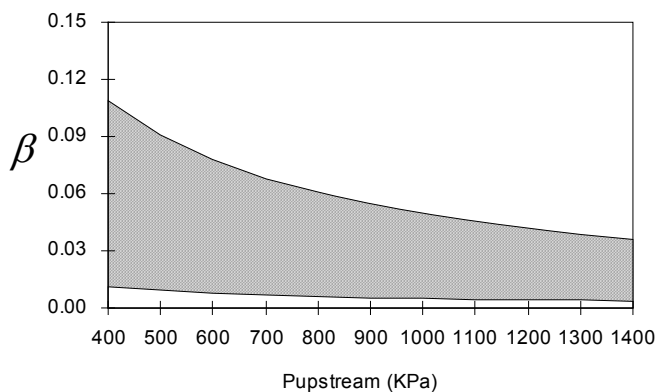


Figure 4.12 Rarefaction effect analysis.

As shown in Figure 4.12, the slip factor is of maximum 1.1 and minimum 1.01 at 400kPa, and only varies between 0.01 and 0.004 at 1400kPa. The higher the pressure ratio, the lower the slip factor. Results prove that under the given pressure range (from 400 to 1400 kPa), the rarefaction effect is negligible in contrast to the laminar flow.

4.3 Analysis of a radial O-ring sealing performance using the Finite Element Method (FEM)

O-ring is commonly used in the MAC systems. Numerical analysis of sealing performance of seals has been reported. Green et al. [GRE94] investigated the contact stress, contact width of O-rings in both restrained and unrestrained cases. Belforte et al. [BEL08] evaluated the contact pressure in seals and validated the experimental procedure by performing pressure sensitive films for calibration.

This study focus on the finite element analysis of O-ring in order to determine the influence of different factors concerning O-ring material properties, pressure load, fitting design parameters, etc. The software MSC.MARC is used to carry out the simulation with its non-linear study option.

4.3.1 Hypothesis for O-ring material

For finite element modeling of elastomers (O-ring material), the material behaviors need to be determined. Linear materials in the model comply with Hook's law where stress is directly proportional to strain. Unlike linear elastic materials, the deformation of an elastomer is not directly proportional to the applied load. Figure 4.13 shows the typical stress-strain relation of an elastomer. As the strains increase, the stress-strain relationships become non-linear. Because of this non-linear stress-strain behavior under the specified loading, a non-linear analysis is required for modeling.

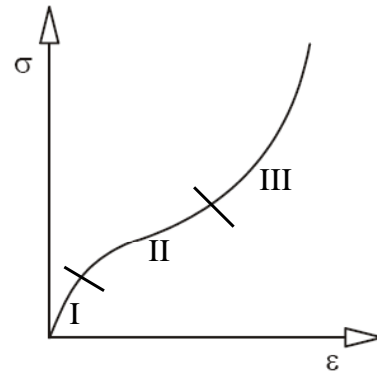


Figure 4.13 Typical stress-strain relation of an elastomer.

In addition to this non-linearity, elastomers present very high deformation capability. Technical strains of 1000% in the operational range are possible. Although for the deformation of rubber comparatively low forces are needed, these deformations occur nearly incompressible. This issue is often described by the *Poisson's ratio* $\nu \rightarrow 0,5$. In this study, O-ring elastomer has been assumed as a hyper-elastic material.

The hyper-elastic material behavior is described mathematically by strain energy density functions W . The stress components are determined by partial derivation with respect to the strain components. One of the most commonly used models, Mooney-Rivlin, is used here. Based on the assumption that rubber is isotropic and incompressible, Rivlin obtained a generic strain energy based model for hyper-elasticity, which takes the following form:

$$W_1 = A(I_1 - 3) + B(I_2 - 3) + X\left(\frac{1}{I_3} - 1\right) + Y(I_3 - 1)^2 \quad (4-27)$$

$$W_2 = C(I_1 - 3)(I_2 - 3) + D(I_1 - 3)^2 + E(I_3 - 3)^2 + F(I_1 - 3)^3 \quad (4-28)$$

and

$$W = W_1 + W_2 \quad (4-29)$$

Where I_1 , I_2 , and I_3 are invariants of the right Cauchy-Green deformation tensor and can be expressed in terms of principal stretch ratios:

$$I_1 = \lambda_1^2 + \lambda_2^2 + \lambda_3^2 \quad (4-30)$$

$$I_2 = \lambda_1^2 \lambda_2^2 + \lambda_2^2 \lambda_3^2 + \lambda_3^2 \lambda_1^2 \quad (4-31)$$

$$I_3 = \lambda_1^2 \lambda_2^2 \lambda_3^2 \quad (4-32)$$

Moreover A, B, C, D, E, and F are called Mooney material constants, and

$$X = 0.5A + B \quad (4-33)$$

$$Y = \frac{[A(5\nu - 2) + B(11\nu - 5)]}{[2(1 - 2\nu)]} \quad (4-34)$$

In case of perfectly incompressible material, $I_3 = 1$, Y approaches infinity. Thus, for values of Poisson's ratio close to 0.5, the last term in W_1 remains bounded, and a solution can be obtained. So that the Mooney-Rivlin 2-term model (using only A and B constants) is applied and can be written as:

$$W = A(I_1 - 3) + B(I_2 - 3) \quad (4-35)$$

Several methods are available to determine the Mooney material constants. One of them is the relationship between hardness and Young's modulus. O-ring material hardness principle implies that the correlation between Shore-A hardness and modulus of elasticity is:

$$E(\text{MPa}) = 7.879 \cdot 10^{-2} \cdot \varepsilon - 3.065 \cdot 10^{-3} \cdot \varepsilon^2 + 4.895 \cdot 10^{-5} \cdot \varepsilon^3 \quad (4-36)$$

Where ε is shore-A hardness. For an incompressible material, constant $A = E/6$, and constant $B = E/4$.

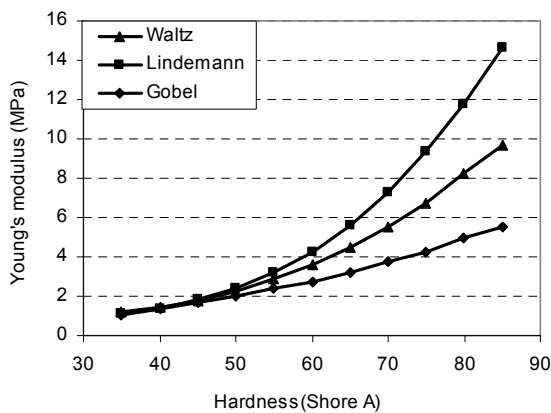


Figure 4.14 Relationship between Young's modulus and shore-A hardness.

Two other methods exist to explain the relationship between the hardness and the Young's modulus (see Figure 4.15). A model is established based on O-ring sample of EPDM material classified by shore-A hardness 85. For instance, the Waltz model has been chosen for simulation. In § 3.1.3.3, numerical results of contact width prove that this model leads to reasonable results compared to experimental data. That means a Young's modulus value of about 8.3 MPa has been used to determine constants A and B as shown in Table 4.5

Table 4.5 Mooney-Rivlin constants.

A	B
1.379 MPa	0.345 MPa

4.3.2 O-ring simulation model

Simulation is made based on a single radial O-ring (see Figure 4.15) where the bore and plug are assembled and fixed together. Knowing that the component is axial symmetric, one can simplify the model by analyzing only one degree instead of a whole 360 degrees (see Figure 4.16). The O-ring model has an inner diameter of 14 mm with a tore of 1.78 mm as shown in Figure 4.16.

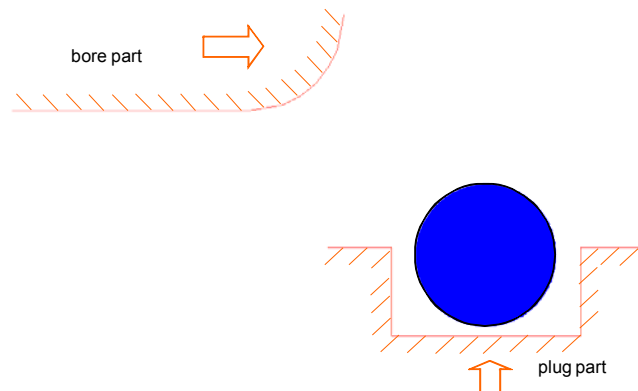


Figure 4.15 Photo of O-ring sample. Figure 4.16 Axis-symmetric finite element model of a radial O-ring.

Figure 4.16 illustrates the principle of the simulation that is carried out in two steps:

- **Step 1:** the bore part slides in the horizontal direction and the plug part slides in the vertical direction to simulate the installation of the fittings;
- **Step 2:** the pressure load is applied on the left side of the deformed O-ring seal and the left side load is the atmospheric pressure.

Those two steps represent the real conditions and allows to comparing the results before and after pressure load.

Both bore and plug parts are considered as rigid bodies for numerical simulation and only the O-ring seal is deformable, so that meshing is only made for the O-ring seal. In order to obtain high accurate results, 12041 nodes and 11900 four-node elements have been generated in this meshing. The cross section of the O-ring is shown in Figure 4.17.

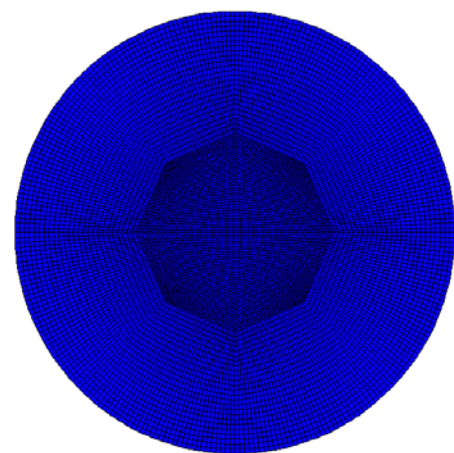


Figure 4.17 Axis-symmetric finite element model of a radial O-ring.

As illustrated in Figure 4.18, sealing performance of O-ring is influenced by several geometrical factors such as:

- Bore diameter (D_{bore})
- Plug diameter (D_{plug})
- Groove diameter (D_{groove})
- Gland depth (G)
- Gap clearance (δ)

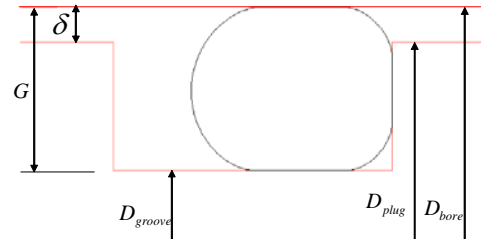


Figure 4.18 O-ring design parameters.

Some of them will be analyzed in detail in next section.

4.3.3 Results and discussions

Simulations have been performed using the software MSC.MARC using Finite Element Method. Contact pressure, contact width, and other parameters have been analyzed based on simulation results.

Analysis

The distribution of the Von Mises' stress after installation and before applying pressure is illustrated in Figure 4.19(a). It is obvious that the Von Mises' stress is not symmetrical between the upside and the downside. The maximum stress occurs at the bottom side as shown in Figure 4.19.

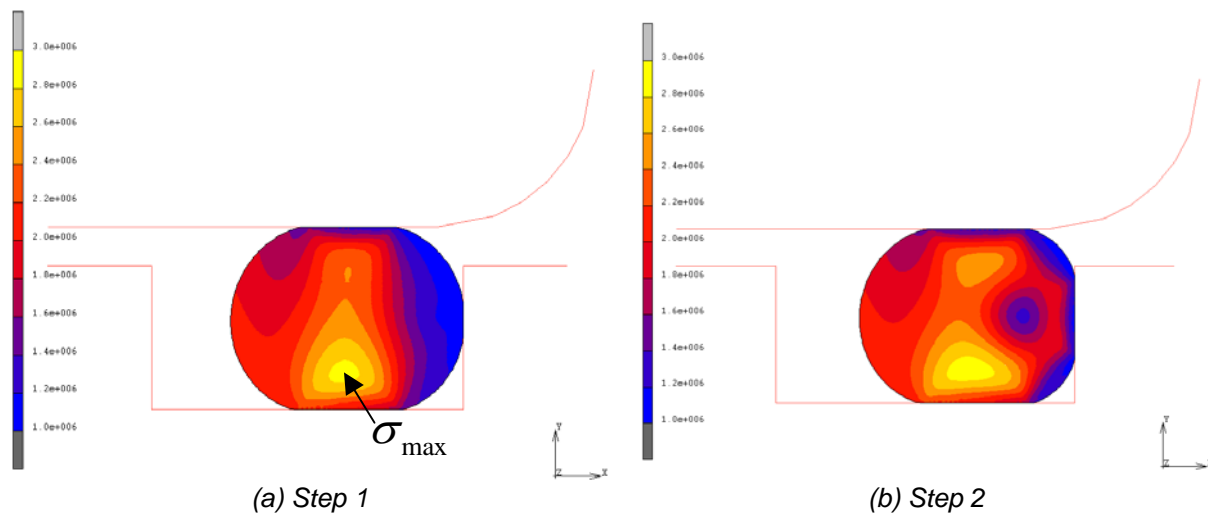


Figure 4.19 Distribution of the von Mises stress of O-ring before and after pressure load.

Pressure is loaded uniformly to the right side of the deformed surface of the O-ring. Figure 4.19(b) shows the case where a pressure load of 1.3 MPa is applied. One can observe that the O-ring is pressed against the right wall of the groove. The maximum stress increases from 3 to 3.6 MPa. It can be seen that, under pressure load, the O-ring is pressed to the right side of the groove and the maximum stress area becomes larger on both the bottom and top sides.

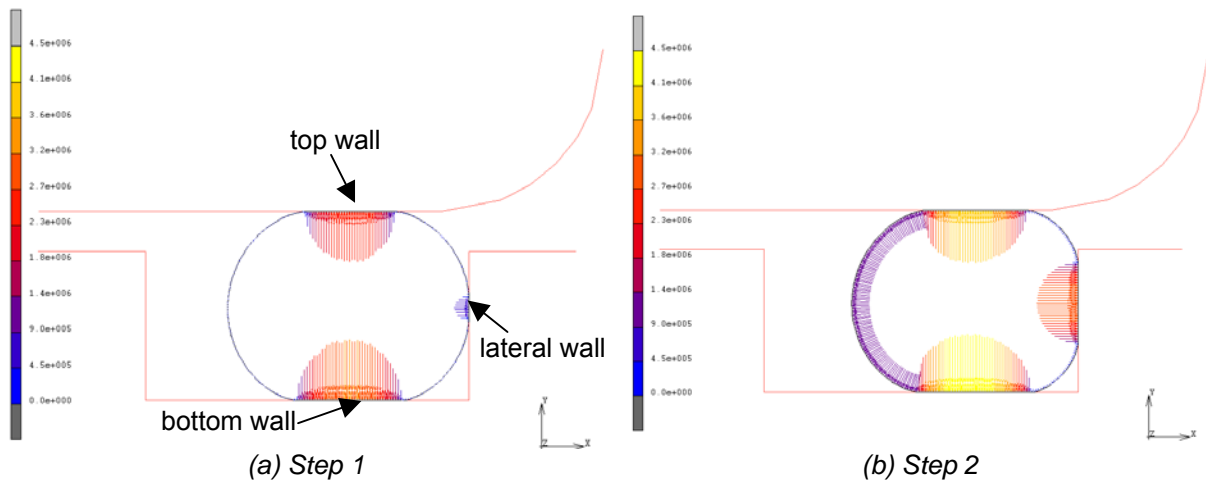


Figure 4.20 Distribution of the normal stress in the area of O-ring before and after pressure load.

Figure 4.20 (a) and Figure 4.20(b) show the normal stress after installation and after a pressure load of 1318 kPa. Before applying the pressure on the left side of the O-ring, the seal is not only in contact with the top and bottom walls, but also slightly in contact with the lateral wall of the groove due to the instroke movement and the friction between the seal and the metallic parts. Once a pressure of 1318 kPa is applied to the left side of the seal, the O-ring is pressed to the right side, and the contact width with the lateral wall becomes larger. The contact stress on the top, bottom, and lateral walls increases with the pressure load and the contact width as well. Figure 4.20(b) shows clearly that the maximum contact pressure is always larger than the pressure load that allows preventing the leakage.

4.3.3.1 Contact pressure analysis

The sealing performance depends directly on the contact pressure distribution between the seal and the metallic parts. Three different pressure loads (770, 1017, and 1318kPa) have been simulated in order to study the relationship between pressure load and pressure distribution.

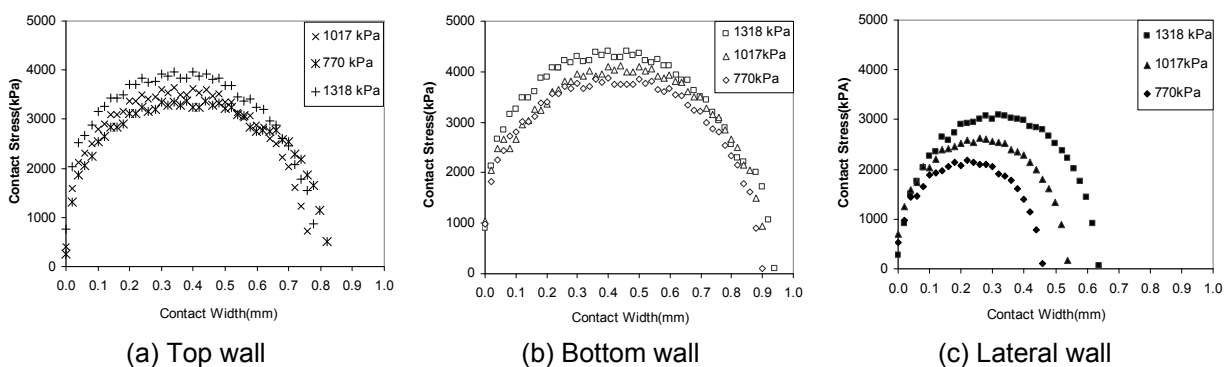


Figure 4.21 Contact stress in contact with the lateral wall of the groove.

Figures 4.21 (a), (b), and (c) show respectively the contact pressure profiles in contact areas: the top wall, the bottom wall, and the lateral wall. In each figure, the pressure follows approximately a parabolic curve. The maximum contact pressure and the contact width are observed at the bottom wall and followed by the top wall. Playing an auxiliary role of leakage prevention, the lowest pressure distribution is observed on the lateral wall.

Table 4.6 Max contact stress under different load pressures.

Pressure load (kPa)	Max Contact stress (kPa)		
	top wall	bottom wall	lateral wall
571	3162	3672	1738
770	3379	3870	2179
1017	3639	4119	2627
1200	3806	4280	2921
1318	3966	4406	3100

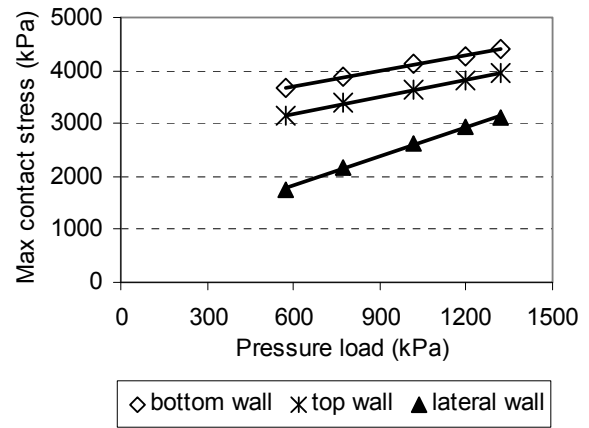


Figure 4.22 Max contact stress as a function of pressure load.

Table 4.6 and Figure 4.22 show the evolution of the maximum contact pressure with the pressure load. When increasing the pressure load, both the maximum contact pressure and the contact width between O-ring and the rigid wall increase. At 571 kPa load pressure, the maximum contact pressures are respectively 3672 kPa at the bottom wall, 3162 kPa at the top wall and 1738 kPa at the lateral wall. When the load pressure raises to 1318 kPa, the maximum contact pressure on the top wall increases by 25% (3966 kPa). An increase of 20% is found on the bottom wall. The greatest change is found on the lateral wall with a factor 1.78. As illustrated in Figure 4.22, a linear regression shows a good agreement between the load pressure and the maximum contact stress.

4.3.3.2 Contact width simulation results and real width observation

Based on the mass flow rate calculations performed in § 4.2.2.3, the mass flow rate is inversely proportional to the contact width. The contact width evolution as a function of the pressure load has been analyzed based on the simulation results.

Table 4.7 Contact widths under different load pressures.

Load pressure (kPa)	Contact width (mm)		
	Top wall	Bottom wall	Lateral wall
571	0.70	0.86	0.36
770	0.74	0.90	0.46
1017	0.76	0.90	0.54
1200	0.77	0.91	0.60
1318	0.78	0.94	0.64

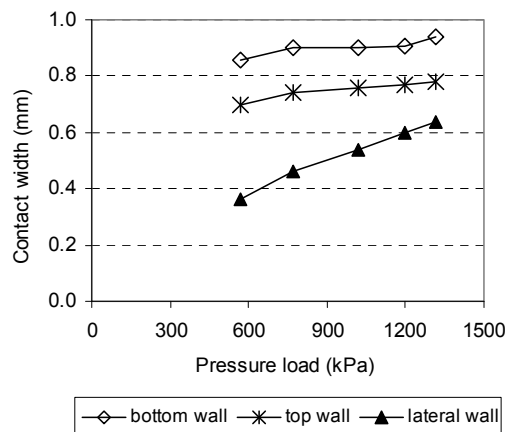


Figure 4.23 Contact width as a function of pressure load.

Table 4.7 summarizes the contact width between O-ring seal and three contact walls. Load pressure varies from 571 kPa to 1318 kPa. The contact width on the top wall varies from 0.70 to 0.78 mm and increases from 0.86 to 0.94 on the bottom wall. Significant increase of

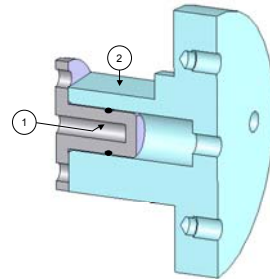
contact width occurs on the lateral wall. Between 0.36 and 0.64 mm, there is a factor of 1.78. Figure 4.21 (c) illustrates also those important changes.

Real contact width observation

In order to validate the simulation results, transparent fitting specimen has been realized. As shown in Figure 4.24, the right and left parts represent respectively the bore and the plug parts of a fitting. A commonly used O-ring is installed in the groove.



Figure 4.24 Transparent fitting specimen.



(1) Bottom wall

(2) Top wall

Figure 4.25 Two ways to observe the contact width.

Once the two parts are assembled together as indicated in Figure 4.25, two possible ways exist to observe the contact width between O-ring and fittings: (1) bottom wall contact and (2) top wall contact.

Figure 4.26 shows the test apparatus for measuring the contact width on the top wall by microscope. The specimen is fixed under a microscope and a light source is applied from both sides of the specimen in order to guarantee a good visualization of the contact area. Pressure gauge is connected to the bore part of the specimen as shown in Figure 4.24 and Figure 4.26. Different feed pressures are controlled by a pressure regulator. Contact surfaces for different feed pressures are visualized by a 2-Megapixel camera connected to a computer. Contact surface is monitored and recorded for each required pressure value.

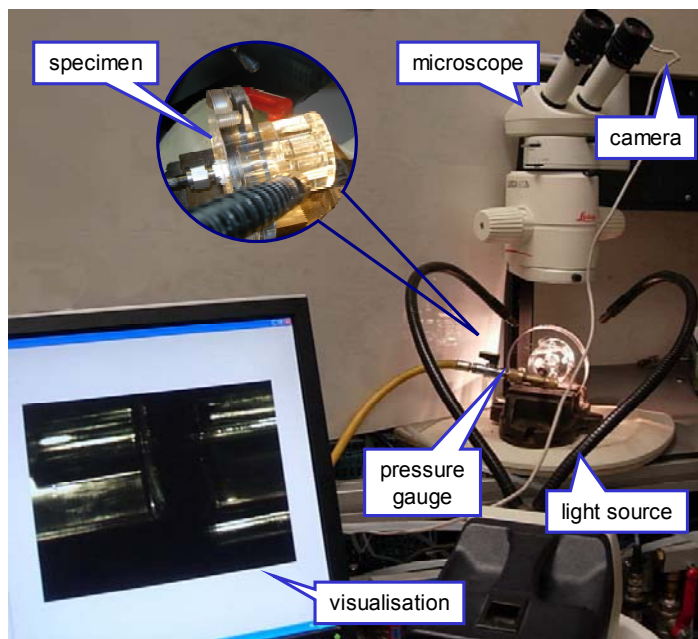


Figure 4.26 Test apparatus for contact width measurement.

The bottom wall contact has been observed by an endoscope as shown in Figure 4.27. The rigid tube with the end of the endoscope is introduced into the hole and provides an image to the camera. The camera is fixed at the end of the endoscope to record the image and make it visualized by the computer as shown in Figure 4.26.

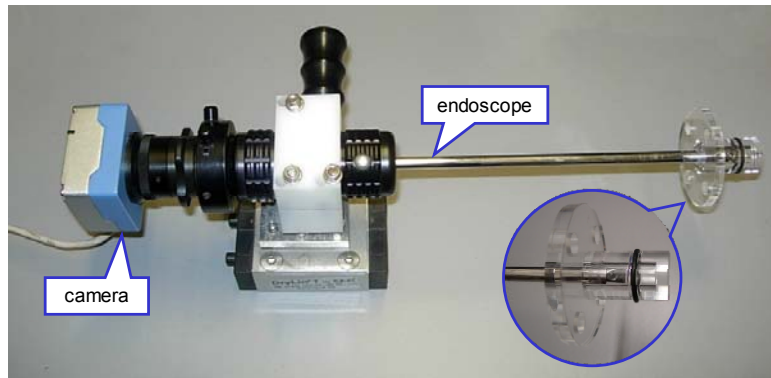
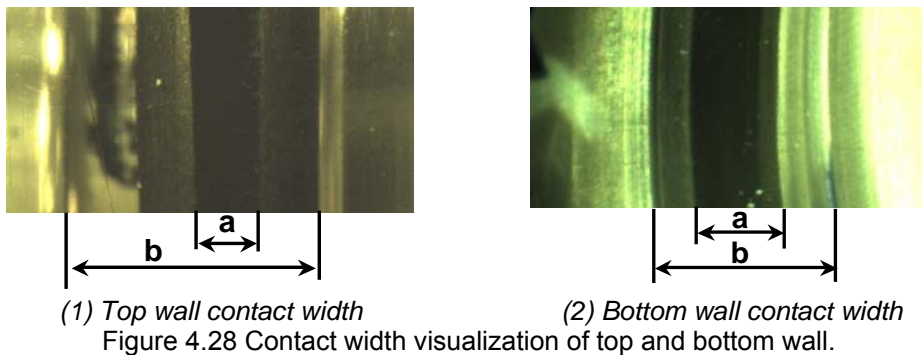


Figure 4.27 Test apparatus for contact width measurement.

Thanks to above measurement apparatus, contact areas of the bottom and top walls have been observed and recorded for several feed pressures. Figures 4.28 (1) and (2) give examples of top and wall visualizations.



(1) Top wall contact width

(2) Bottom wall contact width

Figure 4.28 Contact width visualization of top and bottom wall.

In order to obtain the real contact width, the width of the groove has also been measured. The real dimension of the groove is known as 2.4 mm. The ratio of the width of the contact area to that of the groove is constant. Thus knowing a and b , the contact width L can be calculated using Equation (4-37).

$$\frac{a}{b} = \frac{L}{2.4} \quad (4-37)$$

Figure 4.29 shows the comparison between the measured values and simulation results of both top and bottom wall contact widths. As observed in simulations, the contact width on the bottom wall is larger than that on the top wall. For the bottom wall, the measured contact width is slightly greater than the results of simulations. By contrast, simulations give higher results than measurements for the top wall contact. Nevertheless, simulation results match well the measured values, thus validating the simulation.

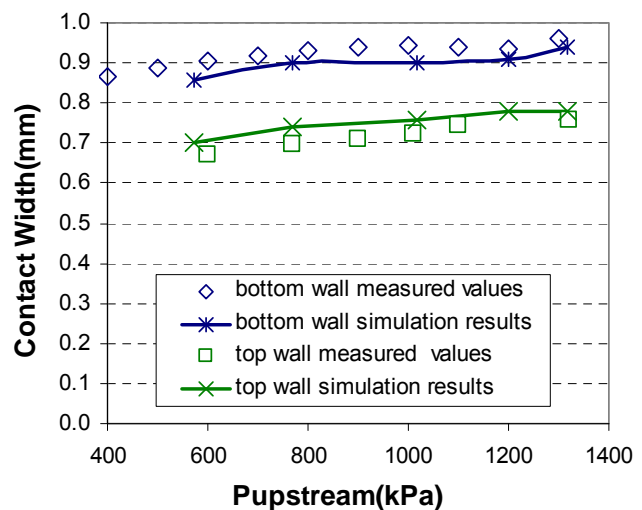


Figure 4.29 Measured contact width vs. simulation results.

4.3.3.3 Squeeze and gland depth influence

Gland depth appears to be one of the most essential factors of O-ring sealing performance. The squeeze is determined by the difference of the bore diameter and the groove diameter. The greater the gland depth, the lesser the O-ring compression, and the lower the contact stress between elastomer and metallic part. Several simulations have been made in order to analyze the influence of the gland depth on O-ring sealing performance. Therefore, the plug diameter is fixed and the bore diameter varies from 17.4 to 18.05 mm. The squeeze is the ratio of the O-ring diameter deformation to the O-ring original cross section diameter. It is calculated from Equation(4-38).

$$\text{squeeze}(\%) = \frac{d_2 - (D_{\text{bore}} - D_{\text{groove}}) / 2}{d_2} \quad (4-38)$$

Table 4.8 details the evolution of maximum contact stress on the top, bottom, and lateral walls. The squeeze plays an important role on sealing performances of the O-ring seal. When the bore diameter decreases O-ring is less deformed, which means the squeeze increases. As shown in Figure 4.30, the maximum contact pressures on the top and bottom walls increase with the increase of the squeeze and $\sigma_{\text{max}}^{\text{bottom}}$ is always greater than $\sigma_{\text{max}}^{\text{top}}$. However, lateral wall maximum contact pressure decreases.

For squeezes lower than 13%, $\sigma_{\text{max}}^{\text{lateral}} > \sigma_{\text{max}}^{\text{bottom}} > \sigma_{\text{max}}^{\text{top}}$ maximum contact pressure occurs on the lateral wall. Squeezes between 13% and 16%, σ_{max} on the three walls are very close to each others. For squeezes > 16%, the dominant contacts are located on the top and bottom walls. When squeezes are lower than 8%, the O-ring seal is not in contact with the top wall after installation, which means that the sealing is defective.

Plug diameter (mm)	Bore diameter (mm)	Squeeze (%)	Max Contact stress (kPa)		
			Top wall	Bottom wall	Lateral wall
14.8	17.4	27%	4870	5258	2828
	17.6	21%	3966	4406	3100
	17.8	16%	3143	3646	3230
	17.9	13%	2692	3263	3290
	18.0	10%	2199	2864	3360
	18.05	8%	1977	2710	3411

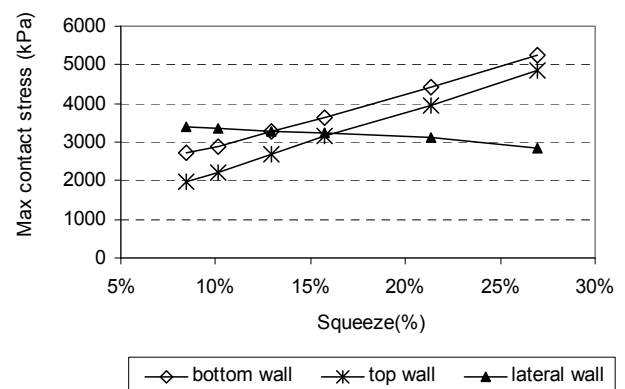


Figure 4.30 Squeeze impact on maxi contact stress.

It is wrong to say that the higher the squeeze, the better the sealing performance, because under high compress force, the stress inside the O-ring body becomes so high that it boosts O-ring damage. The squeeze has to be determined as a function of the loading pressure and has to be studied for a specific fitting design and a type of elastomer material.

4.3.3.4 Gap clearance δ

An O-ring always needs the presence of gap clearance for installation. When the pressure load is relative high, the gap clearance becomes important because part of elastomer material may be extruded in the clearance. Figure 4.31 gives an example of the Von Mises' stress distribution in O-ring seals. Compared to Figure 4.19(b), only the gas clearance is modified to be greater. It is interesting to see than in region close to the right corner, the stress becomes high so that the seal risks to be damaged and extruded in the clearance. Figure 4.32 gives an example of defective O-ring due to extrusion. In brief, the gap clearance should be carefully designed in order to avoid O-ring failure occurrence.

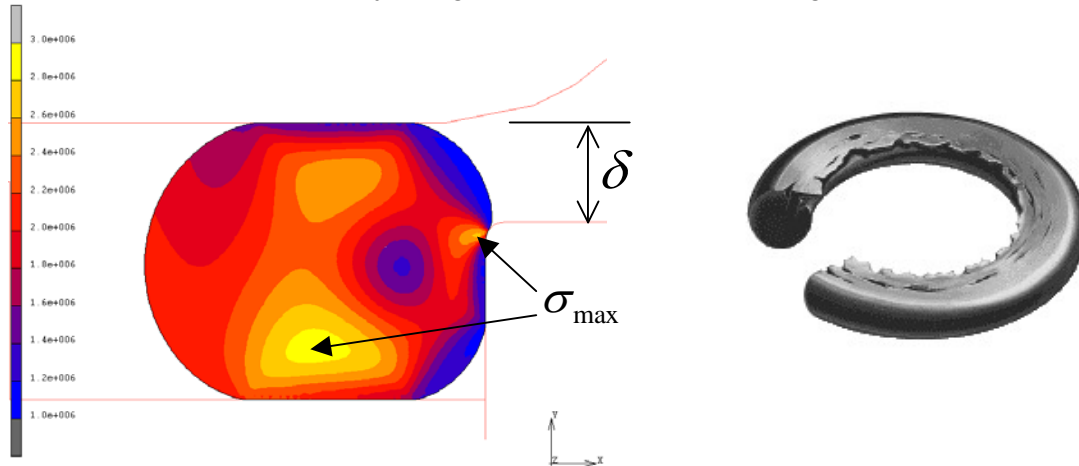


Figure 4.31 Distribution of the von Mises' stress of O-ring. Figure 4.32 Defective O-ring by extrusion.

4.3.3.5 O-ring hardness and temperature dependence

In real working conditions, the ambient temperature varies. That means not only the feed pressure but also the temperature of O-ring seals changes. Therefore the hardness of seal materials is directly influenced by temperature.

As shown in Figure 4.33, elastomers become softer and the hardness decreases with the increase in temperature. Curve 4 gives an example of the EPDM hardness evolution. From the ambient temperature to 50°C, the hardness decreases from 70 to 65. For simulations, the O-ring seal for has a hardness of 85, which is out of its variation range.

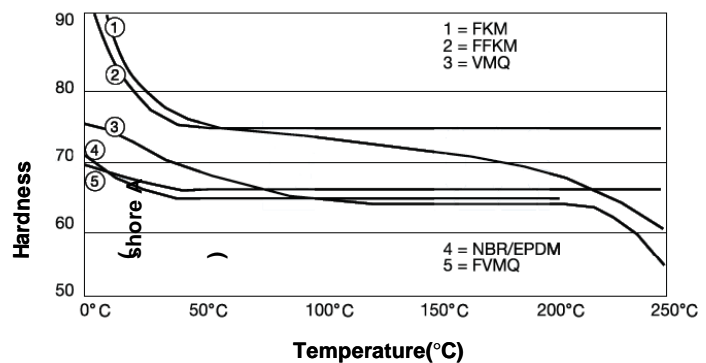


Figure 4.33 Variations of elastomer hardness vs. temperature.

Making the assumption that the decrease rate of the O-ring seal is similar to Curve n°4, the hardness is supposed to vary from 85 to 80 when temperature increases from ambient to 50°C. Simulation has been carried out taking into account the temperature effect. From 30°C to 50°C, the O-ring has been modeled by reducing the hardness from 80 to 85 shore-A, which means that the Young's modulus of the O-ring material decreases with the temperature increase.

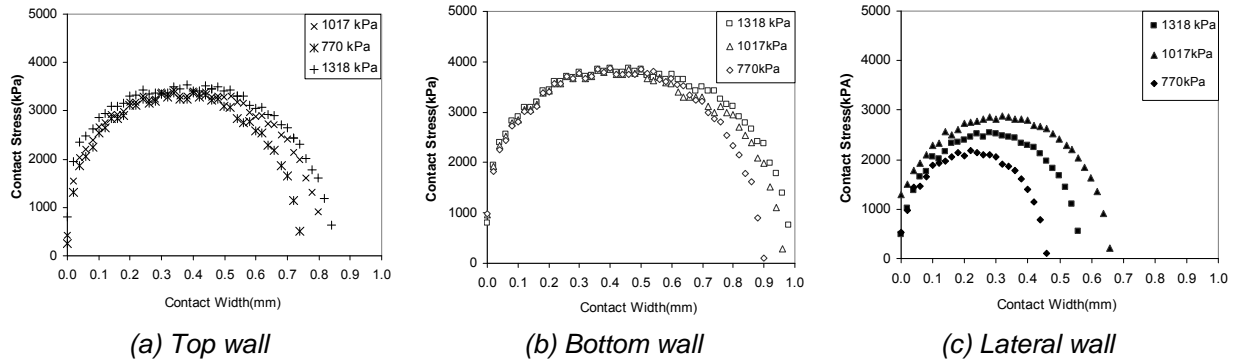


Figure 4.34 Contact stress in contact with the lateral wall of the groove considering hardness effect.

Distributions of contact stress on the top, bottom, and lateral walls taking into account the temperature effect on material hardness are presented in Figure 4.34. It can be seen that the maximum contact pressures change slightly on the top and the bottom walls. The contact width increases when temperature increases. As detailed in Table 4.9 and Figure 4.36, the maximum contact pressure increases of only 4% on the top wall and 1% on the bottom wall. Important increase has been observed only on the lateral wall.

Table 4.9 Maximum contact stress under different load pressures.

Pressure load (kPa)	T (°C)	Max Contact stress (kPa)		
		top wall	bottom wall	lateral wall
770	30°C	3379	3860	2179
1017	40°C	3425	3870	2542
1318	50°C	3530	3883	2882
		Contact width (mm)		
		top wall	bottom wall	lateral wall
770	30°C	0.78	0.94	0.46
1017	40°C	0.80	0.96	0.56
1318	50°C	0.84	0.98	0.66

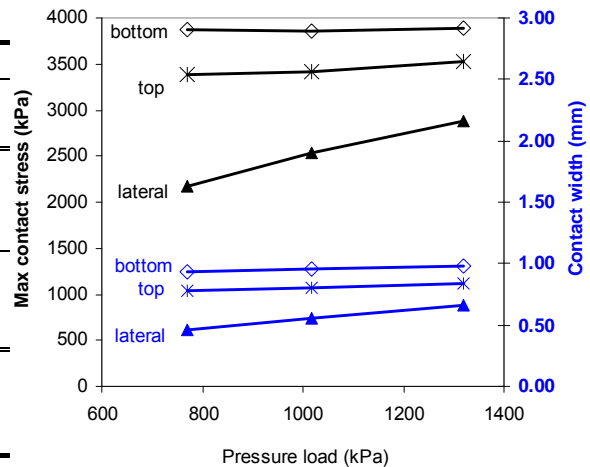


Figure 4.35 Maximum contact stress and contact width as a function of pressure load.

Results give a good explanation for assuming the invariance of channel height regardless of contact pressure. It helps to simplify reasonably the calculation of the mass flow rate (explained in § 4.4.2).

4.4 Establishment of Leak flow rate laws

4.4.1 Leakage behavior of an O-ring fitting

As discussed from the beginning of the chapter, leakage is composed of permeation through seal polymer materials and leakage through micro channels due to the non-perfect contact between seal and metallic parts (see Figure 4.2). The leak flow rate of the fittings is composed of the two leakage modes and can be modeled based on the mass balance equation. It means that for the control volume shown in Figure 4.36, mass entering per unit time is equal to mass leaving per unit time plus increase of mass in the control volume per unit time. There is no increase in the mass inside the control volume for steady flow so that: mass entering per unit time is equal to mass leaving per unit time.

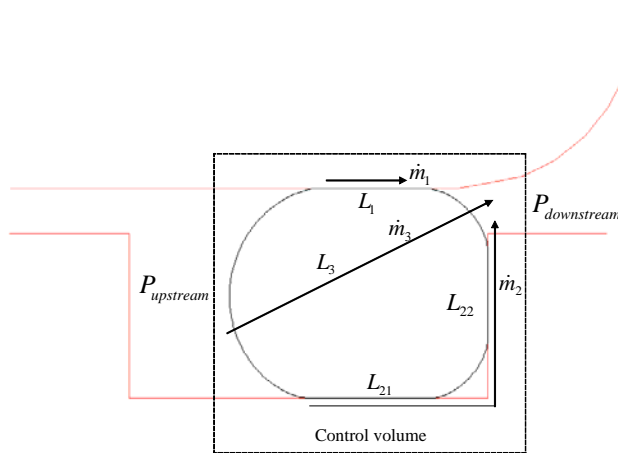


Figure 4.36 Control volume for mass flow calculation.

Therefore, the total leak flow rate due to permeation and micro channels can be calculated by Equation (4-39).

$$\dot{m} = \dot{m}_1 + \dot{m}_2 + \dot{m}_3 \quad (4-39)$$

\dot{m}_1 and \dot{m}_2 belong to micro-channel gas flow, and \dot{m}_3 is caused by gas permeation through polymers. Each term of Equation (4-39) will be studied in next sections.

4.4.2 Leak flow rates of two separate modes

Leak flow rates through overall micro channels

In order to establish the contribution of each leakage mode, an O-ring with low coefficient of permeation has been chosen. The polymer used for the O-ring sample corresponds to membrane F mentioned in Chapter 3. Because the permeability of this polymer is quite low, the leakage due to permeation can be neglected. In this case, Equation (4-39) is simplified to:

$$\dot{m} = \dot{m}_1 + \dot{m}_2 \quad (4-40)$$

$$\dot{m} = \dot{m}_{ch1}n_{ch1} + \dot{m}_{ch2}n_{ch2} \quad (4-41)$$

Where,

$$\dot{m}_{ch} = \frac{w_c H^3}{24\mu r T} \frac{(P_{upstream}^2 - P_{downstream}^2)}{L} \quad (4-42)$$

Some assumptions are made here for further calculations:

- The gas flow is laminar and isothermal. This assumption will be verified by calculating the Reynolds number;
- Because the maximum contact pressures on top and bottom walls are very close, the number of micro channels (n_{ch}) is assumed to be the same for the top and bottom walls;
- The surface roughness is assumed to be the same for the top, bottom, and lateral walls, which means the channel width w_c is the same.

Therefore,

$$\dot{m}_1 = n_{ch} \frac{w_c H_1^3}{24\mu r T} \frac{(P_{upstream}^2 - P_{downstream}^2)}{L_1} \quad (4-43)$$

Let

$$\alpha = \frac{n_{ch} w_c}{24\mu r T} \quad (4-44)$$

Equation (4-44) turns to:

$$\frac{\dot{m}_1}{\alpha} = \frac{P_{upstream}^2 - P_{downstream}^2}{\frac{L_1}{H_1^3}} \quad (4-45)$$

And so the resistance can be defined as:

$$R_1 = \frac{L_1}{H_1^3} \quad (4-46)$$

Similarly, the resistances for contact area on bottom and lateral walls are written as:

$$R_{21} = \frac{L_{21}}{H_{21}^3} \quad (4-47)$$

$$R_{22} = \frac{L_{22}}{H_{22}^3} \quad (4-48)$$

Thus, the total resistance is expressed by Equation (4-49).

$$\frac{1}{R} = \frac{1}{R_1} + \frac{1}{R_{21} + R_{22}} \quad (4-49)$$

Combining Equations (4-46), (4-47), (4-48), and (4-49), leads to

$$\frac{1}{R} = \frac{H_1^3}{L_1} + \frac{H_{21}^3}{L_{21} + L_{22} \left(\frac{H_{21}}{H_{22}} \right)^3} \quad (4-50)$$

Therefore, the total mass flow rate can be calculated using Equation (4-51).

$$\dot{m} = \frac{\pi D_{bore}}{L_1} \frac{w_c}{24\mu r T} (P_{upstream}^2 - P_{downstream}^2) \left(\frac{H_1^3}{L_1} + \frac{H_{21}^3}{L_{21} + L_{22} \left(\frac{H_{21}}{H_{22}} \right)^3} \right) \quad (4-51)$$

Simulation results take into account the temperature dependence of the O-ring seals. As shown in Figure 4-34, because the maximum contact pressures on the top wall and the bottom wall are very close, the heights of the micro channels of both walls can be considered equal: $H_1 \approx H_{21}$. Equation (4-51) becomes:

$$\dot{m} = \frac{\pi D_{bore}}{L_1} \frac{w_c H_1^3}{24 \mu r T} (P_{upstream}^2 - P_{downstream0}^2) \left(\frac{1}{L_1} + \frac{1}{L_{21} + L_{22} \left(\frac{H_{21}}{H_{22}} \right)^3} \right) \quad (4-52)$$

Introducing a parameter R_L , representing the resistance due to contact width, the term H_{21}/H_{22} is assumed to be unity in order to simplify the calculation. R_L turns to:

$$\frac{1}{R_L} = \frac{1}{L_1} + \frac{1}{L_{21} + L_{22}} \quad (4-53)$$

Equation (4-53) shows that the contact area of the different walls does not play the same role in leakage prevention. The major contribution comes from the contact with the top wall. The fitting specimen has been measured at 30, 40 and 50°C in order to have more elements on the geometry of the micro channel: $w_c H^3$.

Table 4.10 Micro-channel calculation based on measured LFRs.

T(°C)	Saturation pressure (kPa)	Leak flow rate (g/yr)	μ ($\mu Pa s$)	L_1 Top wall	L_{21} Bottom wall	L_{22} Lateral wall	R_L	$w_c H^3$
30	770	0.29	11.907	0.78	0.94	0.46	0.0005009	7.873×10^{-28}
40	1017	0.50	12.373	0.80	0.96	0.56	0.0005241	9.342×10^{-28}
50	1318	0.86	12.917	0.84	0.98	0.66	0.0005555	10.361×10^{-28}

The surface roughness is less than $1 \mu m$, so that the height of micro channels is in the order of 10^{-7} . Taking $H = 0.1 \mu m$, w_c is in the range of $0.8 \sim 1.0 \mu m$ based on the values of λH^3 given in Table 4.10. In brief, the width and height of rectangular micro channels is in the range of 0.1 to $1.0 \mu m$. Values of $w_c H^3$ at 40 and 50°C are close to each other. At 30°C the value is smaller. A dispersion of maximum 14% has been found, which is acceptable. Results presented in Table 4.10 validate the simplified Equation (4.53) and so Equation (4-54) can be used for calculating the leak flow rate of O-ring fittings due to gas flow in micro channels.

$$\dot{m} = \frac{\pi D_{bore}}{L_1} \frac{w_c H_1^3}{24 \mu r T} (P_{upstream}^2 - P_{downstream}^2) \left(\frac{1}{L_1} + \frac{1}{L_{21} + L_{22}} \right) \quad (4-54)$$

Laminar flow regime verification

The Reynolds number is defined as

$$Re = \frac{\bar{u} 2h \rho}{\mu} \quad (4-55)$$

Also,

$$Q_v = \bar{u} w_c h \tag{4-56}$$

Then the relationship between the Re and \dot{m} can be found.

$$Re = \frac{2Q_v \rho}{\mu w_c} = \frac{2\dot{m}_{ch}}{\mu w_c} \tag{4-57}$$

For a leak flow rate of 0.86 g/yr at 50°C, the Reynolds number can be calculated from Equation (4-58)

$$Re = \frac{2\dot{m} / n_{ch}}{\mu w_c} = \frac{2 \times 3.9 \times 10^{-10}}{12.917 \times 10^{-6} \times 0.1 \times 10^{-6}} = 604 \tag{4-58}$$

Re is well below the critical Reynolds number 2000, so that the assumption of laminar flow is justified.

Leak flow rates prediction for permeation through polymers

Based on the prediction model for membranes 1 to 6 obtained in § 4.2.1, the leak flow rates at 30, 40, and 50°C have been calculated.

The leak flow rate due to gas permeation is geometrically simplified for an O-ring with inner diameter of D_{groove} , outer diameter of D_{bore} , and a thickness of about 2.2 mm.

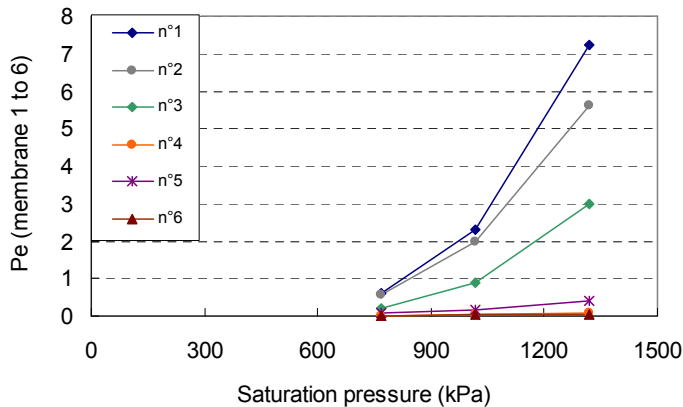


Figure 4.37 Permeations prediction of 6 polymers.

Table 4.11 summarizes the leak flow rate predictions for 30, 40, and 50°C. As it can be seen in Figure 4.37, membranes 1, 2, and 3 present too high leak flow rates and are not convenient to seal fluid HFC-134a. Polymers 4 and 6 show good sealing performance for HFC-134a. It should be pointed out that due to the compression of seal material, the real leak flow rates of each polymer should be lower than the prediction value.

Table 4.11 Predictions of LFRs of membranes 1 to 6.

Temperature (°C)	Saturation Pressure (kPa)	LFR (g/yr)					
		Type 1	Type 2	Type 3	Type 4	Type 5	Type 6
T1 = 30	770	0.60	0.56	0.22	0.01	0.06	0.01
T2 = 40	1017	2.32	1.98	0.91	0.03	0.17	0.02
T3 = 50	1318	7.24	5.61	2.98	0.10	0.41	0.05

4.4.3 Analysis of leak flow rate contributions as a function of permeability

Based on the results obtained on permeation of membrane, large differences exist among seal materials. Figure 4.38 gives a specific example to make clear the contribution of two leakage modes (permeation and micro channels).

As illustrated in Figure 4.38, concentration evolution along time shows the combined transport phenomena at 50°C. Since the mass transport in micro channels takes place rapidly, the straight line from the beginning to 4th hour is considered to be pure micro channel flow (Zone 1). The transient state of diffusion needs at least several hours, Zone 2 is then due to permeation.

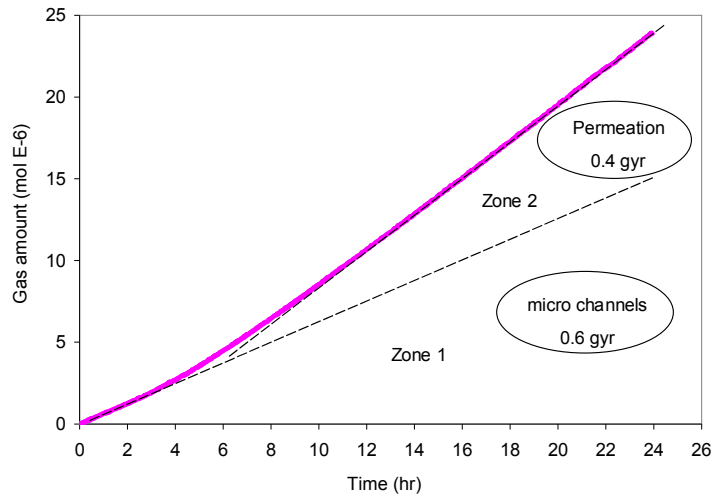


Figure 4.38 Leakage distribution assumptions.

The slope of Zone 1 gives 0.6 g/yr, and the total leak flow rate of this fitting is 1.0 g/yr. By subtraction, the leak flow rate from permeation through seal material is $1.0 - 0.6 = 0.4$ g/yr. Therefore, in this case permeation and micro-channel flow contribute respectively for 40 and 60% to total leak flow rate of the O-ring.

In contrast to the leak flow rate prediction given in Table 4.11, the leakage behavior of the fitting sample is close to that of the polymer Type 5 (0.4 g/yr at 50°C). Replacing the seal by other material gives quite different results. If polymers Types 4 and 6 are chosen, their permeation contributions are 14 and 8 %. When using polymers Type 3, its permeation accounts for 83% of the total leak flow rate.

Figure 4.39 summarizes leak flow rates of 10 fittings samples at 30, 40, and 50°C, and the threshold. At 30°C leak flow rates vary from 0.2 to 0.9 g/yr. At 40°C the minimum leak flow rate is 0.3 and the maximum value is 1.3 g/yr. At 50°C leak flow rates are in the range of 0.4 ~ 2.1 g/yr. This dispersion is primarily due to the permeation difference.

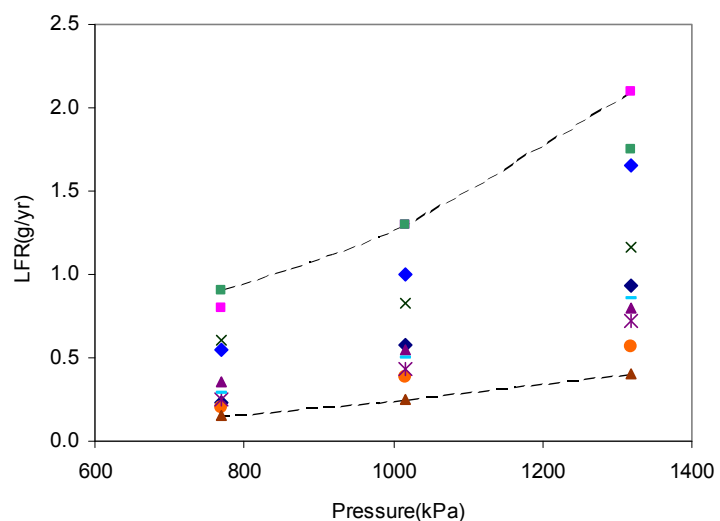


Figure 4.39 LFRs of 10 fitting samples.

To conclude, the leak flow rate of a fitting is determined by both permeation and micro-channel leakage. Low permeation polymers show great interest for leakage prevention. Since the main factor of micro-channel flow is the surface roughness, the leak flow rate of fittings can be possibly reduced by improving the surface finishing or using low permeation polymers,

4.5 Complementary Analyses

As shown at the beginning of this chapter (see Figure 4.2, besides the simple O-ring seals, axial O-ring seals, multiple O-rings and other types of seals exist. In this section, the effect of torque on axial-radial O-rings and multiple O-rings sealing performance will be analyzed.

4.5.1 Effect of torque on an axial-radial O-ring

The contact pressure is directly influenced by the squeeze of O-ring seal. For an axial O-ring seal, the torque applied on the fitting determined directly the squeeze. In order to analyze this effect, a fitting has been measured (see Figure 4.40) with two different torques. As given in Table 4.12, when increasing the torque from 15 Nm to 20 Nm, the mass flow rate decreases from 0.41 to 0.36 g/yr at 30°C; from 0.73 to 0.62 g/yr at 40°C, and from 1.27 to 1.07 g/yr at 50°C. The leak flow rate reduces in the range of 12 to 15%.



Figure 4.40 Fitting specimen.

Table 4.12 LFRs of fitting with axial-radial O-ring.

T(°C)	Saturation pressure (kPa)	Leak flow rate (g/yr)	
		15 Nm	20 Nm
30	770	1.27	1.07
40	1017	0.73	0.62
50	1318	0.41	0.36

Although the torque plays a positive role on leakage prevention, it should not be increase infinitely because extreme stress will occur under high squeeze, and thus increase defective risk of O-ring seals.

4.5.2 Analysis of multiple O-rings

4.5.2.1 Sealing performance of multiple O-rings

A series of tests has been performed to analyze the sealing performance of fittings with multiple O-rings. Figure 4.41(a) presents the 3D drawing and real photo (Figure 4.41 (b) of the fitting specimen. O-ring seals used for measurements are the same (type and dimensions) as the O-ring fittings shown in Figure 4.15. O-ring close to high-pressure side is named first O-ring and the other one facing the ambient downstream pressure is called second O-ring. Pressure gauge is designed on the bore part of the specimen in order to measure the pressure P_m between two O-rings. The pressure is measured from outside of

the accumulation volume so as not to introduce supplementary leakage source for the results.

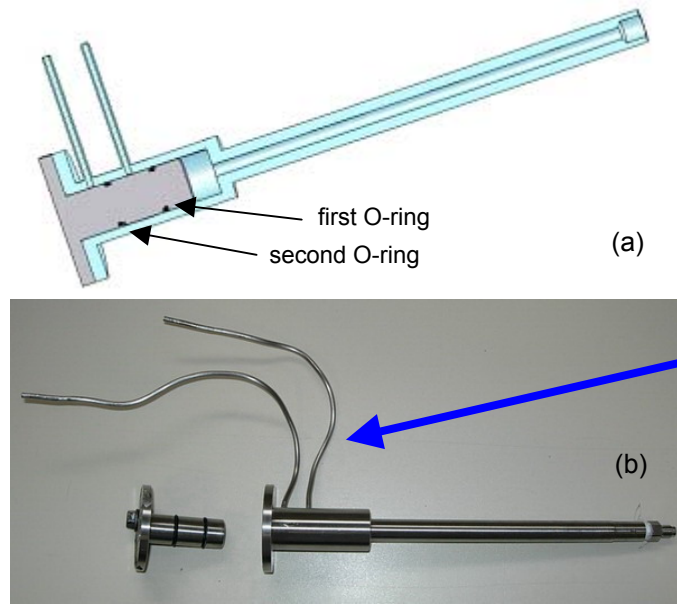


Figure 4.41 Fitting specimen with double O-rings.

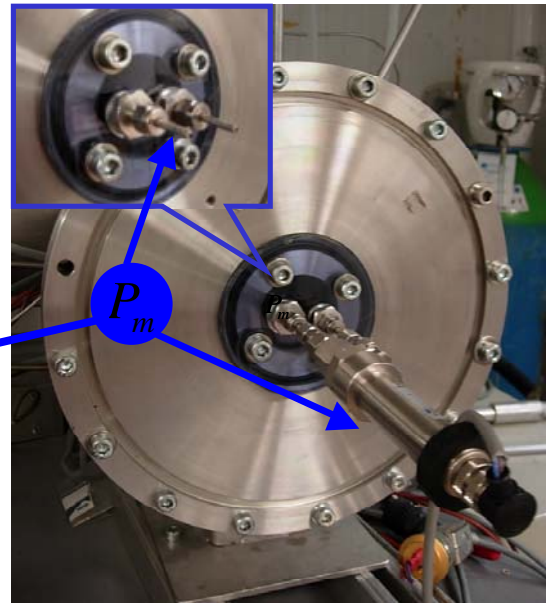


Figure 4.42 Test apparatus for a double O-ring fitting.

Table 4.13 Leak flow rate calculations for a double O-ring fitting.

	Saturation pressure (kPa)	Contact performance					LFR (g/yr)
		Contact width			Leakage Resistance R_{Li}	Total Resistance R_L	
		Top wall	Bottom wall	Lateral wall			
Double O-ring	$P_{upstream}$ 1318	0.78	0.86	0.53	0.0004996	0.0009280	0.49
	P_m 460						
	$P_{downstream}$ 101	0.69	0.82	0.31	0.0004284		
Simple O-ring	$P_{upstream}$ 1318	0.84	0.98	0.66	0.0005555		0.87
	$P_{downstream}$ 101						

P_m measured at steady state of 50°C is 460 kPa. Table 4.13 shows the calculation for a double O-ring fitting and comparison with the simple O-ring result. Contact width on each wall has been obtained by FEM simulation taking into account the temperature effect on polymer hardness. Results on the simple O-ring is taken from Table 4.10.

Because the pressure difference between the two sides of the O-ring seal is different, the contact widths obtained are different. For the first O-ring, larger contact widths have been found than for the second one. The resistances based on contact width for the first O-ring and the second O-ring are 0.0004996 and 0.0004284. The factor of 1.2 between the first O-ring and the second one shows that the role of the first O-ring is more important than the second one. The resistance for double O-ring is 0.0009280 and 0.0005555 is found for the simple O-ring. There is a factor of 1.7 instead of 2 between simple and double O-ring. That

means that leak flow rate does not reduce proportionally to the number of O-rings but less. Leak flow rate measurements give 0.49 g/yr for double O-rings and 0.87 g/yr for simple O-rings. The factor of $0.87/0.49 = 1.8$ close to 1.7 also confirms the numerical results.

4.5.2.2 Influence of rotation

Based on the sealing technology of the fittings, either part can rotate liberally. Measurements have been performed by changing the position of two parts as shown in Figure 4.43.



Figure 4.43 Fitting sample.

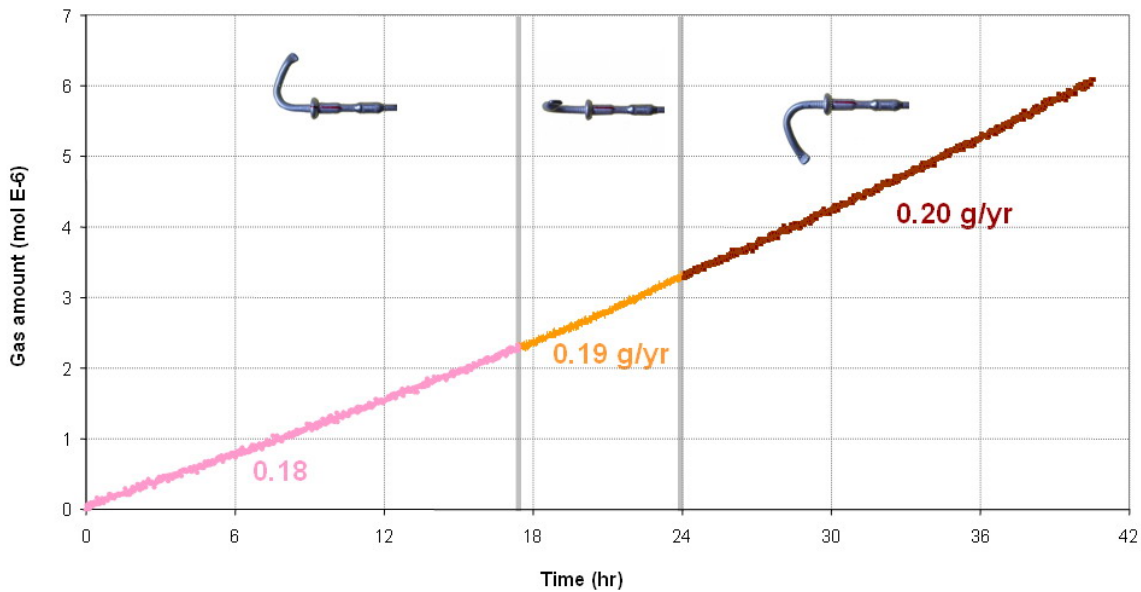


Figure 4.44 Test position for leakage tests.

Figure 4.44 shows the leak flow rate measurements of a triple O-ring fitting at 3 different positions. Concentration evolution has been continuously recorded. No significant influence has been observed when rotating the fittings. After rotation of about 180° , the leak flow rates change from 0.18 to 0.20 g/yr. Similar measurements have been done by removing O-rings one by one. Table 4.14 summarizes the tests results for different test conditions. Great differences occur in the single O-ring case. With only 1 O-ring, the leak flow rate of the fitting varies from 0.57 to 0.78 and a factor of 1.4 has been found. In contrast to 1 O-ring case, leak flow rates of the fitting with 2 O-rings are rather constant (from 0.45 to 0.47 g/yr).

Table 4.14 LFRs of triple O-ring fitting with 1, 2, and 3 O-rings at different positions.

Description	3 O-rings	2 O-ring	1 O-ring
Position			
LFR (g/yr)	0.18	0.45	0.78
	0.19	0.47	0.68
	0.20	0.46	0.57

To conclude, for this triple O-ring fitting, leak flow rate decreases with the increase of O-ring number. Great dispersion due to rotation occurs only for simple O-ring. That is why multiple O-rings are usually used in this type of fittings.

Conclusions

In this chapter, typical O-ring seals have been studied. Sealing performance of fittings with radial O-ring seals has been analyzed in detail. Two leakage modes are distinguished: permeation through sealing materials and gas flow through micro channels. Permeations of 6 membrane samples have been measured. A factor of 66 has been observed at 30°C and 104 at 50°C.

Using software MAC.MARC, stress, maximum contact pressure, and contact width are analyzed. Contact pressure increases linearly with the increase of upstream pressure. Real contact width validated the simulation results with small differences. Squeeze plays an important role on contact pressure. At low squeeze level, the contact of seal on lateral wall becomes dominant.

Leakage behavior combining two leakage modes have been established, which allows understanding the key points of emission dependence and improving the sealing performance.

Supplementary analyses have been done on the influence of torques on an axial-radial O-ring and on multiple O-rings with rotation consideration.

4.6 References

- [BEL08] Belforte, G., Conte, M., Manuello Bertetto, A., Mazza, L., Visconte, C., 2008. Experimental and numerical evaluation of contact pressure in pneumatic seals. Tribology International.
- [BOT07] Bottiglione, F., Carbone, G., Mantriota, G., 2007. Calculation of fluid leakage in ball valves. 12th IFToMM World Congress, Besançon, France, June 18-21, 2007
- [CIA00] Ciavarella, M., Demelio, G., Barber, J.R., Yong Hoon Jang, 2000. Linear elastic contact of the Weierstrass. Proceedings of the royal society (2000) 456, 387-3405.
- [CIA04] Ciavarella, M., Murolo, G., Demelio, G., Barber, J.R., 2004. Elastic contact stiffness and contact resistance for the Weierstrass profile. Journal of the mechanics and physics of solids. 52 (2004) 1247-1265p.
- [DAL00] Daley, J.R., Philips, H.M., 2000. Gas pressure and leakage rate in static seals. 16th International Conference on Fluid Sealing: Successful Sealing. Belgium on 18-20 September 2000.135-146p.
- [DAN79] Daniel, L., Hertz, J.R., 1979. O-Rings for low – pressure service. Machine Design.
- [FLI00] Flitney, R.K., 2000. Fluid sealing. 16th international conference on fluid sealing, 18-20 September 2000, Brugge, Belgium.
- [GAO06] Gao, Y.F., and Bower A.F., Elastic-plastic contact of a rough surface with Weierstrass profile. Proceedings of the royal society (2006) 462, 319-348p.
- [GRE94] Green, I., English, C., 1994. Stress and deformation of compressed elastomeric O-ring seals. 14th International Conference on Fluid Sealing. Italy, on 6-8 April 1994,83-95p.
- [MAN00] Manners, W., 2000. Gas pressure and leakage rate in static seals. 16th International Conference on Fluid Sealing: Successful Sealing. Belgium on 18-20 September 2000.121-133p.
- [MUL98] Muller, H.K., Nau, B.S., 1998. Fluid sealing technology – principles and applications. Marcel Dekker Inc, 504p.

- [OKA02] Okamura, T., Ohtsuka, M., Suetsugu, N., Ohta, T., 2002. Micro surface roughness of O-rings and sealing mechanism. SAE technical paper 2002-01-0662.
- [OKA08] Okada, H., Itoh, T., Suga, T., 2008. The influence of surface profiles on leakage in room temperature seal-bonding. Sensors and Actuators A 144 (2008) 124-129p.
- [PAR07] Parker O-Ring Handbook. 2007. Parker Hannifin Corporation, Cleveland, OH.
- [PER04] Persson, B.H.J., Albohr, O., Tartaglino, U., Volokitin, A.I. and Tosatti. E., 2004. On the nature of surface roughness with application to contact mechanics, sealing, rubber friction and adhesion. Journal of physics, Condensed matter, vol. 17, n^o1, pp. R1-R62
- [PER06] Persson, B.N.J., 2006. Contact mechanics for randomly rough surfaces. Surface science reports 61(2006), 201-227p.
- [PER08] Persson, B.N.J., Yang, C., 2008. Theory of the leak – rate of seals. Journal of physics: condensed matter 20(2008)
- [POL98] Polycarpou, A.A., Etsion, I., 1998. Static sealing performance of gas mechanical seals including surface roughness and rarefaction effects. Tribology Transactions, Vol.41,4,531-536p.
- [POL00] Polycarpou, A.A., Etsion, I., 2000. A model for the static sealing performance of compliant metallic gas seals including surface roughness and rarefaction effects. Tribology Transactions, Vol.43, 2, 237-244p.

General Conclusions

This thesis has presented the development of a generic approach for predicting the refrigerant HFC-134a emissions in MAC systems. It was a considerable interest to study the leakage behavior of basic MAC components such as hoses and fittings.

Generic approach based on experimental data of MAC systems leak flow rate measurements

Chapter 2 introduced a laboratory test method to determine the leak flow rate of MAC systems ensuring good measurement accuracy. The qualified test method has been a basis of the EU regulation 706/2007. Results many systems (about 40) or the sum and of many system components (more than 100) have shown that emissions from MAC systems in standstill mode equal the sum of the emissions of their components within an acceptable uncertainty level. So both methods are proved suitable for determining the leak flow rate of any MAC systems. Knowing the running mode contribution, which is about 5-6% of the total annual emission of a MAC system, the major part of the refrigerant is emitted during the period where the vehicle is standstill, so that the leak flow rate of the MAC system can be determined without performing running mode tests. Once the leakage behavior of a MAC system is determined, the mean annual temperature of a climatic zone is sufficient for leakage prediction based on the proposed correlation factor method. The generic approach of refrigerant emissions is expressed by Equation (1).

$$\dot{m} = k(P_{upstream}^2 - P_{downstream}^2) \quad (1)$$

Permeation approach to leak flow rates of MAC systems

Based on the results obtained in Chapter 3, some conclusions can be drawn:

- HFC-134a leakage through MAC hoses can be simplified to gas transport through polymer material;
- Coefficients of permeability of 6 membrane samples have been determined;
- A prediction model has been developed not only for membranes but also for hoses;
- An overall permeability coefficient has been introduced and good agreements have been observed between the prediction values and experimental data;
- Hoses with the same technology lead to different leakage values that depend on suppliers;
- An in-depth study on temperature and pressure relationship of refrigerant HFC-134a has led to correlate the leakage behavior of hoses to the system leakage behavior.

An approach that takes into account temperature and pressure effects on permeability has been proposed and validated by experimental data with an error of less than 7%, and is written as follows:

$$\dot{m} = M_{HFC-134a} \cdot \frac{\pi r^2}{e} \cdot \kappa_1 e^{\left(\frac{\kappa_2(\Delta P) - \kappa_3}{RT}\right)} \cdot \Delta P \quad (2)$$

The temperature and pressure dependence of leak flow rate is given by Equation (2). The relationship between the saturation temperature of HFC-134a and its vapor pressure is not linear as it is well known and shown in Figure 1. A mathematical model for the pressure increase as a function of temperature should be established to simplify this double effect. Finding out a non-linear regression model, the term of temperature effect can be replaced by pressure. The most common assumption is based on the Clausius-Clapeyron equation:

$$\frac{dP}{dT} = \frac{\Delta H}{T \frac{nRT}{P}} = \frac{\Delta H}{R} \frac{P}{T^2} \quad (2)$$

$$\frac{dP}{P} = \frac{\Delta H}{R} \frac{dT}{T^2} \quad (3)$$

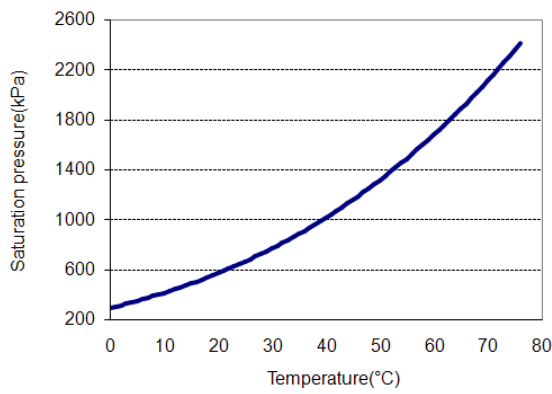


Figure 1 Relationship between temperature and saturation pressure of HFC-134a.

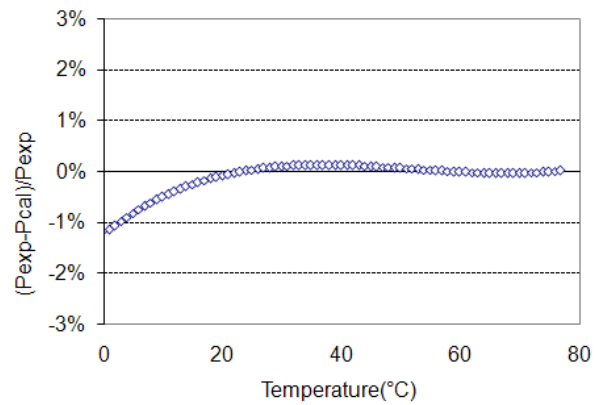


Figure 2 Comparison of simple Clapeyron equation with experimental vapor pressure data.

Equation (2) is rearranged to Equation (3), which integrates to Equation (4) making an assumption that ΔH_{vap} is approximately constant in the temperature limits.

$$P = \exp(A) \exp\left(-\frac{\Delta H_{vap}}{RT}\right) \quad (4)$$

$$\ln P = A - \frac{\Delta H_{vap}}{RT} \quad (5)$$

Equation (5) shows that the pressure P , enthalpy of vaporization, ΔH_{vap} , and temperature T are related. Uncertainties between the calculated pressures and experimental data are lower than 1% (see Figure 2) in the temperature range of 0 to 80°C (see Table 1).

Table 1 Constants for T and P correlation.

A	ΔH_{vap}
15.33	21888

This temperature dependence can be correlated to its corresponding saturation pressure by combining Equation (4) and Equation (5), the leak flow rate as a function of pressure is expressed by Equation(6).

$$\dot{m} \propto e^{c_2 \Delta P} (P_{upstream})^{\frac{E_{pe}}{\Delta H_{vap}}} (P_{upstream} - P_{downstream}) \quad (6)$$

The complex expression should be analyzed term by term. The power and exponential functions of pressure are illustrated in Figure 3 and 4.

The term $e^{c_2 \Delta P}$ as a function of pressure difference is presented in Figure 3. Values of c_2 vary from -0.0006 to 0.0006 according to the results obtained for membrane samples A to E. It can be seen that in the given pressure zone (from 0 to 1500 kPa) the power term varies around 1 and within the limit from 0 to 2.

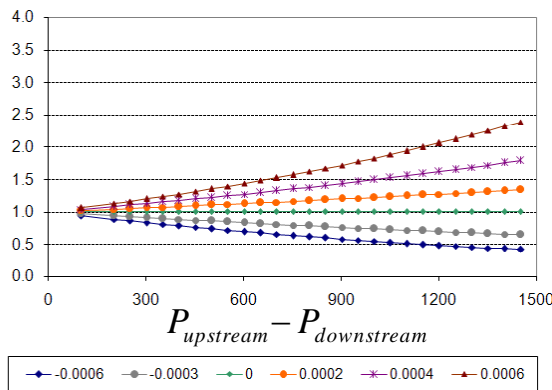


Figure 3 Exponential term vs. pressure.

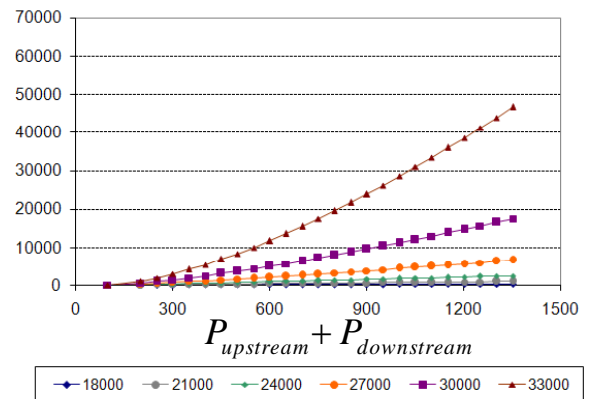


Figure 4 Power term vs. pressure.

The term $(P_{upstream})^{\frac{E_{pe}}{\Delta H_{vap}}}$ is illustrated in Figure 4 as a function of $(P_{upstream} + P_{downstream})$. In some cases, the evolution is nearly linear, meaning that it is possible to consider this term as being proportional to $(P_{upstream} + P_{downstream})$. Therefore, leak flow rate of a given hose is possibly proportional to the difference of the square of pressures.

$$\dot{m} \propto (P_{upstream} + P_{downstream})(P_{upstream} - P_{downstream}) \quad (7)$$

It proves that, the prediction model is adequate in many cases, but some times not. To conclude, leakage behavior of a MAC system can be approximately modeled by Equation (1), which contributes to the total leakage of a MAC system.

Micro-channel laminar gas flow approach to MAC systems leak flow rates

Chapter 4 provides evidence that both permeation and micro-channel laminar flow contribute to emissions fittings. Finite Elements Method simulation has allowed analyzing several important factors such as contact pressure, contact width, and stress. Numerical results on

contact width have been verified by visualization through transparent specimens. Permeation and micro-channel flow have been compared. In addition to the permeation leak flow rate approach, leakage behavior is discussed as well. As demonstrated in Chapter 4, the mass flow rate in micro channels of a fitting can be calculated using Equation (8).

$$\dot{m} = \frac{\pi D_{bore}}{L_1} \frac{w_c H_1^3}{24 \mu r T} (P_{upstream}^2 - P_{downstream}^2) \left(\frac{1}{L_1} + \frac{1}{L_{21} + L_{22}} \right) \quad (8)$$

Analysis on contact width has shown a factor of about 2 between $1/L_1$ and $1/(L_{21} + L_{22})$. Taking this assumption and Equation 8 it comes:

$$\dot{m} = \frac{\pi D_{bore}}{L_1^2} \frac{w_c H_1^3}{16 \mu r T} (P_{upstream}^2 - P_{downstream}^2) \quad (9)$$

For a given fitting, the geometry parameter is fixed. The dispersion of $1/\mu T$ from 30°C to 50°C is 7%.

To conclude, both permeation and micro-channel transport phenomena can be approximately regressed by a parabolic function, which is proportional to the difference of the pressure square.

A MAC system basically depends on hoses and seals in fittings, TXV, service valves, pressure sensor, etc. Shaft seal of compressor in standstill mode is also a combined leakage of permeation and micro-channel flow. A thesis by D. Sousa is dedicated to the detailed study of compressor shaft seals.

In short, the leak flow rates of a MAC system is the sum of leak flow rates of all leak sources. Those sources are of two types: permeation through polymers and flows through micro channels existing between seals and metallic parts of any fittings or seals. For each emission mode, behavior laws have been established and prediction models validated allowing forecasting emission rates with a limiter number of measurements.

Appendix

Leak flow rate of MAC systems and components

LEAK FLOW RATE OF MAC SYSTEMS AND COMPONENTS

1- Laboratory tests, fleet tests and correlation factor

Yingzhong YU, Denis CLODIC

Center for energy and processes, Ecole des Mines de Paris, France

yingzhong.yu@ensmp.fr , denis.clodic@ensmp.fr

Abstract:

According to the EU regulation 706/2007, the leak flow rate of a Mobile Air Conditioning (MAC) system must be tested based on a qualified method. The Center for energy and processes has cooperated with ACEA (European Association of Car Manufacturers) in order to establish the test method. Laboratory tests have been undertaken on 40 MAC systems, more than 100 components and field tests on 40 vehicles. In this paper, we introduce the test protocol for leak flow rate tests in laboratory based on the measurement of HFC-134a concentration evolution inside a test chamber using infrared techniques. Contribution of standstill and running mode leakage has been studied. Comparing the laboratory tests and the fleet test results a correlation factor has been established to predict the annual leak flow rate of a MAC system mounted on a vehicle in real life conditions based on the leak flow rate measured in laboratory.

Keywords: Leak flow rate; Mobile Air Conditioning system; fleet tests; correlation factor

Nomenclature		Abbreviations	
$\dot{m}_{HFC-134a}$	Mass flow rate (LFR) of HFC-134a (kg s ⁻¹)	HFC-134a	1,1,1,2-tetrafluoroethane
$n_{HFC-134a}$	Number of moles of HFC-134a (mol)	LFR	leak flow rate
n_{total}	Total number of moles inside the test chamber (mol)	ppm	Parts per million volume/volume equivalent to mol/mol
C	Concentration of HFC-134a (ppm)		
$M_{HFC-134a}$	Molar mass of HFC-134a (= 102 kg kmol ⁻¹)	ppb	Parts per billion volume/volume equivalent to mol/mol
P_{amb}	Pressure in the test chamber (Pa)		
T_{amb}	Temperature in the test chamber (K)		
u	Uncertainty		
V_{accum}	The accumulation volume (m ³)		
$V_{FreeVolume}$	The free volume inside the test Chamber (m ³)		
$V_{component}$	The volume of the MAC system or a component (m ³)		
R	Gas constant (= 8.314x10 ³ kJ kmol ⁻¹ K ⁻¹)		
t	Time(s)		
$P_{upstream}$	Upstream pressure (Pa)		
$P_{downstream}$	Downstream pressure (Pa)		

1 INTRODUCTION

The development of a test bench for leak flow rate tests at the CEP-Paris has begun early in 1995. New generation test benches have been built using an infrared spectrophotometer or an infrared photo-acoustic spectroscope. The method of the concentration measurement in an accumulation volume allows calculating the leak flow rate of a Mobile Air Conditioning (MAC) system at a given temperature [Clodic and Zoughaib, 2004]. Moreover, a procedure for recovery operation on vehicle has been established in order to reach an accuracy of +0 / -1 g.

2 LEAK FLOW RATE TEST OF MAC SYSTEMS – LABORATORY METHOD

2.1 Test method based on measurement of concentration evolution in an accumulation volume

The method used to determine the leak flow rate (LFR) [Blanc, Henry and Leclerc, 1981; Clodic, 1996.] is based on Equation (1).

$$\dot{m}_{\text{HFC-134a}} = M_{\text{HFC-134a}} \cdot \frac{\partial n_{\text{HFC-134a}}}{\partial t} \quad (1)$$

Where,

$$n_{\text{HFC-134a}} = n_{\text{total}} \cdot C = \frac{P_{\text{amb}} \cdot V_{\text{accum}}}{R \cdot T_{\text{amb}}} \cdot C \quad (2)$$

The mass flow rate is the product of molar mass and the derivative of the number of moles of HFC-134a along the time in a tight volume, the test chamber. The perfect gas law is used to take into account the small variations of pressure and temperature inside the test chamber. According to Equation (2), the following parameters need to be determined for leak flow rate calculation: the accumulation volume of the test chamber V_{accum} , the temperature T_{amb} and the pressure P_{amb} inside the test chamber, the evolution of concentration along the time.

2.2 Test apparatus and measurement system

Two types of concentration measurement analyzer are introduced here.

1) *The infrared spectrophotometry method* uses characteristics of individual gas absorbing specific infrared wavelength when infrared light is radiated to the sample gases. An infrared source reaches a sample cell via a chopper wheel. The sample cell in shape of a tube is divided by a wall into sample and reference sides, where two

equal-energy infrared beams pass through. The pressure effect produced in the receiver is received by a diaphragm capacitor and converted into an electrical signal, which is translated to the concentration.

2) *The infrared photoacoustic method* is based on the conversion of light energy into sound energy. The light source, modulated with a mechanical chopper, passes through an optical filter before entering the photo-acoustic gas cell. Infrared radiation is absorbed by the gas and generates heat and pressure variations in the closed cell, where a pair of microphones are mounted in the wall to measure the acoustic signal. The electrical signals from the microphones are amplified and converted to the concentration of the gas present in the cell.

Infrared spectro-photometry can measure HFC-134a concentration of 0.5 ppm. Infra-red photo-acoustics has a detection limit of 15 ppb [Morgado, Legras and Clodic, 2007]. The typical measurement scale of those apparatuses varies from 0 to 50 ppm. According to the measurement principles of analyzers, spectrophotometry is especially suitable for the continuous scan mode and photo-acoustic spectroscopy is capable of operating in step scan and a nearly continuous mode, which means that each step of scan is performed one after the other. Either one of those apparatus is integrated in a measurement system designed to use the concentration raise of a tracer gas (here HFC-134a) in a tight volume to measure the leak flow rate (LFR) of any component of refrigeration systems as well as system themselves.

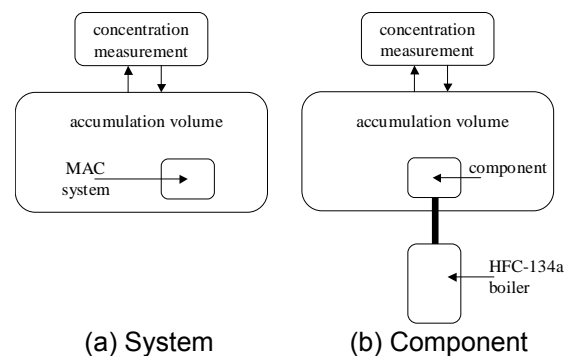


Fig. 1. Scheme of the measurement system.

As shown in Fig. 1, the test bench is composed of an accumulation volume V_{accum} at atmospheric pressure where the component to be analyzed is installed and connected to a HFC-134a boiler generating a given level of pressure inside the component (see Figure 1(b)). In the case of system measurement (see Figure 1(a)), the operation becomes simpler because the refrigerant is directly charged in the MAC system. The temperature of the component is controlled

by heat resistance and fans, in order to be maintained always above the saturated temperature of HFC-134a at the test pressure. The concentration analyzer is connected to the accumulation volume by a closed circuit and measures continuously the accumulated concentration of HFC-134a inside the volume. Knowing:

- the volume of the accumulation volume,
 - the time,
 - the concentration at each time step,
- and using Equation (1), the leak flow rate of a component can be calculated.

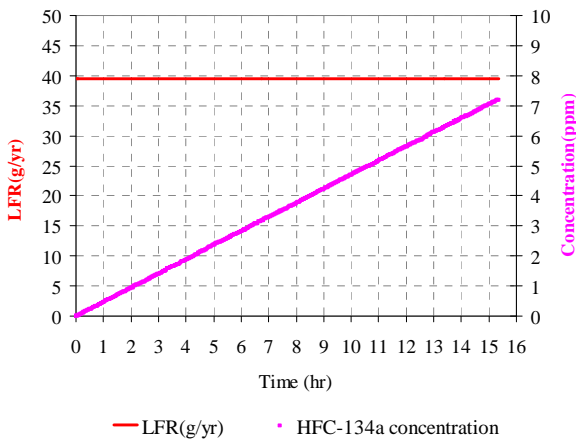


Fig. 2. Concentration measurement and LFR.

Fig. 2 shows an example of concentration measurement along the time (the pink line) and the calculated leak flow rate (the red line). As it can be seen for a constant slope of the concentration rate, the mass leak flow rate is proportional to the slope according to Equation (2). Moreover, the accuracy of a constant leak flow rate measurement can be improved by a larger sample size, which means a longer measurement time in our case. This will be mentioned in Section 2.4.

2.3 Test protocol

The test protocol is described step by step in Fig. 3.

Step 1: Standardization of the concentration measurement apparatus

The first step is to verify the concentration measurement apparatus. As shown in Fig. 4, a standardized concentration of HFC-134a in nitrogen (delivered by accredited companies) is connected to the measurement apparatus, and the measured value is compared to the standardized concentration. This verification is repeated with a second higher concentration

These two measurements verify both the offset and the linearity of the measurements of concentration by the apparatus.

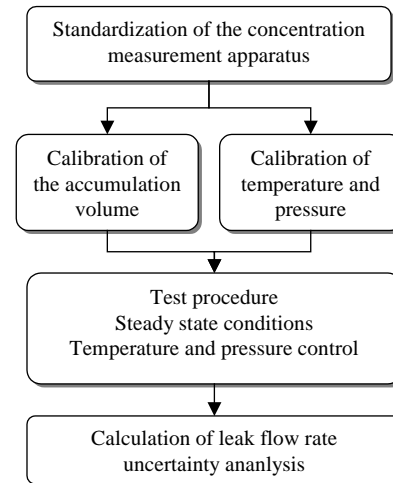


Fig. 3. Flowchart of test protocol.



Fig. 4. Standardized gas of HFC-134a/N₂.



Fig. 5. HFC-134a calibrated leak.

Step 2-1: Calibration of the test chamber

The uncertainty of the LFR is directly related to the uncertainties on the free volume of the test chamber. First the volume is calculated based on the geometric descriptions. Then a standard calibrated leak (see Fig. 5), which has been calibrated on a specific test chamber, is installed inside the test chamber to be calibrated.

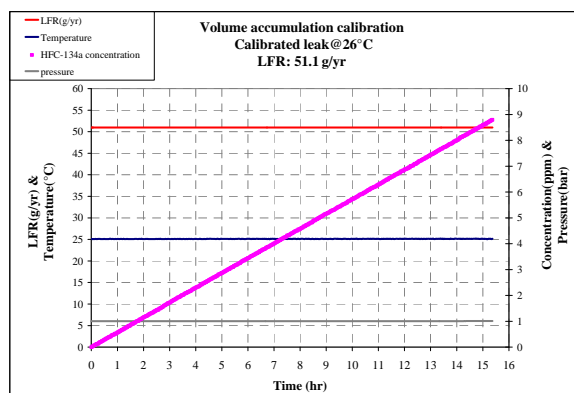


Fig. 6. Volume calibration data.

Fig. 6 gives an example of calibration of the volume accumulation. The calibrated leak is measured at constant temperature of 26°C. As

indicated in the figure, all parameters such as temperature, pressure and concentration inside the test chamber are recorded at each time step. The leak flow rate of calibrated leak at 26°C is known as 51.1 g/yr. The accumulation volume can be obtained by reverse calculation of the mass flow rate, which is expressed by Equation (3) and consequently its uncertainty is established, which will be discussed in the following section.

$$V_{accum} = \frac{\dot{m}_{HFC-134a}}{\frac{M_{HFC-134a} P_{amb}}{RT_{amb}} \frac{\partial C}{\partial t}} \quad (3)$$

Step 2-2: Calibration of temperature and pressure sensors

As shown in Equation (2), both temperature and pressure values inside the test chamber contribute to LFR value. Before installation in the test bench, temperature and pressure sensors are carefully calibrated. The accuracy of both sensors is established through their calibration, which will be discussed later in the paper.

Step 3: Testing procedure

After installation of the test sample, the test chamber is closed and then rinsed by a reference gas (reconstructed air: 80% N₂ + 20% O₂) in order to exclude all possible suspicious particles and guarantee the accuracy of measurement. The pressure is kept at atmospheric pressure. The temperature is maintained constant as well as during the test period. At each time interval, concentration, temperature, and pressure are recorded by the data acquisition system.

Step 4: Calculation of leak flow rate

Based on Equations (1) and (2) the leak flow rate is calculated and measurement uncertainty is established. Estimation on the uncertainty of leak flow rate test plays an important role, which indicates the reliability of a measurement, so that we will focus on the uncertainty analysis.

2.4 Uncertainty analysis

The uncertainty due to the repeatability can be estimated from experimental results. As illustrated in Fig. 7, a series of temperature values are recorded during the test, which gives a mean temperature value of 313.94 K and a standard deviation of 0.034 K. This value can be used directly as an uncertainty of type A.

Based on the principle of indirect measurements from the propagation of distributions, the uncertainty of leak flow rate is achievable [Guide to the Expression of Uncertainty in Measurement, 1993].

Since the temperature and pressure are maintained constant during the test, the leak flow rate of the component under test can be calculated according to Equations (1) and (2). The uncertainties associated which each parameter are combined in Equation (4). All these uncertainty sources and their influences will be analyzed based on the experimental data (presented in Fig. 2):

$$\frac{u_{\dot{m}}}{\dot{m}_{HFC-134a}} = \sqrt{\left(\frac{u_{V_{accum}}}{V_{accum}}\right)^2 + \left(\frac{u_{T_{amb}}}{T_{amb}}\right)^2 + \left(\frac{u_{P_{amb}}}{P_{amb}}\right)^2 + \left(\frac{u_{\partial C / \partial t}}{\partial C / \partial t}\right)^2} \quad (4)$$

Generally, there are two types of contributors to measurement uncertainty.

Type A: this type of uncertainty can be determined statistically by measuring the dispersion of values obtained from well-chosen standards of samples. The uncertainty of type A is quantified by calculating the standard deviation from repeated measurements.

Type B: this type of uncertainty must be determined by non-statistical methods. Type B contributors will be the uncertainty of the reference standards and reference materials, which can never be picked up statistically.

1) Temperature inside the test chamber

According to manufacturer's specifications, the tolerance for a temperature sensor Pt100 of class A is written as: $\Delta T = 0.15 + 0.002 \times |T|$, where T is the measured temperature in °C. The estimated uncertainty of type B can be calculated using the assumption of a rectangular distribution for the temperature variation.

$$u_{T(\text{typeB})} = \frac{\Delta T}{\sqrt{3}} \quad (5)$$

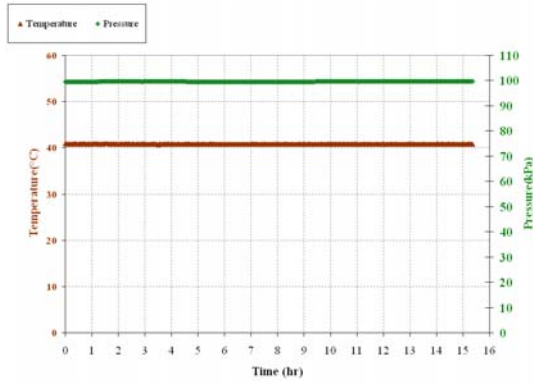


Fig. 7. Temperature and pressure variation vs. time.

Therefore, the uncertainty of the temperature u_T can be determined by combining the uncertainties of type A and type B:

$$u_T = \sqrt{u_{T(\text{typeA})}^2 + u_{T(\text{typeB})}^2} = \sqrt{\frac{\sum_{i=1}^n (T_i - \bar{T})^2}{n-1} + \left(\frac{\Delta T}{\sqrt{3}}\right)^2} \quad (6)$$

2) Pressure inside the test chamber

Depending on the same principle, the uncertainty of the ambient pressure value is measured by using a pressure sensor of 0-200 kPa abs, which has an accuracy of 0.2% of full scale. The estimated uncertainty of type B can be calculated:

$$u_{P(\text{typeB})} = \frac{0.2\% \times 2 \cdot 10^5 \text{ Pa}}{\sqrt{3}} = \frac{400 \text{ Pa}}{\sqrt{3}} \quad (7)$$

The type A uncertainty is obtained based on the data given by Fig 7. The uncertainty coming from the pressure is expressed by Equation (8).

$$u_P = \sqrt{u_{P(\text{typeA})}^2 + u_{P(\text{typeB})}^2} = \sqrt{\frac{\sum_{i=1}^n (P_i - \bar{P})^2}{n-1} + \left(\frac{400}{\sqrt{3}}\right)^2} \quad (8)$$

3) The accumulation volume

The accumulation volume consists of two parts: the free volume of the test chamber before installation of a MAC system or a component and the volume of the system/component, calculated by Equation (9).

$$V_{\text{accum}} = V_{\text{FreeVolume}} - V_{\text{component}} \quad (9)$$

The free volume of the test chamber ($V_{\text{FreeVolume}}$) is determined by using a calibrated

leak (Fig. 5). The calibrated leak has been installed inside the test chamber and measured at constant temperature of 26°C, at which temperature the leak flow rate is already known. The obtained leak flow rate value helps to calculate the free volume. This calibration step leads to an uncertainty of about 6%. Moreover, the volume of the system/component can only be obtained by geometrical measurement of all components, some of which contain many complex parts. As a result, its uncertainty rises up to 20%. Nevertheless, the uncertainty of this part is negligible comparing to the huge free volume inside the test chamber. As demonstrated in Equation (10), the relative combined standard uncertainty ($u_{V_{\text{accum}}}$) is 6%.

$$\frac{u_{V_{\text{accum}}}}{V_{\text{accum}}} = \frac{\sqrt{u_{V_{\text{FreeVolume}}}^2 + u_{V_{\text{component}}}^2}}{V_{\text{accum}}} = 0.06 \quad (10)$$

4) Concentration vs. time $\frac{\partial C}{\partial t}$

As illustrated in Fig. 2, the concentration evolution according to time is recorded at each interval time. The slope of the curve is obtained by the method of the least squares, which ensures that the value fits the sample data best, in the sense of minimizing the sum of the squared residuals. Consequently, the standard deviation is obtained.

The relationship between concentration and the time is of the form: $\hat{C}_i = \hat{a} + \hat{b}t_i$, where $b = \partial C / \partial t$ is the slope of the line. Without taking errors in time axis into account, the standard deviation of the slope ($\partial C / \partial t$) is explained by Equation (11).

$$s_{\partial C / \partial t} = \sqrt{\frac{\sum (C_i - \hat{C}_i)^2 / (n-2)}{\sum (t_i - \bar{t})^2}} \quad (11)$$

where,

n is the number of the samples

t_i is the time of the measurement

\bar{t} is the mean of all t_i

$\sum (C_i - \hat{C}_i)^2$ is the sum of squared residuals.

All the values of the uncertainty parameters of a given example are summarized in Table 1, so that the leak flow rate is 39.5g/yr with a relative uncertainty of 6%.

Table 1. Uncertainty budget for a given example.

Parameter	Mean Value x_i	Standard uncertainty u_{xi}	Relative standard uncertainty u_{xi} / x_i
V_{accum} (m ³)	2.443	0.147	0.06
T_{amb} (K)	313.79	0.14	0.00045
P_{amb} (Pa)	99731	368	0.0037
$\frac{\partial C}{\partial t}$ (ppm)	1.3×10^{-4}	2.3×10^{-8}	0.00018

Taking into consideration all parameters, the uncertainty coming from the accumulation volume is obviously the major source. Others contribute to less than 1%.

It should be pointed out that the uncertainty associated to concentration evolution depends on the sample size. Longer test duration leads to more concentration samples, which reduces the standard uncertainty. Fig. 8 illustrates the relative uncertainty of leak flow rate taking into account the test duration. When the leak flow rate varies from 5 to 30 g/yr, the uncertainty of leak flow rate of MAC system is controlled below 7% after 2 hours test.

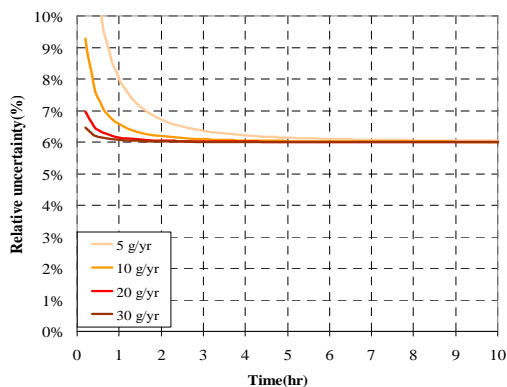


Fig. 8. Relative uncertainty of LFRs vs. time.

For component tests, the test chambers are smaller than that of the system, so that the relative uncertainty is smaller than that of system tests and can be managed in the range of 5%.

3 TESTS OF MOBILE AIR CONDITIONING SYSTEMS AND COMPONENTS

3.1 Preconditioning before measurements

Preconditioning step is necessary for all MAC components having polymer materials in order to reach a steady state permeation rate through these polymer materials. As

presented in Fig. 9, a MAC system is mounted on supports and then fixed on a duckboard. After applying the tightening torques to all fittings, the MAC system is evacuated and then charged with its nominal HFC-134a charge. Preconditioning can now be started.



Fig. 9. MAC system installed on a duckboard for LFR test.

Figure 10 gives an example of concentration measurements during the preconditioning phase of a MAC system at 50°C. The concentration evolution is recorded from the beginning. It can be seen that the curve comes to be straight after 6 days measurement. That means this system needs to be preconditioned during at least 6 days at 50°C before reaching the steady state. The emission behavior during the transient phase is very similar to the permeation curve of polymer materials that can be found in published data [Kimura and Hirose, 1992; Flaconnèche, Martin and Kolpffer, 2001]. Based on experimental data, 50°C during 10 days is an appropriate and sufficient condition for a MAC system reaching the steady state emission rate.

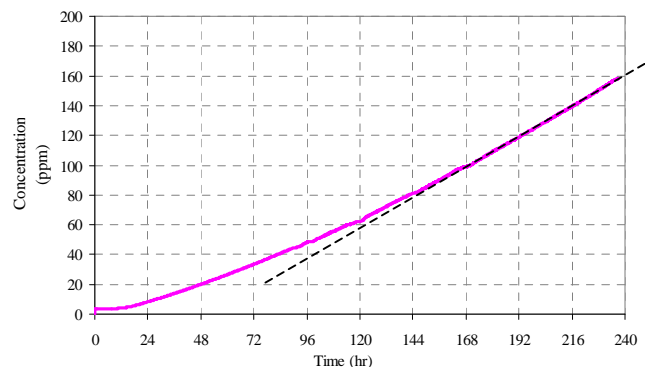


Fig. 10. Concentration measurement during preconditioning phase.

3.2 Description of the system test bench

Figure 11 presents the test bench for leak flow rate tests of Mobile Air Conditioning system.



Fig. 11. Test chamber used for LFR tests of MAC system.

Once installed inside the test chamber, the MAC system is heated and maintained at the required temperature by an electric heat resistance associated a powerful fan (1500 m³/hr) to reach homogenous temperature as well as homogenous concentration inside the test chamber. The constant temperature inside the accumulation volume allows controlling the corresponding saturation pressure. In order to limit the control volume, leak tight cylinders are installed inside allowing accelerating the raise of concentration and so limiting the measurement duration for a given accuracy.

3.3 Measurements of 10 MAC systems in standstill mode

Measurements of 10 types of MAC systems have been accomplished at three different temperatures. Results are summarized in Table 2.

Table 2. LFRs of MAC system a-j.

LFRs of system a to j (g/yr)				
system	Temperature(°C)	30°C	40°C	50°C
	Saturation Pressure(kPa)	770	1017	1318
a		11	29	41
b		17	35	57
c		14	27	43
d		20	36	54
e		21	35	58
f		15	27	39
g		8	15	28
h		20	34	50
i		10	20	31
j		12	25	45
Average LFR(g/yr)		15	28	45

3.4 Description of the component test bench

Fig. 12 presents the layout of the test bench for leak flow rate measurement of components. The test method for components is identical to the method of test for systems installed in test chamber, except that for the system tests the refrigerant charge is inside the MAC system, and for component tests, a refrigerant boiler is

mounted outside the accumulation cell. This pressurization circuit is outside the accumulation volume and is separately controlled by a heat resistance to define the required pressure. Heat resistance and fans are installed inside the measurement cell to set the component under required temperature condition. Once the steady state is reached, measurement using the gas analyzer is performed.

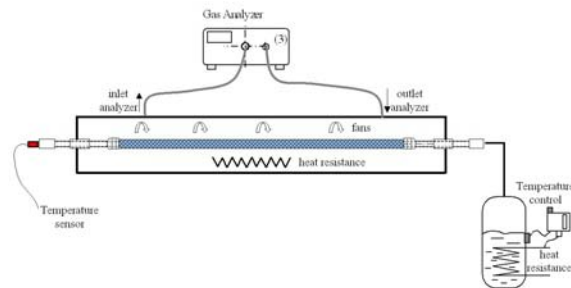
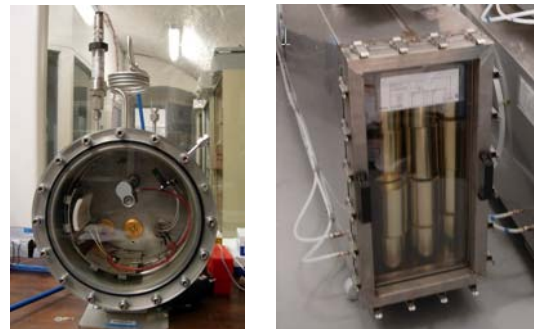


Fig. 12. Layout of component measurement test bench.

Fig. 13 presents different measurement cells designed for different types of components, such as fittings, hoses, and macro-components like condenser, evaporator, etc.



Cell for fittings.

Cell for macro-components.



Cell for hoses

Fig. 13 Test bench for component leakage measurement.

3.5 Measurements of MAC components

Once MAC systems have been tested, each one has been cut into parts and macro-components have been measured. Depending on the complexity of the system, the number of components may vary from 6 to 20. As shown in Fig. 14, the system has been separated into:

compressor, condenser, evaporator, Thermo expansion valve (TXV), liquid lines 1 and 2, suction line, discharge line, liquid receiver, inlet and outlet compressor fittings, inlet and outlet condenser fittings, making 13 components. Each macro-component has been tested at 3 different temperatures: 30, 40, and 50°C. Leak flow rates of all macro-components have been summed with the purpose of being compared to the leak flow rate of the system.



Fig. 14. MAC system cut into parts making macro-components.



Fig. 15. Welded end and connecting tube going through the wall of the cell.

Once one component has been cut, a complementary preparation is necessary: as illustrated in Fig. 15, one end of the component is closed by welding and the other end is equipped with a special tube for going through the wall of the accumulation cell. After preparation, all components have been tested in corresponding cells shown in Fig. 13. Table 3 shows the leak flow rates of each component at 3 different temperatures. The sum of all parts leads to 20.7 g/yr at 30°C, 36.7 g/yr at 40°C and 56.5 g/yr at 50°C, which are very close to the leakage values of system: 17, 35, and 57g/yr.

Table 3 summarizes in detail the mean leak flow rates of 10 systems, both in terms of system and macro-components level. Results illustrate that the sum of the emissions of components equals the emission of these systems. That means tests either at the

system level or the component level are appropriate to measure the leak flow rate of a given MAC system.

Table 3. LFRs of MAC components of MAC system B.

Reference	Component list	LFR(g/yr)		
		50°C 1318 kPa	40°C 1017 kPa	30°C 770 kPa
1	compressor without fittings	19.5	16.0	8.0
2	discharge line	13.4	7.5	4.63
3	condenser	1.3	0.7	0.3
4	liquid branch 1	2.5	2.0	1.0
5	liquid receiver + fittings	1.55	0.62	0.28
6	liquid line 2	1.5	0.6	0.3
7	TXV	4.52	2.52	1.5
8	evaporator	3.9	3.3	2.6
9	suction line	7.2	2.9	1.8
10	BP compressor fitting	0.3	0.15	0.08
11	HP compressor fitting	0.3	0.14	0.1
12	inlet condenser fitting	0.25	0.15	0.1
13	outlet condenser fitting	0.24	0.12	0.05
Component tests	Sum of LFRs	56.46	36.7	20.74
System tests results		57	35	17

3.6 Leakage behavior based on regression curve

Seals made from polymer materials are used in the MAC system to connect different elements and prevent the refrigerant loss from inside the MAC system. Hoses are commonly used to prevent the propagation of vibrations from one part to any other ones. Therefore two types of leakage sources are distinguished here [Muller and Nau., 1998]:

a) *Leakage due to the escape of refrigerant between sealing parts.* The contact area between the seal and the rigid parts of fittings is never perfect. It always exist micro-passages for gas to pass through [Daniel and Hertz, 1979]. According to the Poiseuilles' law, the mass flow rate due to the viscous flow between sealing parts is approximately proportional to the differences of the squares of the upstream and downstream pressures..

b) *Leakage due to gas permeation through polymer materials is the other contributor of leak flow rate.* The phenomena of gas diffusion through polymer is also related to the pressure [Crank, 1975; Magg, 1990; Moore, Damle, Willams and Koros, 2004].

Fig. 16 illustrates the evolution of leak flow rate as a function of pressure. Using the method of least squares, a good agreement between the measured values and the regression curve of binomial expression has been verified and is expressed by Equation (12).

$$LFR = k(P_{upstream}^2 - P_{downstream}^2) \quad (12)$$

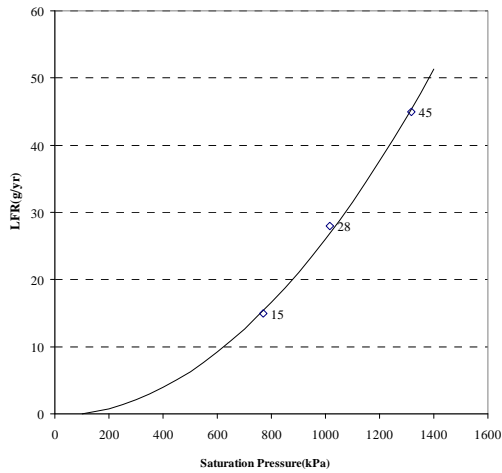


Fig. 16. LFRs experimental data and its regression curve.

The objective of this approximation is to find a general approach for MAC system leakage behavior as a function of pressure, which will be useful in the flowing section for establishing the correlation factor.

Table 4. LFRs and linear regressions.

Temperature (°C)	Mean LFRs of 10 MAC systems			Linear Regression	
	30°C	40°C	50°C	k	R^2
Sum of macro-components	15.6	27.4	44.5	2.61E-11	0.998
System level	15	28	45	2.63E-11	0.997

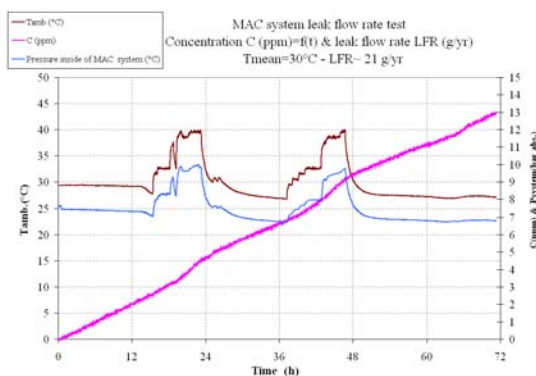


Fig. 17. Test by simulating real climatic condition.

Based on the data given in Table 4, regression models have been made for systems and components. Related parameters are summarized in Table 4. The constants k are respectively 2.63×10^{-11} and 2.61×10^{-11} . The parameter R^2 , the coefficient of determination,

gives a statistical measure of how well the regression line approximates the real data points. As shown in Table 4, R^2 in both cases being very close to 1 indicates that the regression model fits correctly the data.

Fig. 17 shows regression curves at system levels and sum of system components. It is obvious that both curves are very close to each other. In a word, the tests carried out at the system level or the component level lead to the same leak flow rate. Both can be used to determine the leakage value of a given MAC system.

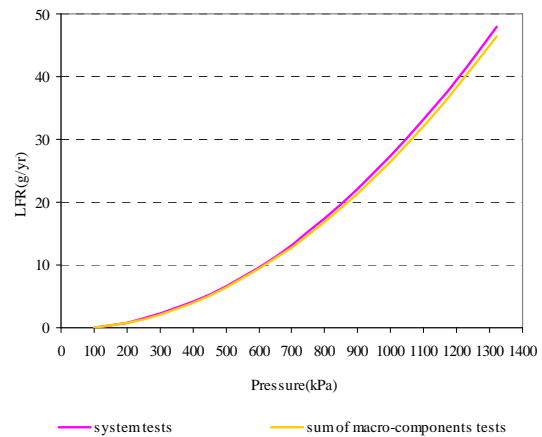


Fig. 17. Regression curves for systems and sum of macro-components.

4 CORRELATION FACTOR BASED ON LEAKAGE BEHAVIOR

4.1 Standstill mode tests taking into consideration the climate conditions

In real life conditions, the temperature is never constant and varies with time. A test on a MAC system in standstill mode has been performed by simulating the real daily climatic conditions with the purpose of comparing the result to that of average constant temperature tests.

Simulation has been carried out on MAC system X according to the temperature variation of Seville city, that means the temperature inside the test chamber has been controlled to reproduce the temperature variation along the time.

As illustrated in Fig. 17, test being performed for 72 hours leads to an average temperature of 30°C. The brown curve represents the temperature variation inside the test chamber and the blue one shows that of the pressure inside the MAC system, which changes

immediately with temperature. The pink curve presents the accumulated HFC-134a concentration inside the test chamber along time. The total quantity of HFC-134a (0.17 gram) permits evaluating the annual HFC-134a emission: 20.7 g/yr. The same system has also been tested at constant temperatures of 30, 40, and 50°C and results are summarized in Table 5. 21 g/yr is very close to 20.7 g/yr.

Table 5. LFRs of MAC system X at 3 different temperatures.

Temperature (°C)	Saturation pressure (kPa)	Leak flow rate (g/yr)
30	770	21
40	1017	36
50	1318	58

It means that in spite of the temperature variation, the leak flow rate corresponding to the yearly average temperature can be used to predict the real life annual emissions of the MAC system.

Based on the assumption made in Section 3.6, the leakage behavior of a MAC system can be described by Equation (12). Fig. 18 presents the regression curve of leak flow rate of system X as a function of the pressure. The constant $k = 3.42E-11$, allows finding out the leak flow rate at any temperature. For example, yearly temperature in Paris is 11°C corresponding to saturation pressure of 429 kPa. Using the constant k , the leak flow rate corresponding to this pressure is 5.9 g/yr. In the city of Rome, where the yearly average temperature is 15.4°C, a leak flow rate value of 8.0 g/yr is found at saturation pressure of 495 kPa.

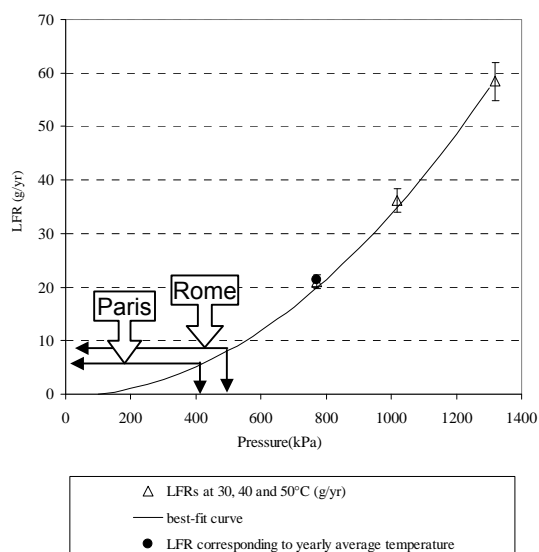


Fig. 18. LFR of MAC system vs. saturation pressure.

To conclude, knowing the mean annual temperature of a city, one can predict the leak flow rate in standstill mode by testing the MAC system at constant temperature.

4.2 Analysis of running mode contribution

In order to measure the contribution of the running mode emission, several analyses have been performed. Taking into account the current average mileage of vehicles in the European Union, the running time of the vehicle is comprised between 250 and 450 hrs/yr, representing 3 to 5% of the annual time. Moreover, the MAC system operates only a limited part of this running time, so the annual use of MAC systems ranges typically from 80 to 250 hours.

A specific test bench has been built to measure the leak flow rate in both standstill mode and in running mode of MAC system. As shown in Fig. 19, a fan and a hopper are installed in front of the evaporator. The condenser is also installed in front of blowers, and a water heat exchanger is installed within the test chamber in order to extract heat by a water-cooling circuit and so maintain the temperature within the test chamber at the set value. The compressor is driven by a direct-current variable speed electrical motor to vary the speed with respect to time. The design of this test bench, enables to measure precisely the annual emission of MAC system in running mode.



Fig. 19. Test bench for leak flow rate test in running mode of MAC system.

The NEDC (New European Driving Cycle) is supposed to represent the typical usage of a car in Europe, and is commonly used to assess the emission levels of car engines. For this reason, the NEDC has been produced for running mode tests.

Table 6. LFRs of 3 MAC systems (V1, V2, and V3).

MAC system	Standstill mode		Running mode		LFR (g/yr)	Contribution of running mode	Standstill mode Total LFR
	LFR (g/yr)	Duration (h)	Duration (h)	Emission (g)			
V1	8.8	8529	231	0.52	9.1	5.7%	8.8/9.1=0.97
V2	7.7	8524	236	0.54	8.0	6.7%	7.7/8.0=0.96
V3	5.2	8543	217	0.25	5.3	4.7%	5.2/5.3=0.98

As shown in Table 6, three MAC systems have been tested both in standstill mode and in running mode. The MAC system V1 kept running during 231 hours, the mass of HFC-134a accumulated in the test chamber is 0.52 gram. That means 0.52 gram has been lost after 231 hours running period. Test in standstill mode of this system gives 8.8 g/yr, which is then translated into $365 \cdot 24 \cdot 231 = 8529$ hours. Therefore the leakage due to the standstill mode is 8.57 g/yr. The total leak flow rate rises up to 9.1g/yr.

Two other MAC systems have also been tested under the same protocol. Converting the emissions in running mode into annual leak flow rate, one gets respectively 19.7, 20.0, and 10.1 g/yr. To conclude, although running mode shows a leakage value twice higher than that of standstill mode, its contribution remains low (about 5-6%) due to the short operation period. When predicting the total leak flow rate of a MAC system, taking into consideration the running mode, one can use the convention ratio between standstill mode and total leak flow rate. As detailed in Table 6, the factor varies from 0.96 to 0.98. Considering the worse case, 0.96 can be used to calculate the running part contribution.

4.3 Fleet tests on vehicles

40 vehicles of 10 different types of MAC systems, which represent nearly all European types of passenger vehicles, have been chosen to perform fleet tests.

Recovery operation has been carried out with a precise procedure with a high recovery accuracy, which means an uncertainty of ± 0.1 g on initial refrigeration charge and on refrigerant recovery made nine months later, with less than 1g not recovered [D. Clodic, Y. Yu, 2007].



Fig. 20. Refrigerant Recovery equipment.

As shown in Fig. 20 the recovery equipment consists of the following parts:

- an oilless compressor
- a recovery cylinder of 5-liter volume;

- a balance of precision in the scale of ± 0.1 gr;
- a pair of suction and discharge hoses equipped with ball valves at their ends.

Table 7. Average annual losses for 10 types of vehicles.

Vehicle	Annual loss (g/yr)
J	7.2
B	7.6
G	7.6
I	7.8
A	8.1
F	9.4
D	12.1
E	14.8
C	15.0
H	21.6
Average value	10.0

As shown in Table 7 and Fig. 21, the annual leak flow rates of different MAC systems vary from 7.2 to 21.6 g/yr. It is necessary to point out that vehicles C and H are double-evaporator systems. The mean leak flow rate of all 37 vehicles makes 10.0 g/yr.

Note: 3 vehicles out of the 40 were not available for final recovery.

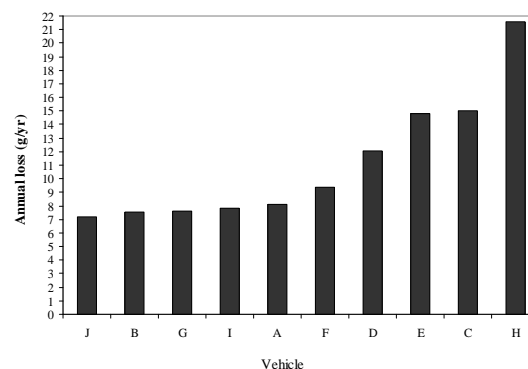


Fig. 21. Results of fleet tests.

4.4 Establishing the correlation factor

These 10 types of MAC systems have also been tested in laboratory (4 samples for each type) at three different temperatures. Results are summarized in Table 8.

The regression curve is established according to the average value of 19.2, 37.6, and 68.8 g/yr. A correlation factor can be established between the results of laboratory tests and fleet tests. The regression curve is then established according to these points with $k = 3.856 \times 10^{-11}$.

Table 8. Arithmetical average LFRs of system A-J.

System	Leak flow rates (g/yr)		
	30°C	40°C	50°C
	15.8 ^{+5.2} _{-3.8}	34.7 ^{+4.3} _{-3.7}	67 ^{+9.0} _{-10.0}
B	18.2 ^{+1.8} _{-2.2}	45 ^{+2.0} _{-2.0}	82.5 ^{+3.5} _{-4.5}
C	17.2 ^{+4.8} _{-5.5}	33 ^{+2.0} _{-3.0}	60.6 ^{+6.4} _{-7.6}
D	26.5 ^{+17.5} _{-9.5}	47.5 ^{+15.5} _{-13.5}	87.2 ^{+53.8} _{-33.2}
E	33.5 ^{+2.5} _{-2.5}	58.5 ^{+3.5} _{-1.5}	118.2 ^{+6.8} _{-5.2}
F	22.7 ^{+1.3} _{-2.7}	33.5 ^{+5.5} _{-6.5}	52.7 ^{+6.3} _{-4.7}
G	11.7 ^{+3.3} _{-3.7}	26.2 ^{+5.8} _{-5.2}	49.7 ^{+21.3} _{-15.7}
H	21.0 ^{+3.0} _{-3.0}	45.0 ^{+12.0} _{-8.0}	80.2 ^{+14.8} _{-10.2}
I	12.1 ^{+1.9} _{-1.1}	24.7 ^{+3.3} _{-2.7}	41.5 ^{+5.5} _{-3.5}
J	12.5 ^{+2.5} _{-1.5}	26.2 ^{+0.8} _{-1.2}	46.2 ^{+7.7} _{-7.2}
Average value	19.2 ^{+24.8} _{-11.2}	37.6 ^{+25.4} _{-16.6}	68.8 ^{+72.2} _{-34.8}

Taking into account the hour-by-hour temperature in different European climatic zones where the 40 vehicles have run, the annual average temperature is 15.5°C. Finding out the point, which corresponds to this temperature: 9.1 g/yr at 496 kPa (see Fig. 22). Supposing there is additionally 5-6% coming from running mode of MAC system, the total leak flow rate makes $9.1/0.96 = 9.5\text{g/yr}$. This acceptable difference between laboratory tests and fleet tests (10.0 g/yr) proves the possibility to predict the leak flow rate of a MAC system only by laboratory tests at constant temperatures.

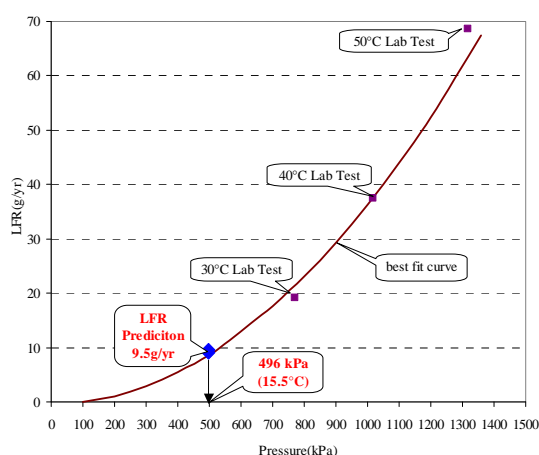


Fig. 22. Establishing the correlation factor

In brief, the procedure for leak flow rate prediction consists of three steps:

(1) Tests at 3 different temperatures to establish the leakage behavior of a given MAC system;

(2) Finding out the leak flow rate value on the regression curve, which corresponds to the average annual temperature of a city;

(3) Real life leak flow rate calculation taking into account the running mode.

Table 9 gives some examples for annual leak flow rate predictions. Firstly, tests at 3 temperatures allows calculating the regression curve using the least square method. For system n°1, the constant k is 3.79×10^{-11} . Using Equation (12), the leak flow rate at constant temperature of 15.5°C is 9.0 g/yr. As a result, the predictive annual leak flow rate of system n°1 is 9.4 g/yr. Annual leak flow rates for two other systems are obtained likewise, which lead to 7.7 and 15.5 g/yr.

Table 9 Annual LFR predictions of 3 MAC systems based on the method of correlation factor.

T(°C)	P(kPa)	Leak flow rate (g/yr)		
		System n°1	System n°2	System n°3
30	770	21.1	19.9	36.4
40	1017	40.0	33.3	64.2
50	1318	65.3	52.8	109.4
(1) Constant k		3.80×10^{-11}	3.13×10^{-11}	6.31×10^{-11}
(2) LFR @ 15.5°C		9.0	7.4	14.9
(3) Annual LFR prediction (g/yr)		9.4	7.7	15.5

5 CONCLUSION

This paper introduces a laboratory test method to determine the leak flow rate of MAC systems ensuring good measurement accuracy. The qualified test method fits well the EU regulation 706/2007. Results on either an overall system or the sum of all system components are equal under the uncertainty level, so that both methods are proved suitable for determining the leak flow rate of a MAC system. Knowing the running mode contribution, which is about 5-6% of total emission, the major part of the refrigerant is emitted during the period where the vehicle is standstill, so that the leak flow rate of the MAC system can be determined without performing running mode tests. Once the leakage behavior of a MAC system is determined, the mean annual temperature of a city is sufficient

for leakage prediction based on the proposed correlation factor method.

REFERENCES

- Blanc, B., Henry, R.P., and Leclerc, J., 1981. Guide de l'étanchéité. Vol. 2, Les Fuites—Aspects théoriques, calculs pratiques. Société Française du Vide, pp. 33-51.
- Clodic, D., Zoughaïb, A., 2004. Measurement of leak flow rates of MAC components by infrared spectrophotometry, and calculations of annual leak flow rates. VDA Alternate Refrigerant Wintermeeting, Saalfelden, Austria, 18 - 19 February.
- Clodic, D., 1996. Zero leaks - Limiting emissions of Refrigerants. Ashrae. 189 p.
- Clodic, D., Yu, Y., 2007. Elaboration of a correlation factor based on fleet tests and Mobile Air Conditioning(MAC) system laboratory tests. SAE technical paper 2007-01-1187.
- Crank, J., 1975. The mathematics of diffusion. Clarendon Press, Oxford, 432 p.
- Daniel, L., Hertz, JR., 1979. O-rings for low-pressure service. Machine Design.
- Flaconnèche, B., Martin, J., Kolpffer, MH., 2001. Transport properties of gases in polymers: experimental methods. Oil and Gas Science and Technology, Vol. 56, pp. 245-259.
- Guide to the Expression of Uncertainty in Measurement. ISO, Geneva, Switzerland, 1993.
- Kimura, S., Hirose, T., 1992. Polymers for Gas Separation. Wiley, 245 p.
- Magg, H., 1990. Elastomers for automotive air-conditioning hoses. SAE technical paper 900575.
- Moore, T.T., Damle, S., Willams, P.J., Koros, W.J., 2004. Characterization of low permeability gas separation membranes and barrier materials; design and operation considerations. Journal of Membrane Science, Vol. 245, pp. 227-231.
- Morgado, I., Legras, J-C., Clodic, D., 2007. Primary standard for measuring refrigerant leak flow rate. Congrès de métrologie. Lille, France, 18-21 juin.
- Müller, H.K., and Nau, B.S., 1998. Fluid sealing technology. Hardcover. pp.2-16.



ED n° 432 : « Sciences des Métiers de l'Ingénieur »

T H E S E

pour obtenir le grade de
Docteur de l'Ecole des Mines de Paris
Spécialité "Energétique"

présentée et soutenue publiquement par
Yingzhong YU
le 23 octobre 2008

**GENERIC APPROACH OF REFRIGERANT HFC-134a EMISSION
MODES FROM MOBILE AIR CONDITIONING (MAC) SYSTEMS
APPROCHE GENERIQUE DES MODES D'EMISSIONS DE HFC-134a
DE SYSTEMES DE CLIMATISATION AUTOMOBILE**

RESUME en FRANCAIS

Introduction

Le CFC-12, utilisé dans les systèmes de climatisation mobile a été remplacé par le HFC-134a à partir de 1991 et, depuis 1994, presque tous les nouveaux véhicules vendus dans les pays développés utilisent le HFC-134a.

Les paramètres physiques à la base des fuites de fluide frigorigène dans les systèmes de climatisation automobile ne sont pas encore pleinement compris. Le but de ce travail de recherche est d'établir une méthode de mesures des débits de fuite de fluide frigorigène des systèmes de climatisation automobile ainsi que des composants de ces systèmes, et aussi de développer une approche générique de prévision de ces émissions.

Dans le cadre du projet de recherche réalisé par ARMINES pour ACEA dont l'objectif était de définir les bases pour établir la réglementation européenne 706/2007, un grand nombre de mesures de débits de fuite ont été effectuées et fournissent des données expérimentales solides pour cette thèse. Les projets de recherche avec l'ADEME ont apporté un soutien complémentaire pour l'analyse des émissions de ces systèmes en fonctionnement. Concernant la caractérisation de polymères de tuyaux et de joints toriques utilisés, les travaux ont été réalisés en coopération avec HUTCHINSON. Les nombreux essais et les simulations effectués au cours de cette thèse ont permis d'élaborer un modèle pour la prévision des émissions de fluide frigorigène des systèmes de climatisation et de leurs composants.

Le chapitre 1 présente le contexte des émissions des systèmes de climatisation automobile. Les principaux types d'émissions du système pendant le cycle de vie du véhicule sont classés. Les fuites chroniques des différents composants des systèmes de climatisation automobile sont évaluées et hiérarchisées.

Dans le chapitre 2, une méthode d'essai en laboratoire, basée sur la mesure de concentration dans un volume d'accumulation, est présentée pour déterminer les débits de fuite de systèmes et de composants. La précision de la mesure est justifiée. Des mesures en régime permanent et pour plusieurs températures contrôlées sont effectuées afin de comparer le débit de fuite de l'ensemble du système et la somme des débits de fuite de tous les composants. Les simulations de la variation de température permettent de prédire les impacts des conditions climatiques annuelles quel que soit le climat. Les essais en régime dynamique sont également traités pour analyser la contribution du temps de fonctionnement du système aux émissions annuelles du système. Afin de vérifier la méthode d'essai en laboratoire, des opérations de récupération du fluide frigorigène ont été effectuées sur une quarantaine de véhicules avec une précision de +0 / -1 g. Sur la base des résultats des essais en laboratoire et de ceux obtenus sur la flotte de véhicules, un facteur de corrélation a été établi pour corréler les tests en laboratoire aux émissions mesurées sur le terrain.

Le chapitre 3 se concentre sur les prévisions des émissions de flexibles utilisés dans les systèmes de climatisation automobile. Six polymères sont caractérisés par la détermination de leurs coefficients de transport, en particulier les coefficients de perméabilité. Des modèles

prédictifs ont été développés pour prévoir les débits de fuite de flexibles en prenant en compte les effets de température et de pression.

Le chapitre 4 traite le comportement des fuites de raccords utilisés dans les systèmes de climatisation automobile. Les joints toriques typiques sont étudiés et deux modes de fuite: la perméation à travers des matériaux polymères et l'écoulement du gaz dans les micro-canaux sont distingués. Les performances d'étanchéité d'un joint torique radial sont étudiées en utilisant la méthode des éléments finis. Le comportement non-linéaire des déformations des polymères est pris en compte. L'analyse des facteurs principaux tels que la contrainte, la pression de contact maximale et le contact est basée sur les résultats de simulation numérique. Les deux modes de fuites permettent de comprendre les phénomènes clés des émissions et donc d'améliorer les performances d'étanchéité.

CHAPITRE 1 Contexte

La flotte mondiale de véhicules équipé de systèmes de climatisation fonctionnant au CFC-12 a diminué d'environ 212 millions de véhicules en 1990 à 119 millions de véhicules en 2003, tandis que celle des véhicules dont les systèmes fonctionnent au HFC-134a a augmenté de 1 million en 1992 à 338 millions en 2003. Selon un scénario BAU (business as usual), cette valeur va atteindre 965 millions en 2015 [IPC05]. Les émissions de fluides frigorigènes se traduisent en équivalent CO₂ selon leur GWP. En raison de l'énorme différence de leur pouvoir de réchauffement global (PRG), une diminution importante des émissions de fluides frigorigènes (848 Mt CO₂-éq en 1990 à 610 Mt CO₂-éq en 2003) a été observée. Par conséquent, le passage du CFC-12 au HFC-134a a un effet positif pour limiter le réchauffement planétaire.

Fonctionnement d'un système de climatisation automobile

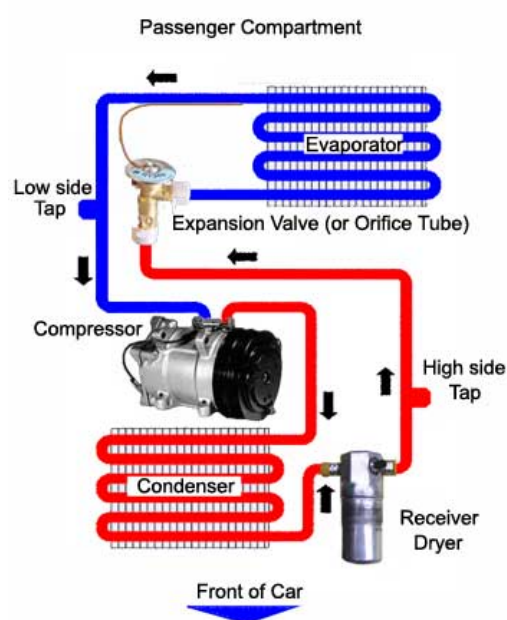


Figure 1.1 Schéma de fonctionnement d'une boucle de climatisation automobile

Le rôle du circuit frigorifique est de refroidir l'air qui va entrer dans l'habitacle en appliquant le principe de la détente d'un gaz qui va absorber la chaleur du milieu extérieur.

Le fluide à l'état gazeux est comprimé par un compresseur. Cette montée en pression entraîne une forte élévation de la température du liquide. La vapeur à haute pression passe dans le condenseur traversé par l'air extérieur. Le fluide est transformé en liquide à haute pression en arrivant au détendeur (TXV) qui fait chuter la pression du liquide dans l'évaporateur. Après la détente, le liquide se transforme en vapeur basse pression qui retourne au compresseur. L'air traversant l'évaporateur échange de la chaleur avec le fluide et donc se refroidit.

Classement des sources de fuites d'un système de climatisation automobile

Selon les résultats d'essais, 50 % à 60 % des fuites identifiées sont dues au compresseur et aux flexibles ou aux sertissages. D'autres sources de fuite viennent des raccords, du détendeur, du capteur de pression et des vannes de service. On peut dire que tous les composants fuient mais à des niveaux très différents. Les fuites ne doivent pas être confondues avec les émissions, les émissions de fluide frigorigène sont aussi dues à d'autres causes que les fuites, ce qui va être détaillé ci-dessous.

1. Les émissions initiales dues à la charge du système

Elles sont généralement faibles, si un équipement adéquat de charge du fluide frigorigène est adopté. Néanmoins, la gestion des capacités de fluide est une source d'émissions variant de 1 à 10 % selon la récupération du frigorigène restant dans les talons gazeux et liquide des containers ou des bouteilles de fluide frigorigène.

2. Fuites régulières d'un véhicule neuf

Les flexibles, les joints et le joint tournant du compresseur sont des points faibles constituant les sources essentielles de fuites régulières de fluide frigorigène dans les systèmes de climatisation automobile. Les origines de ces fuites seront analysées en détail dans ce travail de thèse.

3. Fuites dues à la dégradation des composants

Les fuites dues à la dégradation des composants sont difficiles à simuler, même si certains essais de compresseurs montrent que la dégradation semble faible grâce à la lubrification. Les données spécifiques ne sont pas disponibles pour les véhicules de plus de 8 ans. Cependant, le marché des fluides frigorigènes pour l'entretien des équipements indique que ce type de fuites peut expliquer l'utilisation de grandes quantités de fluide frigorigène pour la maintenance.

4. Fuites irrégulières dues aux accidents et aux défaillances des composants

Les accidents sont les principaux facteurs des fuites irrégulières des systèmes de climatisation automobile, comme le percement du condenseur, la rupture de flexibles, la dégradation des sertissages et les accidents de la route.

5. Emissions durant la maintenance

Pendant la maintenance, les émissions surviennent en raison de l'insuffisance de pratique et de connaissance des opérateurs, et de l'utilisation non adéquate de l'équipement de récupération et de recharge du frigorigène. Au-delà de l'usage, la conception des matériels de récupération est aussi en cause, le réglage du pressostat basse pression du système de récupération à une valeur trop haute entraîne des pertes de fluides d'au moins 100 à 150 g par opération de récupération. De plus, dans certains pays, l'usage par des particuliers de petites bouteilles de recharge est une source d'émissions significatives lors de la maintenance du système.

6. Emissions en fin de vie

Le défaut de récupération ou la faible efficacité de la récupération du fluide frigorigène, lorsque le système est démonté en fin de vie doit être pris en compte.

Maintenant regardons les différentes sources de fuite d'un système de climatisation automobile.

Le compresseur est un composant critique de l'étanchéité des systèmes de climatisation automobile. Le joint tournant du compresseur doit assurer l'étanchéité à la fois statique et

dynamique. Les résultats expérimentaux prouvent que le joint tournant contribue pour plus de 50 % au débit de fuite du compresseur. [SOU08]

Les matériaux polymères sont utilisés pour les flexibles afin de connecter différentes parties du système. Ils sont également une source importante de fuite de fluide frigorigène. On distingue trois types de flexibles en fonction des technologies : tout caoutchouc, barrière interne, barrière intermédiaire (appelée veneer).

Les sertissages sont utilisés pour fixer le tuyau flexible sur le tube en aluminium. Les mesures des débits de fuites des sertissages montrent que leur contribution est très faible ($< 0,1$ g/an). Trois types de raccords sont généralement utilisés : (1) raccord avec simple support, (2) raccord avec embout vissé, et raccords clips (voir Figure 1.10). L'évaporateur et le condenseur étant entièrement soudés, le niveau d'émission de ces composants est supposé inférieur à 0.1 g/an. Le détendeur, de type "H block", est une combinaison de 4 joints toriques, le débit de fuite de ce composant est donc important. De plus, les autres composants comme les vannes de service et le capteur de pression sont aussi montés avec des joints.

Pour conclure, les phénomènes des fuites sont très complexes et dépendent de nombreux facteurs : la température et la pression du fluide frigorigène, les vibrations, la géométrie et le matériau de chaque composant du système, les couples appliqués aux raccords, le mode d'assemblage du système, etc.

CHAPITRE 2 Méthode de mesure du débit de fuite

La méthode utilisée pour déterminer le débit de fuite (LFR) [CLO04b], [CLO96] est basée sur la mesure de l'élévation de la concentration dans un volume fermé. Elle repose sur l'équation (2.1).

$$\dot{m}_{\text{HFC-134a}} = M_{\text{HFC-134a}} \cdot \frac{\partial n_{\text{HFC-134a}}}{\partial t} \quad (2.1)$$

où,

$$n_{\text{HFC-134a}} = n_{\text{total}} \cdot C = \frac{P_{\text{amb}} \cdot V_{\text{accum}}}{R \cdot T_{\text{amb}}} \cdot C \quad (2.2)$$

Le débit massique est le produit de la masse molaire et de la dérivée du nombre de moles de HFC-134a par rapport au temps. La loi des gaz parfaits est utilisée pour prendre en compte des niveaux de température et de pression à l'intérieur de la cellule d'essais. Selon l'équation (2.2), les paramètres suivants doivent être déterminés pour calculer le débit de fuite :

- le volume d'accumulation,
- la température dans la cellule de mesure,
- la pression dans la cellule de mesure,
- et l'évolution de la concentration dans le temps.

Protocole d'essais

Le protocole d'essais se compose de quatre étapes :

Etape 1: Etalonnage de l'appareil de mesure de la concentration. Une bouteille d'étalonnage d'une concentration donnée (mélange de HFC-134a et d'azote) est connectée à l'appareil de mesure afin de l'étalonner.

Etape 2-1: Etalonnage du volume de la cellule de mesures. L'incertitude de mesure est directement liée aux incertitudes sur le volume libre de la cellule de mesures. Tout d'abord le volume est calculé à partir de sa description géométrique. Puis une fuite calibrée avec un débit de fuite connu est installée à l'intérieur de la cellule pour calibrer le volume libre de la cellule de mesure.

Etape 2-2: Etalonnage des sondes de température et des capteurs de pression. Avant l'installation dans le banc d'essais, la température et les capteurs de pression sont soigneusement calibrés.

Etape 3: Condition d'essais. Après l'installation de l'échantillon, la cellule d'essais est fermée, puis rincée avec de l'air reconstitué (80 % N₂ + 20 % O₂) afin d'éliminer toute concentration résiduelle de R-134a et garantir la précision de la mesure. La pression est maintenue à la pression atmosphérique. La température est maintenue constante ainsi que pendant la période d'essai. A chaque intervalle de temps, la concentration, la température et la pression sont enregistrées par un système d'acquisition.

Etape 4: Calcul du débit de fuite. Le débit de fuite peut être calculé par les équations (2.1) et (2.2). L'incertitude de mesure peut ensuite être établie.

Calculs de l'incertitude de mesure

L'incertitude de mesure du débit de fuite est réalisable [GUI93], basée sur le principe de mesures indirectes. La température et la pression étant maintenues constantes pendant l'essai, le débit de fuite du composant en essai peut être calculé par les équations (2.1) et (2.2). Le débit de fuite est fonction de différents paramètres, comme l'indique l'équation 2.3 :

$$\dot{m} = f(x_i) = f(T_{amb}, P_{amb}, V_{accum}, \frac{\partial C}{\partial t}) \quad (2.3)$$

Donc, l'incertitudes de mesure peut être obtenue par l'équation (2.4) :

$$u(\dot{m}) = \sqrt{\left(\frac{\partial \dot{m}}{\partial V_{accum}}\right)^2 u^2(V_{accum}) + \left(\frac{\partial \dot{m}}{\partial T_{amb}}\right)^2 u^2(T_{amb}) + \left(\frac{\partial \dot{m}}{\partial P_{amb}}\right)^2 u^2(P_{amb}) + \left(\frac{\partial \dot{m}}{\partial C / \partial t}\right)^2 u^2(\partial C / \partial t)} \quad (2.4)$$

L'incertitude relative sera calculée par l'équation (2.5).

$$\frac{u_{\dot{m}}}{\dot{m}_{HFC-134a}} = \sqrt{\left(\frac{u_{V_{accum}}}{V_{accum}}\right)^2 + \left(\frac{u_{T_{amb}}}{T_{amb}}\right)^2 + \left(\frac{u_{P_{amb}}}{P_{amb}}\right)^2 + \left(\frac{u_{\partial C / \partial t}}{\partial C / \partial t}\right)^2} \quad (2.5)$$

Le tableau 2.1 résume les incertitudes de chaque paramètre qui conduisent au débit de fuite de 39,5 g/an avec une incertitude relative de 6 %.

Tableau 2.1 Bilan de l'incertitude de mesure.

Paramètre	Valeur moyenne	Incertitude absolue	Incertitude relative
	x_i	u_{x_i}	u_{x_i} / x_i
V_{accum} (m ³)	2.443	0.147	0.06
T_{amb} (K)	313.79	0.14	0.00045
P_{amb} (Pa)	99731	368	0.0037
$\frac{\partial C}{\partial t}$ (ppm)	1.3x10 ⁻⁴	2.3x10 ⁻⁸	0.00018

Comme l'indique le tableau 2.1, la contribution du volume d'accumulation à l'incertitude globale est la plus importante. De plus, l'incertitude associée à l'évolution de la concentration dépend du nombre de mesures. La figure 2.1 montre l'incertitude relative sur la valeur du débit de fuite en fonction de la durée des essais (120 s pour chaque intervalle de temps) avec le plus grand écart type de 0,10 trouvé statistiquement selon les mesures expérimentales. Lorsque le niveau de fuite varie de 5 à 50 g/an pour les essais de systèmes, il est donc inutile d'effectuer plus de 24 heures d'essai parce que les incertitudes relatives deviennent négligeables par rapport à la contribution sur l'incertitude du volume.

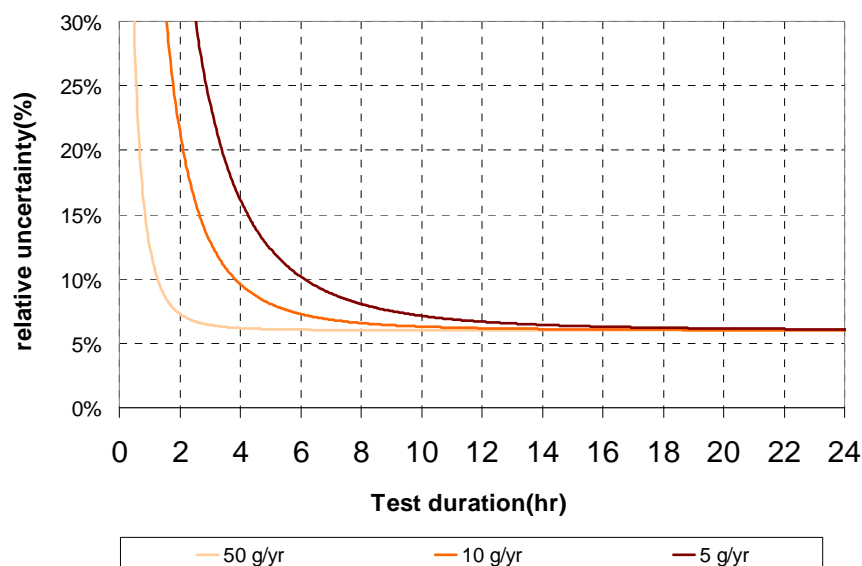


Figure 2.1 Incertitude relative de mesure du débit de fuite vs. durée de l'essai (niveau système).

En ce qui concerne le banc d'essais des composants, les cellules de mesure sont plus petites que celle du système, de sorte que l'incertitude relative est inférieure à celle des essais de systèmes, de l'ordre de 5 %. La figure 2.2 illustre l'évolution de l'incertitude relative du débit de fuite en fonction de la durée d'essai.

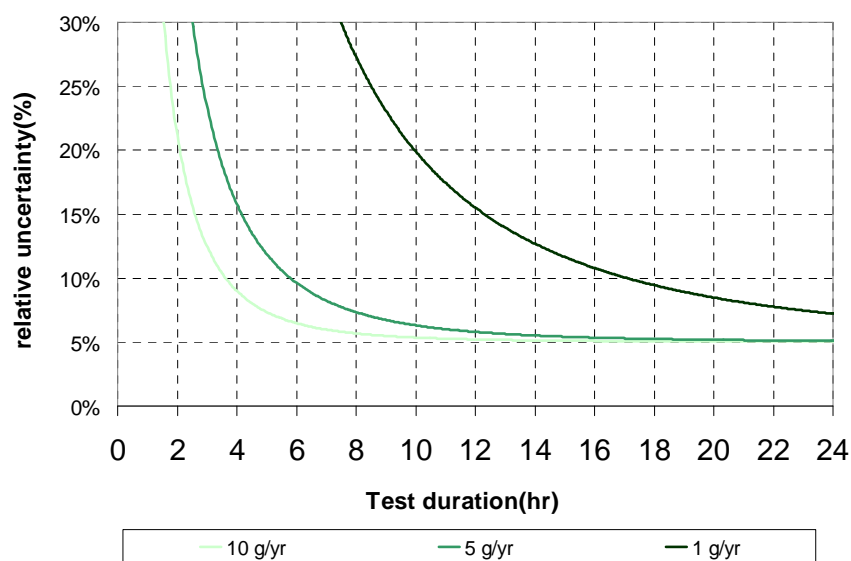


Figure 2.2 Incertitude relative de mesure du débit de fuite vs. durée d'essai (niveau composant).

Banc d'essais de mesures de débit de fuite d'un système complet et de composants

Les bancs d'essais de mesures se composent de trois principaux éléments :

- Le système ou le composant à tester,
- Le volume d'accumulation où le système ou le composant est installé, et l'évolution de la concentration est mesurée
- L'analyseur. Deux technologies : spectrophotomètre infrarouge et spectroscopie photo acoustique infrarouge sont utilisées pour mesurer la concentration.



Figure 2.3 Banc d'essais pour l'étude des systèmes de climatisation automobile

Comme l'indique la figure 2.3, la cellule de mesures est un parallélépipède en inox dotée d'une porte transparente. Une fois monté, le système est installé dans la cellule de mesures. Un ventilateur et des résistances chauffantes sont installés à l'intérieur de la cellule de mesures pour contrôler la température et homogénéiser le mélange d'air et de HFC-134a. Avant la mesure, la cellule de mesures est rincée par de l'air reconstitué (80 % N₂, 20 % O₂) afin d'enlever toute trace de HFC-134a qui risquerait d'influencer la mesure de concentration. L'analyseur est connecté à la cellule de mesures par un circuit fermé. Les paramètres nécessaires pour calculer le débit de fuite comme la pression, la température, la concentration en fonction du temps sont mesurés et enregistrés par le système d'acquisition.

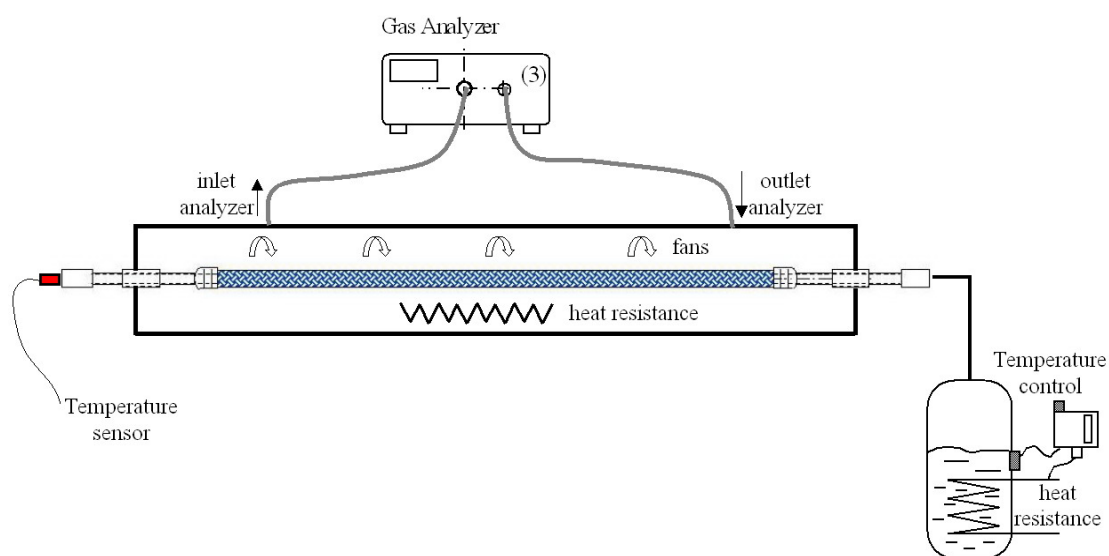


Figure 2.4 Schéma de principe du banc d'essais des composants.

La figure 2.4 présente le principe du banc d'essais de mesures du débit de fuite de composants. La méthode d'essais pour les composants est identique à celle des systèmes installés en cellule d'essais, sauf que pour les essais du système, le fluide frigorigène est directement chargé dans le système. Pour les composants, un bouilleur externe est monté à l'extérieur de la cellule et alimente le composant par connexion externe. La température du fluide frigorigène est contrôlée par une résistance chauffante. Une fois que la cellule est tirée au vide par une pompe à vide, le volume est rempli d'air reconstitué. Les résistances de chauffage et les ventilateurs sont installés dans la cellule de mesures pour réguler la température. Le composant est chauffé afin que la température du composant soit légèrement supérieure à la température de la saturation afin d'éviter toute condensation.

Résultats d'essais

Le pré-conditionnement est nécessaire pour tous les composants de systèmes de climatisation automobile contenant des matériaux polymères. Les résultats expérimentaux montrent qu'une période de 10 jours est suffisante pour que le régime permanent de la diffusion à travers ces matériaux soit atteint.

Les débits de fuites de 10 systèmes différents ont été mesurés et les résultats sont présentés Tableau 2.2.

Table 2.2 Débits de fuite de 10 types de systèmes

LFRs of system a to j (g/yr)				
MAC system	Temperature(°C)	30°C	40°C	50°C
	Saturation Pressure(kPa)	770	1017	1318
a		11	29	41
b		17	35	57
c		14	27	43
d		20	36	54
e		21	35	58
f		15	27	39
g		8	15	28
h		20	34	50
i		10	20	31
j		12	25	45
Average LFR(g/yr)		15	28	45

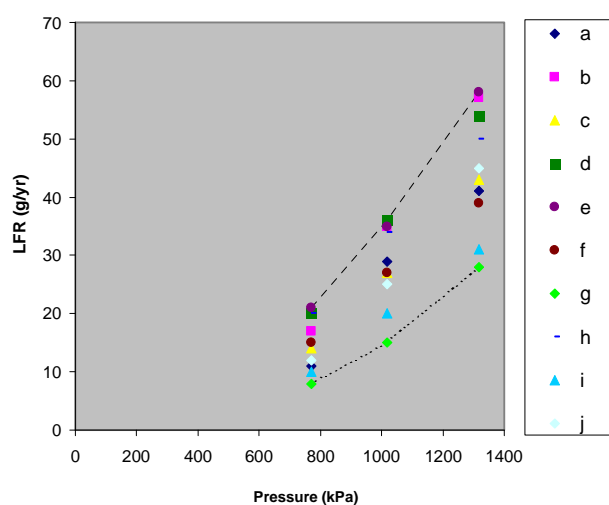


Figure 2.5 Débits de fuites vs. pression

Les débits de fuite des 10 systèmes ont ensuite été mesurés au niveau de leurs macro-composants. Comme l'indique la figure 2.6, chaque système a été soigneusement découpé en environ 13 macro composants. Le compresseur, le condenseur, l'évaporateur, la ligne de refoulement, la ligne d'aspiration, deux lignes liquide, la bouteille d'accumulation, le TXV, les raccords entrée et sortie du compresseur, et les raccords entrée et sortie du condenseur. La figure 2.7 montre un exemple de la préparation du composant. L'évaporateur subit une préparation spéciale puisque le composant sera mis en place dans la cellule et raccordé au bouilleur extérieur, ce qui implique la soudure d'un tube qui est inséré dans un passage étanche installé sur une des parois de la cellule de mesures.

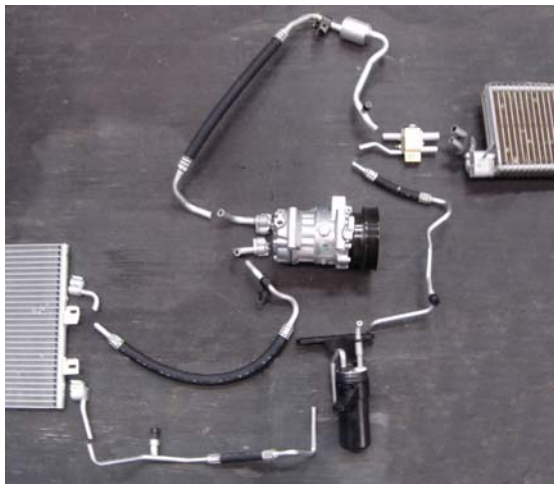


Figure 2.6 Composants découpés d'un système de climatisation

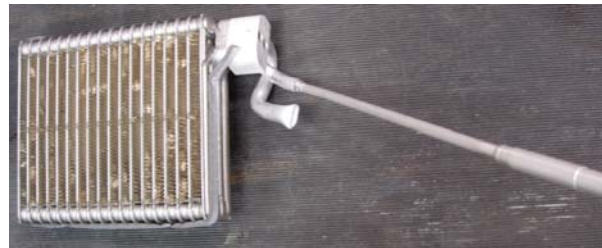


Figure 2.7 Évaporateur muni du tube de raccordement pour le passage étanche

Les résultats des essais au niveau des composants ont été classés et permettent de tirer certaines conclusions en terme de valeurs de débits de fuites.

Les débits de fuites de six sertissages de conception récente sont de l'ordre de 0,02 à 0,06 g/an. On peut donc en déduire que les débits de fuite de sertissages neufs sont généralement assez bas.

Les résultats des 10 détendeurs montrent que, selon la technologie et la conception, les émissions de détendeurs sont très différentes (de 0,5 g/an à 4,8 g/an à 30 °C) et peuvent donc être 10 fois plus élevées d'un détendeur à un autre.

Les débits de fuite de compresseurs sont les plus élevés de tous les composants du système. La contribution du compresseur représente 40 à 60 % du débit de fuite total d'un système de climatisation automobile.

Le tableau 2.3 résume la valeur moyenne des débits de fuite des dix systèmes complets et de la somme des débits de fuites des macro-composants des dix systèmes. L'analyse des valeurs présentées dans ce tableau montre que la somme des émissions de composants est égale à l'émission globale de ces systèmes dans les limites de l'incertitude des mesures. En conséquence, les essais peuvent être effectués soit au niveau du système complet, soit au niveau des composants. En fait les deux sont nécessaires. Les essais au niveau du système permettent de vérifier une performance globale d'étanchéité. Les essais au niveau des composants indiquent quels sont les composants les plus sujets aux fuites et ainsi les modifications nécessaires au niveau de la conception, des tolérances ou des matériaux.

Table 2.3 Débits de fuite et régressions

Température (°C)	Débits de fuite moyens de 10 systèmes de climatisation automobile			Régression linéaire	
	30 °C	40 °C	50 °C	k	R^2
Somme des macro-composants	15,6	27,4	44,5	2,61E-11	0,998
Système complet	15	28	45	2,63E-11	0,997

Lois de régression des débits de fuites en régime statique

Les joints en polymères sont utilisés dans un système de climatisation automobile pour connecter différents éléments et prévenir la perte de fluide frigorigène à l'extérieur du système. Les flexibles sont couramment utilisés pour prévenir la propagation de vibrations. Ainsi deux types de sources de fuites sont distingués [MUL98].

- a) Fuite due à l'écoulement dans les micro-canaux.** La surface de contact entre le joint et les parties rigides des raccords n'est jamais parfaite. Il existe toujours des micro-passages par lesquels le gaz peut s'écouler [MUL98]. Selon la loi de Poiseuille, le débit masse dû au flux visqueux entre les joints d'étanchéité est approximativement proportionnel à la différence des carrés des pressions amont et aval.
- b) Fuite due à la perméabilité des polymères.** Ce type de fuite est l'autre contributeur au débit de fuite. Le phénomène de diffusion des gaz à travers les polymères est également lié à la pression [KIM92], [MAG90], [MOO04].

En utilisant la méthode des moindres carrés, un bon accord entre les valeurs mesurées et la courbe de régression de l'expression binomiale a été vérifié et est exprimé par l'équation (2.6).

$$LFR = k(P_{upstream}^2 - P_{downstream}^2) \quad (2.6)$$

Selon les résultats présentés dans le tableau 2.3, des modèles de régression ont été établis pour les systèmes et les composants. Les paramètres ont été calculés et résumés dans le tableau 2.3. Les constantes k sont respectivement $2,63 \times 10^{-11}$ et $2,61 \times 10^{-11}$. Le paramètre R^2 , le coefficient de détermination, donne une mesure statistique de la façon dont la courbe de régression se rapproche des valeurs mesurées. Comme le montre le tableau 2.3, R^2 dans les deux cas est très proche de 1 (0,998 et 0,997), ce qui indique que le modèle de régression s'accorde correctement aux données.

La figure 2.8 montre les courbes de régression pour les systèmes complets et pour la somme des composants des systèmes. Il est clair que les deux courbes sont très proches l'une de l'autre. Les essais réalisés au niveau des systèmes ou au niveau des composants conduisent aux mêmes résultats. Les deux peuvent être utilisés pour déterminer la loi de comportement du débit de fuite d'un système.

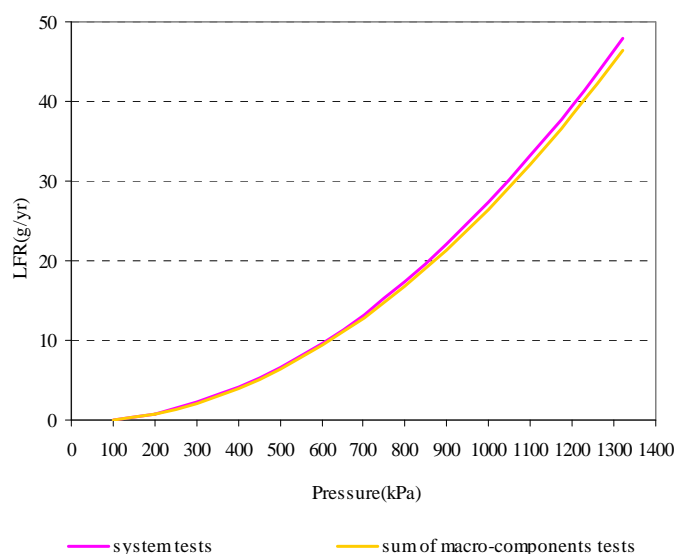


Figure 2.8 Courbes de régression de système global et de la somme des macro-composants

Mesures du débit de fuite prenant en comptes les conditions climatiques

Dans la réalité, la température n'est jamais constante et varie avec le temps. Les essais sont effectués pendant 72 heures en simulant les conditions de température jour / nuit de Séville pour analyser l'effet de la variation de la température.

Les essais réalisés sur une durée de 72 heures donnent une température moyenne de l'ordre de 30 °C. La perte de fluide (0,17 g) permet d'évaluer le débit de fuite de HFC-134a à 20,7g/an. De plus, le système a été caractérisé sur les trois températures habituelles (30, 40 et 50 °C) qui conduisent à 21, 36 et 50 g/an. Le faible différence entre 20,7 g/an et 21 g/an montre que la variation de températures peut être moyennée sur différents intervalles de temps y compris l'année.

La figure 2.9 montre la courbe de régression du débit de fuite d'un système X en fonction de la pression. La constante $k = 3,42 \cdot 10^{-11}$, permet de trouver le débit de fuite à n'importe quelle température. Par exemple, la température moyenne annuelle à Paris est de 11 ° C correspondant à la pression de saturation de 429 kPa. En utilisant la constante k, le débit de fuite correspondant à cette pression est de 5,9 g / an pour ce système.

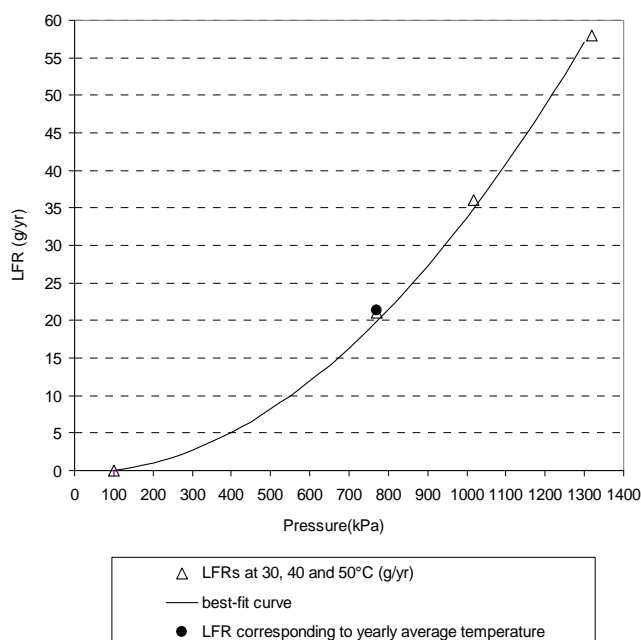


Figure 2.9 Débit de fuite d'un système de climatisation automobile et courbe de régression

Pour conclure, une fois les débits de fuite du système caractérisés par une courbe de régression, il est possible, connaissant la température moyenne annuelle de prévoir le débit de fuite annuel.

Contribution des débits de fuite en régime statique et en régime dynamique

Afin de mesurer la contribution des émissions du système en fonctionnement, plusieurs analyses ont été effectuées. En prenant en compte le kilométrage moyen des véhicules dans l'Union européenne, la durée de fonctionnement d'un véhicule est comprise entre 250 et 450 heures par an, représentant 3 à 5 % du temps annuel. En outre, le système de climatisation fonctionne seulement une partie limitée de cette durée de roulage, le système de

climatisation fonctionne donc entre 80 et 250 heures par an. Le cycle NEDC (New European Driving Cycle) représente l'usage typique d'une voiture en Europe, et est couramment utilisé pour évaluer les niveaux d'émissions des moteurs. Pour cette raison, le NEDC a été défini pour les essais en régime dynamique.

Trois systèmes ont été testés en statique à trois températures de 30, 40 et 50°C correspondant aux pressions de saturation de 770, 1017, et 1318 kPa. Ils sont ensuite testés en fonctionnement en simulant le cycle NEDC.

Le système V1 a fonctionné pendant 231 heures, la masse de HFC-134a accumulé dans la cellule de mesure est de 0,52 g. Le test en mode statique de ce système donne un débit de fuite de 8,8 g/an. En assumant que pendant le reste de l'année le système ne fonctionne pas, cette période en mode statique est ensuite traduite en $365 * 24 - 231 = 8529$ heures. Par conséquent, le débit de fuite en mode statique est de 8,57 g/an. Le total des débits de fuite s'élève à $8,57 + 0,52 = 9,1$ g/an.

Table 2.4 Contribution des débits de fuites en mode statique et en fonctionnement

MAC system	Standstill mode		Running mode		LFR (g/yr)	Contribution of running mode	<u>Standstill mode</u> Total LFR
	LFR (g/yr)	Duration (h)	Emission (g)	Duration (h)			
V1	8.8	8529	8.57	231	9.1	5.7%	8.8/9.1=0.97
V2	7.7	8524	7.49	236	8.0	6.7%	7.7/8.0=0.96
V3	5.2	8543	5.07	217	5.3	4.7%	5.2/5.3=0.98

Pour conclure, bien qu'en mode de fonctionnement la valeur du débit de fuite soit deux fois plus élevée que celle du mode statique, sa contribution demeure faible (environ 4 à 6 %). Quand on prévoit le débit de fuite total d'un système de climatisation automobile, en prenant en compte le mode dynamique, le ratio conventionnel entre le mode statique et le débit de fuite total peut être utilisé. Comme indiqué dans le tableau 2,4, le facteur varie de 0,96 à 0,98. En considérant le pire des cas on peut considérer qu'il faut majorer le résultat de mesure en condition statique de 4% pour rendre de compte de l'usage du véhicule.

Mesures sur une flotte de véhicules - Débit de fuite annuel obtenu par des opérations de récupération sur des véhicules

La récupération du fluide frigorigène de systèmes de climatisation sur véhicules permet de vérifier le débit de fuite pendant l'usage réel du véhicule. Des mesures ont été réalisées sur 40 véhicules pour comparer les émissions réelles des systèmes complets et celles mesurées en laboratoire. Les 40 véhicules sont de dix types différents avec quatre échantillons de chaque type afin de couvrir les différentes technologies, les différents fabricants de véhicules ainsi que les types de véhicules (petits, moyens et de luxe tels que les SUV, et les décapotables). Le choix a été fait par l'Association européenne des fabricants d'automobiles (ACEA).

Les étapes majeures du protocole de mesures sont les suivantes.

La charge initiale: pour chaque type de véhicule, quatre exemplaires ont été soigneusement chargés en décembre 2004 ou janvier 2005. La précision de la méthode de

récupération a été démontrée +0/-1 g pour chaque type de véhicule [CLO07]. Cela signifie la masse de fluide frigorigène récupérée est égale à celle de la charge à un gramme près.

La récupération finale: après 9 mois, la procédure de récupération a été effectuée sur ces quarante véhicules en août 2005 ou en septembre 2005.

Les débits de fuite moyens des dix types de systèmes varient de 7,2 à 21,6 g/an. Il est nécessaire de souligner que les véhicules C et H sont équipés d'un double évaporateur. Le débit de fuite moyen sur l'ensemble des véhicules est de l'ordre de 10 g/an.

Détermination du facteur de correction

Les mêmes dix types de systèmes ont été testés en laboratoire (4 échantillons pour chaque type) à trois températures différentes. Les résultats sont résumés dans le tableau 2.18.

Tableau 2.5 Moyenne arithmétique des débits de fuites des systèmes A à J

Système	Débit de fuite (g/an)			
	Température (°C)	30 °C	40 °C	50 °C
A		15.8 ^{+5.2} _{-3.8}	34.7 ^{+4.3} _{-3.7}	67 ^{+9.0} _{-10.0}
B		18.2 ^{+1.8} _{-2.2}	45 ^{+2.0} _{-2.0}	82.5 ^{+3.5} _{-4.5}
C		17.2 ^{+4.8} _{-5.5}	33 ^{+2.0} _{-3.0}	60.6 ^{+6.4} _{-7.6}
D		26.5 ^{+17.5} _{-9.5}	47.5 ^{+15.5} _{-13.5}	87.2 ^{+53.8} _{-33.2}
E		33.5 ^{+2.5} _{-2.5}	58.5 ^{+3.5} _{-1.5}	118.2 ^{+6.8} _{-5.2}
F		22.7 ^{+1.3} _{-2.7}	33.5 ^{+5.5} _{-6.5}	52.7 ^{+6.3} _{-4.7}
G		11.7 ^{+3.3} _{-3.7}	26.2 ^{+5.8} _{-5.2}	49.7 ^{+21.3} _{-15.7}
H		21.0 ^{+3.0} _{-3.0}	45.0 ^{+12.0} _{-8.0}	80.2 ^{+14.8} _{-10.2}
I		12.1 ^{+1.9} _{-1.1}	24.7 ^{+3.3} _{-2.7}	41.5 ^{+5.5} _{-3.5}
J		12.5 ^{+2.5} _{-1.5}	26.2 ^{+0.8} _{-1.2}	46.2 ^{+7.7} _{-7.2}
Valeur moyenne		19.2 ^{+24.8} _{-11.2}	37.6 ^{+25.4} _{-16.6}	68.8 ^{+72.2} _{-34.8}

Un facteur de corrélation a été établi entre les résultats des essais en laboratoire et les mesures effectuées sur la flotte de véhicules (voir la Figure 2.10). Les débits de fuite de ces 10 types de systèmes aux trois températures 30, 40, 50°C sont respectivement de 9,2, 37,6 et 68,8 g/an et la courbe de régression est ensuite établie avec $k = 3,856 \times 10^{-11}$.

En prenant en compte les conditions climatiques européennes correspondant aux 9 mois où les 40 véhicules ont été suivis, la température moyenne a été de 15,5°C. Trouvons le point, qui correspond à cette température : 9,1 g/an à la pression de 496 kPa. En supposant un supplément de 6 % provenant du régime dynamique du système, le débit de fuite total devient $9,1/0,96 = 9,5$ g/an. Cette différence acceptable entre les essais de laboratoire et les mesures sur la flotte de véhicules (10.0 g/an) prouve la possibilité de prévoir le débit de fuite d'un système de climatisation sur la seule base d'essais en laboratoire à température constante.

En résumé, la procédure de prévision du débit de fuite d'un système de climatisation automobile se compose de trois étapes :

- (1) Mesurer les débits de fuites à 3 températures différentes permettant d'établir la loi de comportement du système en fonction de la pression;**
- (2) Tracer sur la courbe de régression le point correspondant à la température moyenne de la région;**
- (3) Prévoir le débit de fuite du système en prenant en compte l'effet du fonctionnement.**

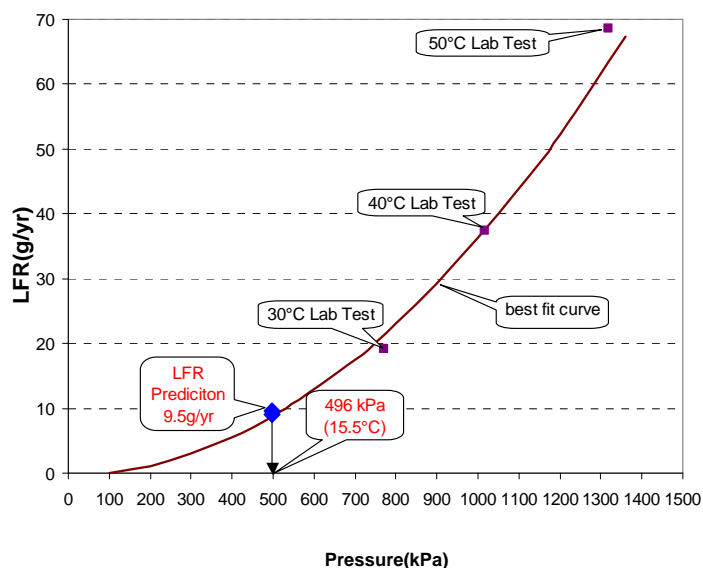


Figure 2.10 Détermination du facteur de correction

Pour conclure, ce chapitre présente une méthode de mesures en laboratoire pour déterminer le débit de fuite d'un système de climatisation automobile en assurant une bonne précision de mesure. Les essais réalisés montrent que la contribution associée au fonctionnement du système de climatisation automobile est faible (de l'ordre de 4 à 6 % du débit total) car la durée de fonctionnement est elle-même courte. Ceci confirme le rôle dominant du débit à l'arrêt du système. L'étanchéité d'un système de climatisation automobile peut donc être caractérisée uniquement en régime statique.

CHAPITRE 3 Prévisions des émissions des flexibles

Essais de perméabilité des membranes

Le phénomène de transport de gaz traversant les membranes de polymères est un processus de "solution – diffusion" qui se compose en 3 étapes (voir Figure 3.1)

- Dissolution de molécules dans le polymère suivant l'adsorption en surface
- Diffusion moléculaire du gaz dans le matériau,
- Désorption du gaz de la surface aval.

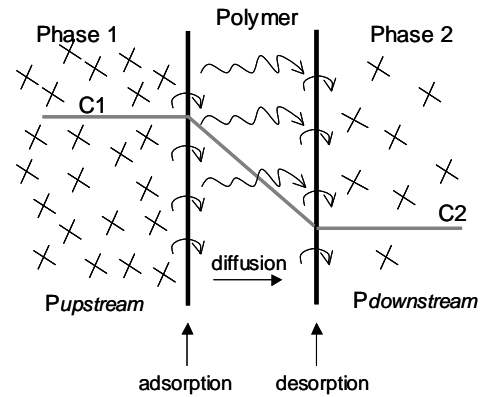


Figure 3.1 Processus de perméation

La première loi de Fick permet de décrire le transport du gaz à travers une membrane polymère. Le flux spécifique, J , du gaz est égal à :

$$J = -D\nabla C \quad (3-1)$$

Avec,

J flux molaire ($\text{mol s}^{-1} \text{m}^{-2}$)

D coefficient de diffusion du gaz ($\text{m}^2 \text{s}^{-1}$).

C concentration du gaz dans la membrane (mol m^{-3})

Si on considère une relation linéaire entre la pression de gaz et sa concentration à l'interface suivant la loi de Henry, l'équation (3-2) s'applique :

$$J = -DS \frac{\partial P}{\partial x} = -Pe \frac{\partial P}{\partial x} \quad (3-2)$$

En introduisant la définition du coefficient de perméabilité, Pe , le débit de fuite d'une membrane d'épaisseur e , (dans le cas où le diamètre de la membrane est beaucoup plus grand que l'épaisseur), peut être obtenu par l'équation (3-3).

$$J = \frac{dn}{dt} \frac{1}{A} = Pe \frac{\Delta P}{e} \quad (3-3)$$

Par conséquent, le débit de fuite de HFC-134a peut être calculé par l'équation (3-4).

$$\dot{m} = \frac{dm}{dt} = M_{\text{HFC-134a}} \cdot \frac{dn}{dt} = M_{\text{HFC-134a}} \cdot J \cdot A = M_{\text{HFC-134a}} Pe A \frac{\Delta P}{e} \quad (3-4)$$

Connaissant le débit masse d'une membrane d'épaisseur e et de rayon r , le coefficient de perméabilité de ce matériau peut être calculé par l'équation (3-5).

$$Pe = \frac{\dot{m}}{M_{\text{HFC-134a}}} \cdot \frac{e}{\pi r^2 (P_{\text{upstream}} - P_{\text{downstream}})} \quad (3-5)$$

La figure 3.2 montre le schéma de principe de la mesure de débit de fuite d'une membrane. La pression est initialement appliquée sur la surface amont de la membrane; la pression est maintenue à la pression atmosphérique sur la surface opposée de la membrane.

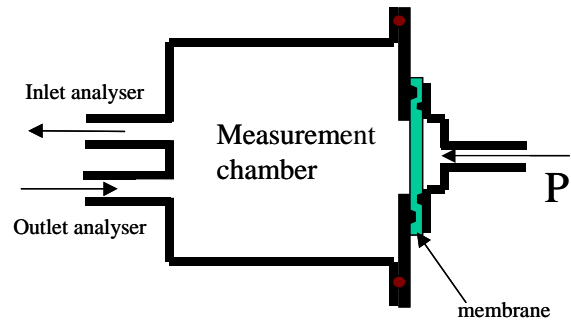


Figure 3.2 Représentation schématique du dispositif de mesure de perméation d'une membrane

Les évolutions de la concentration, de la pression et de la température à l'intérieur du volume d'accumulation en fonction du temps sont mesurées et enregistrées continuellement par un système d'acquisition. Selon la méthode de mesure de débit de fuite décrite au chapitre 2, le débit de fuite de la membrane peut être déterminé et les coefficients de transport peuvent être identifiés. La figure 3.3 montre l'évolution de la quantité (en moles) de HFC-134a gazeux accumulé à l'intérieur de la cellule de mesure. La méthode "time lag" est utilisée pour déterminer les coefficients de transport.

$$D = \frac{e^2}{6\theta} \quad (3-6)$$

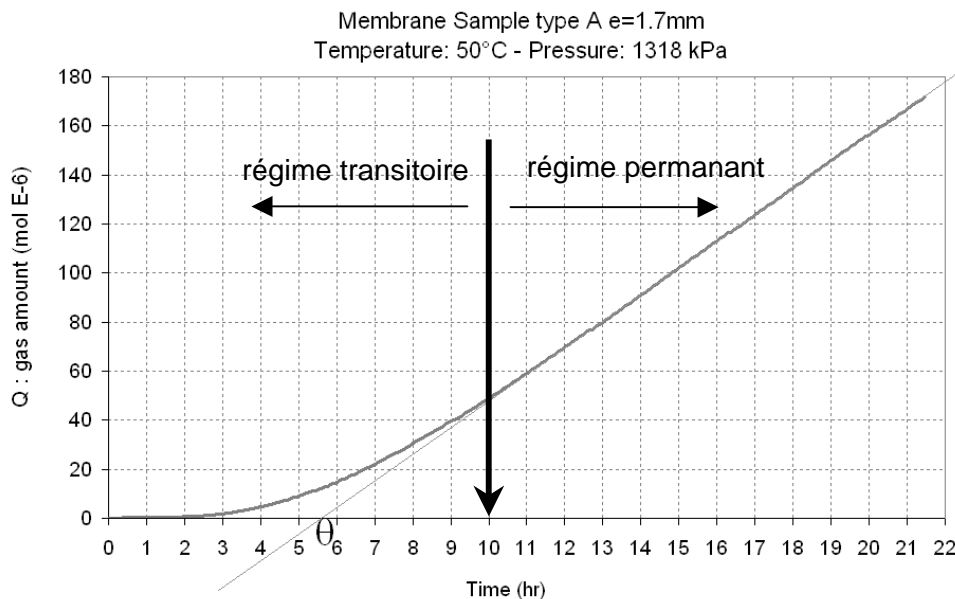


Figure 3.3 Courbe typique "time lag" pour la membrane A

Par conséquent, le coefficient de diffusion peut être obtenu en trouvant le point θ , couramment appelé "time lag", sur l'axe t en utilisant l'équation (3-6). Connaissant les pressions en amont et en aval, le coefficient de perméabilité, P_e , est directement proportionnel à la pente, comme écrit dans l'équation (3-5), et le coefficient de solubilité, S , est calculé comme le ratio de P_e/D .

Le tableau 3.4 résume les résultats des mesures de débits de fuites de 6 membranes ainsi que les coefficients de perméabilité calculés. Le coefficient de perméabilité le plus élevé est observé pour la membrane B (145,1 à 50 ° C). Le plus faible parmi ces 6 membranes est

celui de la membrane F pour 0,54 à 50 ° C. Il y a un facteur de 272 à 50 ° C et un facteur de 195 à 30 ° C.

Table 3.1 Débits de fuites de 6 membranes et coefficients de perméabilité calculés

Membrane Type	Epaisseur e(mm)	T(°C)	Pression de saturation (kPa)	Débit de fuite (g/an)	$Pe \left[\frac{10^{-10} \text{ mol} \cdot \text{m}}{\text{m}^2 \cdot \text{s} \cdot \text{MPa}} \right]$
A	1.7mm	T = 30 °C	770	2.6	29.1
		T = 40 °C	1017	5.4	44.1
		T = 50 °C	1318	10.7	65.7
B	2.5 mm	T = 30 °C	770	5.6	58.9
		T = 40 °C	1017	12.8	98.3
		T = 50 °C	1318	25.1	145.1
C	3.8 mm	T = 30 °C	770	1.4	12.9
		T = 40 °C	1017	2.7	18.2
		T = 50 °C	1318	5.5	27.8
D	1.7 mm	T = 30 °C	770	0.22	2.46
		T = 40 °C	1017	0.43	3.51
		T = 50 °C	1318	0.80	4.91
E	2.4 mm	T = 30 °C	770	0.10	1.58
		T = 40 °C	1017	0.17	1.96
		T = 50 °C	1318	0.29	2.52
F	2.7 mm	T = 30 °C	770	0.017	0.30
		T = 40 °C	1017	0.030	0.39
		T = 50 °C	1318	0.055	0.54

L'analyse du tableau 3.1 indique que les coefficients de perméabilité ne sont pas constants et dépendent de plusieurs facteurs. Les résultats pour des membranes constituées de matériau de même type mais d'épaisseurs différentes prouvent, qu'en général, l'effet de l'épaisseur est négligeable. L'analyse des effets de la pression et de la température permet de développer un modèle prédictif du coefficient de perméabilité qui prend en compte ces doubles-effets (Equation (3-7)).

$$Pe = \kappa_1 e^{\left(\kappa_2 (\Delta P) - \frac{\kappa_3}{RT} \right)} \quad (3-7)$$

Par conséquent, le débit de fuite s'écrit :

$$\dot{m} = M_{134a} \cdot \frac{\pi r^2}{e} \cdot \kappa_1 e^{\left(\kappa_2 (\Delta P) - \frac{\kappa_3}{RT} \right)} \cdot \Delta P \quad (3-8)$$

Selon l'équation (3-8), les paramètres κ_1 , κ_2 et κ_3 peuvent être calculés pour chaque membrane en utilisant la méthode des moindres carrés. Les résultats sont détaillés dans le Tableau 3.2. Les erreurs relatives entre les données expérimentales et les valeurs obtenues par le modèle prédictif ont été calculées. Les erreurs relatives sont assez faibles et varient dans la limite de $\pm 5\%$ (cf. figure 3.4).

Comme l'indique le Tableau 3.2, la valeur de κ_1 varie fortement selon le type de membranes. Les valeurs de κ_2 changent dans la limite de 0,0001. Il faut noter que $\kappa_2 > 0$ signifie un effet positif de la pression sur la perméabilité et vice versa. Prenons F comme un exemple, la valeur κ_2 de F est de $-0,000609$, ce qui signifie que la perméabilité diminue avec l'accroissement de la pression. Une dispersion est observée pour κ_3 , qui varie de 19 950 à 33 293.

Table 3.2 Paramètres κ_1 , κ_2 et κ_3 pour les membranes de A à F

Membrane	Paramètres κ_1 , κ_2 et κ_3		
	κ_1	κ_2	κ_3
A	1503897	0.000133	27441
B	101060	0.000675	19771
C	24880	0.000542	20043
D	5340	0.000358	19950
E	1260431	-0.000609	33293
F	23157	-0.000170	28140

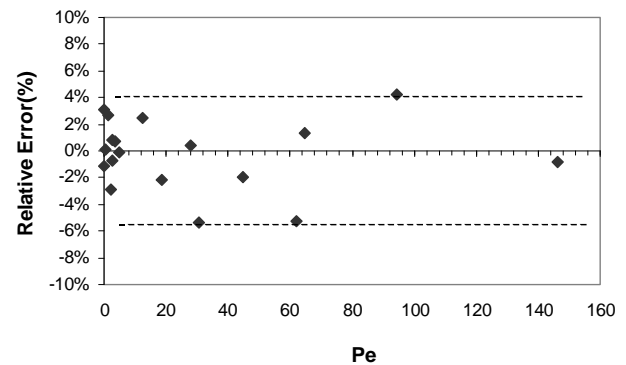


Figure 3.4 Erreur relative due à la régression

Selon les trois constantes déterminées pour chaque type de membrane, le coefficient de perméabilité peut être utilisé pour prédire le débit de fuite à la température donnée. Comme l'indique la Figure 3.5, pour une pression de 537 kPa, les coefficients de perméabilité de chaque membrane peuvent être déterminés, ce qui permet de prévoir leurs débits de fuite.

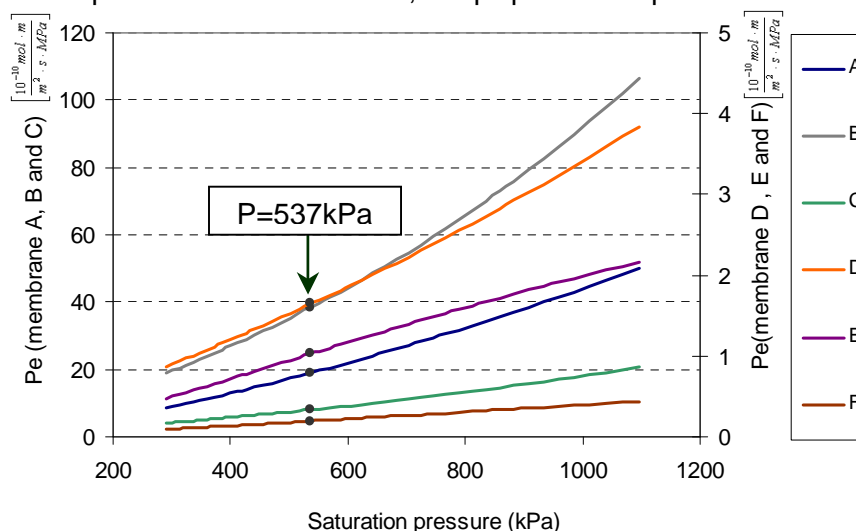


Figure 3.5 Modèles prédictifs de débits de fuites des 6 membranes

Tests de perméabilité des flexibles

L'équation (3-9) montre que, connaissant le coefficient de perméabilité de chaque couche et les rayons correspondants, le débit de fuite d'un flexible avec une longueur donnée peut être déterminée. Cette hypothèse est vraie sous certaines conditions :

- Le coefficient de perméabilité est identique qu'il s'agisse d'une membrane ou d'un flexible;

- La couche de renforcement (tresse) est considérée comme négligeable à la contribution au débit de fuite.

$$\dot{m} = M_{HFC-134a} \cdot \frac{2\pi L}{\sum_{i=1}^n \frac{1}{Pe_i} \cdot \ln\left(\frac{r_{i+1}}{r_i}\right)} (P_{upstream} - P_{downstream}) \quad (3-9)$$

Des mesures ont été effectuées sur un flexible pour vérifier le modèle. Prenons comme exemple une technologie simple, un flexible composé d'une couche interne de polymère F et une couche extérieure de polymère A. Le débit de fuite de ce flexible peut être obtenu par l'équation (3-10).

$$\dot{m} = M_{HFC-134a} \cdot \frac{2\pi L}{\frac{1}{Pe_A} \cdot \ln\left(\frac{r_3}{r_2}\right) + \frac{1}{Pe_F} \cdot \ln\left(\frac{r_2}{r_1}\right)} (P_{upstream} - P_{downstream}) \quad (3-10)$$

Table 3.3 Débits de fuite calculés et mesurés

Température (°C)	Pression de saturation (kPa)	A		F		Débit calculé (g/an)	Débit mesuré (g/an)		
		Pe	Diamètre (mm)		Pe			Diamètre (mm)	
			d_2	d_3				d_1	d_2
T1 = 30	770	29,1			0,30	2,5	2,9		
T2 = 40	1017	44,1	19,6	24,8	0,39	4,5	5,3		
T3 = 50	1318	65,7			0,54	8,3	10,1		

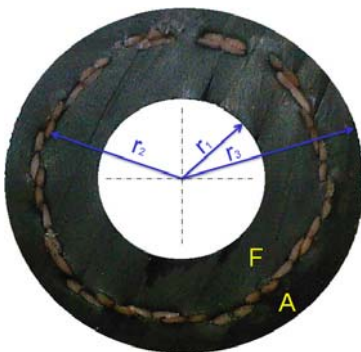


Figure 3.6 Flexible échantillon pour l'essai de perméabilité

Les diamètres des couches intérieure, médiane, et extérieure sont respectivement de 16,2, 19,6 et 24,8 mm. Le flexible lui-même, d'une longueur de 1,17m a été mesuré à trois températures, qui conduisent à des débits de fuite respectivement de 2,9, 5,3 et 10,1 g/an. En utilisant le coefficient de perméabilité des polymères A et F, la prédiction du débit de fuite peut être obtenue par l'équation (3-10) pour la même longueur et les résultats sont de 2,5, 4,5 et 8,3 g/an.

La différence observée entre la valeur calculée du modèle de prédiction et la valeur mesurée sur le flexible peut être expliquée par plusieurs raisons :

- Les effets du processus de fabrication de la membrane et celui du flexible ne sont pas tout à fait les mêmes;
- le diamètre de chaque couche n'est pas parfait et les incertitudes sur les épaisseurs ne sont pas connues.

Néanmoins, le modèle peut être utilisé pour prédire le débit de fuite d'un flexible avec une tolérance acceptable.

Modèle prédictif du débit de fuite de flexibles

D'un point de vue pratique, il est intéressant pour les fournisseurs de flexibles, de définir un coefficient de perméabilité global des flexibles selon un petit nombre de mesures. La même méthodologie peut donc être appliquée, même si les résultats sont moins génériques et liés au processus fabrication.

Selon le modèle prédictif de perméabilité des flexibles, une perméabilité globale du flexible est représentée par l'équation(3-11) :

$$\frac{1}{Pe_{overall}} \ln\left(\frac{r_{outer}}{r_{inner}}\right) = \sum_{i=1}^n \frac{1}{Pe_i} \cdot \ln\left(\frac{r_{i+1}}{r_i}\right) \quad (3-11)$$

L'équation (3-12) prend en la variation de la perméabilité globale en fonction de la pression et la température.

$$Pe_{overall} = c_1 e^{\left(c_2(\Delta P) - \frac{c_3}{RT}\right)} \quad (3-12)$$

Selon l'équation (3-12), la loi de comportement du débit de fuite d'un flexible peut être caractérisée selon les débits de fuite à différentes températures constantes. Les figure 3.7 et 3.8 présentent les modèles prédictifs de deux types de flexibles en fonction de la pression. Un bon accord a été observé entre les données expérimentales et les modèles prédictifs dans les deux cas. En appliquant ce modèle, le débit de fuite du flexible peut être calculé à toute autre température. Les débits de fuite de flexibles de même technologie mais de différents fournisseurs ont été étudiés. Les résultats montrent que les débits de fuite des flexibles dépendent non seulement des matériaux mais aussi des fournisseurs qui peuvent avoir des recettes différentes.

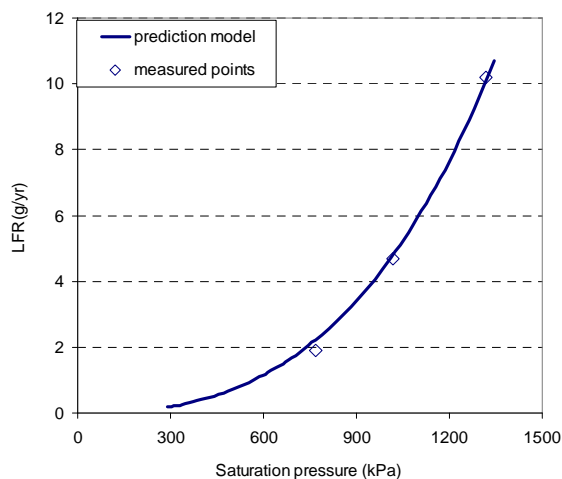


Figure 3.7 Modèle prédictif d'émission du flexible n°2

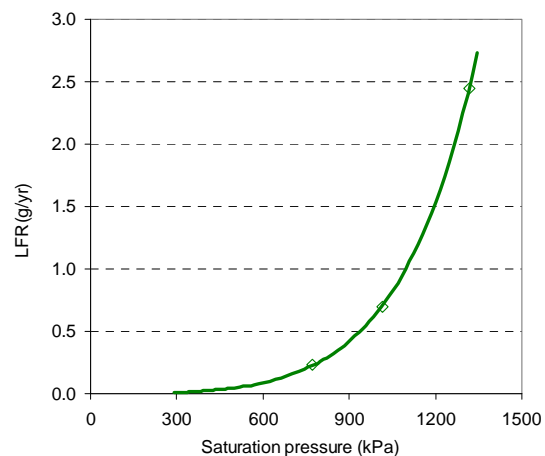


Figure 3.8 Modèle prédictif d'émission du flexible n°3

Figure 3.8 Emi

Les résultats obtenus permettent de tirer certaines conclusions.

- Les débits de fuites des flexibles peuvent être simplifiés basés sur le transport du gaz à travers les matériaux polymères ;
- Les coefficients de perméabilité des six membranes échantillons ont été déterminés ;
- Les modèles prédictifs ont été mis au point non seulement pour les membranes mais aussi pour les flexibles ;
- Un coefficient de perméabilité global de flexible a été introduit et un bon accord a été observé entre les valeurs du modèle de prédiction et les données expérimentales ;
- Des flexibles de même technologie conduisent à des débits de fuite différents qui dépendent des recettes des fournisseurs.

CHAPITRE 4 Comportement des fuites de raccords utilisés en climatisation automobile

Les raccords utilisés pour connecter des tuyaux métalliques avec d'autres tuyaux ou avec les principaux composants comme le compresseur, le détendeur, l'évaporateur et le condenseur doivent garantir l'étanchéité des connections par les joints intégrés dans les raccords. Parmi les joints utilisés, les joints toriques sont les plus utilisés parce qu'ils sont peu coûteux, fiables, faciles à fabriquer et simples à monter. Par conséquent, la loi de comportement du débit de fuite d'un joint torique a été étudiée en détail dans ce chapitre.

La figure 4.1 montre deux types de joints toriques : axial et radial.

- (a) Axial : le joint torique est déformé par deux forces appliquées sur les surfaces supérieure et inférieure du joint ;
- (b) Radial : le joint est déformé par deux forces appliquées sur les surfaces intérieure et extérieure du joint.

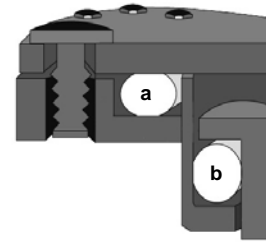


Figure 4.1 Dessins d'un joint torique

Le mécanisme d'étanchéité des joints toriques est dû à l'élasticité et l'incompressibilité des matériaux polymères. Le joint torique est comprimé par la partie métallique du raccord pendant le montage. La pression maximum de contact entre le joint et les parois métalliques devrait être plus élevée que la pression du fluide afin de limiter les fuites. On distingue deux types de fuites :

1. Fuite due aux micro-canaux.
2. Fuite due à la perméabilité des polymères.

Transport de gaz dans les micro-canaux

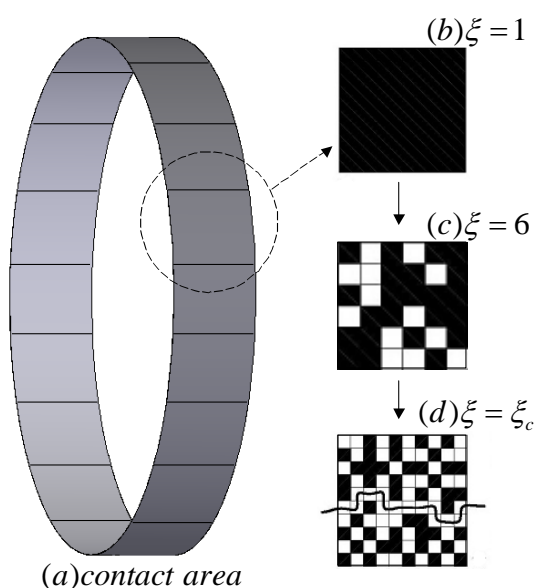


Figure 4.2 Théorie de la percolation

En considérant un carré pour la zone de contact de côté, L , et à un grossissement $\xi = 1$ (cf. figure 4.2 (b)), l'ensemble du carré est noir, ce qui signifie que le contact est parfait. Avec l'augmentation du grossissement, la résolution augmente, de sorte que certaines régions de non-contact apparaissent comme le montre la figure 4.2 (c). ξ est défini comme l'agrandissement et est exprimé sous la forme:

$$\xi = \frac{L}{w} \quad (4-4)$$

Où w est la résolution.

La surface de contact entre les joints et les zones de raccords rigides n'est jamais parfaite. Il existe toujours des micro-passages par lesquels le gaz peut passer. Le mécanisme de contact est basé sur la théorie de la percolation qui a été largement étudiée [BOT07, PER04, PER06, PER08, OKA08]. La zone de contact entre le joint torique et les parties métalliques (parties mâle et femelle) est de forme cylindrique (voir la figure 4.2 (a)). Comme la surface de contact des deux organes n'est pas parfaitement lisse, la zone de contact effective est plus petite que la zone de contact nominale (voir figure 4.2(b)). En augmentant le grossissement de la zone de contact, un plus grand nombre de zones de non contact est observé.

La simulation du mécanisme de contact est basée sur un joint torique où les parties mâle et femelle sont assemblées et fixées ensemble. Sachant que le composant est symétrique par rapport à son axe, le modèle est simplifié en 2D axisymétrique (voir la figure 4.3).

La figure 4.3 illustre le principe de la simulation qui est menée en deux étapes :

- Étape 1 : la partie femelle glisse dans le sens horizontal et la partie mâle dans le sens vertical pour simuler le montage du raccord ;
- Etape 2: La pression du fluide est appliquée sur le côté gauche du joint torique et sur le côté droit la pression est atmosphérique.

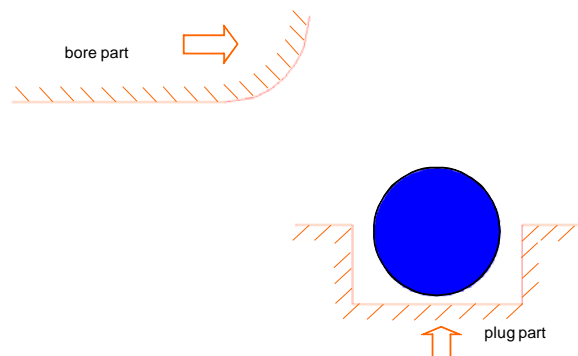


Figure 4.3 Modèle 2D axisymétrique

Comme le montre la figure 4,4, la performance d'étanchéité d'un joint torique est influencée par plusieurs facteurs géométriques tels que :

- Le diamètre de la partie femelle du raccord (D_{bore})
- Le diamètre de la partie mâle du raccord (D_{plug})
- Le diamètre de la gorge (D_{groove})
- La profondeur de la gorge (G)
- Le jeu (δ)

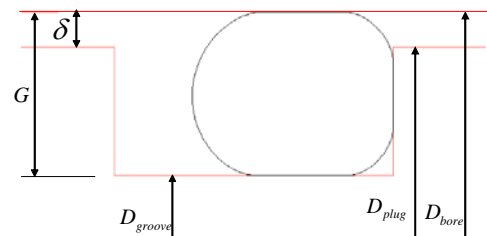


Figure 4.4 Paramètres géométriques d'un raccord

Afin de valider les résultats de modélisation, des raccords transparents ont été réalisés pour visualiser les surfaces de contact entre le joint et les parois du haut et du bas (voir la figure 4.5). Une bonne concordance a été observée entre les largeurs obtenues par la simulation et les mesures par visualisation.

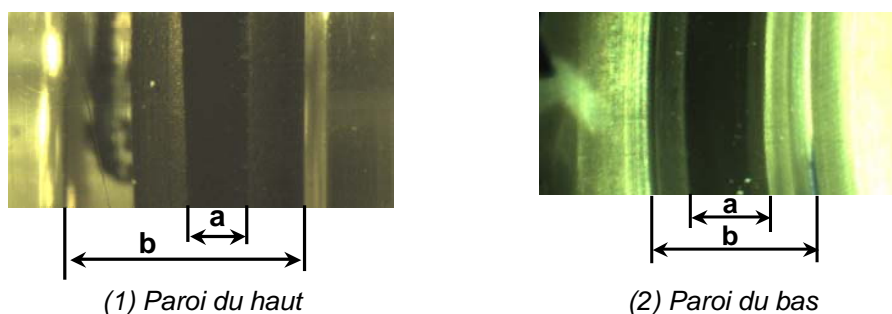


Figure 4.5 Largeurs de contact sur les parois du haut et du bas

Comme le montre la figure 4.4, lorsque le joint monté est soumis à la pression du fluide, il se plaque du côté opposé à la pression. La déformation du joint est fonction de la pression. Plus la pression P augmente, plus les forces de contact deviennent élevées, renforçant l'étanchéité.

Calcul du débit de fuite du joint torique

Comme nous l'avons vu depuis le début de ce chapitre, la fuite est composée de perméation dans les matériaux polymères et de fuites dans les micro-canaux en raison du contact non parfait entre le joint et les pièces métalliques.

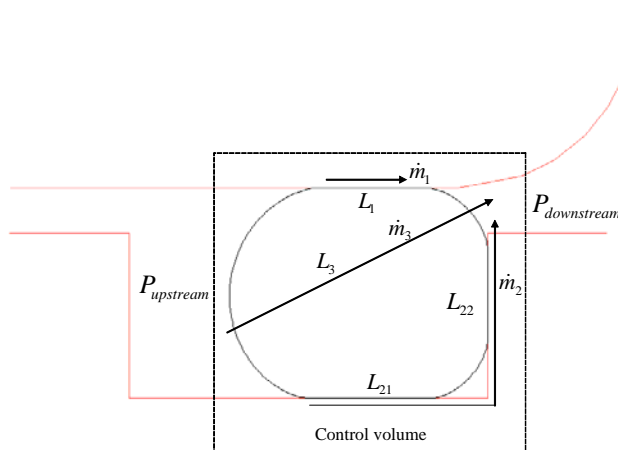


Figure 4.6 Volume de contrôle pour le calcul du débit

Par conséquent, la somme des débits de fuite dus à la perméabilité et aux micro-canaux peut être calculée par l'équation (4-1).

$$\dot{m} = \dot{m}_1 + \dot{m}_2 + \dot{m}_3 \quad (4-1)$$

Comme l'indique la figure 4.6, \dot{m}_1 et \dot{m}_2 appartiennent à l'écoulement du gaz dans des micro-canaux et \dot{m}_3 est la perméation du gaz dans le polymère.

Débit de fuite lié aux micro-canaux

Les résultats obtenus ont montré de grandes différences de perméabilité entre les différentes membranes. En choisissant un matériau de type F, qui présente une très bonne étanchéité, le débit de fuite dû à la perméabilité peut être négligé.

Donc, le débit de fuite lié aux micro-canaux s'écrit

$$\dot{m} = \dot{m}_1 + \dot{m}_2 \quad (4-2)$$

$$\dot{m} = \dot{m}_{ch1} n_{ch1} + \dot{m}_{ch2} n_{ch2} \quad (4-3)$$

Le débit total peut être calculé avec l'équation (4-4).

$$\dot{m} = \frac{\pi D_{bore}}{L_1} \frac{w_c H_1^3}{24 \mu r T} (P_{upstream}^2 - P_{downstream0}^2) \left(\frac{1}{L_1} + \frac{1}{L_{21} + L_{22} \left(\frac{H_{21}}{H_{22}} \right)^3} \right) \quad (4-4)$$

La rugosité de la surface est généralement inférieure à 1, de sorte que la hauteur des micro-canaux est de l'ordre de 10^{-7} . En prenant $H = 0.1 \mu m$, w_c est de l'ordre de 0,8 ~ 1,0 selon les valeurs de λH^3 résumées dans le tableau 4,1. En résumé, la largeur et la hauteur de micro-canaux rectangulaires sont de l'ordre de 0,1 à $1,0 \mu m$. Les valeurs de $w_c H^3$ à 40 et 50 ° C

sont proches l'une de l'autre. À 30 ° C, la valeur est plus faible que les deux autres. Une dispersion acceptable de 14% a été observée.

Table 4.1 Calculs de débits de fuite liés aux micro-canaux

T(°C)	Pression de saturation (kPa)	Débit de fuite (g/an)	μ ($\mu Pa s$)	L_1 Paroi Sup.	L_{21} Paroi inf.	L_{22} Paroi latérale	R_L	$w_c H^3$
30	770	0,29	11,907	0,78	0,94	0,46	0,0005009	$7,873 \times 10^{-28}$
40	1017	0,50	12,373	0,80	0,96	0,56	0,0005241	$9,342 \times 10^{-28}$
50	1318	0,86	12,917	0,84	0,98	0,66	0,0005555	$10,361 \times 10^{-28}$

Les résultats présentés dans le tableau 4.1 valident l'équation simplifiée (4-4) et l'équation (4-5) peut être utilisée pour calculer le débit de fuite dans les micro-canaux d'un joint torique radial.

$$\dot{m} = \frac{\pi D_{bore}}{L_1} \frac{w_c H_1^3}{24 \mu r T} (P_{upstream}^2 - P_{downstream}^2) \left(\frac{1}{L_1} + \frac{1}{L_{21} + L_{22}} \right) \quad (4-5)$$

Débit de fuite lié à la perméabilité du polymère

Les même procédures d'essais que celles utilisées au chapitre 3, ont été réalisées afin de caractériser les membranes. En effectuant trois points de mesures à 30, 40 et 50°C, les trois paramètres ont été déterminés pour chaque type de membranes (voir le tableau 4.2), le coefficient de perméabilité peut ensuite être utilisé pour prévoir le débit de fuite des membranes à la température donnée (voir la figure 4.7). Comme l'indique la figure 3.5, à une pression de 537 kPa, les coefficients de perméabilité de chaque membrane ont été déterminés, ce qui permet de prévoir leurs débits de fuite.

Table 4.2 Paramètres κ_1 , κ_2 et κ_3 pour les membranes de A à F.

Membrane	Paramètres κ_1 , κ_2 et κ_3		
	κ_1	κ_2	κ_3
1	16281486	-0.000141	30072
2	16282234	-0.000431	29772
3	16278922	-0.000204	32514
4	102443	-0.000076	28031
5	132438	-0.000408	23248
6	12944	-0.000114	23447

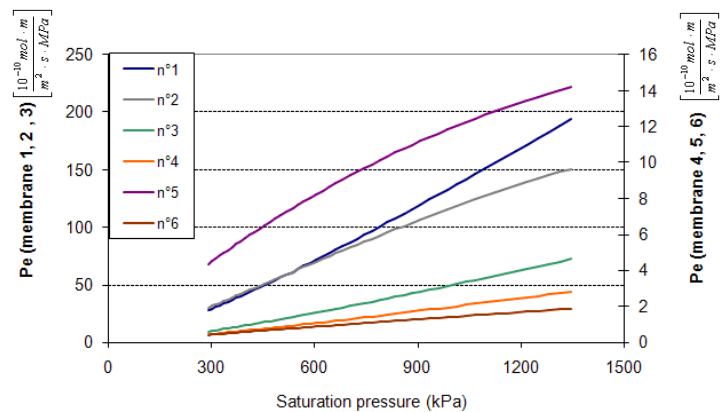


Figure 4.7 Modèles de prédiction pour membranes 1 à 6.

Analyse des contributions des débits de fuite en fonction de la perméabilité

L'évolution de la concentration en fonction du temps associée aux phénomènes de transport combinés (à 50 ° C) est montrée figure 4.8. Comme le transport de gaz dans les micro canaux se déroule rapidement, la ligne droite sur les 4 premières heures est considérée comme la contribution unique de débits de fuite via les micro canaux (zone 1). La perméabilité se manifeste après plusieurs heures. La zone 2 est considérée comme l'effet de la perméabilité seule.

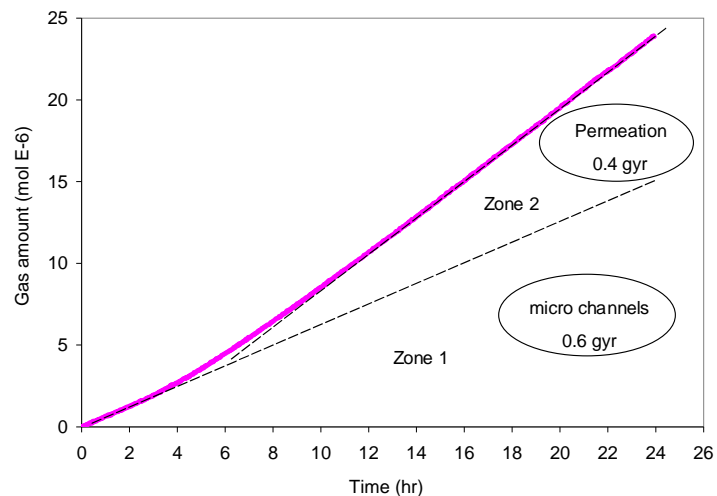


Figure 4.8 Hypothèses sur les distributions des fuites

La pente de la zone 1 donne 0,6 g / an, et le total du débit de fuite de ce montage est de 1,0 g/an. Par soustraction, le débit de fuite dû à la perméabilité dans les polymères est de 0,4 g/an. Par conséquent, la perméabilité et les micro-canaux contribuent respectivement pour 40 et 60 % au débit de fuite total du joint étudié.

La figure 4,9 résume les valeurs des débits de fuite de 10 raccords à 30, 40 et 50 ° C. À 30 ° C les débits varient de 0,2 à 0,9 g/an. À 40 ° C, le débit de fuite est au maximum de 0,3 g/an et la valeur minimale est de 1,3 g/an. À 50 ° C, les débits de fuite sont de l'ordre de 0,4 ~ 2,1 g/an. Cette dispersion est principalement due à la différence de perméabilité.

Pour conclure, le débit de fuite d'un raccord est déterminé par la perméabilité et l'écoulement dans les micro-canaux. Les polymères ayant de faibles coefficients de perméabilité présentent un grand intérêt pour la prévention des fuites. Le débit de fuite d'un raccord peut être réduit en améliorant le traitement de surface et/ou en utilisant des polymères à faible perméabilité.

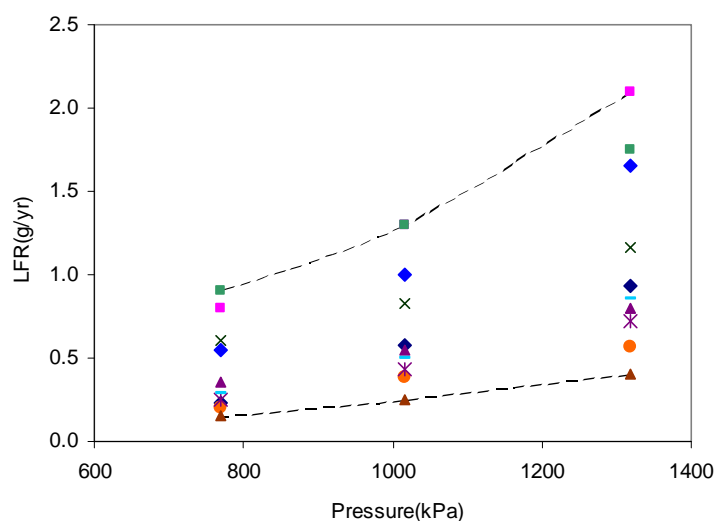


Figure 4.9 Débits de fuites de 10 raccords

Conclusions

Dans ce chapitre, la performance d'étanchéité d'un raccord avec un joint torique type radial a été analysée et modélisée en détail. Deux modes de fuite sont distingués: la perméabilité du gaz dans les polymères et l'écoulement du gaz dans les micro-canaux.

A l'aide d'un logiciel MAC.MARC, la contrainte, la pression de contact maximale et la largeur de contact ont été simulées et analysées. La pression de contact augmente linéairement avec l'augmentation de pression en amont. La largeur réelle de contact a validé les résultats de simulations avec de petites différences. L'écrasement joue un rôle important sur la pression de contact. Pour un faible écrasement, le contact du joint sur la paroi latérale devient dominant.

La combinaison de deux modes de fuite : écoulement et perméation a été établie, cette analyse permet de comprendre les comportements des débits de fuite de chaque type et de trouver les paramètres influençant et améliorant les performances d'étanchéité du joint.

Des analyses supplémentaires ont été effectuées sur l'influence des couples de serrage sur un joint type radial-axial et sur l'effet de la rotation d'un raccord avec de multiples joints toriques.

Conclusions

Cette thèse a présenté le développement d'une approche générique qui permet de prévoir les émissions de systèmes de climatisation automobile. L'étude du comportement de fuites de composants de base de ces systèmes, tels que les flexibles et raccords présente un grand intérêt.

Approche générique basée sur les données expérimentales de mesures de débits de fuite de systèmes de climatisation automobile

Le chapitre 2 a introduit une méthode d'essais en laboratoire pour déterminer le débit de fuite de systèmes de climatisation automobile en assurant une bonne précision de mesure. Cette étude a été à l'origine de la méthode de test européenne introduite par le règlement européen 706/2007. Les résultats d'essais sur de nombreux systèmes (environ 40) aussi bien que de nombreux composants du système (plus de 100) ont montré que les émissions provenant des systèmes sont égales à la somme des émissions de leurs composants avec un niveau d'incertitude acceptable. Ainsi, les deux méthodes se sont révélées appropriées pour la détermination du débit de fuite de n'importe quel système. En connaissant la contribution en mode fonctionnement de la climatisation automobile, qui est d'environ 2 à 4% du total annuel des émissions d'un système, la majeure partie du fluide frigorigène est émise pendant la période où le système est à l'arrêt, de sorte que le débit de fuite du système peut être déterminé sans effectuer d'essais en fonctionnement.

Une fois la loi de comportement du débit de fuite d'un système déterminée, la température annuelle moyenne d'une zone climatique est suffisante pour prévoir le débit de fuite annuel du système en utilisant le facteur de correction. L'approche générique des émissions de fluide frigorigène est exprimée par l'équation (1).

$$\dot{m} = k(P_{upstream}^2 - P_{downstream}^2) \quad (1)$$

Approche du débit de fuite au niveau du système complet par perméabilité du gaz dans les polymères

Une approche prenant en compte des effets de la température et de la pression sur la perméabilité a été proposée et validée par des données expérimentales avec une erreur inférieure à 7 %, et s'écrit comme suit:

$$\dot{m} = M_{HFC-134a} \cdot \frac{\pi r^2}{e} \cdot \kappa_1 e^{\left(\kappa_2 (\Delta P) - \frac{\kappa_3}{RT}\right)} \cdot \Delta P \quad (2)$$

Comme la relation entre la température de saturation du HFC-134a et sa pression de vapeur n'est pas linéaire, une équation basée sur l'équation de Clausius-Clapeyron a été utilisée pour exprimer de manière simplifiée la relation entre la température et la pression:

$$\ln P = A - \frac{\Delta H_{vap}}{RT} \quad (3)$$

L'équation (3) montre que la pression P , l'enthalpie de vaporisation, ΔH_{vap} , et la température T sont liées. Les incertitudes calculées entre les pressions et les données expérimentales sont inférieures à 1 % dans la gamme de températures de 0 à 80 °C. En combinant l'équation (2) et l'équation (3), le débit de fuite en fonction de la pression est exprimé par l'équation (4).

$$\dot{m} \propto e^{c_2 \Delta P} (P_{upstream})^{\frac{E_{pe}}{\Delta H_{vap}}} (P_{upstream} - P_{downstream}) \quad (4)$$

Le terme $e^{c_2 \Delta P}$ exponentiel en fonction de la différence de pressions varie dans la limite de 0 à 2 pour les échantillons de membranes $\frac{E_{pe}}{\Delta H_{vap}}$ à E dans cette zone de pression (de 0 à 1500 kPa). Le terme de puissance $(P_{upstream})^{\frac{\Delta H_{vap}}{E_{pe}}}$ est approximativement linéaire vis à vis de $P_{upstream} + P_{downstream}$. Par conséquent, le débit de fuite d'un flexible peut être considéré comme proportionnel à la différence des pressions au carré (voir Equation (5)). Cela prouve que le modèle de prédiction est adéquat pour l'ensemble des cas étudiés. Pour conclure, le comportement des fuites d'un système de climatisation automobile peut être modélisé par une équation (5), qui permet de représenter le débit de fuite total d'un système.

$$\dot{m} \propto (P_{upstream} + P_{downstream})(P_{upstream} - P_{downstream}) \quad (5)$$

Approche du débit de fuite au niveau du système complet par l'écoulement du gaz dans les micro-canaux

Le chapitre 4 a présenté l'étude des lois de comportement des débits de fuite des joints toriques. La méthode des éléments finis a permis d'analyser plusieurs facteurs importants tels que la pression de contact, la largeur de contact et la contrainte. Les résultats de modélisation de la largeur de contact ont été vérifiés par la visualisation des raccords transparents. Les contributions de la perméabilité et des micro-canaux ont été comparées. L'écoulement du gaz dans les micro-canaux est calculé par l'équation (6).

$$\dot{m} = \frac{\pi D_{bore}}{L_1} \frac{w_c H_1^3}{24 \mu r T} (P_{upstream}^2 - P_{downstream}^2) \left(\frac{1}{L_1} + \frac{1}{L_{21} + L_{22}} \right) \quad (6)$$

L'analyse de la largeur de contact a montré un facteur d'environ 2 entre $1/L_1$ et $1/(L_{21} + L_{22})$. Compte tenu de cette hypothèse et de l'équation (6), il vient :

$$\dot{m} = \frac{\pi D_{bore}}{L_1^2} \frac{w_c H_1^3}{16 \mu r T} (P_{upstream}^2 - P_{downstream}^2) \quad (7)$$

Pour conclure, à la fois la perméabilité du gaz dans les polymères et l'écoulement du gaz dans les micro-canaux peuvent être représentés par une fonction parabolique qui est proportionnelle à la différence des pressions au carré.

En résumé, le débit de fuite d'un système de climatisation automobile est la somme des débits de fuite de toutes les sources de fuites. Ces sources sont de deux types:

1. la perméabilité du gaz dans les polymères
2. l'écoulement du gaz dans les micro-canaux existant entre les joints et les parties métalliques des raccords.

Pour chaque mode d'émission, une loi de comportement a été développée et les modèles prédictifs permettent de prévoir les débits de fuite avec un nombre limité de mesures.